LARES: Lifesaving Aerial Rescue and Emergency Service

Providing timely delivery of fire emergency masks to facilitate a successful fire escape

AE3200: Design Synthesis

DSE Project Group 10

Delft University of Technology

TUDelft

This page is intentionally left blank

LARES: Lifesaving Aerial Rescue and Emergency Service

Providing timely delivery of fire emergency masks to facilitate a successful fire escape

by

DSE Project Group 10

Student Name	Student Number
Alex de Ruijter	4666291
Brian Püroja	4153847
Ilaria Rosa	4841743
Jelmer de Haan	4864131
Joey Herbold	4838351
Patrick Sheppard	4672828
Ran Chen	4770153
Rinto de Vries	4881699
Romy Harink	4850181

TUDelft

Executive Overview

In Europe alone, over 5,000 people die of residential fires every year. The vast majority of those deaths are caused by smoke inhalation. Many of these victims were trapped in their rooms and apartments, unable to leave through fire- or smoke-filled hallways. Rescue by the fire brigade can take up to an hour, by which time people are often dead. Especially in high-rise buildings, the fire brigade already needs half an hour to set up a forward command post on a higher floor. These delays cost lives and a better solution must be found.

This report aims to provide an overview of the design of a drone that can solve precisely these problems. By delivering easy-to-use emergency flight masks to people in high-rise buildings, victims of fire can rescue themselves. Flight masks enable humans to walk through smoke-filled corridors which would otherwise be impossible. If these masks are delivered in a timely fashion, people can evacuate the building before the fire brigade is fully deployed. An unmanned aerial vehicle (UAV) to accomplish this goal is discussed in this report.

Based on criteria such as size, controllability, flight efficiency, cost, and repairability an X8-copter design was determined to give the best results. A sensitivity analysis on the trade-off confirmed the choice for this concept.

Extensive analyses have been done into the sustainability of the operational part of the project and the design itself. Furthermore, a market and functional analysis have been performed. This resulted in a complete list of requirements for an effective mission.

The UAV's mission starts after receiving a signal from the control center. It will take off to a cruise altitude of 90 [m] and start cruising at 100 [km/h] to the GPS location received. The flight computer will predetermine a flight path to avoid any buildings and the vehicle is equipped with a collision-avoidance system that detects any unexpected obstacles. Once on-site, the UAV streams camera footage, over a 4G network with a latency of 40 [ms], to a trained operator that can detect the presence of life in the building and find a suitable place to deliver the masks. The first choice for delivery would be a roof or balcony. If these options are not available the operator will attach the drone to the building with the adhesion mechanism.

The adhesion mechanism is a one-of-a-kind system. Attached to the landing gear of the vehicle are suction cups capable of carrying 22 [kg] each. The suction is enabled by a vacuum pump and the system can adhere to flat non-porous surfaces.

Once attached to the building, a glass cutting mechanism can be deployed to get through the window pane. The choice for a cutting mechanism stems from two factors: The safety of people around the building and minimizing the additional oxygen supply through the new entry point. After performing tests on different types of glass, the most suitable solution was found to be scoring the pane with a tungsten-carbide wheel and inducing the required tensile stress through thermal expansion with a blowtorch. A custom design allows for a hole of 33 [cm] in diameter to be cut. This enables the flight masks of 8x16x14 [cm] and handheld transceivers of 11x6x4 [cm] to be taken out by the people in despair. The handheld transceiver allows the people inside to communicate with the fire department for navigating the building.

The vehicle will then take off from the building again and - if enough battery capacity and emergency equipment are left - it will look for other people in the building. If this is not the case, the UAV will touch down next to the building where it can be resupplied with equipment and charged batteries. After that, it can continue its mission.

The operating conditions call for a design that can withstand temperatures of up to 300 [°C]. The woven carbon fiber with epoxy that the frame is built out of cannot withstand such temperatures. Therefore, a thermal barrier coating is used to protect the carbon fiber. Furthermore, strict thermal operation limits

are in place for different internal subsystems giving a maximum temperature of 50 [°C]. This asks for an additional layer of glass mineral wool to insulate the system.

The system has a maximum operating range of 15 [km] and a maximum service speed of 115 [km/h]. Within its anticipated average 7 [km] range, the UAV can deliver up to 12 masks (assuming restocking the masks after the first delivery), with the same set of batteries. When the batteries are changed on-site, an additional 18 masks can be delivered on the new set. Furthermore, it is estimated that the UAV will be deployed eight times a year. The weight is anticipated to be 39 [kg] and the outer dimensions will be 2.3x1.9x0.6 [m].
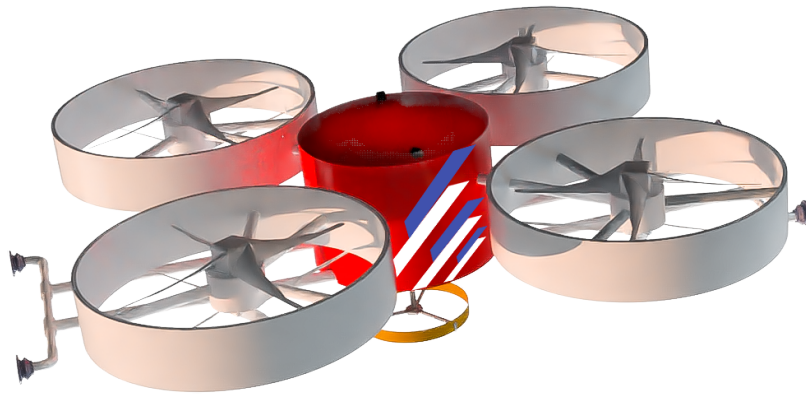
Figure 1: Render of the UAV design.

The design discussed above requires a variety of production methods. As the expected production number is low (a need of approximately twenty units is forecast for The Netherlands), it is not sensible to construct an entire production facility. Production thus takes place in multiple locations, where equipment such as autoclaves can be found. Assembly is then finally done at a central location.

The total price of the drone, including production, then adds up to 25,305 [EUR]. While not inexpensive, it is calculated that the return will be 15%, above the international average. It is thus a feasible design.

Before the product can be brought to market, however, there are still some steps to perform. Besides more design work, prototypes must be built and tested. Based on this testing, the UAV can eventually be certified by aviation authorities and only then go into manufacturing. This process must also be financed in some way by external investors. If such financing is secured, the design should be ready for market by 2023. In that year, it could start saving lives.

Contents

Nomenclature

Abbreviations

Abbreviation	Definition
AED	Automated External Defibrillator
AHRS	Attitude and Heading Reference System
AM	Additive Manufacturing
BEMT	Blade Element Momentum Theory
BPF	Blade Pass Frequency
C&S	Control & Stability
CAD	Computer-Aided Design
CAS	Collision Avoidance System
CFD	Computational Fluid Dynamics
CFRP	Carbon Fiber Reinforced Polymer
c.g.	Center of Gravity
CTE	Coefficient of Thermal Expansion
DoD	Depth of Discharge
DSE	Design Synthesis Exercise
EASA	European Aviation Safety Agency
EoM	Equation of Motion
ESC	Electric Speed Controller
FBD	Free Body Diagram
FBS	Functional Breakdown Structure
FFD	Functional Flow Diagram
FR	Fineness Ratio
GNSS	Global Navigation Satellite System
GPS	Global Positioning System
IEEE	Institute of Electrical and Electronics Engineers
IMU	Inertial Measurement Unit
IR	Infra-Red
LARES	Lifesaving Aerial Rescue and Emergency Service
LED	Light-Emitting Diode
LiDAR	Light Detection And Ranging
LTE	Long Term Evolution
MMoI	Mass Moment of Inertia
MMW	Millimeter wave
MTBF	Mean Time Between Failures
MTOW	Maximum Take-Off Weight
PCB	Printed Circuit Board
RADAR	Radio Detection And Ranging
RAMS	Reliability, Availability, Maintainability and Safety
RPM/RPS	Rotations Per Minute/Second
SCF	Safety Critical Functions
SF	Safety Factor
SONAR	Sound Navigation and Ranging
SWOT	Strength, Weakness, Opportunity and Threat
TBC	Thermal Barrier Coating
UAV	Unmanned Aerial Vehicle
VHF	Very High Frequency

Abbreviation	Definition
VTOL	Vertical Take-Off and Landing

Symbols

Symbol	Definition	Unit
a	acceleration	[m/s^2]
A	Area	[m^2]
A_{prop}	Area swept by propellers	[m^2]
b	Wing span	[m]
c	Crack depth	[m]
$\bar{c}$	Chord length	[m]
C_d	2D Drag coefficient	[-]
C_D	Drag coefficient	[-]
C_l	2D Lift coefficient	[-]
C_L	Lift coefficient	[-]
C_m	Stability coefficient for moments	[-]
C_X	Stability coefficient for forces in x-direction	[-]
C_Y	Stability coefficient for forces in y-direction	[-]
C_Z	Stability coefficient for forces in z-direction	[-]
d	Diameter	[m]
D	Distance	[m]
D	Drag	[N]
D	Non-dimensional differential operator	[-]
E	Young's modulus	[Pa]
F	Force	[N]
g	Gravitational Acceleration	[m/s^2]
h	Height	[m]
H	Compressive force	[N]
H_f	Flame height	[m]
i_{prop}	Propeller inclination angle	[rad]
I	Moment of inertia	[m^4]
I	Mass moment of inertia	[kg · m^2]
I_e	Battery current supplied	[A]
I_m	Motor Input current	[A]
J	Friction	[N]
K_{1c}	Fracture toughness	[Pa·m$^{1/2}$]
K_t	Stress concentration factor	[-]
K_T	Motor Torque constant	[-]
K_V	No-load speed	[RPM/V]
K_{V0}	Nominal no-load motor constant	[RPM/V]
K_Y	Non-dimensional radius of gyration about the Y-axis	[-]
k	Thermal conductivity	[W/(m·K)]
l	Length	[m]
L	Lift	[N]
M	Moment	[Nm]
m	mass	[kg]
n_r	Number motors	[-]
p	Roll rate	[rad/s]
P_{req}	Power required	[W]
q	Pitch rate	[rad/s]
Q_b	Battery Capacity	[mAh]

Symbol	Definition	Unit
Q_w	Heat release per unit wall length	[kW/m]
R_b	Internal Resistance of the battery	[Ω]
R_m	Internal Resistance of the motory	[Ω]
r	Yaw rate	[rad/s]
r	Radius or Radius of gyration	[m]
s_y	Vertical displacement	[m]
S	Surface area	[m^2]
t	Thickness	[m]
t	Time	[s]
T	Thrust	[N]
T	Temperature	[°C]
U	Voltage	[V]
U_{eu}	Voltage required by the ESC	[V]
U_m	Motor Input voltage	[V]
U_P	Incoming airspeed	[m/s]
U_T	Rotational velocity of the blade	[m/s]
u	Linear speed in x-direction	[m/s]
v	Linear speed in y direction	[m/s]
V	Shear force	[N]
V	Velocity	[m/s]
v_i	Induced Velocity	[m/s]
w	Linear speed in z-direction	[m/s]
w	Width	[m]
W	Weight	[N]
α	Helix angle screw	[rad]
α	Angle of Attack	[rad]
α_L	Linear thermal expansion coefficient	[°C^{-1}]
η	Efficiency	[-]
θ	Pitch angle	[rad]
μ	Relative density	[-]
μ	Static friction coefficient	[-]
ρ	Density	[kg/m^3]
σ	Stress	[Pa]
τ	Torque	[Nm]
ϕ	Friction angle or Roll angle	[rad] or [deg]
ψ	Yaw angle	[rad]
ω	Rotational speed	[rad/s]

1 Introduction

In 2019 alone, the United States fire brigades responded to more than a million fires, causing over 3700 civilian deaths[1]. In Europe, these numbers are even higher, with over 5000 deaths in residences alone[1]. Smoke inhalation was the cause of the majority of those deaths, in both the United States[2] as well as in Europe[2]. Usually, people are left trapped in their rooms while smoke is building up. As the fire brigade can take up to half an hour to arrive on-site in the European Union[3], let alone come to rescue people from higher floors, there is a clear need for a better and faster solution. Having spoken to multiple experts[3,4], timely delivery of fire escape masks is a promising solution.

This report aims at reporting the design of an emergency drone to provide people in need with timely delivery of fire escape masks. Important user requirements include the need for vertical take-off and landing, for an autonomous and fast cruising phase to the building on fire, the possibility to be used in urban areas, and being sufficiently sustainable. Besides, this report is part of a series of reports for the Design Synthesis Exercise (DSE) of the aerospace engineering faculty of the TU Delft. Nine bachelor students work eleven weeks to come up with a design solution for a specific problem. As a follow-up of the midterm report, in which a preliminary design was generated, this design will be finalized into a detailed design. The preliminary design is a quadcopter with eight co-rotating propellers. The drone will fly from a fire station to the emergency location and can deliver fire escape masks by adhering to the building and cutting through the glass in case there is no open window or balcony to land.

The report will be presented in the following structure. Chapter 2 describes the market analysis for a drone supplying fire escape masks. Chapter 3 provides the approach for sustainable development. Chapter 4 describes the mission profile of the drone. Chapter 5 dives deeper into the exact functions the drone needs to perform to fulfill the mission profile. The requirements follow from the functional analysis and are described in Chapter 6. Chapter 7 presents the preliminary design from the midterm report. This is followed by the detailed design of the subsystems. The design of the adhesion mechanism is discussed in Chapter 8. Chapter 9 presents the detailed design of the glass cutting mechanism. Chapter 11 and Chapter 12 describe the process of material selection and the sizing of the structural component respectively. Chapter 13 describes an analysis of the stability and control parameters. The data handling and communication system is designed in Chapter 14. The design is summarized in Chapter 15. The compliance of the user requirements is given in Chapter 16. This is followed by Chapter 17, in which a risk analysis is performed. Chapter 18 presents the production plan. Eventually, Chapter 19 describes a cost and financial analysis and describes the development logic for post-DSE.

2 Market Analysis

Before the UAV will be designed, it is important to analyze the market to see whether this product will be viable. Therefore, first, the demand for the product will be analyzed in Section 2.1, whereafter the market size will be described in Section 2.3. The expected market share will be discussed in 2.4. This chapter will be concluded with a SWOT analysis in Section 2.5.

2.1. Demand for UAV to assist the Fire Brigade
In the United States, in 2019 alone, the fire brigade had to respond to 1,291,500 fires. This resulted in around 3,700 deaths of civilians[1]. Of these deaths, the vast majority, 3,275 to be exact, were caused

---

[1] https://www.europeanfiresafetyalliance.org/our-focus/statistics/, Retrieved on 22/06/2021

[2] https://ameriburn.org/who-we-are/media/burn-incidence-fact-sheet/, Retrieved on 22/04/2021

[3] Robbert Heinecke (Head of corporate Information and Procurement of the fire brigade), on 28/05/2021

[4] Mark Bokdam (project manager of the fire brigade's Droneteam in The Netherlands), on 03/05/2021

by either the fire or smoke inhalation[1]. Also in Europe, most fire fatalities are due to smoke or toxic combustion gasses inhalation[2]. Therefore, smoke inhalation was deemed to be a serious problem, of which the number of casualties could and should be decreased. To fully understand what is specifically needed by the fire department to save lives, contact has been made with several firemen: Jan Reiling (member of the fire brigade, manages fire practices), Mark Bokdam (project manager of the fire brigade's Droneteam in The Netherlands) and Robbert Heinecke (Head of corporate Information and Procurement of the fire brigade). The main outcome from those conversations was that bringing supplemental oxygen inside with a UAV can result in dangerous situations due to the risk of the explosion of the oxygen tank. However, they saw an opportunity in delivering flight masks to people that are trapped in a burning building due to smoke. In the Netherlands, the fire brigade's average response time is 30 [min]. This includes the time needed to reach the site, deploy their material, and make a plan of attack. In the European Union, however, the time to reach the emergency site can already take up to 30 [min][3]. By using a UAV to deliver flight masks within the first 30 [min], people can already be saved, since UAVs do not experience traffic delays and can fly in overcrowded urban areas. Furthermore, the use of UAVs results in a safer environment for the firefighters, since UAVs can inspect the emergency site and can help people without putting the life of firefighters at risk.

The demand for assistance of UAVs in life-saving areas is not new. For example, medical drones that can deliver AEDs have already been successfully tested in Canada by Drone Delivery Canada in 2019. They had a 100% success rate, and their idea reduced the response time and therefore increased the survival rate of cardiac arrests[2]. Lastly, fire departments in the United States have acquired 69 UAVs between 2009 and 2017, to assist them in saving lives[3].

2.2. Market Description

A UAV that can deliver flight masks to people trapped inside a burning building will enter the general fire-fighting UAV market. This is a rather broad market, as applications can be categorized in the following functions: Scene monitoring, search & rescue, post-fire/disaster assessment, and finally wildland firefighting[4]. The UAV design that is proposed in this report will fall under the category search & rescue.

The most important players on the firefighting UAV market are: "Lockheed Martin Corporation, Elistair, Harris Corporation, BSS Holland B.V., Aerones, Yuneec International Company Limited, Dronefly, DSLRPros, Draganfly Innovations Inc., AeroVironment Inc."[5] Since these players operate in different segments of the market, some of them will be discussed in more detail to illustrate the diversity of the market.

- **Lockheed Martin Corporation** developed the Stalke XE UAS drone. The purpose of this UAV is to analyze wildfires by finding their exact location. This location data is subsequently relayed to helicopters of the fire brigade, to extinguish the fire more effectively[6].
- **Elistair** created a tethered UAV intending to assure continuous surveillance for a perimeter of 3 [km]. The fact that it is tethered, allows the UAV to stay in the air without having to change batteries, which increases operational time. This UAV enables the fire brigade to give real-time information to the firefighters on the ground.
- **Aerones** made a UAV that can extinguish fires. The UAV is connected with a hose on the fire truck and flies up to the place where the fire needs to be extinguished. This is especially useful for high rises, as a normal ladder of the fire brigade will not suffice in such a situation. Next to the hose, there is also a power line between the truck and the drone, which enables continuous

---

[1] https://ameriburn.org/who-we-are/media/burn-incidence-fact-sheet/, Retrieved on 22/04/2021

[2] https://www.coherentmarketinsights.com/ongoing-insight/ambulance-drone-market-39,   Retrieved on 20/04/2021

[3] https://www.dronefly.com/firefighting-drones-drones-in-the-field-infographic, Retrieved on 20/04/2021

[4] See footnote 3

[5] https://ksusentinel.com/2021/02/09/firefighting-drone-market-2021-28-new-way-of-fire-prevention-lockheed-martin-corporation-elistair-harris-corporation-bss-holland-b-v-aerones-yuneec-international-company-limited-dronefly-dslr/, Retrieved on 20/04/2021

[6] https://newatlas.com/unmanned-helicopter-drone-lockeed-martin/40706/, Retrieved on 20/04/2021

use[7].

Another important factor to take into account while analyzing the market is the market barriers. For this UAV, the largest market barrier will be the UAV regulations imposed by EASA. The UAV will fly in overcrowded areas, close to buildings, and is relatively heavy (30+ [kg], as will be further explained in Chapter 15). Therefore, this product has to be certified in the high-risk category: the certified category. This results in additional measures that need to be taken into account, to ensure a safe flight, thereby increasing development time and cost. It is important to note that before 2021, these regulations were administered by the national governments of the European Union or EASA member states. However, after 2021 this will be done by EASA. An advantage of this change in regulatory oversight is that the UAV only requires certification in one of the European Union or EASA member states, to be allowed to fly in all member states[8]. It is, however, difficult to predict the impact of the new regulations, as 2021 is a transition year, and the regulations for the certified category have not been written yet. Contact has been made with EASA concerning noise regulations. However, those two have not been determined yet[9].

Another expected market barrier stems from the projected operational conditions of the UAV. Technical challenges arise from the harsh conditions encountered in fire emergencies, including high temperatures and obscured vision due to smoke. Therefore, the design process will take significantly more time and funding compared to delivery UAVs manufactured from off-the-shelf components.

2.3. Market Size

As the fire brigade will be the only client for this UAV, it is important to determine how many UAVs they would like to implement. The UAV use case is primarily for high-rise buildings, therefore it will be located in large cities with proportionally more high rises. Cities with a considerable number of high-rise buildings in the Netherlands are grouped as G5: Amsterdam, Eindhoven, Rotterdam, The Hague, and Utrecht. In these five cities, there are 173 high rises built, 41 under construction, and 151 are currently planned for construction. Next to the G5, there is also the G40, which are the next 40 cities with high rises. The amount of high rises within the G40 varies between one and five. It is however important to include these cities as well since the housing shortage and increasing population will lead to an exponential increase of high rises[4]. As the UAV will have a range to cover an entire Dutch city (15 [km]), only one UAV will be positioned per city.

Based on this information, the market size can be estimated to be 20 UAVs. This batch size is determined based on the projected rapid increase of high rises within the G40 cities[4], and the expected completion date of the first product in 2023. However, not all G40 cities will use the UAV, because if a city has only a relatively small number of high rises it is not expected that they will buy a UAV. This will anticipate the additional building projects to be completed by that time. Following a successful implementation of the system within The Netherlands, the market can be expanded to Europe and other continents.

2.4. Predicted Market Share

The predicted market share is difficult to predict on the current firefighting UAV market, as there are only a few UAVs in use by fire brigades that perform a similar mission. To give an idea of the market share, two aspects will be looked into: competitors (and the aim of their products) and competitiveness of the cost.

The main competitors are already specified in Section 2.2. For the specific application of delivering flight masks, no other products currently exist on the market. Although a temporary monopoly can be expected because of the uniqueness of the product, large companies in the fire-fighting UAV market such as Lockheed Martin Corporation and DJI can relatively easily take over a part of the market share.

---

[7]https://www.aerones.com/other/drone/, Retrieved on 20/04/2021

[8]https://www.easa.europa.eu/newsroom-and-events/news/get-ready-new-drones-regulation, Retrieved on 23/06/2021

[9]Contact via mail with G. Malaval, an Aircraft noise expert at EASA, on 23/06/2021.

However, the market as a whole will also enlarge as the company can expand to more countries. Therefore it is expected that the market share will only decrease slightly over time.

Most companies are on the market with prototypes that are not yet mass-produced. Therefore, to evaluate the competitiveness of the estimated cost (16,413 [EUR], which will be further elaborated upon in Chapter 19), as discussed in detail in Section 19.1, a comparison will be made with a selection of UAVs that can be used in either a firefighting application or delivery of a payload of similar weight. For example, DJI has multiple UAVs that can be used to aid the fire brigade[10]. Table 2.1 presents three examples of UAVs on the market that can be used to aid the fire brigade, together with relevant technical specifications.

Table 2.1: Examples of UAVs on the market that can be used to aid the fire brigade.

Name	Flight time [min]	Max. operating temperature [°C]	Payload	Price [EUR]
Parrot ANAFI Thermal[11,12]	26	40	Thermal camera, no additional payload	2,299
DJI Matrice 300 RTK[13,14]	55	50	2.7 [kg]	9,999
DJI Matrice 600 Pro[15,16]	40	40	6 [kg]	4,210

As can be observed, the UAVs mentioned have a lower average price than the UAV that is designed in this report. However, it is important to note that none of these UAVs can withstand temperatures beyond 50 [°C], which drastically limits their application in close proximity to the fire. Additionally, the Parrot ANAFI Thermal cannot carry an additional payload besides the thermal camera. Therefore, it is concluded that the total price of 25,305 [EUR] is competitive on the fire fighting drone market, as this UAV has a lot of extra features compared to the UAVs mentioned in Table 2.1.

2.5. SWOT Analysis

To analyze the position of this company on the market a Strength, Weaknesses, Opportunities, and Threats (SWOT) analysis is made. This analysis can be found in Table 2.2.

Table 2.2: SWOT analysis for the emergency drone market.

		Helpful	*Harmful*
		STRENGTHS	WEAKNESSES
Internal		S1. All members have considerable knowledge of aerospace engineering, therefore a proper and feasible drone design can be expected.	W1. The members are all specialized in aerospace engineering, so any knowledge on other fields needs to be externally sought, which takes up resources. Additionally, external contacts often have limited time available to help out the members.
			Continued on next page

---

[10]https://enterprise.dji.com/public-safety/firefighting, Retrieved on 23/04/2021

[11]https://www.parrot.com/assets/s3fs-public/2021-02/anafi-thermal-product-sheet-white-paper-en.pdf, Retrieved on 23/04/2021

[12]https://droneshop.nl/parrot-anafi-thermal, Retrieved on 23/04/2021

[13]https://www.dji.com/nl/matrice-300/specs, Retrieved on 23/04/2021

[14]https://www.bol.com/nl/p/dji-matrice-300-rtk/9300000004667857/, Retrieved on 23/04/2021

[15]https://www.dji.com/nl/matrice600-pro/info, Retrieved on 23/04/2021

[16]https://www.skytools.com/flight-shop/sales/sales-outlet/dji-matrice-600-pro/, Retrieved on 23/04/2021

Table 2.2 – continued from previous page

	Helpful	*Harmful*
	S2. The members are helped by tutors who have more specific knowledge of drone design. They can be consulted by the members about design considerations. S3. The members are helped by a PM/SE teaching assistant, who can give feedback on the organization of the team, thereby increasing the workflow within the team. S4. The members are helped by external contacts, who can provide the team with information on, for example, how the fire brigade operates. This is useful as the team members have limited knowledge of this field. S5. The members are not paid during the project, which results in fewer development costs, as man-hours do not have to be paid.	W2. The team has limited experience with the complete design process. This could result in mistakes during the process that would not be made by a more experienced company. W3. The team does not have the capital at the moment to further implement the UAV.
	OPPORTUNITIES	**THREATS**
External	O1. The team could make alliances with existing (UAV) design companies, to share knowledge, thereby making a better and more efficient UAV. O2. Grants might be available for this application of UAVs. This will increase the capital of the team. O3. The EASA regulations on UAVs enable the team to use the UAV in different member states. Whereas if the national UAV regulations were still in place, it had to be certified in each of the different countries it is flying in.	T1. Initially, the firefighting UAV market will not be crowded, however, that can quickly change over time when the practicality of the product is proven. This could drastically decrease the market share of this team. T2. It is predicted that the use of UAVs will increase drastically over the years, for example, UAVs to deliver parcels. This will increase air traffic, hence making it more difficult for the product to fly effectively and without collisions. As an example: If Amazon would deliver half of its packages in New York by drone, 50.000 UAVs would be required, which results in a crowded airspace[3]. T3. If a large accident happens involving a UAV of a competitor, public support and the interest of companies might drop fast. This will result in fewer customers for the product.

Table 2.2 – continued from previous page

	Helpful	*Harmful*
	O4. As discussed in Section 2.4, there is a limited amount of companies that produce fire-fighting UAVs so far. Therefore, when entering the market, only a few competitors will be present. O5. The idea of using UAVs for emergency response is generally supported by the public. Of the general public in the UK, 87% tends to support drones for this use case[17]. This means there is public support for the use of UAVs by emergency services.	

3 Sustainable Development Approach

Sustainable development may be defined as "meeting the needs of the present without compromising the ability of future generations to meet their own needs."[1]. Engineering is a discipline that plays a major role in development: by designing, prototyping, and building innovative products, engineers greatly contribute to the development of new techniques across all industries. As the world shifts towards a more sustainable future, for instance by adopting new, greener techniques, it is fundamental that the impact of the solutions found during this design project is considered.

Before analyzing each solution into a greater level of detail, the definition of sustainability adopted throughout this report is presented. Next follows the strategy adopted during the design to ensure sustainability and finally, this chapter is concluded by concrete examples on how the adopted solutions help meet sustainability.

3.1. Sustainable Approach

Sustainability is a vast concept. To have a better understanding of its meaning, the term is often divided into three concepts, which are depicted into Figure 3.1.
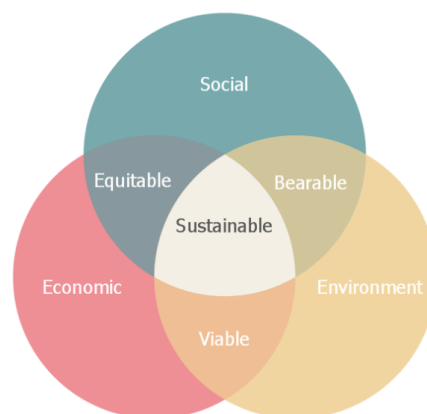
Figure 3.1: The three sustainability principles.[2]

---

[17]Drone Polling executed by ComRes for the Royal Aeronautical Society (RAS): `https://2sjjwunnql41ia7ki31qqub1-wpengine.netdna-ssl.com/wp-content/uploads/2018/05/Royal-Aeronautical-Society_DronesPolling_Tables_Wave-2.pdf`, visited on 26/04/2021

[1]`https://www.un.org/sustainabledevelopment/development.agenda/`, visited on 11/06/2021

These three core principles have been used throughout the complete project. How this has been done is explained below, per aspect of sustainability:

- **Environmental** sustainability has been ensured as follows. Firstly, the environmental impact of each solution has been weighted. This includes the amount of CO_2 in tonnes that the production of every material or part requires, as well as the impact that it has on the land. The water usage has also been taken into account. Moreover, in the manufacturing plan, an effort has been made to follow the principles of the lean thinking philosophy, to reduce waste. Detailed examples of how this has been done can be found in the next section. The concept of a circular economy has been kept in mind throughout by designing out waste and pollution, keeping products and materials in use, and regenerate natural systems[3]. A life cycle assessment has been performed to minimize waste across the drone's lifetime.
- **Social** sustainability refers to the contribution of the drone to society. This was ensured by considering night noise regulations, which improve the well-being of communities and individuals. Additionally, the drone is designed to improve the health of individuals trapped in a fire, by reducing the casualties due to smoke inhalation, thereby focusing on access to healthcare for everyone. With regards to the maintenance of the product and the well-being of the workers involved, fair treatment will be ensured. The Technology Readiness Level (TRL) is also a measure of social sustainability: it ensures that the technology plan is feasible and beneficial for the development of the drone. This was assessed throughout the design.
- **Economic** sustainability has been ensured by performing market analysis to clearly understand the demand for the drone. A budget has also been set up so that during the drone development the most economically viable solution is sought. The projected costs, as well as the analysis of all the expenditures involved in the design and manufacturing of the drone, have also been taken into account.

3.2. Sustainable Solutions

After the overall approach to sustainability has been commented upon in the previous section, the engineering solutions adopted have been scored in terms of sustainability.

Before moving into an in-depth discussion on sustainable engineering solutions, the overall sustainability of the project was assessed. This has been done by focusing on all three aspects of sustainability and attempting to score the main contributions that the drone has to each. To have a numerical score, a reference had to be taken. Although the designed drone is a first in its field, a choice has been made to compare it with the ANAFI thermal drone. This drone has a slightly different mission specification, however, it still presents a similar mission profile, albeit at lower speeds and with lower temperature requirements. The scores have been based on the documentation available on the website[4]. The scores have been decided as follows. A lower score means that the subject performs worse for a given parameter. Firstly, emissions have been compared: these are in terms of materials used, as well as the power source. As both ANAFI and LARES use batteries and a thermal coating, their score is equal. The noise was compared according to simulations performed for LARES and the available reports of ANAFI: this shows that ANAFI performs better, as it does not have corotating rotors, thereby generating less overall noise. ANAFI is also more compact. Technology-wise, ANAFI does not present the ambitious glass cutting mechanism that LARES has: thereby, LARES will need more technological resources to be completed, compared to ANAFI which uses well-resourced technologies. With regards to regulations, both drones adhere to the same EASA certifications, hence the equal score. The manufacturing of ANAFI is simpler compared to LARES as the payload of LARES is very fragile and must be installed correctly. Additionally, LARES uses carbon fiber, whose production can sometimes be tricky with hand layup. The lower score stems from these considerations. ANAFI can be disassembled almost completely, and so can LARES. However, the fact that LARES has a payload of maximum importance (while ANAFI was only designed as fireproof) makes it more

---

[2]Picture taken from `https://www.conceptdraw.com/examples/sustainable-development`, Retrieved on 17/06/2021

[3]`https://www.ellenmacarthurfoundation.org/circular-economy/concept`, Retrieved on 17/06/2021

[4]`https://www.parrot.com/en/drones/anafi-thermal`, Retrieved on 17/06/2021

complex to replace the payload compared to a drone where no replacement is needed. The cost of LARES is however cheaper than ANAFI: this may be also related to the fact that this cost estimation is preliminary, and that ANAFI is a drone with military purposes. The recyclability of the two drones is the same, as they can be re-purposed in similar ways since they present similar materials. Finally, LARES has been designed with re-usability in mind: it can last up until 10 years and its modular design allows for simple repairs, justifying the higher score compared to ANAFI, where modularity was not accounted for.
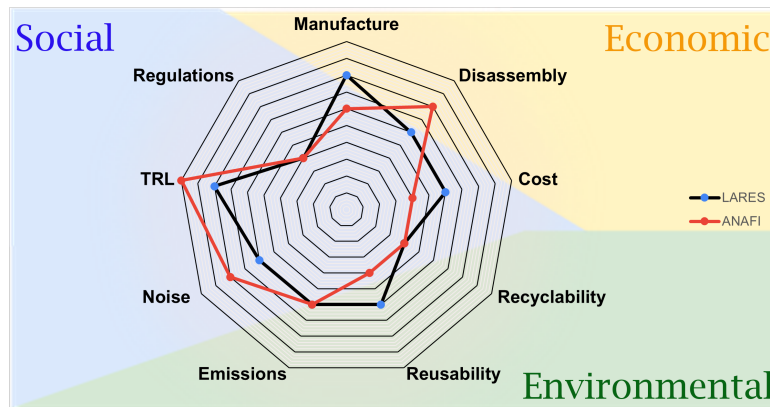
Figure 3.2: The sustainability aspects of the designed UAV scored in a spider diagram.

The Sustainability section is concluded with in-depth examples of how the design solutions affect the environment, and what possible mitigation techniques can be adapted.

Use of Carbon Fiber
Carbon fiber is vastly used in the design of this UAV, because of its lightweight and strength. However, with regards to sustainability, there are different concerns associated with the production and use of carbon fiber. To manufacture 1 ton of carbon fiber, 20 tons of CO_2 are emitted[5]. However, one advantage of carbon fiber is its low degradability: this is much lower than metals, therefore the UAV designed can be used for longer without the need for new carbon fiber to be purchased. Another mitigation strategy that can be adapted to reduce the impact of carbon fiber is to re-purpose the panels, by making for instance casings or other parts out of them.

LiPo Batteries
For the power supply, the UAV uses Lithium Polymer batteries. These are lightweight, powerful, and have a very high energy density. However, the delving of lithium is impactful[6]: holes are drilled in Lithium rich soil, which is then left uncovered for 18 months until the water has evaporated. Per tonne of Lithium produced, 2000 tonnes of water are needed. There are numerous mitigation strategies available to reduce the impact of Lithium batteries: these include new manufacturing techniques, focused on new electrode designs which yield higher energy and power density or longer lifetime. Other options, based on circular economy principles, include reuse of batteries in alternative vehicles, as well as reuse in less demanding energy storage applications and material recovery through recycling[5]. These solutions will always be sought when the lifetime of the batteries for the UAV reaches its end.

Noise quantification
Finally, with regards to social sustainability, an effort is made to quantify the maximum noise that the UAV produces. One of the requirements is that the UAV shall be able to fly during night times: for this, there are strict requirements on the maximum level of noise that can be produced by the UAV, namely 40 [dB]. The set of co-rotating rotors used in the design is known for being significantly noisier compared to the single rotor option; the mitigation strategy, in this case, has been to implement a duct,

---

[5]https://www.torayca.com/en/aboutus/abo_003.html, Retrieved on 17/06/2021

[6]https://energyx.com/resources/are-lithium-batteries-bad-for-the-environment/, Retrieved on 17/06/2021

which reduces the noise. The noise level has also been quantified: this was done through XRotor, however only for a single propeller case. The extension to a set of four coaxial propellers can be done through the results obtained in [6]. A more in-depth aeroacoustics calculation may be done via computational methods of analysis.

Using XRotor it was found that, for an altitude of 25 [m] above the ground, the maximum noise that can be heard is at most 25 [dB]. This is for an RPM value of 3000, a rather high operating point. As much as this is below the maximum acceptable noise for operation at night, this result only refers to a single propeller setup.

According to[6], the noise produced by having a corotating set of identical propellers can be estimated by superimposing the noise produced by each. This would give a total noise of 50 [dB], which is 10 [dB] above the maximum allowed. To keep the noise on the ground below the acceptable level, it is necessary to fly at an altitude of 90 [m] or to lower the RPM to 1250. Albeit the high amount of noise produced is not ideal, it is significantly lower than the first results without a duct; furthermore, the UAV will take off from a fire station, therefore the amount of noise for emergency use may vary. With regards to maximum noise production during the day, the limit is not reached. A fundamental conclusion is that the total noise produced by the set of rotors is very variable with the blade geometry, therefore it is unclear whether these findings can be generalized for this case. The best practice would be to test the aeroacoustic properties of these propellers as designed.

Renewable Energy
To improve the sustainability of the mission, renewable energy will be used to charge the batteries of the UAV. Types of renewable energy that can be used are solar power, wind energy, or water energy. It is therefore important that the place at which the UAV is stored has the services to provide renewable energy. Fire stations are already shifting more and more to renewable energy: In Friesland, all new fire stations are built to be carbon neutral[7].

4 Operations and Logistics

The UAV discussed in this report aims to deliver flight masks to people trapped by fire in high-rise buildings. In this chapter, the operations and logistics of this UAV will be outlined to provide a demonstration of the usage of the whole system. At first, a short overview of the selected payload will be given in Section 4.1.The operations will be then outlined in Section 4.2, the logistical issues will be addressed in Section 4.3 and finally Section 4.4 discusses the interaction between users and the UAV.

4.1. Selected Payload
The flight mask selected for this mission has dimensions as given in Table 4.1[1]. The UAV will carry six flight masks at once. With this number, it will be able to provide for either one large family or two families of three. Considering the average size of a household in The Netherlands is 2.2, and even below 3 for multi-person households[7], it is deemed likely that in most cases, the UAV will perform two deliveries before having to return to base or land near the fire trucks to restock the payload.

As will be discussed in Chapter 14, handheld transceivers will be used to enable rapid communication between the fire brigade and the recipient. Although no detailed selection has been made, as it is unknown which system the fire brigade currently uses, current systems weigh approximately 200 [g] and have the size given in Table 4.2.

---

[7]https://www.duurzaamgebouwd.nl/artikel/20200330-de-blauwdruk-van-circulaire-brandweerkazernes
[1]https://www.bol.com/nl/p/narwahl-fire-escape-mask-vluchtmasker-brandmasker/9200000066188378/, Retrieved 12/06/2021

Table 4.1: Dimensions of a flight mask

Parameter	Value	Unit
Width	8	[cm]
Height	16	[cm]
Length	14	[cm]
Weight	482	[g]

Table 4.2: Dimensions of a handheld transceiver

Parameter	Value	Unit
Width	11	[cm]
Height	6	[cm]
Length	4	[cm]
Weight	200	[g]

4.2. Operations Plan

The operations of this UAV can be generally illustrated using Figure 4.1. The diagram details seven steps during operation, which will be concisely discussed below.
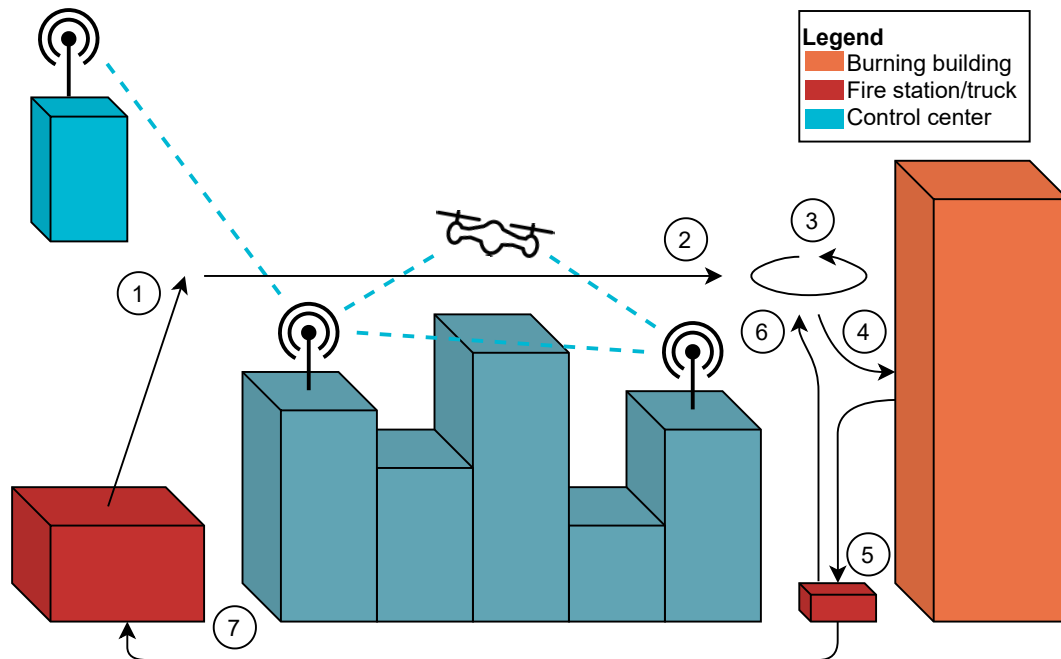
Figure 4.1: Overview of operations performed by the UAV

1. **Take-off:** Upon receiving the command from the control center, the UAV performs its pre-flight checks before autonomously taking off. It then climbs to its cruising altitude, which lies just above the height of most buildings in the area. A straight flight path between the base station and the burning building is desired and should be chosen if feasible. The operator is being called for visual verification during this phase.

2. **Cruise:** Once reaching the correct altitude, the UAV cruises to its destination. Since a maximum response time of 10 [min] is required, the UAV has to fly at a significant velocity in a nearly straight flight path. Even though the flight is autonomous, the operator must be in contact for visual verification.

3. **Surveillance:** When the UAV arrives, it hovers around the building and scans the situation. The operator in the control center takes on a more active role at this stage, practically taking over control to properly survey the developing fire. The operator is in close communications with the firefighters on the ground to determine the most critical rooms to deliver the flight masks to and to determine the best point of entry: The roof, a balcony, or a window.

4. **Delivery:** Once the operator has selected the point of entry, the drone can proceed to deliver the masks. This process can be split into three phases, which are attachment, glass cutting, and instruction. Note that the exact procedure for these phases will be discussed in more detail in Chapter 8 and Chapter 9.

    (a) **Attachment:** The UAV will first attach to the building at the location selected in step three.

This stabilizes the UAV in preparation for the glass cutting system.

(b) **Glass cutting:** Once the UAV is attached, it needs to force a window open. This is most effectively and safely achieved using a glass cutting mechanism. This opens a small hole for recipients to grab their masks through.

(c) **Instruction:** After the hole is created, recipients are instructed to grab the mask and place it over their heads. They can then be guided out of the building using, for example, a handheld transceiver.

5. **Landing:** Once the payload is delivered, the drone detaches and lands on the ground near the fire trucks. The fire brigade can then pick up the drone and restock it with additional flight masks and replace the batteries, preparing for the second delivery.

6. **Repeating missions:** After the UAV is restocked, it can take off again and repeat its mission. It then returns to step three of the operations.

7. **Return to base:** Once the situation is under control, the fire brigade and the UAV must return to base. The simplest way is to take the UAV back with the fire trucks. However, if its remained energy in batteries is still sufficient, it can also fly back to its base. After the mission is completed, the UAV will be inspected and prepared for future missions.

Note that as the UAV is controlled from the control center, and not by an operator on the ground, the base station of the drone is flexible. Ideally, the UAV would be stationed on top of a fire station, as this allows for easy resupply by the personnel already knowledgeable on the topic of fire emergencies. It also allows the fire brigade to take the UAV with them when returning from an emergency. However, stationing the drone on top of a hospital, for example near its helicopter pad, could also be possible if this improves coverage. A disadvantage is that flight masks would have to be separately delivered to this location. This does not, however, significantly change the mission as described in Figure 4.1.

Some final notes can be placed on the flight frequency of the UAV. In the years between 1996 and 2017, the highest death toll due to fire was 80 deaths in a year[2]. Taking a safety factor of two, and assuming for now all recipients can be successfully evacuated by the UAV, annually 160 flights would have to be performed. From Section 2.3 it was estimated that 20 UAVs will be manufactured, which means that on average 8 flights per UAV would have to take place per year.

4.3. Logistics

The operations plan outlined above covers the main aspects of the operations of the UAV. There are some logistical challenges, however, that should be addressed before the product can be brought to market. These concern the operations plan itself, but also production and testing. All of these topics will be discussed in this section.

4.3.1. Logistical Challenges with the Operations Plan

There are some logistical issues with the operations plan which are worth discussing. The first and most notable challenge lies at the base station. The base station will in most cases be the fire station, while a different location is technically possible as well, such as a hospital helipad or an airfield. In either case, sufficient supplies need to be delivered to restock the UAV. This includes the flight masks and handheld transceivers as discussed in Section 4.1, the replacement batteries, gas tanks, and in general spare parts for maintenance. As mentioned previously, stationing on top of a fire station eases this process, as fire stations already receive a number of these components in regular deliveries (e.g. flight masks).

A related challenge is the delivery of these supplies to the scene of the fire. Ideally, multiple missions can be performed from the forward base near the fire. However, this does require replacement batteries, flight masks, and handheld transceivers at the scene. It is too expensive to equip each fire truck

---

[2]https://opendata.cbs.nl/#/CBS/en/dataset/81452ENG/table?searchKeywords=fire%20alarm,   Retrieved 12/06/2021

with these parts, which leaves two options: The first is to have a separate bus built and equipped with the exclusive purpose of UAV support. This is expensive and could be excessive for the frequency of use the UAV will experience. The second is to equip one fire truck with these special supplies, and have that truck always sent to fires where the drone is deployed. There is a risk here, however, that the fire engine that is equipped to resupply the drone is working on combating another fire, which results in it being unavailable for another emergency. Despite this, it is deemed a better option than the expensive special UAV bus and thus recommended.

Another challenge is maintenance. As will also be discussed in Section 17.1.3, inspections are necessary after every flight. Although not much training is necessary, multiple firefighters will have to be trained to make sure that after each flight there is skilled personnel to inspect the UAV, which is a logistical challenge.

One final logistical challenge is how the UAV returns to base. Most frequently, the battery will be too drained to fly back to the base, which is the reason that the current operations plan discusses a return-to-base by the fire truck. However, as the UAV discussed in this report is large, it will not fit in a standard fire truck. Different solutions thus have to be found.

Partial disassembly should not be the first choice, as a mechanism to perform this easily increases the UAV weight. There is also no room for the drone to be placed on the outside of a standard fire engine. A completely separate vehicle just for the drone seems excessive. The Dutch fire brigade, however, also employs hook-lift trucks, which allow for easy change of truck payload.[3] This payload would then be a form of docking station for the drone, on which its landing gears can be clamped into place. Additionally, the truck payload can be equipped with flight masks, batteries, and even replacement parts. It then becomes a small mobile base station for the UAV.

A related challenge, considering a large size, is that it possibly does not fit through doors after return and landing at the roof of the fire station. In this case, a partial disassembly could also be a solution.

4.3.2. Logistical Challenges with Production and Testing

The production and testing phase also gives several logistical challenges. First, it should be noted that a large part of component production will be outsourced, as will be explained in Chapter 18. This gives significant challenges, as all components will have to be delivered, collected, and stored. It also introduces significant uncertainties on component delivery times: It could occur that, due to delays in production at an external party, there are weeks or even months between deliveries of certain parts. Therefore, it is of necessity to carefully schedule the production and tests, to minimize the delivery interval storage time.

A second and final challenge can be identified in the testing phase. As many of the tests will be performed at external locations, there is a great dependency on the facility's availability. Tests must thus be planned in a very early stage, which introduces the risk of not meeting certain deadlines (and thus being unable to perform certain tests). For flight tests, airspace must also be made available by the air traffic authorities, which can be a lengthy process and must thus be requested far in advance. All in all, these are challenges that can be overcome with proper planning, but challenges that must be faced early on in the process nonetheless.

4.4. User Interaction

As the person is trapped inside a burning building, the stress levels will be quite high. Therefore the person mustn't feel more anxious if a UAV flies towards the building. It is therefore important that it is identifiable that the UAV belongs to the fire brigade and is there to help. To this end, the main color of the UAV will be red. Color accents will be made with blue and white stripes, as this is the pattern used by the Dutch fire brigade on for example fire trucks[4].

---

[3]https://brandweer-informatie.nl/brandweerwagens/, Retrieved on 29/06/2021.

[4]https://www.brandweer.nl/brandweernederland, Retrieved on 28/06/2021
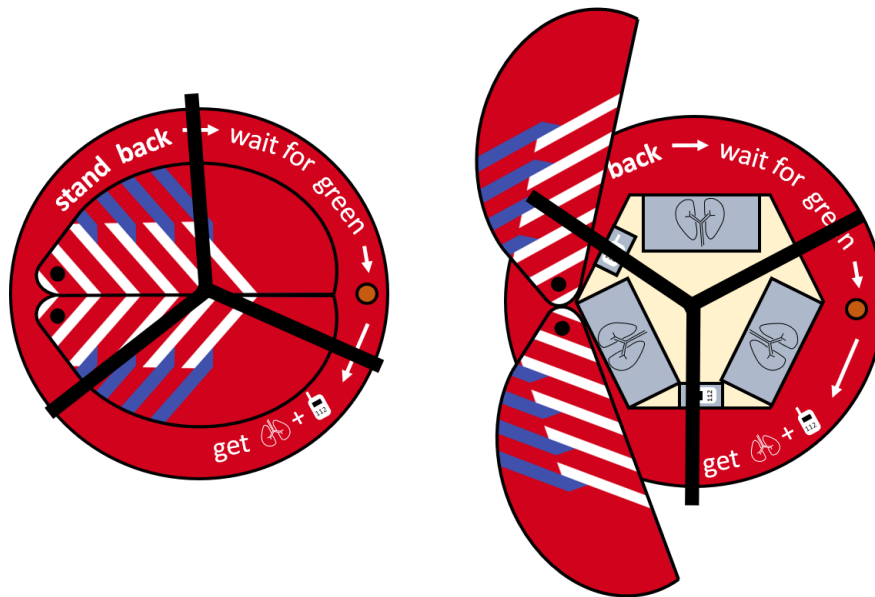
Figure 4.2: Bottom of the main body indicating the steps the person trapped in the building needs to take to get the flight masks and handheld transceiver.

Next to the fact that it should be identifiable, it is also important the design is easy to use as untrained people (i.e. the people trapped in a burning building) will be interacting with it. Therefore the usability will be assessed. Usability consist out of 5 main principles[5]:

- **Learnability**: How easy is it for the user to learn to use the system?
- **Flexibility:** How many users can use the system?
- **Robustness:** How well are users supported if they face errors?

These are mainly aimed for software development, but can similarly be used for product development. To make it easy for the users to learn the system, text, icons, and colors are used to indicate what is expected from the user. As can be seen in Figure 4.2 the bottom of the UAV indicate the three steps:

- **Stand back.** This needs to be done so that the person on the other side of the window cannot be accidentally hurt in case something goes wrong. This text is no longer visible when the doors have opened, which is done on purpose as it is no longer required to stand back.
- **Wait for green.** This is done so that the person does not try to reach for the flight masks too fast. This might result in dangerous situations, as the cutting mechanism might still be rotating or the doors have not fully opened yet. A red/green light is added to visually indicate the moment at which the person can reach for the payload. When it is green it also starts to blink to clearly indicate a new phase and also make it clear for colorblind people that a new step can be taken.
- **Get flight masks and a handheld receiver.** This is indicated with symbols to more clearly indicate the different packages that need to be taken out. It was also considered to do this with different colors instead of icons, however, this makes it unclear to the person what it is they are taking and this makes it difficult for color blind people to get the right packages.

All of this enables the person to get the flight masks and escape the building. These indications on the bottom of the main body are primarily important if there is no contact yet via telephone with the fire brigade. If the trapped person is already in contact with them (by calling the emergency number, e.g. 112 in The Netherlands) this can also be extra explained over the phone.

To test the usability of the system an experiment has been conducted. For that, it is important to

---

[5]https://www.uxbooth.com/articles/complete-beginners-guide-to-interaction-design/#methodologies, Retrieved on 28/06/2021

determine when a task is completed successfully (when the person grabs a flight mask and a handheld transceiver) and who the target audience is (everyone above 8 years, as everyone can be trapped inside a burning building and someone above 8 should be able to do the necessary actions and to follow the instructions). During the testing, any problems and their severity can be found and analyzed[6].

The questions asked were in three categories: General, task-related, and evaluation questions. The first refers to age and education level, as that might influence how well someone can understand the task. Task-related questions were questions in which was asked what the respondent thinks he/she has to do based on a shown image. Evaluation questions concern for example how easy the respondent think it was to understand the tasks and how stressful it was.

The questionnaire was not distributed on a small scale (nine respondents), therefore it only indicates the user interaction. However, it does have added value as based on this questionnaire it can be determined whether a large-scale questionnaire can be conducted or that the questionnaire/design should be changed. Around 80% of the respondents knew based on the design shown that it was a UAV for the fire brigade. The other 20% thought it was of the police, which is not necessarily problematic as the police also help people out. The vast majority of the people was able to perform the tasks correctly, i.e. stand back (maybe even call the emergency number), wait for green (even if the drone has the doors open, the people waited for the green light before they reached inside) and get the items.

Figure 4.3: Overview of choices for symbols for the flight mask. A, B, C and D were choices, the 'new' icon is a suggestion of one of the respondents.

The first evaluation question was concerning the symbols used, especially the one of the flight mask as that is a relatively unknown object. The question showed icons A, B, C, and D of Figure 4.3. Three out of nine respondents thought the lungs were a clear symbol. The others would prefer picture B or D, as it would be more memorable and recognizable. One of the respondents also suggested using an airplane oxygen mask as that is a recognizable situation for people. Therefore it is recommended to investigate the use of this symbol in further research. Also, it was recommended to enlarge the antenna of the handheld transceiver to differentiate it more from a normal phone.

Additionally, the respondents replied that the difficulty to understand what to do was medium (5/10, with 1=very easy, 10=very difficult). It was noted that the respondents would be quite anxious (7.5/10, with 1=not anxious, 10=very anxious), however more research needs to be done to identify where the largest part of that anxiety comes from (being trapped in a burning building or from the UAV).

For future research, it is recommended to do larger-scale research with a more diverse group (the majority of the respondents were between 20 and 23 years old). Additionally, it should be done with a prototype, as identifying what things are on a 2D scale is found to be difficult by the respondents.

5 Functional Analysis

The design cannot start without an overview of the drone's function. This is done through functional analysis. This functional analysis is performed by generating a functional flow diagram (FFD) and a functional breakdown structure (FBS), which are based on the operations specified in Chapter 4.

---

[6]https://www.interaction-design.org/literature/topics/usability-testing, Retrieved on 28/06/2021

These two functional diagrams will be again used to make a requirement analysis, which will be given in Chapter 6.

Section 5.1 presents the FFD. The FFD describes all functions that need to be performed to fulfill the mission. The functions are specified in blocks, categorized into four levels, and in time order. Section 5.2 presents the FBS. The FBS is an AND-tree that breaks down the mission need statements and provides a compact overview of all functions in detail. It is consistent with the FFD.

5.1. Functional Flow Diagram
In the FFD, AND and OR branches are presented. This is to highlight that the product is expected to perform several functions simultaneously (AND) while remaining flexible to deal with multiple situations (OR). The dotted arrows are meant to link the same function throughout the FFD. If the same block appears twice in the diagram, the second instance is clarified by REF. Dashed arrows indicate a feedback relationship between the function blocks. The diagram is given in the next two pages.

5.2. Functional Breakdown Structure
The FBS is a tool used to present all functions in parallel that are needed to fulfill the mission need statement. Different from the FFD, the FBS is an AND tree. This means that the FBS is a summation of all the functions which can be regarded as a base of requirements. Note that the FBS can only be detailed up to a certain level since the FBS should not exclude any design options. The FBS can be found after the FFD.

Stand-by / Flight Phases Process Flow

Top-level phases
- 1.0 Stand-by phase
- 2.0 Start-Up phase
- 3.0 Take-off & Climb Phase
- 4.0 Cruise Phase
- 5.0 Mission Phase
- 6.0 Return-to-Base Phase
- 7.0 Storage and Maintenance Phase

1.0 Stand-by phase
- 1.0 REF Stand-by phase
- 1.1 Perform System Checks
  - 1.1.1 Turn on Flight Computer
  - 1.1.2 Relay Weather Information
  - 1.3 Perform System Checks
    - 1.3.1 Synchronize Information with Flight Computer
    - 1.3.2 Perform Subsystem Checks
      - 1.3.2.1 Check Last Maintenance Cycle
      - AND
      - 1.3.2.2 Check GPS
      - 1.3.2.3 Check Sensors
      - 1.3.2.4 Check Power System
      - 1.3.2.5 Update Status of Subsystems
- 2.0 REF Start-Up phase

2.0 Start-Up phase
- 2.0 REF Start-Up phase
- 2.1 Start-Up Systems
  - 2.1.1 Power on Electronics
  - 2.1.2 Turn on Flight Computer
    - 2.1.2.1 Start-up Sensors
    - 2.1.2.2 Start-up Communications
    - 2.1.2.3 Confirm Operational Status
- 2.2 Receive Mission Data
  - 2.2.1 Receive Coordinates of Emergency Site
  - 2.2.2 Calculate Optimal Flight Path within constraints
- 3.0 REF Take-off & Climb Phase

3.0 Take-off & Climb Phase
- 3.0 REF Take-off & Climb Phase
- 3.1 Open Hangar Door
- 3.2 Release from Docking Station
- 3.3 Perform Planned Taxing route out of hangar
- 3.4 Perform Vertical Take-Off
- 3.5 Perform Climb to Cruise Altitude (Defined by Optimal Flight Path)
- 4.0 REF Cruise Phase

4.0 Cruise Phase
- 4.0 REF Cruise Phase
- 4.1 Transit from Climb to Cruise
  - 4.1.1 Set Control Variables to Optimum Cruise Configuration
- 4.2 Cruise and Control
  - 4.1.2 Accelerate towards Optimum Cruise Speed
  - 4.2 REF Cruise Control
    - 4.2.1 Calculate Cruising Conditions when changes occur
    - 4.2.2 Perform Corrections to Flight Configurations when necessary
- 4.3 Transit from Cruise to Descend
  - 4.3.1 Change Flight Configurations to Approach setting
  - 4.3.2 Activate Acoustic and Visual Warning Systems
  - 4.3.3 Start Approach to Emergency Site
- 5.0 REF Mission Phase

5.0 Mission Phase
- 5.0 REF Mission Phase
- 5.1 Search & Detect
  - 5.1.1 Detect Lifesigns
  - 5.1.2 Measure Absence of Heat/Fire Source
- 5.2 Approach Recipient
  - 5.2.1 Communicate with Recipient
  - 5.2.2 Confirm if Window can be Opened
  - OR — Yes / No
  - 5.2.3 REF Adhere to the Building
  - 5.2.3 Adhere to the Building
    - 5.2.3.1 Activate Front Suction Set
    - 5.2.3.2 Reduce Thrust Level
    - 5.2.3.3 Rotate Main Body Downwards
    - 5.2.3.4 Activate Rear Suction Set
  - 5.2.4 Breach Window
    - 5.2.4.1 Check for Multiple Layers
    - 5.2.4.2 Position Scoring Mechanism on Window
    - 5.2.4.3 Check if Equipment is Properly Positioned
    - 5.2.4.4 Start Cutting through the Glass
    - 5.2.4.5 Remove Glass Chunk
- 5.3 Deliver Payload
- 5.4 Reload
- 6.0 REF Return-to-Base Phase

Facilitate escape of persons trapped in high rise fire scenarios by use of an UAV

1.0 Stand-by phase
- 1.1 Turn on Flight Computer
- 1.2 Relay Weather Information
- 1.3 Perform System Checks
  - 1.3.1 Synchronize Information with Flight Computer
  - 1.3.2 Perform Subsystem Checks → F

2.0 Start-Up phase
- 2.1 Start-Up Systems
  - 2.1.1 Power on Electronics
  - 2.1.2 Turn on Flight Computer → A
- 2.2 Receive Mission Data
  - 2.2.1 Receive Coordinates of Emergency Site
  - 2.2.2 Calculate Optimal Flight Path within constraints

3.0 Take-off & Climb Phase
- 3.1 Open Hangar Door
- 3.2 Release from Docking Station
- 3.3 Perform Planned Taxiing route out of hangar
- 3.4 Perform Vertical Take-Off
- 3.5 Perform Climb to Cruise Altitude (Defined by Optimal Flight Path)

4.0 Cruise Phase
- 4.1 Transit from Climb to Cruise
  - 4.1.1 Set Control Variables to Optimum Cruise Configuration
  - 4.1.2 Accelerate towards Optimum Cruise Speed
- 4.2 Cruise and Control
  - 4.2.1 Calculate Cruising Conditions when changes occur
  - 4.2.2 Perform Corrections to Flight Configurations when necessary
- 4.3 Transit from Cruise to Descend
  - 4.3.1 Change Flight Configurations to Approach setting
  - 4.3.2 Activate Acoustic and Visual Warning Systems
  - 4.3.3 Start Approach to Emergency Site

5.0 Mission Phase
- 5.1 Search & Detect
  - 5.1.1 Detect Lifesigns
  - 5.1.2 Measure Absence of Heat/Fire Source
- 5.2 Approach Recipient
  - 5.2.1 Communicate with Recipient
  - 5.2.2 Confirm if Window can be Opened
  - 5.2.3 Adhere to Building → C
  - 5.2.4 Breach Window → G
- 5.3 Deliver Payload
- 5.4 Reload
  - 5.4.1 Flip to Hover Mode → D
  - 5.4.2 Land at Supply Vehicle → B
  - 5.4.3 Reload the UAV and Repeat the Mission → E

6.0 Return-to-Base Phase
- 6.1 Descend and Land
  - 6.1.1 Locate Supply Vehicle
  - 6.1.2 Descend and Approach Vehicle
  - 6.1.3 Land on Top of Supply Vehicle
- 6.2 Shutdown Systems
  - 6.2.1 Switch off Propulsion Systems
  - 6.2.2 Switch off Visual and Acoustic Signal Systems
  - 6.2.3 Switch off Electronics and Flight Computer

7.0 Storage and Maintenance Phase
- 7.1 Return UAV to Docking Station
- 7.2 Inspect UAV
  - 7.2.1 Inspect UAV for Structural Damages
  - 7.2.2 Inspect Flight Logs for Abnormalities
  - 7.2.3 Inspect Payload Deployment Systems
  - 7.2.4 Inspect Scoring Mechanism for Wear
  - 7.2.5 Check Battery Health and Electric Components
- 7.3 Connect Powering Cables for Battery Charging
- 7.4 Switch to Stand-by Mode

8.0 Detection and Emergency Mode
- 8.1 Self-detect
  - 8.1.1 Assess Power
  - 8.1.2 Assess Propulsion
  - 8.1.3 Assess Control and Communication
  - 8.1.4 Assess Sensors
  - 8.1.5 Assess Payload Deployment Systems
- 8.2 Perform Emergency Landing
  - 8.2.1 Locate Nearest Clearing Suitable for Landing
  - 8.2.2 Descent to Emergency Landing Site
  - 8.2.3 Decelerate and Land
  - 8.2.4 Switch off all Systems (except beacon if still operable)

A
- 2.1.2.1 Start-up Sensors
- 2.1.2.2 Start-up Communications
- 2.1.2.3 Confirm Operational Status

B
- 5.4.2.1 Receive Supply Vehicle Coordinates
- 5.4.2.2 Land at Supply Vehicle
- 5.4.2.3 Switch off Thrusters

C
- 5.2.3.1 Activate Front Suction Set
- 5.2.3.2 Reduce Thrust Level
- 5.2.3.3 Rotate Main Body Downwards
- 5.2.3.4 Activate Rear Suction Set

D
- 5.4.1.1 Deactivate Rear Suction Set
- 5.4.1.2 Increase Thrust
- 5.4.1.3 Rotate Main Body Upwards
- 5.4.1.4 Deactivate Front Suction Set and Detach

E
- 5.4.3.1 Replace Batteries and Refill Payload
- 5.4.3.2 Receive Clear to Take-off
- 5.4.3.3 Start VTOL Procedure
- 5.4.3.4 Climb to Point of Departure

F
- 1.3.2.1 Check Last Maintenance Cycle
- 1.3.2.2 Check GPS
- 1.3.2.3 Check Sensors
- 1.3.2.4 Check Power System
- 1.3.2.5 Update Status of Subsystems

G
- 5.2.4.1 Check for Multiple Layers
- 5.2.4.2 Position Scoring Mechanism on Window
- 5.2.4.3 Check if Equipment is Properly Positioned
- 5.2.4.4 Start Cutting through the Glass
- 5.2.4.5 Remove Glass Chunk

6 Requirements

This chapter includes all user, subsystem, and safety requirements agreed upon in earlier stages of the design. The user requirements are described in Section 6.1, the subsystem requirements in Section 6.2 and finally the safety requirements in Section 6.3.

6.1. User Requirements

This section describes the user requirements that were established in close contact with the client. These requirements define what the user wants the product to fulfill. The compliance of these requirements will be checked in Chapter 16, including an explanation of the verification method.

- TL-USER-01: The minimum weight of the payload shall be 10 [kg].
- TL-USER-02: The payload shall have a maximum indicative volume of 1 [m^3].
- TL-USER-03: The vehicle shall have a maximum cruise speed of 100 [km/h].
- TL-USER-04: The vehicle shall respect European night noise regulations.
- TL-USER-06: The vehicle shall have a minimum range of 7 [km].
- TL-USER-07: The lifetime of the vehicle shall be 10 years minimum.
- TL-USER-08: The system shall be exposed to a temperature of 300 [$^\circ$C] for at least 5 [min] without any structural damage.
- TL-USER-09: The system shall be exposed to a temperature of 300 [$^\circ$C] for at least 5 [min] without any functional damage.
- TL-USER-10: The system shall be fully autonomous.
- TL-USER-11: The system shall use GPS for guidance.
- TL-USER-12-01: The vehicle shall use acoustic warning systems when approaching the ground.
- TL-USER-12-02: The vehicle shall use visual warning systems when approaching the ground.
- TL-USER-13: The vehicle shall be equipped with proximity sensors.
- TL-USER-14-01: The vehicle shall be able to operate in densely populated areas.
- TL-USER-14-02: The vehicle shall be able to operate at a minimum distance of 5 [m] from people.
- TL-USER-14-03: The vehicle shall be able to operate at a minimum distance of 3 [m] from any object.
- TL-USER-15: The system shall respect aeroacoustic regulations for emissions over urban areas.
- TL-USER-16: The vehicle shall be allowed to fly overnight.
- TL-USER-17: The vehicle shall be able to fly with a maximum of 8 [bft].
- TL-USER-18: The vehicle shall be able to fly in wet and dry weather conditions.
- TL-USER-19: The vehicle shall be able to fly at 50% of the propulsive system working.
- TL-USER-20: The system shall not cost more than 10,000 [EUR] including the fireproof structure and the cost of the payload.
- TL-USER-21-01: The main structure shall be able to be reused for at least another 10 years after the UAV lifetime of 10 years has been completed.
- TL-USER-21-02: The vehicle components shall be modular to facilitate reuse.
- TL-USER-22: The batteries, if any, shall be reusable.
- TL-USER-23: The vehicle shall be VTOL capable.
- TL-USER-24: The payload release system shall be able to be operated by a layman with minimal instructions from a remote operator.
- TL-USER-25: The system shall be equipped with a two-way communication system to allow instructions and observations between a dispatcher and on-site persons.
- TL-USER-26: The system can be operated by a certified pilot.

6.2. Sub-system Requirements

The subsystem requirements are derived from the user requirements and include all the technical details to which the system is designed. In subsequent chapters, the compliance of these will be elaborated upon where appropriate.

- TECH-OR-01: The system shall have an interface to allow for remote piloting.
- TECH-OR-02: The system shall allow for human-in-the-loop control.
- TECH-OR-03: The flight system shall respond to manual inputs within 50 [ms].
- TECH-ADH-01: Two of the four suction cups shall be able to support the UAV when it is attached to a building.
- TECH-ADH-02: The suction cups shall be able to withstand temperatures up to 200 [°C].
- TL-GCM-01: The glass cutting mechanism shall cut through one layer of glass within 1 [min].
- TL-GCM-02: The glass cutting mechanism shall extend the tri-arm for at least 20 [cm].
- TL-GCM-03: The glass cutting mechanism shall not plastically deform under the loads induced by the cutting of the glass.
- TL-GCM-04: The mass of the glass cutting mechanism shall be no more than 1.5 [kg].
- TL-GCM-05: The forces induced to the adhesion system by the glass cutting mechanism shall be no more than twice the pull-off force of one suction cup.
- TECH-PROP-01: The propulsion system shall provide a force of 574 [N].
- TECH-PROP-03: The propulsion system shall guarantee power for autonomy for 10 [km].
- TECH-PROP-04: The propulsion system shall deliver a total power of more than 10,500 [W] during flight.
- TECH-PROP-05: It shall be possible to refill the power storage in 60 [min].
- TECH-PROP-06: The power system shall have an efficiency of at least 95%.
- TECH-PROP-07: The propulsion system shall use renewable energy.
- TECH-PROP-08: The propulsion system PCB component shall be insulated from the outside.
- TECH-PROP-09: Static electrical charge shall be released to the environment.
- TECH-GEN-05: During cruise, the vehicle shall cruise at a minimum altitude of 25 [m].
- TECH-TEMP-01: The materials that can be in contact with fire shall not be flammable.
- TECH-OC-03: The materials that can come into contact with water during rain shall be corrosion resistant.
- TECH-OC-04: The materials that can come into contact with water during rain shall be water-proof.
- TECH-PAY-02: The payload shall be protected against the outside heat.
- TECH-STRUC-01: The material properties of the used structural materials shall have no degradation during the UAVs operational lifetime.
- TECH-STRUC-02: All principal structural elements shall be inspectable via non-destructive tests.
- TECH-AR-01: The assembly methods used shall be able to maintain their functionality at a temperature of 300 [°C] for a minimum of 5 [min].
- TECH-AR-02: The assembly methods used shall withstand the critical load cases (ultimate loads).
- TECH-SPAIR-01: The structure shall enable the drone to carry a payload of at least 10 [kg].
- TECH-SPAIR-02: The interface of the structure with the payload shall carry the payload without loss of functionality.
- TECH-PAY-04: The payload shall be delivered without a loss of function.
- TECH-SPAIR-03: The structure shall be able to support a payload of six flight masks and two handheld transceivers.
- TECH-SPAIR-04: The structure shall enable external access to the payload.
- TECH-SPRIR-01: The structure shall accommodate for removal of the power source.
- TECH-SPRIR-02: The structure shall accommodate for recharging of the power source.
- TECH-SCIR-01: The structure shall allow access to the onboard computer.
- TECH-CS-04: The C&S system shall use a maximum power of 50 [W].
- TECH-CS-05: The sensor input-processing time shall be no more than 0.25 [sec].

- TECH-CS-06: The C&S system shall maintain controllability of the vehicle with a loss of propulsive power of maximum 50%.
- TECH-ATT-01: The system shall be able to keep track of its attitude during its operational lifetime.
- TECH-GEN-01: The vehicle shall be able to land and take off from most urban areas, such as buildings, streets, and parks.
- TECH-GEN-03: The vehicle shall be dynamically stable at all flight conditions.
- TECH-GEN-04: The vehicle shall be statically stable at all flight conditions.
- TECH-OC-02: The C&S system should be able to compensate for disturbance inputs up to 8 [bft] of wind speed.

6.3. Safety Requirements

The safety requirements refer to design considerations that improve the safety of external parties during the mission of the UAV. In Chapter 16 the compliance to these requirements will be checked.

- TECH-SSR-01-01: The vehicle shall be visible at a range of 500 [m] during the night.
- TECH-SSR-03: The vehicle shall have no sharp edges that may damage the user.
- TECH-SSR-04: The vehicle shall be able to apply for EASA certification for a high-level risk drone.
- TECH-SSR-05: The vehicle shall produce a maximum noise of 85 [dB] during the day, as per European regulations.
- TECH-SSR-06: The vehicle shall produce a maximum noise of 40 [dB] during nighttime, as per European regulations.
- TECH-SSR-08: The vehicle shall initiate autonomous landing procedures after a LOS of 3 [s].
- TECH-SSR-09: The vehicle shall be able to maintain communications with an operator 99% of the operational time.
- TECH-SSR-10: The vehicle shall be able to recover altitude after a physical control system failure.

7 Preliminary Design Overview

The basis of the detailed design discussed in this report is a preliminary design that has been established in previous reports[8, 9]. This preliminary design was obtained using a concept trade-off. The purpose of this chapter is to summarize this trade-off and to provide an overview of the starting point of the design. First, the initial concepts will be given, after which the trade-off will be summarized. Afterward, the chosen concept will be worked out further into a preliminary design.

7.1. Initial Concepts

For the preliminary design, four design candidates were considered, as also defined in the baseline report[8]. The four design candidates can be seen in Figure 7.1: an X-8 quadcopter design, a Y-6 tricopter design, a blended wing body design, and a tiltwing UAV. Each of these candidates was found to be capable of fulfilling the mission as stated in Chapter 4. A trade-off was made between these four concepts to find the most suitable design candidate to be developed into a detailed design.

7.2. Trade-off

The trade-off was performed using a graphical comparison method: Each criterion was quantified and then given a certain color based on its value. In total five trade-off criteria were considered: size, controllability, flight efficiency, cost, and repairability. Below, their definitions and manners of assessment are listed.

- **Size:** The size of the four configurations was determined by the payload. The width and length of all concepts are primarily dominated by the size of the propellers. These were sized based on a statistical relationship between the MTOW and propeller area. The height of the concepts

(a) X-8 and Y-6 multicopter UAV configurations

(b) Tricopter UAV with aerodynamic body concept

(c) Tiltwing UAV
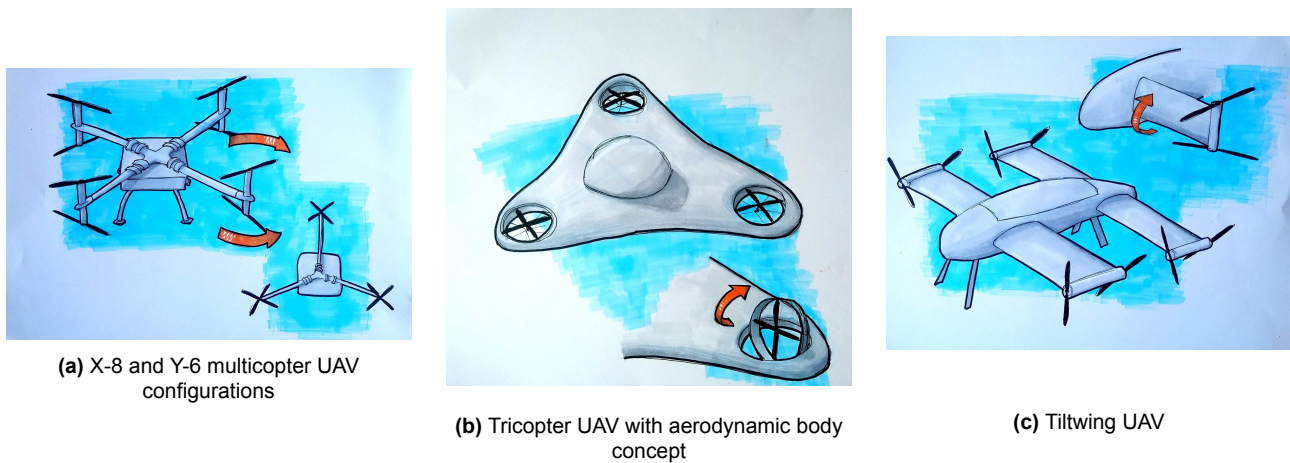
Figure 7.1: Sketches of the design concepts

is primarily determined by the height of the payload, except for the tiltwing configuration: For that concept, the height should be at least the propeller radius.

- **Controllability:** Controllability is defined as the ease with which and the extent to which the aircraft can be controlled. Redundancy and agility were also taken into account for this criterion. In general, more rotors increase redundancy. Multicopter designs are also lighter than winged aircraft and thus more agile. (Tilt)winged aircraft are more of a hassle, as they have to satisfy stability requirements in a variety of flight modes: Hover, cruise, and the transition phase.
- **Flight Efficiency:** Flight efficiency is a representation of the power used to perform the flight. A distinction must be made between efficiency in hover and cruise. Multicopter aircraft perform better in the former, whereas aircraft with wings are more efficient in cruise. As hover is the dominant flight state for this mission, efficiency in this phase is deemed more important and the tricopter and quadcopter UAV concepts thus score better.
- **Cost:** For the cost criterion, the tri-, and quadcopter designs are preferable, as there is a lot of research done on those already. Their parts can be bought from multiple sources, and even self-producing them is well-documented. As the tiltwing and the blended body concepts are new concepts, they are harder to develop, and also harder, thus cost more, to produce and maintain.
- **Repairability:** Here, the quad- and tricopter are preferable, as those designs are made out of standard components and are therefore easy to repair. The tiltwing concept has a complicated mechanism, as the wing should be able to rotate. This causes an extra point of failure. This design also consists of non-standard components. Finally, the blended body UAV is not desirable from a repairability perspective, as one crack in the hull would result in a need for an entirely new hull.

The results of the analysis of these criteria can be found in Table 7.1. It can be seen that the quadcopter is the clear winner. This is the design candidate for which a preliminary design was made. Note that the only case in which this outcome significantly changes is when the mission profile shifts from mostly hover to mostly cruise. All other criteria stay the same regardless of a shift in mission.

7.3. Preliminary Design

Upon conclusion of the trade-off, a preliminary quadcopter design could be made. Based on the requirements and reference aircraft, initial sizing was performed for mass, size, thrust, and power. Using these parameters, initial design choices could also be made for the rotors, the batteries, and the structure. The preliminary design of these subsystems will be shortly discussed here.

For the power system, four options were considered: Batteries, hydrogen, solar panels, and combustion engines. It was decided to discard the option of combustion as it does not fit the sustainability requirement of this design. Solar panels were deemed infeasible due to the high required surface area. This left only hydrogen and batteries. Analyzing the performance of hydrogen showed that for

Table 7.1: Trade-off between the four configurations. The width of each column correlates with the weight of the criterion.

Options	Size [m] (l, b, h)	Controllability	Flight Efficiency	Cost	Repairability
			Criteria		
Weights:	10 [%]	25 [%]	15 [%]	25 [%]	25 [%]
Tricopter UAV	1.92, 1.61, 0.675	Better controllability than winged configuration and less redundancy than quadcopter	Best hover efficiency (highest disk loading). Poor cruise efficiency	Well-researched design, low production and development costs	Mostly standard items
Quadcopter UAV	1.52, 1.52, 0.675	Better controllability than winged configuration and more redundancy than tricopter	Good hover efficiency, poor cruise efficiency	Well-researched design, low production and development costs	Mostly standard items
Tiltwing UAV	1.19, 1.88, 0.35	Less agility than multicopter due to wing/propeller interference	Good cruise efficiency, poor hover efficiency	Sparsely researched and more complex mechanism increases costs	Custom tiltwing mechanism
Blended body UAV	1.48, 2.13, 0.2	Complicated controllability, can't fly backwards	Good cruise efficiency, poor hover efficiency	Sparsely researched and more complex mechanism increases costs	Custom body, custom mechanism to rotate propellers

Legend

	Excellent, exceeds requirements
	Good, meets requirements
	Correctable deficiencies
	Unacceptable deficiencies

the low endurance requirement, batteries would be a more efficient option. The relative bulkiness and higher risk of the hydrogen system are criteria that reinforced this decision.

After the power system had been determined, a statistical method for sizing lithium polymer batteries was employed. Through an iterative process, sizing from the maximum take-off weight was performed. From this point and working with the aerodynamics department, the batteries and motors were sized and an initial power budget was developed. The conclusion was that 10 batteries with a capacity of 23000 [mAh] would be required for a maximum take-off weight of 30kg.

The propeller subsystem was sized using the program XRotor, developed at MIT. This program follows the Blade Element Theory, for which each blade is divided into smaller elements of which the lift and the drag can be calculated. The final design is optimized for minimum induced loss. At the start of the design, the velocity was set to 13.89 [m/s], to reach the final destination in under 10 minutes. The tip radius and hub radius were set at 0.29 [m] and 0.05 [m] respectively. A literature study was carried out to determine the most suitable airfoil to start with, which is the NACA4412. In this first iteration, the airfoil was kept fixed. The best configuration possible with these parameters was sought by iterating between the rotational speed (RPM), the angle of attack of the blade, and the tip radius. In Table 7.2, the final propeller design is shown.

Table 7.2: The final parameters for the propeller preliminary design

Parameter	Value	Unit
Tip radius	0.29	[m]
Hub radius	0.05	[m]
Hub wake displacement body radius	0.025	[m]
Airspeed	13.89	[m/s]
Rotational velocity	4500	[RPM]
Thrust generated per rotor	73.575	[N]
Power generated per rotor	1670	[W]
Airfoil type	NACA4412	
2D Lift coefficient	1.3564	[-]
Blade angle of attack	7	[deg]

The payload module consists of two parts: an autonomous glass cutting mechanism and emergency flight masks. The method for cutting the glass was chosen with input from Telesilla Bristogianni, a PhD researcher in the glass research group of architecture at Delft University of Technology. The system is estimated to be about 1.5 [kg], though a final design needs to be elaborated upon. The delivered payload will consist of six flight masks with a mass of 3.5 [kg].

For the collision avoidance system (CAS), different sensors and CAS strategies were explored. Sensors were chosen that can perform in all weather conditions, and be able to detect obstacles through the smoke. Therefore, a combination of LiDAR and Ultrasound was selected to provide accurate obstacle detection, while also being able to detect transparent surfaces with the use of ultrasound. Lastly, the CAS strategies sense & avoid and optimization-based methods were selected, due to their relatively low complexities, reducing the computational power required. Also, the optimization method provides a reduction of the response time by having the optimal flight route calculated based on known geographical information within the action radius of the UAV.

The structure was sized based on the main loads acting on it (thrust and weight). It is divided into three parts: The main body (48x43x33 [cm]), the feet (retracted length: 25.6 [cm], extended length: 66.6 [cm]) and the propeller arms (length: 32 [cm]). Note that in the final design, the landing gears can no longer be retracted. The main limit for the material selection for the structure is based on the heat it needs to withstand. This resulted in the choice of titanium and nickel alloys and stainless steel. Additionally, foam will be used to insulate the batteries to prevent them from becoming too hot due to the fire.

The preliminary design discussed in this section forms the basis for the detailed design in later sections. Note that even some conceptual changes were made in later stages. However, certain parameters proved to stay close to their initial value. This detailed design will be discussed in the remainder of this report.

8 Detailed Design: Adhesion to a Building

From a control and payload deployment perspective it is desired to keep the UAV as stable and close to the building as possible. As this will be difficult to realize while flying since the heat of the fire will generate turbulence, it was decided to land or adhere the UAV to the building. Therefore, this chapter will first elaborate on the flight mask delivery methods where no window has to be breached in Section 8.1 and then on when a window does need to be breached in Section 8.2. Finally, the vacuum system to be used will be discussed in Section 8.3.

8.1. Flight Mask Delivery without Breaching Glass
To not breach the glass when delivering the flight masks is by landing on a roof or balcony or adhering to a window that can be opened.

8.1.1. On a Roof or Balcony

The simplest method to deliver the flight masks is by landing the UAV on a roof or balcony. It is important to note that the space available should be big enough for the UAV to land and that the location should be accessible by the people inside. The flight mask delivery will happen in the following fashion: The UAV will land on the designated area and will wait for the persons to arrive. The persons will take out the flight masks via the bottom hatch. When the necessary flight masks have been taken out and the persons have walked away from the UAV, the UAV can take off again.

8.1.2. At a Window that can Open

Another possibility to deliver the UAV that does not require breaching glass is delivering the flight masks at a window that can be opened. First, the UAV will hover before the window and will communicate with the person inside that he/she has to open the window. When the window is opened the UAV will adhere to the building as explained in the following section.

8.2. Flight Mask Delivery with Breaching Glass

To design a proper adhesion procedure, multiple concepts have to be analyzed. This section will provide a trade-off of two adhesion methods in Section 8.2.1 and will elaborate upon the final adhesion method in Section 8.2.2

8.2.1. Trade-Off

To adhere the UAV to a building, suction cups will be used which will be further elaborated upon in Section 8.3. To adhere the suction cups to the building, two methods were designed: The duct adhesion concept, where the suction cups are located on the ducts around the propellers, and the landing gear adhesion concept, where they are located on the landing gear. Both are shown in Figure 8.1.

Ring adhesion   **Feet adhesion**
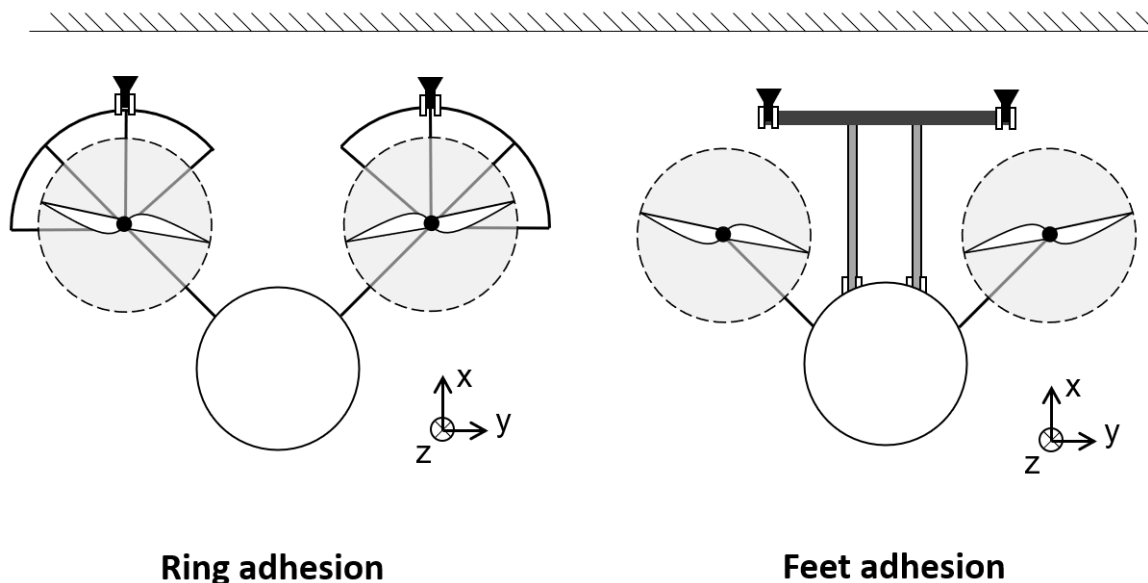
Figure 8.1: Top view of the ring and landing gear adhesion concept.

To choose between the two concepts, advantages and disadvantages were listed in three categories: Complexity, reliability, and impact on the UAV. An overview can be found in the lists below.

Ring adhesion concept

Impact on weight: The ducts need to be partially hollow to allow for the vacuum tubes to go through. This increases the thickness of the duct and therefore increases the overall mass. However, the added weight and the propeller arm cause bending relief in flight.

Complexity: The integration of the suction system with the ring will be complex, as the vacuum tubes cannot be exposed to the outside heat. Additionally, the suction cup should stick out far, to prevent

the duct from scraping to the side of the building. This adds to the complexity of the system.

Reliability: The ring around the propellers also functions as a safety mechanism, as the rotors cannot collide with the building. It, therefore, increases the reliability of the continuation of the mission.

Landing gear adhesion concept
Impact on weight: The relatively long landing gear is necessary to prevent the rotors from colliding with the building, this adds extra weight. On the other hand, the landing gear is not used during the mission when using the ring adhesion concept and is just dead weight then.

Complexity: The propeller arms already have avionics inside them. The landing gear on the other hand does not have anything in them yet. Therefore there will be less interference between different subsystems, hence decreasing the complexity.

Reliability: The landing gear can be rotated to an angle optimal for the suction system to work. Additionally, the forces when attaching to the building are exerted on the landing gear (which is structurally strong) and not on the propeller arms which have a lot of sensitive components in/on them.

Looking at the lists above, both concepts have advantages and disadvantages. However, the landing gear adhesion concept is considered to have considerable advantages over the ring adhesion concept, especially in the complexity category. Therefore the landing gear adhesion concept was chosen.

8.2.2. Final adhesion method
As a result of the trade-off performed in Section 8.2.1, the landing gear adhesion concept was chosen. This concept is visualized in Figure 8.2, where the suction cups are mounted at the tips of the landing gear.
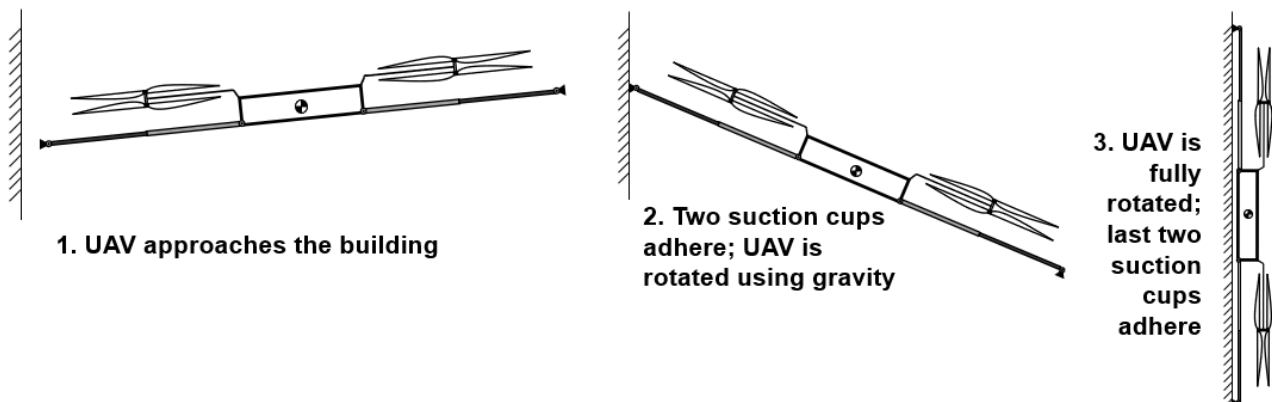
Figure 8.2: Graphical representation of the adhesion mechanism.

First, the UAV orientates one part of the landing gear towards the building, then the suction cups on the landing gear will be activated to attach the UAV to the building. The fact whether the vacuum is in place in the suction cups will be checked before the next step is executed. If the vacuum is not in place, another adhesion place should be found. Subsequently, the thrust will be decreased so that the UAV starts to rotate due to gravity. The thrust will gradually decrease during the rotation to prevent damage to the drone due to a collision with the wall. When the UAV is fully rotated, the two suction cups on the other part of the landing gear will be activated, which means that the UAV is now fully secured to the building. To leave the building after the payload is deployed, the above-described process has to be followed in reverse.

8.3. Vacuum System
A vacuum system is a complex system, especially when it is incorporated in a UAV as it poses extra limits on the weight, power consumption, and size. The vacuum system essentially consists of four

parts: Suction cups, a vacuum pump, a vacuum switch, and a three-way valve[1].

The **suction cups** need to be designed properly for it to support the UAV. Therefore, the suction cups should have flexible edges, as this eases the adhesion to the building if the approach angle of the landing gear is not optimal. Additionally, the suction cups should be made out of material that can withstand heat and weather conditions like rain. Luckily, the latter is beneficial for the suction cups, as water helps seal the suction cups. Concerning the heat: the suction cups can withstand temperatures up to 200 [$^\circ$C], which is deemed sufficient, as they will largely be protected by the landing gear and the glass will not get hotter than this or the glass will already be broken[2]. The suction cups primarily work on even and non-porous surfaces, therefore when deciding upon the payload deployment location this should be taken into account as a constraint. Additionally, two suction cups should be able to carry the entire weight of the UAV, as only two suction cups have adhered at the beginning of the adhesion to a building.

A **vacuum pump** is needed to create a vacuum within the suction cups. This pump will be activated once the UAV starts adhesion and deactivated after the drone is ready to detach.

A **vacuum switch** measures the vacuum percentage in the suction cups when the UAV has adhered to the building. If the vacuum percentage is above a set threshold the vacuum pumps will be turned off as a vacuum is created. If the suction cups are not perfectly attached and air slowly flows in, resulting in a vacuum percentage below the threshold, the vacuum pump will be turned on again.

The **three-way valve** is needed to terminate the vacuum in the suction cups, as a three-way valve enables outside air to get into the suction cup. This is needed as the vacuum cannot be terminated just by shutting down the vacuum pump, as the vacuum will still stay intact (or decreases only slowly) because the suction cups are sealed.

To distribute the vacuum to all suction cups a **vacuum distributor** is necessary. This component splits the central vacuum tube up into the tubes towards the suction cups.

The chosen components for the suction cups[3], vacuum pump[4] and switch[5], the three-way valve[6] and vacuum distributor[7] are listed in Table 8.1. This table also gives the required power, weight and cost, which are important design parameters for the integration of subsystems.

---

[1]Based on a conversation with R. Kerkvliet, technical advisor at Schmalz, a company specialized in vacuum systems.

[2]`https://www.interfire.org/features/glass_breakage.asp` Retrieved on 22-06-2021

[3]`https://www.schmalz.com/en/vacuum-technology-for-automation/vacuum-components/vacuum-suction-cups/suction-cups-for-handling-sheet-metal/bellows-suction-cups-sab-ht2-1-5-folds-303931/10.01.06.03318` Retrieved on 22-06-2021

[4]`https://www.schmalz.com/nl-nl/vacuuemtechniek-voor-de-automatisering/vacuuem-componenten/vacuuemgenerator/vacuuempompen/dry-running-vacuum-pumps-eve-tr-308333/10.03.01.00192` Retrieved on 22-06-2021

[5]`https://www.schmalz.com/nl-nl/vacuuemtechniek-voor-de-automatisering/vacuuem-componenten/schakelaars-en-systeembewaking/mechanische-vacuuemschakelaars/vacuum-switches-vs-v-pm-em-st-308806/10.06.02.00456` Retrieved on 22-06-2021

[6]`https://www.macvalves.com/wp-content/uploads/PDFs/Series_Pages/Sm3ways/35catalog.pdf` Retrieved on 22-06-2021

[7]`https://www.schmalz.com/nl-nl/vacuuemtechniek-voor-de-automatisering/vacuuem-componenten/filters-en-aansluitingen/vacuuemverdeler/vacuum-compressed-air-distributors-vtr-309029/10.09.03.00058` Retrieved on 22-06-2021

Table 8.1: Overview of the chosen components for the vacuum system, their weight, required power and cost.

	Suction cups (4)	Vacuum pump	Vacuum switch (4)	Three-way valve (4)	Vacuum distributor
Component name	SAB 80 HT2-65 G1/4-IG	EVE-TR-M 2.3 24V-DC	VS-V-PM-NO	3/2 NO-NC, 2/2 NO-NC	VTR G1/4-IG 5xG1/8
Forces [N]	217 ($\parallel$to wall), 238 ($\perp$to wall)				
Required power [W]	-	48	-	1.8-12.7	-
Weight [kg]	0.92	2.4	0.132	0.32 (approximation)	0.36
Dimensions [mm]	88 (diameter), 54.8 (height)	154x82x123 (lxwxh)	58x19.8x40 (lxwxh)	60.5x24.1x50 (lxwxh)	60x35x20 (lxwxh)
Cost [EUR]	468	475	110.38	120	81

8.4. Sub-system Compliance Matrix

Table 8.2 shows the compliance matrix for the adhesion system.

Table 8.2: Compliance matrix adhesion requirements

Requirement	Verification method	Compliance
TECH-ADH-01	As can bee seen in Table 8.1 two suction cups can hold 434 [N], whereas the UAV only weighs around 383 [N].	Yes
TECH-ADH-02	As explained in Section 8.3 the suction cups are able to withstand 200 [$^\circ$C].	Yes

9 Detailed Design: Glass Cutting Mechanism

To get the flight masks to the people inside the building, a window needs to be breached if it cannot be opened or there is no option to drop it on a roof or balcony. This chapter will elaborate on the mechanism used for this. First, the problem will be discussed in Section 9.1 where after Section 9.2 will three concepts to breach the window. Additionally, an experiment has been conducted to show a proof of concept in Section 9.3. The glass cutting design will be elaborated upon in more depth in Section 9.4. Finally, Section 9.5 gives an overview of the design and shows the integration in a rendered image.

9.1. Problem Description

As described in Chapter 8, to deliver the flight masks, first a convenient location is sought, e.g. a roof, big balcony, or a window that can be fully opened. However, when this is not possible a window needs to be breached. As the main use case for the UAV is high rises buildings where windows cannot be (fully) opened, research has to be done into breaching glass. Below different the three main types of glass and their properties will be elaborated upon.

- **Annealed glass** is the most common type of glass in windows being the most simple (thus cheap) type of glass[1]. Most windows use annealed glass with a thickness of approximately 2.4 [mm][2].
- **Laminated glass** is a type of safety glass that consists of two or more layers of glass that have a layer of polymers in between the layers of glass that hold the glass together in case it breaks.

---

[1] https://waspecialprojects.com.au/types-of-glass/, Retrieved on 16/06/2021

[2] https://www.breakglass.org/double-strength-glass.html, Retrieved on 16/06/2021

Due to this layer, the crack can't propagate to the next layer, making it impossible for a cutting mechanism to break it.
- **Tempered glass** is a type of safety glass that breaks into small non-sharp fragments. Tempered glass can be up to five times stronger than annealed glass, but breaks spontaneously (i.e. the entire window breaks in one go[3].) The cutting strategy for tempered glass would be different in the sense that you only need to break the glass on one spot (this causes the rest of the window to break too).

Regulations specify that safety glass must be used if the window is closer than 30 [cm] from a doorway or less than 80 [cm] from the ground[4]. The type of safety glass (and thus also the strength) that is used is labeled on the window itself[5].

9.2. Concept Analysis
There are multiple ways to breach through glass, therefore research has been performed to determine the best way for this application. The following subsections will give a description, disadvantages, and advantages of the three methods. It is, however, important to note that none of the designs will be able to get through the laminated glass, as was explained in Section 9.1.

Smashing the Glass
The first option to breach the glass is to let the person inside break the glass. This will be communicated with the person through audio or visuals. The UAV will hover slightly away from the window so that the UAV is not damaged by the breaching of the window.

- **Advantages**: The main advantage of this concept is that it does not influence the rest of the UAV. It is also therefore a less complex system compared to the other ones. Finally, this will be the lightest solution in terms of weight.
- **Disadvantages**: This method is dependent on the person inside, for example, a child or injured person might not be able to break the glass. Additionally, by breaking the glass in this fashion the glass will shatter and fall together with the object used for it. Which can result in harmful situations. Finally, this results in a rather large hole in the window, which causes a danger of falling for the person inside when he/she reaches for the flight masks.

Breaching the Glass using Explosives
The second option is breaching the glass utilizing small explosives. The small explosives will be placed on the window in strategic places. These explosives will be attached, where after the UAV will wait at a safe distance for the glass to shatter.

- **Advantages:** This is a relatively fast method, as the glass will shatter in one go. Additionally, it effectively shatters the glass and is not dependent on the person inside. Also, explosives can break any type of glass (assuming the building doesn't collapse due to the blast). Lastly, this is a relatively lightweight solution: One kilogram of dynamite can already break a concrete wall.
- **Disadvantages:** The main disadvantage of this method is a lack of safety. Putting explosives (even small ones) on a burning building, of which the structural integrity might be less, can cause dangerous situations. The glass will shatter, also to the inside, which will be harmful to the person on the other side of the glass. Additionally, the vibrations caused by the small explosion can result in shattering more windows than desired. This drastically increases the amount of oxygen flowing into the building and hence increasing the fire. It is also important to note that up until today no explosives are used by the fire brigade as it is simply too dangerous for that application.

---

[3]`https://www.dillmeierglass.com/news/what-it-means-to-temper-glass#:~:text=Tempered%20glass%2C%20or%20toughened%20glass,annealed%2C%20or%20untreated%2C%20glass`, Retrieved on 16/06/2021
[4]`https://parkglass.co.uk/glass/safety-regulations/`, Retrieved on 16/06/2021
[5]`https://build.com.au/safety-glass-requirements`, Retrieved on 16/06/2021

Cutting the Glass

The final mechanism to breach the glass is by cutting it. This will be done by exerting force on a blade on the window, by which a crack will be created. Hereafter the glass will be heated, resulting in a predefined cutout due to the thermal stress.

- **Advantages**: Of the three concepts, this is the safest process as no pieces of glass will fly around. Additionally, the window largely stays intact, therefore the UAV can stay attached to the building.
- **Disadvantages**: Compared to the other concepts this is a slower and more complex process as it requires cutting and heating the glass. Additionally, the glass cutting concept requires the UAV to stay still, so that an accurate cut can be made. However, this is already solved with the adhesion mechanism. This does add extra weight and complexity to the UAV. Finally, the glass you can cut through will be weaker than for breaching the glass for the same weight: Only one kilogram of dynamite can break a concrete wall, whereas a cutting mechanism of one kilogram wouldn't be able to do that. This implies that this will be the heaviest option.

Conclusion

As the main objective of the UAV is to safely get people out of burning buildings it is not desirable to make the situation unsafer for the people inside or the people on the ground. Therefore the safest concept, cutting the glass, is chosen.

9.3. Glass Cutting Experiment

This section describes how a simple test is performed to get an idea of how long it will take to cut the glass, how much force is needed and what the quality of the cut is. For the test, the following items were used:

- A blowtorch
- A glass cutter
- One annealed glass panel, 6 [mm] thickness
- One laminated glass panel, 6 [mm] thickness
- Fire resistant gloves

A glass cutter is a handheld tool that supports a glass cutting wheel[6]. In the experiment, a butane/propane mixed gas tank was used for the blowtorch. This creates a flame with a temperature of approximately 1300 [°C][7].

Four different types of cuts were made with the glass cutter on each glass panel: Three continuous cuts with approximately 10, 50, and 100 [N] of force applied to the glass cutter and one dashed score with approximately 100 [N] of force applied. Note that there is some uncertainty in the exact force applied since the force was applied by hand. After the scoring, the time needed for the blowtorch to break the glass was measured. The results can be summarized in Figure 9.1, Figure 9.2 and Table 9.1.

---

[6]`https://en.wikipedia.org/wiki/Glass_cutter`, Retrieved on 16/06/2021

[7]`https://www.thoughtco.com/flame-temperatures-table-607307`, Retrieved on 16/06/2021
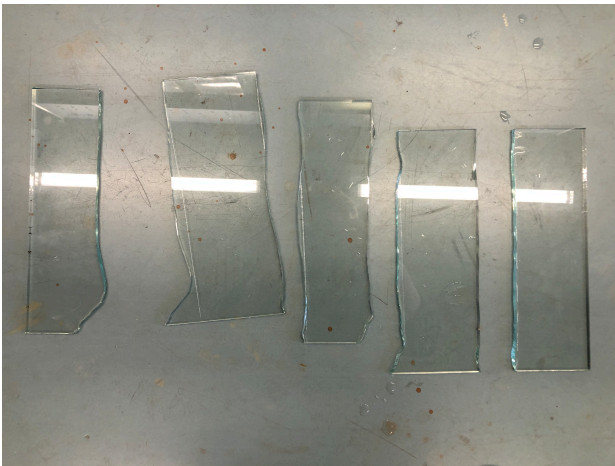
Figure 9.1: Cutting of a glass panel.
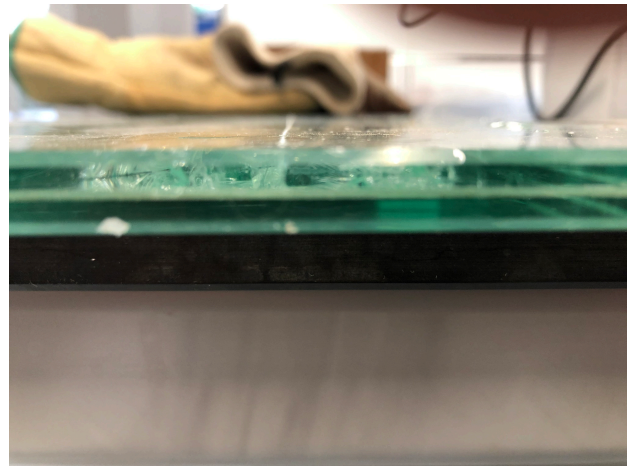
Figure 9.2: Cutting of a laminated glass panel.

Table 9.1: Results of glass cutting experiment.

Force applied [N]	Required time [s]
10 (continuous)	35.3
50 (continuous)	30.1
100 (continuous)	12.5
100 (dashed)	33.6

As can be seen in Figure 9.1 the quality of the cut is dependent on the force applied to the sheet. This is likely because it is harder to apply a consistent load on the glass cutter by hand for higher loads. The cut is not perfect, so some margin is needed to ensure the flight masks will fit through the cut hole. Meanwhile, Figure 9.2 shows that the cutting did not work for laminated glass. Due to the laminated layer in the middle, the crack could not propagate to the other side. Additionally, it can be seen that the larger the force applied, the shorter the blowtorch needs to break the glass.

A dashed cut is comparable to a cut with a relatively low force applied in terms of time and also adds complexity to the cutting mechanism, therefore that option is discarded. Since every minute counts in an emergency, the fasted option (force of 100 [N]) is selected for a first iteration. Since there are three blades, this imposes a load of 300 [N] on the adhesion mechanism. However, these relatively high loads need to be taken into account while designing the mechanism.

9.4. Glass Cutting Design

Having chosen one of the design concepts (cutting the glass), the next step is to start the detailed design phase of the glass cutting mechanism. This design will be done based on the subsystem requirements as presented in Chapter 6. Compliance with these requirements will be discussed in Section 9.6. First, a trade-off will be performed between different mechanisms, where after the sub-components are sized.

9.4.1. Trade-off Design

To be able to design the glass cutting mechanism, first, its functions need to be specified:

- Extension towards window: To get from the bottom of the drone towards the window some kind of extension of the cutting mechanism is needed.
- Cutting the window: This is the operation of the blade kerfing its way through the window.
- Heating the window: This is the operation to heat the window to break it at the kerf.
- Extracting the payload: This is the operation of removing the flight masks from the UAV.

For the first two functions, multiple solutions are described. These solutions can be found in the morphological chart in Table 9.2:

Table 9.2: Morphological chart glass cutting mechanism.

Sub-function	Option 1	Option 2	Option 3	Option 4
Extension towards window	Scissor mechanism	Actuator	Rotating rod (like a one leg of a pair of compasses)	Robot arm
Cutting the window	Open ring with multiple blades	Rotating rod	Rotating "tri-arm"	

For the last two functions, the options were limited and therefore no morphological chart was made for this. For the heating of the window a blowtorch with a tank inside will be used as this is found to be the safest way of heating the window. For extracting the payload function there are two options: Bringing the payload to the people or letting the people get it. The former of these two options would result in a complex and heavy system, therefore the latter was chosen. The payload will be packed as multiple smaller packages to make it easier to extract them from the UAV and it also reduces the size of the hole that needs to be cut.

To choose the design for the first two functions, three design options were made and compared.

Design option 1: 1-1
This design consists of a scissor mechanism with an open ring with multiple blades. This offers easy payload accessibility because the blades are mounted on an open ring. A disadvantage, however, is that to rotate blades you have to rotate the extension mechanism too.

Design option 2: 2-3
This design consists of a linear actuator with a tri-arm at the end with blades on it to cut the glass. This is a simpler configuration than design option 1, as the scissor mechanism has a lot of moving parts. Additionally, linear actuators and motors to rotate it are readily available. This design, however, asks for smart positioning of the flight masks, as the tri-arm will partially block the payload access.

Design option 3: 3-n/a
The third and last design option is inspired by a pair of compasses. This design combines the extension and rotation in one single item. The advantage of combining these two motions is that it decreases the number of parts. However, exerting the proper magnitude of force will be challenging, as the arm on which the blade is attached is positioned with an angle with respect to the window.

Conclusion
Considering the design options elaborated upon above, design option 2 was chosen for its relative simplicity and off-the-market parts. Design option 1 was discarded because it resulted in a heavy and complex system and a similar implementation of such a system could not be found. Finally, design option 3 was not chosen because of the complexity of applying pressure to one of the legs.

9.4.2. Extension Mechanism Design
As described earlier, the linear actuator is an extension mechanism that will bring the blades from the drone to the window. This is especially important for sunken windows. The linear actuator needs to extend the "tri-arm" over a distance of 20 [cm] from the body of the drone to the window. This was considered an acceptable distance by looking at various types of windows in buildings. This section will design a linear actuator to obtain reliable data on the mass, size, and cost.

Linear actuators are essentially really simple: They consist of an electric motor connected to a gear. The gear is connected to the screw thread of a bolt which transfers the rotating motion of the motor to the desired translational motion. This subsection focuses on finding the size and material of the bolt, a suitable electric motor, and the size and material of the gear.

To do this, the first step is to analyze the structure. This can be done based on a free body diagram. In this free body diagram, Figure 9.3, the glass cutting mechanism is drawn with all the external forces and moments acting on it.
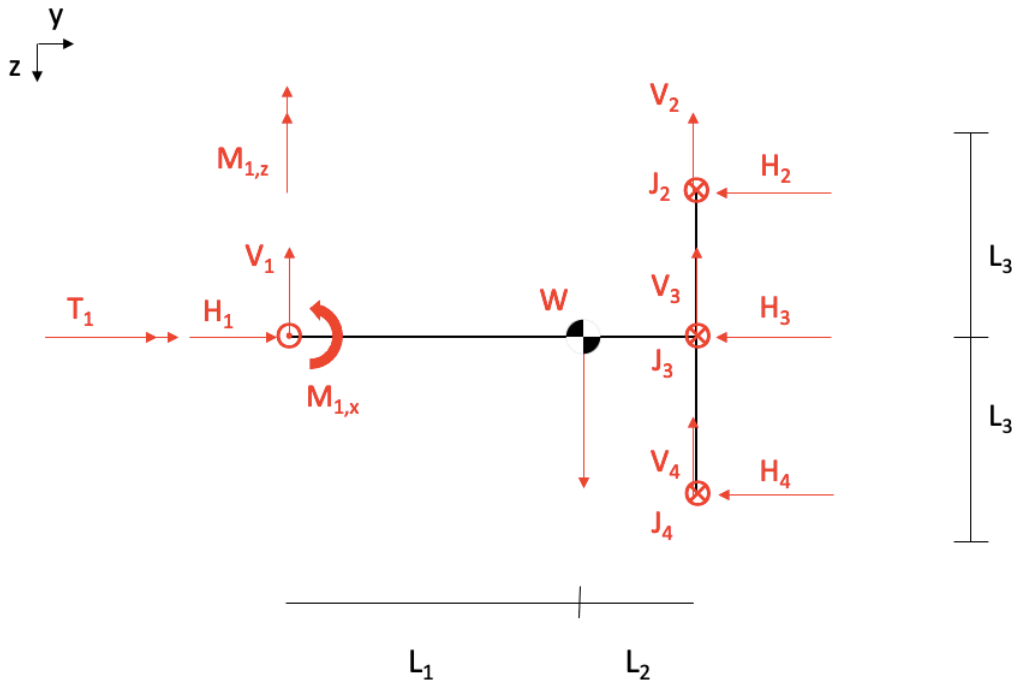

Figure 9.3: Free body diagram glass cutting mechanism.

In this free body diagram, it can be seen that the glass cutting mechanism applies pressure to the window to make the cut, thus the window applies three compressive forces (H_2, H_3, and H_4) on the glass cutting mechanism at three points (the blades). Moreover, the blades can also carry shear forces due to friction (V_2, V_3, V_4, J_2, J_3, J_4). To cut the window, the glass cutting mechanism has to rotate. This is done by applying a torque on the linear actuator at the drone's body T_1. Assuming the linear actuator is clamped at the drone's body this also results in reacting bending moments $M_{1,x}$ and $M_{1,z}$. The weight of the mechanism acts at the center of gravity, at a distance of L_1 from the drone's body. L_3 is the length of the rods of the "tri-arm" construction. Note that L_3 is drawn a factor $2/\sqrt{3}$ longer than the distance from 3 to 2 since it is a two-dimensional projection of a three-dimensional shape. Note that this free body diagram is simplified since in reality, the shear forces of the blades act by an offset from the rod. A safety factor on the critical stresses will be used to compensate for this.

Rods Tricopter
Having analyzed the free body diagram, the next step is to size the blades of the "tri-arm". The blades will have a circular cross-section for simplicity and will have to be sized.

The goal is to find the maximum stress in the rod and size the rod based on that stress. Since the rod is hollow, two dimensions are needed: the thickness and the diameter. In general, thin hollow shapes are efficient at carrying bending stress since they have a larger moment of inertia than solid shapes. However, an excessively large diameter results in a bulky design, which is also undesirable. Thus, a few iterations may be necessary.

To find the maximum stress, it is possible to define a new coordinate system in which $M_{y'} = 0$ and where $M_{x'}$ is caused by the resultant of H_2 and J_2. This resultant force can be calculated by:

$$F_r = \sqrt{H_2^2 + J_2^2} = \sqrt{1 + \mu^2} \cdot H_2 \tag{9.1}$$

where F_r is the resultant force of H_2 and J_2, while μ is the static friction coefficient between the blades and the window.

The maximum stress can be calculated by Equation 9.2[10]:

$$\sigma_{z,max} = \frac{M_{x'}r}{I} = \frac{F_r L_3 \frac{d}{2}}{\pi \frac{td^3}{8}} \tag{9.2}$$

where M is the bending moment in [Nm], σ is the stress in [Pa], M is the moment in [Nm], I is the moment of inertia in [m^4] of the rod cross section, r is the radius in [m], d is the diameter in [m] and t is the thickness in [m] of the rod. The maximum stress should be lower than the yield stress of the material.

All final parameters are summarized in Table 9.3.

Table 9.3: Parameters for the "tri-arm" rod.

Property	Final value	Unit	Comment
Density	2930	[kg/m^3]	As can be found in [11],
$H_2 = H_3 = H_4$	100	[N]	Equal due to symmetry.
L_3	165	[mm]	Based on the payload dimensions, see Section 12.2.
Mass	19	[g]	Volume multiplied with density.
Material	Aluminum		Based on a material trade-off, see Chapter 11.
Outer diameter	12.5	[mm]	
μ	0.12	[-]	Retrieved from[12].
Thickness	1	[mm]	
Yield strength	384.65	[MPa]	As can be found in Chapter 11.

Rod of the Linear Actuator
As can be seen in the free body diagram in Figure 9.3 the rod of the linear actuator is loaded in compression due to the forces H_2, H_3 and H_4. The resultant bending moment is only due to bending of the weight, assuming the blades don't carry any weight, which is a conservative assumption. Note that there is no induced moment from the "tri-arm" part, due to the symmetry of the three rods and the assumption of the blades no load carrying.

Using similar methods as before we can achieve an expression for the stress:

$$\sigma_{y,max} = \frac{M_x r}{I} + \frac{H_2 + H_3 + H_4}{A} \tag{9.3}$$

The extra term comes from the compression due to the force of the blades. This stress should be lower than the yield stress.

However, because there is also compression, also buckling needs to be checked. The stress should also be lower than the critical buckling stress, which can be determined using Equation 9.4[10]:

$$\sigma_{cr} = \frac{\pi^2 E}{(KL/r)^2} \tag{9.4}$$

where σ_{cr} is the critical buckling stress, E is the Young's modulus, K is a constant equal to 2[10], L is the length [m] and r is the radius of gyration equal to $\sqrt{I/A}$.

Note that the mass of the rod is dependent on M_x, which is dependent on the location of the center of gravity and the weight, which is dependent on the mass of the rod. Therefore, an initial estimate is used and iteration is required to obtain convergence. For the weight of the "tri-arm" rods, a safety factor of two was used to compensate for the assembly of the three rods and the glass cutting wheels.

Additionally, the weight of the nozzle for the blowtorch was estimated to be 50 [g].

Summarizing all the parameters in Table 9.4:

Table 9.4: Parameters rod linear actuator.

Property	Final value	Unit	Comment
Outer diameter	19	[mm]	
L_1	178	[mm]	Location of center of gravity from drone's body.
L_2	22	[mm]	200 [mm] minus L_1.
Mass linear actuator	33	[g]	
Mass "tri-arm"	164	[g]	Safety factor of 2 (connection material and nozzle) multiplied with 3 rods multiplied by 19 (weight per rod) plus 50 (nozzle) = 164 [g] for the "tri-arm" part.
Material	Aluminum		See Chapter 11.
Thickness	1	[mm]	

9.4.3. Motor of the Linear Actuator Design

As mentioned earlier, the motor exerts a torque on the rod of the linear actuator which translates forward, because it has a screw thread. A linear actuator (and any object with screw thread) can be modeled as a screw using a block on a ramp model[8]. This results in the following equation:

$$Q = W \tan{(\phi + \alpha)} \tag{9.5}$$

Where Q is the force applied to the screw in [N] (in this case it would be T_1/r, W is the force the screw applies to an object in [N] (in this case to the blades), ϕ is the friction angle [deg] (equal to $\arctan \mu$, r is the radius of the screw in [m], and α is the helix angle of the screw in [deg].

Using this formula the force required by the motor can be calculated to push the blades against the window. Note that α is dependent on the screw used and can either be negative or positive depending on which way the cutting mechanism moves. To be conservative, α is assumed to be positive, but in reality, the screw will be mounted such that α is negative when applying force to the window with the blades. If α is bigger than ϕ, the screw is not self-locking, since a positive W results in a negative P. This is undesirable, since the mechanism would automatically extend during the cruise. As a starting point, α is assumed to be equal to ϕ.

Using the equation above one can come up with the following values in Table 9.5:

Table 9.5: Parameters of the motor of linear actuator.

Property	Final value	Unit	Comment
Q	198	[N]	
Torque	1.83	[Nm]	
W	300	[N]	H_2+H_3+H_4
α	16.7	[deg]	Set equal to ϕ
ϕ	16.7	[deg]	$\arctan{(\mu)}$
μ	0.3	[-]	Based on data in[9], aluminum on aluminum and lubricated

Note that electric motors are power limited (assuming the shaft can handle the torque) by the following formula:

$$P = T \cdot \omega \cdot \eta \tag{9.6}$$

---

[8] https://www.youtube.com/watch?v=tKv-Ilr3AhE&t=471s&ab_channel=MichelvanBiezenMichelvanBiezen, Retrieved on 14/06/2021

[9] https://www.engineeringtoolbox.com/friction-coefficients-d_778.html, Retrieved on 14/06/2021

where P is the power in [W], ω is the rotational speed in [rad/s], η is the efficiency compensating for losses due to friction. This means for a given torque the rotational speed defines the power of the motor. The rotational speeds define the time it takes to extend the mechanism from fully retracted to the window (maximum 20 [cm]). The rotational speed is connected to translation velocity by the following formula:

$$V_{req} = \text{lead} \cdot RPS = 2\pi^2 d \tan(\alpha)\omega \tag{9.7}$$

where V_{req} is the required translational speed in [m/s], d is the diameter of the linear actuator in [m], α is the helix angle in [deg] and ω is the rotational speed in [rad/s].

The final parameters of the motor can once again be summarized in a Table 9.6:

Table 9.6: Parameters of motor for linear actuator[10] .

Property	Final value	Unit	Comment
Efficiency	0.62	[-]	
Mass motor	325	[g]	
P_{out}	12.2	[W]	
P_{in}	19.8	[W]	
Time	11	[s]	Time to translate 20 [cm], this defines V_{req}
Voltage	12	[V]	
ω	6.6	[rad/s]	

9.4.4. Motor to Rotate Mechanism Design

An extra motor is needed to rotate the mechanism, i.e. overcome the friction of the glass cutter, which equals T_1. All these parameters can be summarized in Table 9.7:

Table 9.7: Parameters of motor for rotation of mechanism[11] .

Property	Final value	Unit	Comment
Efficiency	0.64	[-]	
Mass motor	≈ 230	[g]	
P_{out}	4.5	[W]	
P_{in}	7	[W]	
Torque	7.2	[Nm]	$T_1 = \mu\, L_3 (H_2 + H_3 + H_4)$
Voltage	12	[V]	
ω	0.63	[rad/s]	

9.4.5. Glass Cutting Wheel

The scoring of the glass will be done with a glass cutting wheel, or informally: A glass cutter. Glass cutting wheels are usually made out of tungsten carbide and are approximately 5 [mm] in diameter[12]. The glass cutting wheel will be mounted to a bracket that is connected to the tri-arm.

---

[10]https://docs.rs-online.com/75ac/A700000007082309.pdf, Retrieved on 14/06/2021

[11]https://nl.rs-online.com/web/p/dc-motors/8347631/, Retrieved on 14/06/2021

[12]https://www.fletcher-terry.com/frame-joining-material-cutting-products/carbide-cutting-wheels, Retrieved on 14/06/2021

9.4.6. Gas Tank and Transport

The smallest readily available gas tanks contain 100 [g], which weighs approximately 200 [g][13]. These small gas tanks can burn for approximately 30 [min][14], which is more than enough for this use case, taking the size of the hole and the results of Table 9.1 into consideration. This tank will be placed in the main body of the drone.

This gas needs to be transported from the tank inside the main body of the drone to the nozzle, which is mounted at the tip of one of the rods of the tri-arm, close to the glass cutting wheel. This transport will be done with a tube from the tank to the linear actuator. From there on the gas will be transported through the linear actuator and through one of the rods of the "tri-arm" (both are hollow after all) with a tube to the nozzle.

9.4.7. Protection Ring Design

One thing that hasn't been discussed yet is a mechanism/ construction that will protect the people grabbing the payload from the window through which a hole was cut (since the window can be sharp and hot). For this, a Kevlar ring is used, since Kevlar is both cutting resistant as well as heat resistant. It was estimated that this ring will weigh approximately 210 [g] by assuming 1 [mm] thick, 40 [mm] wide and a density of 1400 [kg/m^3][11]. The implementation of this ring will be visible in Section 9.5.

9.5. Overview

This section summarizes the design and gives an overview of the current design of the glass cutting mechanism. The design has been modeled in CAD software (CATIA) to create a render that visualizes the part of the mechanism that is outside of the drone (so not the gas tank, the motors, and the wiring). This render can be found in Figure 9.4.

Figure 9.4: Design overview glass cutting mechanism.

To summarize, the glass cutting mechanism works as follows:

- **Adhesion/ Landing**: In case there is an accessible balcony or roof available, the drone will land as a normal drone would. In the case there is no available balcony or roof available, the drone adheres to the building using the adhesion mechanism, as described in Chapter 8.
- **Glass cutting**: In case the window cannot be opened and the drone adhered to the window the next mission stage is the cutting of the window itself. This will be done as follows: Firstly the linear actuator extends the tri-arm from the drone's body to the window. This motor of the linear actuator is mounted on the inside of the drone's body, close to the bottom. After the extension,

---

the second motor will rotate the tri-arm, while the linear actuator still applies the pressure and the blowtorch is ignited. The rotation, pressure, and blow torch will continue till the glass breaks. This cutting process is controlled by the operator of the drone. Meanwhile, the doors at the bottom of the drone are opened.

- **Extraction of the payload**: The next step is dependent on whether the drone has landed somewhere or cut a window. In the case that the mechanism cuts the window, this step involves communicating to people inside the building to extract the payload. The people inside the building will grab the fire escape masks from the drone. They can safely stick their arm through the wall, because of the protection from the Kevlar ring. In case the drone has landed on the roof or a balcony, the payload doors will open and the people can directly grab their fire escape masks from underneath the drone.
- **Retraction of system**: The last step is to retract the mechanism if needed, and close the payload doors. The drone can now land and be loaded with more fire escape masks (and new batteries if needed).

9.6. Subsystem Compliance Matrix

Table 9.8 shows the compliance matrix of the requirements related to the glass cutting mechanism.

Table 9.8: Compliance matrix of glass cutting mechanism requirements.

Requirement	Verification method	Compliance
TL-GCM-01	In the glass cutting experiment, a speed of 2 [cm/s] was achieved for an annealed glass of 6 [mm] thick. However, this test was performed by hand and this requirement has to be validated for different kinds of glasses.	TBD
TL-GCM-02	The mechanism was designed for this requirement, as can be read in Section 9.4.	Yes
TL-GCM-03	The mechanism was designed for this requirement, as can be read in Section 9.4.	Yes
TL-GCM-04	The total mass of the cutting mechanism is: 114 (tri-arm, including assembly) + 33 (linear actuator) + 325 (motor linear actuator) + 230 (motor for rotation) + 200 (gas tank) + 50 (nozzle) + 210 (Kevlar ring) = 1162 [g].	Yes
TL-GCM-05	The system is designed for a load of 300 [N], as can be read in Section 9.4. The pull-off force of one suction cup is 238 [N] (as can be seen in Table 8.1, so therefore this requirement is verified.	Yes

9.7. Conclusion

Concluding, the design proofs to have a high potential, since the mechanism can cut through multiple layers of float glass, without creating many shards in a reasonable amount of time. However, there is still some research to do before this glass cutting mechanism can take its place in real-life scenarios. This glass cutting mechanism is designed by bachelor students of aerospace engineers and the design needs to be checked by mechanical engineers and material experts. Future work includes testing the glass cutting mechanism for tempered glass and glass panes of different thicknesses. Additionally, it needs to be tested whether the mechanism can handle the required loads. These tests are all validation procedures for this glass cutting mechanism.

10 Detailed Design: Propulsion and Power System

This chapter will address the sizing of the propulsion and power system. The system is responsible for the overall performance of the UAV, as well as providing power to all subsystems to accomplish

the mission.

This process starts with an analysis of the mission profile in Section 10.1, where thrust-to-weight ratios will be established for different mission phases. Then, in combination with the thrust-to-weight ratios, the propeller design will be finalized in Section 10.2. From the airfoil analysis, the motors, electric speed controllers, and batteries will be sized, as explained in Section 10.3. Lastly, the circuit setup will be displayed and performance analysis will be done, culminating in a compliance matrix as presented in Section 10.4.

10.1. Mission profile

This section discusses the mission profile considered for sizing the propulsion system. This is relevant, as it determines the thrust required for different flight phases, and the power required and battery capacity required in general. The mission can be split up into three parts: take-off, cruise, and hover for the mission-specific phase. The following subsections will discuss these phases in more detail.

10.1.1. Take-off

For take-off, the thrust opposes the weight of the UAV. From this, the required upward acceleration can be computed using Equation 10.1, where g is the gravitational constant. It can then be determined that for an upward acceleration, the displacement is given by Equation 10.2.

$$a_y = (\frac{T}{W} - 1)g \qquad (10.1) \qquad\qquad s_y = \frac{1}{2}(\frac{T}{W} - 1)gt^2 \qquad (10.2)$$

This puts a constraint on the required thrust to weight ratio for take-off, as the minimum cruise altitude is set to 90 [m], to comply with cruise noise requirements. Checking the time required to reach this altitude with a thrust over weight ratio of 1.2 yields 10 [s], which is deemed adequate. For subsequent sizing of the batteries, the time available is set to 30 [s], to facilitate take-off for potential higher altitudes, wind gusts, or multiple take-offs.

10.1.2. Cruise

During cruise, the thrust must overcome an additional drag force. To analyze the cruise condition, this force must first be quantified. The drag will vary with the dynamic pressure, but also with the pitch angle θ. From literature[13], it was found that the drag coefficient of a quad-copter varies with the pitch angle according to Equation 10.3. The original relation from the book assumes pitch down as positive. To be consistent with the reference frame as presented in Figure 13.1, this has been transformed to use pitch up as the positive direction.

$$C_D = C_{D_1}(1 + sin^3(\theta)) + C_{D_2}(1 - cos^3(\theta)) \qquad (10.3)$$

where C_{D_1} is the drag coefficient at a pitch angle of 0 [deg] and C_{D_2} is the drag coefficient at a pitch angle of -90 [deg]. It must be noted that this formula was found through curve fitting from a CFD analysis, and a more accurate result can be obtained through similar CFD analysis for this specific UAV. Furthermore, it is assumed that for positive pitch angles, the original formula can also be used which takes the form as shown in Equation 10.4.

$$C_D = C_{D_1}(1 - sin^3(\theta)) + C_{D_3}(1 - cos^3(\theta)) \qquad (10.4)$$

where C_{D_3} is the drag coefficient at a pitch angle of 90 [deg]. To use these formulas, the 3 unknown drag coefficients have to be determined. This will be done by splitting up the problem into the 3 main contributors to the drag: the main body, propeller arms, and the landing gear. They are assumed

to be made up of cylindrical-shaped elements, which have known drag coefficients as described in Table 10.1. Where the length over diameter ratio (L/D) will be interpolated as needed.

Table 10.1: Coefficient of drag for a cylinder in an air stream from two different sides[14].

L/D	0.5	1	2	3	4	5	8	10	20	40	∞
Head-on C_D	1.15	0.9	0.85	-	0.87	-	0.99	-	-	-	-
Parallel C_D	-	0.64	0.68	0.72		0.74	-	0.82	0.91	0.98	1.20

Main body drag

The drag caused by the main body in the -90, 0 and 90 [deg] pitch angles can simply be derived from Equation 10.5. Here, C_D is the drag for a cylinder as can be found from Table 10.1, and S is equal to $l \cdot d$ for 0 [deg] pitch and $0.25\pi d^2$ for -90 and 90 [deg] pitch.

$$D = C_D \frac{1}{2}\rho V^2 S \qquad (10.5)$$

Propeller arm drag

The propeller arms are offset by 45 [deg] in the XY-plane, at 0 [deg] of pitch. What this effectively means is that instead of the airflow seeing a circular cylinder it will see an elliptical cylinder. The drag coefficients for 2D elliptical cylinders with different fineness ratios (FR) have been summarized in Table 10.2. Furthermore, the ratio between the elliptical drag coefficient and its circular counterpart has been given. It is assumed that this ratio also holds for the 3D case and is thus combined with the findings from Table 10.1 to attain the final drag coefficient for the elliptical cylinder.

Table 10.2: Drag coefficients for varying fineness ratios (FR) of 2D elliptical cylinders.

FR	1	2	4	8
$C_{D,FR}$	1.2	0.6	0.35	0.25
$C_{D,FR}/C_{D,1}$	1	0.5	0.292	0.208

Considering the 45 [deg] angle, the fineness ratio of the ellipse will be $\sqrt{2}$, from which the ratio can be interpolated. Furthermore, the frontal area is equal to $l \cdot d/\sqrt{2}$. This gives everything necessary to calculate the drag caused by the propeller arms, which can simply be calculated by four times Equation 10.5.

For the other two pitch angles, the orientation of the arms in the airflow boils down to a cylinder again. The drag coefficient can be determined from Table 10.1 and the frontal area is simply $l \cdot d$. Special attention needs to be paid to the -90 [deg] pitch angle though. This is because the propeller arms are in the wake of the propeller itself. This means that the velocity experienced by the propeller arms will be significantly higher. The induced velocity can be derived from Equation 10.6[15].

$$v_i = v_\infty \left\{ 1 + \left(-\frac{1}{2} + \frac{1}{2}\sqrt{1 + \frac{8}{\pi}T_c} \right) \left(1 + \frac{x}{\sqrt{x^2 + R_d^2}} \right) \right\} \qquad (10.6)$$

where v_∞ is the free stream velocity, T_c is the thrust coefficient of the top propeller, x is the distance behind the propeller the velocity needs to be known and R_d is the radius of the top propeller. With this velocity, the drag on the propeller arms can again be calculated using Equation 10.5. What is found is that the wake's velocity induces a significant amount of drag; for 4 propeller arms of 0.374 [m] length and 0.022 [m] diameter, flying at a cruise speed of 27.8 [m/s], the induced velocity causes 5 times as much drag if the velocity of the wake is included.

Landing gear drag

Lastly, the drag caused by the landing gear is investigated. As previously discussed, the wake causes a significant amount of drag. Therefore the design choice was made to fit the landing gear in between the propellers, thus eliminating the propeller-induced drag. The landing gear is modeled as four cylindrical arms with two cylindrical struts attached to it. With 0 [deg] of pitch, only the arms will be in the flow and the drag will be the addition of drag on these four. At -90 and 90 [deg] of pitch, all six elements are in the flow and again, using the drag coefficient from Table 10.1 and areas of $l \cdot d$, the drag can be found.

Total drag

Finally, the drag can be added together to find the total drag for different velocities. For the different pitch angles, the drag curves have been plotted in Figure 10.1. From this plot the drag coefficients C_{D_1}, C_{D_2} and C_{D_3} can be determined using a reference area of 1 through Equation 10.7. Finally, Equation 10.3 and 10.4 can be used to get the drag coefficient versus pitch curve described in Figure 10.2. Because the reference area used here is equal to one, this can also be seen as $C_D \cdot S$.

$$C_D = \frac{D}{\frac{1}{2}\rho V^2 S} \tag{10.7}$$
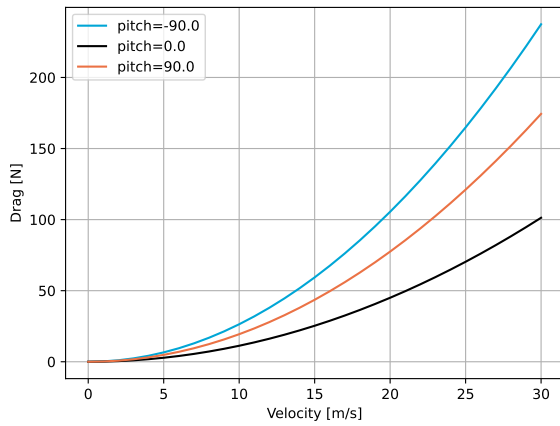
Figure 10.1: Drag for different pitch angles.
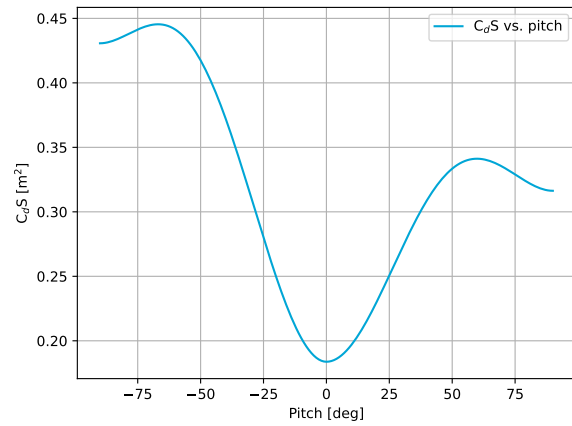
Figure 10.2: Drag coefficient for different pitch angles.

Now moving on to the equations of motion. These are described in Equation 10.8a and 10.8b.

$$\xleftarrow{+} \sum F_x; \quad -Tsin(\theta) = D \tag{10.8a}$$

$$+\downarrow \sum F_z; \quad W - Tcos(\theta) = 0 \tag{10.8b}$$

Solving for thrust in the z-direction gives $T = W/cos(\theta)$, which can be substituted in Equation 10.8a. The right and left-hand sides of Equation 10.8a can be plotted to find the equilibrium pitch for cruise at 100 [km/h]. From Figure 10.3, it can be seen that the equilibrium point for the pitch is at -17.4 [deg] of pitch. This also means that the thrust-to-weight ratio for a stable cruise will be $1/cos(-17.4) = 1.048$. The time calculated for this phase is based on the range required, which must be a minimum of 7 [km]. At a cruise speed of 27.8 [m/s], this gives a cruise time of 252 [s]. This is then rounded up to 300 [s] as a safety factor.
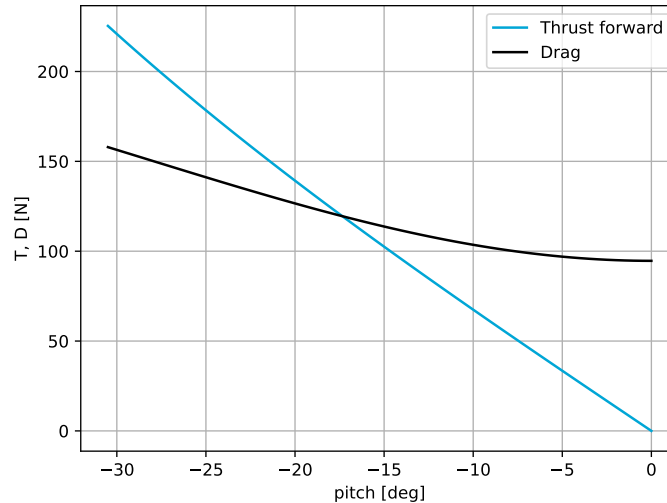
Figure 10.3: Thrust and drag versus pitch angle.

10.1.3. Hover

In hover, without disturbances, a minimum thrust to weight ratio of one is required. There are however disturbances that will require momentary higher thrust outputs. Therefore it was decided to cover the energy required for those situations by taking the conservative thrust to weight ratio of 1.1 for the entire mission-specific hover phase. The hover phase of the mission is split up into several sections. Firstly, after the cruise phase, there will be the search phase, this will mainly be hovering with some slow movement. This is to locate the victims inside the building to create a plan for the payload deployment. This is estimated to be 5 [min]. Once the first point of entry has been established, the payload delivery phase can begin. The glass cutting phase has been budgeted to take 2 [min]. During this time, the propellers do not rotate, the main power needs originate from communications and the glass cutting mechanism. It is then assumed that another 2 [min] of search time will be carried out to find a secondary point of entry to deliver the remaining masks. Once this has been completed, the drone must land to be restocked, with the landing procedures estimated to take around 1 [min].

10.1.4. Overview

To summarize the findings of this section, an overview of the mission is given in Table 10.3.

Table 10.3: Duration and required thrust over weight for different mission phases.

Mission phase	Duration [s]	T/W [-]
Take-off	30	1.2
Cruise	300	1.039
Hover	720	1.1

10.2. Propeller Design

The design of the propeller blades is fundamental for the UAV to have enough thrust and lift to safely perform its mission. This section will deal with the steps taken to design optimum propeller blades: as the design is based upon blade element theory, the governing principles will first be explained. Then, the necessary inputs will be gathered. A suitable program for analysis is then selected: Crotor, an extension to XRotor, developed by MIT[1]. This section is concluded with the results and the final geometry of the propeller.

---

[1]http://www.esotec.org/sw/crotor.html, Retrieved on 08/06/2021

10.2.1. Blade Element Momentum Theory

A propeller blade generates thrust in the same way that the airfoil of a wing generates lift. Blade element theory is the most common method for predicting propeller's performance. It was first suggested by Glauert (1935)[16]. At its most basic level, it consists of dividing the blade element into sections of length dR, whose 2D lift, drag, thrust, and torque are quantified. These forces along with the flow environment are shown on the blade element in Figure 10.4, where θ represents the pitch angle, found between the rotational plane of the rotor and the chord of the airfoil; α is the angle of attack, measured between the airspeed vector and the airfoil's chord, as is custom; U_P is the incoming airspeed, which lowers the effective angle of attack; Finally, U_T is the rotational velocity of the blade, which is on the same plane as the main plane where rotation occurs. The remaining forces are the standard aerodynamic forces, lift, drag, and pitching moment. One main drawback of this theory is that the thrust and theoretical efficiency tends to be oversized by approximately 5-10%[17]. This will be taken into account in the final design through the use of a safety factor.
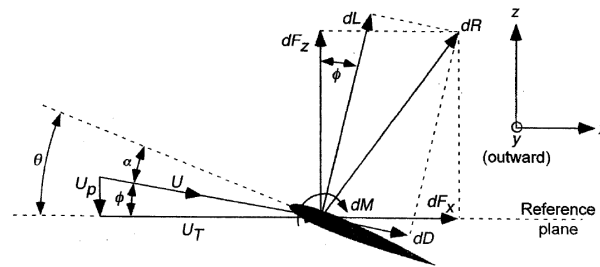
Figure 10.4: The aerodynamics forces on a 2D section of a rotating propeller blade. Image from[16].

The lift, drag, thrust and torque of one element can thereby be found by:

$$\Delta L = C_l \rho V^2 c \cdot dr$$
$$\Delta D = C_d \rho V^2 c \cdot dr$$
$$dT = N_b (dL \cos \phi - dD \sin \phi)$$
$$dQ = N_b (dL \sin \phi + dD \cos \phi) y$$

(10.9)

The total lift, drag, thrust, and torque can be found by performing the integrals arising from Equation 10.9. Due to the number of unknowns, to have a closed-form solution, some assumptions must be made: the inflow velocity can be assumed uniform, from simple momentum theory[16], giving a closed-form solution once the integrals are solved with an iterative process. Tip losses can also be accounted for, and this is done through Prandtl's tip loss factor, a value between 0.85-0.95 which is a correction factor applied to the blades' lift to account for the effect of the locally high induced velocities caused by the trailed tip vortices at the blade tip. A solution to the equations of blade element theory is found by coupling it with momentum theory, in what is known as Blade Element Momentum Theory (BEMT). This involves the equivalence between circulation and momentum theories of lift. Momentum theory consists of dividing the blade section into different disks, of area $dA = 2\pi y dy$. The thrust on each element can be calculated based on simple momentum theory, based on the product of velocity and mass flow rate. Numerical solutions of the relevant coefficients are available (and can be found in [16]), such that a numerical integration can be performed. Solving BEMT numerical equations allows for the determination of the overall propeller geometry; however, some initial values are needed to start the iteration. Thereby, Figure 10.5 shows the process that will be taken to determine the propeller geometry.
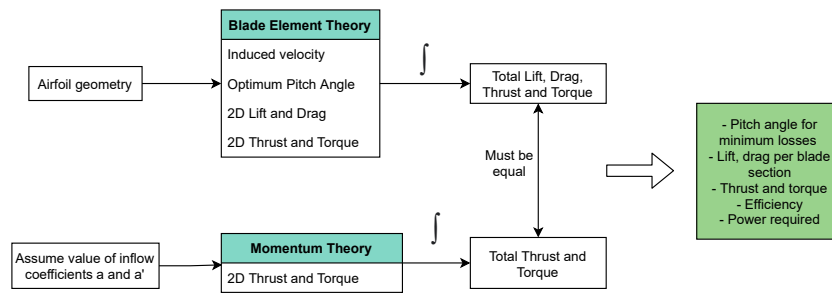
Figure 10.5: The BEMT process, with its inputs and outputs.

10.2.2. XRotor: a suitable program for analysis

Solving the equations of blade momentum theory is complex. There are many different options available online for solvers that aid in this iterative process: examples are Javaprop, XRotor, Crotor, QPROP. Due to the wide acknowledgment of XRotor as a good solver of BEMT[18], the latter is selected for the analysis[2]. Coaxial propellers are being used in this drone, therefore the extension CRotor, which is made specifically for the analysis of coaxial propellers, will also be used. From the description of the program[3], XRotor is an interactive program that allows for the design of minimum induced loss propellers, once a certain geometry is selected. It also performs acoustic analysis, which will be valuable to estimate the social sustainability of the final product. Naturally, no program can be used without thorough verification and validation, therefore these will be conducted on the program too.

10.2.3. Airfoil selection

The first step in the design of the propeller is to determine the airfoil geometry. As seen during the preliminary design, the propeller blade experiences different velocities along its radius. Closer to the hub, the Reynold's number is lower (approximately 80000), then it increases towards the middle section (between 150000 and 200000) and again reduces towards the tip (below 50000). Lower Reynolds numbers at the hub are due to lower local velocities, while lower Reynolds numbers at the tip are due to a smaller chord. A given airfoil has a range of Reynolds numbers for which its lift to drag ratio is maximized. Therefore, to optimize the performance of the blade across its radius, different airfoils can be used. Each shall have the highest lift to drag ratio for a certain Reynold's regime. To select an airfoil for a given location, an investigation was conducted into the behavior of the most commonly used airfoils in propeller blades, according to[19, 20, 21, 22]. These airfoils (all cambered) are: Clark Y, NACA4412, Wortmann FX 60-125 and GOE225[4]. The relevant properties for all airfoils were then investigated at low and high Reynolds. The criteria used to determine which airfoil suits best are: a large operational range (many angles of attack possible without stall occurring), a wide drag budget (drag relatively constant per angle of attack variation), and a high lift-over-drag ratio, especially at angles of attack between 5 [deg] and 10 [deg], as those are the most commonly used[16]. Figure 10.6 shows the lift over drag ratio for a range of angles of attack, for Reynolds numbers of 50000 and 200000. The data was gathered from XFOIL[5].

Firstly, at low Reynolds, two airfoils perform relatively similar: these are the Clark Y and the Wortmann FX 60-125, which present the highest lift to drag ratios. The Wortmann FX 60-125 slightly outperforms the Clark Y profile, while also having a wider range of angles of attack, thereby it was chosen for applications at low Reynold's numbers. Meanwhile, at high Reynold's numbers, the GOE225 outperforms every other airfoil. It has a much higher lift coefficient per angle of attack compared to its competitors, as well as a higher lift to drag ratio. Thereby the GOE225 is chosen for the middle sections of the

---

[2]The same consideration stemmed from a private conversation with Daniele Ragni, Associate Professor at the Aerodynamics and Wind Energy Department at TUDelft.

[3]http://web.mit.edu/drela/Public/web/xrotor/xrotor_doc.txt, Retrieved on 08/06/2021

[4]https://www.google.com/url?q=https://www.apcprop.com/technical\protect\discretionary{\char\hyphenchar\font}{}{}information/engineering/&sa=D&source=editors&ust=1622116232127000&usg=AFQjCNGF8Qxn86Yx6w1i_iQYbV-u4DuOLQ, Retrieved on 08/06/2021

[5]https://web.mit.edu/drela/Public/web/xfoil/, Retrieved on 08/06/2021
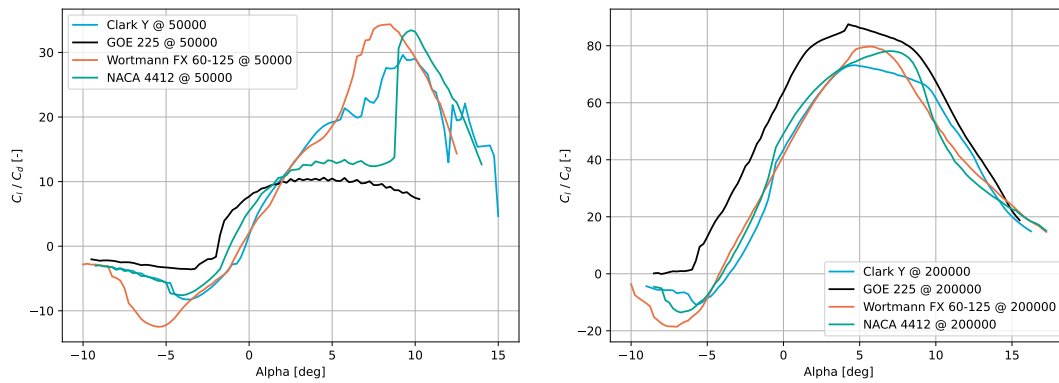
Figure 10.6: The left graph shows the comparison of the selected airfoils at low Reynolds numbers ($R_e = 50000$), while the right graph shows the same airfoils at high Reynolds numbers ($R_e = 200000$).

airfoil, the ones that experience higher Reynolds numbers. At points along the blade where the transition of the airfoils occurs, the resulting airfoil will be a linear interpolation of the two profiles. With regards to the angle of attack, the optimal operation point generally lies within 5 and 10 [deg][16]. Due to the high cruise velocity, which affects the effective angle of attack by lowering it, a relatively high angle of attack was chosen for the blades, a value of 8 [deg]. This is lower close to the root, where the induced velocities are also lower, thereby the angle of attack here is kept at 5 [deg]. Table 10.4 shows the different sections airfoil, as well as the angles of attack. The angles of attack refer to the case in which incoming flow is parallel to the airfoil's chord at an angle of 0 [deg]. At the tip, it was observed that the Reynolds numbers are low again, which justifies the choice of the Wortmann for the remaining ends of the blade.

Table 10.4: Airfoil used at different sections.

r/R	Airfoil	Angle of Attack [deg]
0 - 0.1	Wortmann FX 60-125	5
0.11 - 0.90	GOE225	8
0.92 - 1.0	Wortmann FX 60 -125	8

Before proceeding with the design of the optimal blade, some additional design considerations will be made, as they do affect the amount of thrust that is generated. The final analysis will also help in determining the angle of attack of the propeller airfoil at each radial station.

10.2.4. Coaxial propellers

A design choice has been made to use coaxial propellers. The main reason that led to this design choice is that coaxial propellers have a high efficiency when high disk loadings are required, as is the case where the UAV has to be wind resistant and as compact as possible, as well as enable to produce more thrust while keeping the dimensions contained when compared to an X8 configuration. A major drawback is however the higher level of noise produced and naturally, the fact that a coaxial pair of propellers will never produce the same amount of thrust as having two separate propellers.

The design of a coaxial propeller system is notoriously more complex than that of a single rotor. There are two possibilities for the design of coaxial propellers: co-rotating or contra-rotating. Contra-rotating propellers require a gearbox, due to the difference in the rotating direction, which adds weight. Co-rotating propellers on the other hand do not require a gearbox, however, they produce a net moment on the propeller arm that is not zero anymore, thereby adding complexity to the structure.

The rear rotor influences the flow upstream, thereby influencing the wake and performances of the upper rotor, which in turn then alters the inflow on the rear rotor[23]. To maximize the efficiency of this configuration, it is custom to have an upstream propeller with a slightly smaller diameter, to reduce

the contraction of the flow, and a slightly higher pitch angle of the blades due to operation in an already accelerated flow[24]. The distance between the two propellers is also a variable that must be investigated carefully. Based on the data from[24], it was concluded that there is not a significant difference with respect to the efficiency for varying propeller distance, so the distance between coaxial propellers is approximately equal to the radius of the propeller, as is custom, according to[25]. This distance has been chosen to accommodate for the presence of the propeller arm as well. Finally, coaxial propellers will be analyzed in Crotor.

10.2.5. Duct

The use of coaxial propellers greatly increases the noise of the system. As aeroacoustics sustainability is a concern, the possibility to use a ducted propeller design was considered. This offers some great gains: higher efficiency and thrust per propeller's radius and RPM, as well as greater user safety, as the blades are shielded from the outside environment. One of the downsides of having a duct pertains mostly to the structural side, as it adds weight and complexity to an already complex system. The reason that the duct generates a higher total thrust is due to the low-pressure region that forms on the duct lip, which intensifies inflow distribution by accelerating flow towards the outboard sections of interior rotors[26]. To perform a quantitative trade-off between having or not a duct, the performances of both cases, with or without a duct, were tested. This was done in XRotor, for an incoming airspeed of 10 [m/s] and a single propeller setup with a radius of 0.29 [m]. As some parameters of the design were not yet fixed, the simulation has been run for a fixed RPM of 4500 and a power of 1900 [W], which were values obtained during the preliminary design. The investigation was initially performed for a single propeller, however, the analysis of coaxial propellers revealed the same trend. The results are reported in Figure 10.7. The simulation was carried out for the simplest duct possible, which is one having an area ratio $(= A_{exit}/A_{inlet})$ of 1. The results show that the relative improvement with the duct is in the range of 9 to 11% more thrust, depending on the speed.
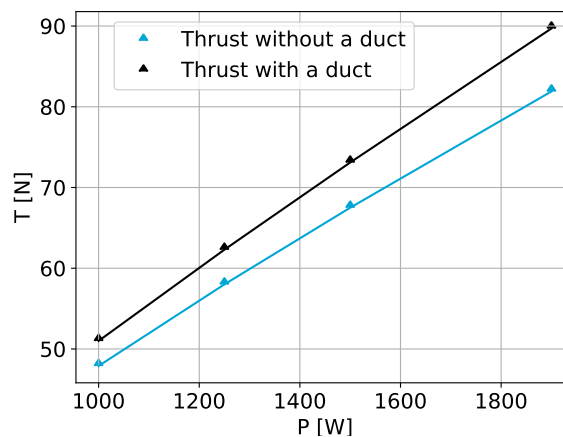
Figure 10.7: The thrust generated by a ducted propeller system versus a non ducted system.

To consider the performance improvements from an overall point of view, the weight of the duct was also estimated: this was in order to answer the question of whether the net extra thrust was still positive (as the increase in weight due to the duct does increase the thrust requirements). For this, the duct was assumed to be made of carbon fiber, laminated over foam, with a maximum thickness of 5 [mm]. It was found that, for an increase in thrust of approximately 64 [N], four ducts as proposed above would only require approximately 40 [N] more thrust, giving a net increase of approximately 24 [N]. This final consideration led to the introduction of a duct in the design of the propulsive system. Due to time constraints, this duct will be kept as simple as possible, also to improve the producibility. Hence, the area ratio is maintained at 1, and no further optimizations are performed. The duct will have a thickness of 1 [mm], and will also present a leading-edge shape like an airfoil, to maximize aerodynamic efficiency.

Design case

There are two main phases, concerning design decisions, that need to be analyzed during the flight of the UAV: cruise flight and hover. The required thrust-to-weight ratios were already defined in Section 10.1. To accurately size the propeller, it is important to decide which of the two cases is more limiting.

At cruise, the airspeed over the propeller blades is the highest. Due to the local angle of attack of the blade, the effective airspeed as seen by the propeller is not the same as the total cruise speed. With a calculated UAV angle of attack of 16 [deg], for a travel velocity of 100 [km/hr], the propeller only experiences 27 [km/h] of perpendicular airspeed. At higher airspeeds, the angle of attack is lowered due to the induced velocity, as shown by the velocity triangle in Figure 10.8. The system then produces less trust than it does at zero incoming airspeed (which is the case for hover), where the angle of attack is higher. This reasoning led to the decision that cruise is the most demanding phase for the propeller sizing: for the propellers sized at maximum cruise speed, it is still possible to generate enough thrust to keep the drone at hover. Thereby the cruise speed is used as a sizing condition.
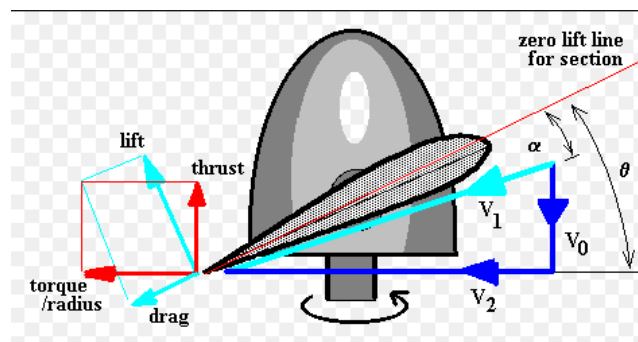
Figure 10.8: The velocity triangle for the propeller blade. The effective velocity v_2 is lowered by the perpendicular velocity v_0. The higher the incoming velocity v_0, the more prominent this effect becomes.[6]

Results

Finally, following the considerations made in the above chapters, the set of co-rotating propellers has been designed. The most important parameters for the two blades are reported in Table 10.5 below.

Table 10.5: The final parameters of the designed propeller blades.

Parameter	Upper Propeller	Lower Propeller	Unit
Blade length	0.29	0.34	[m]
Root chord	0.104	0.0586	[m]
Tip chord	0.029	0.0139	[m]
Hub radius	0.04	0.04	[m]
Pitch angle at root	84.85	75.71	[deg]
Total lift generated per blade	26.36	68.89	[N]
Total drag generated per blade	0.688	1.764	[N]
Maximum Mach number along blade	0.355	0.35	[-]

The drag and sectional lift generated by each blade, a measure of the efficiency of the blade, is also presented in the graph in Figure 10.9 below. The integration of the drag and the lift along the blade will be useful for the determination of the maximum loads and moments experienced by the system, which gives the required structural thickness of the propeller blade. This was found at 3000 [RPM].

---

[6]Image from http://www-mdp.eng.cam.ac.uk/web/library/enginfo/aerothermal_dvd_only/aero/propeller/prop1.html, Retrieved on 28/06/2021
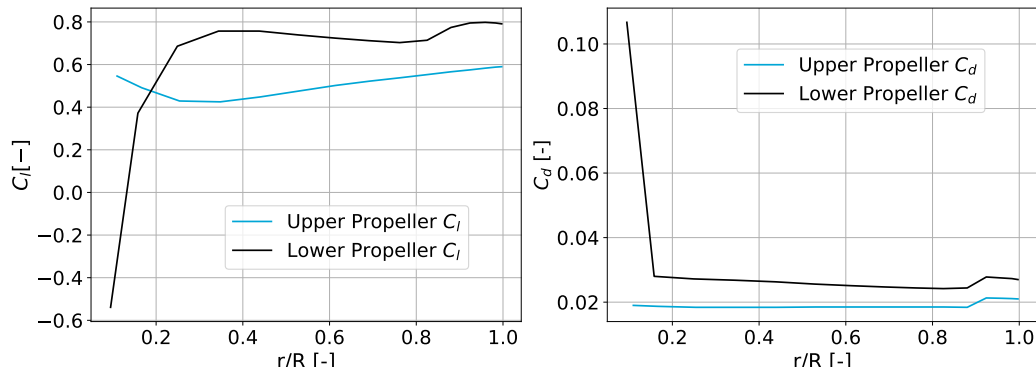
Figure 10.9: The lift coefficient per blade section (left) for the upper and lower propeller and the drag coefficient per blade section (right) for the upper and lower propeller blade. Note that the results are for one blade.

What can be seen in Figure 10.9 is that, for the top propeller, the lift and drag distribution is quite constant per blade sections. The lower propeller, on the other hand, experiences a high amount of drag and even produces a negative lift when close to the hub. That might be due to the wake related to the upper rotor. The duct dimensions have also been determined: it will have a radius of 0.45 [m], for a height of 0.195 [m].

10.2.6. Verification
With regards to code verification, the verification of XRotor must be carried out. This has been done by using experimental results from a paper by Grande et al[27] to verify that the output of the code was correct. As the experimental results obtained in [27] are relative to an airfoil NACA4412 (which is not the same that was chosen for this propeller blade) the program XRotor will be run with the same input values of the research, and the output will be compared. Verification was carried out as follows: as the optimum design of the propeller blade in [27] was determined using an efficiency program, the same inputs will be given to XRotor to verify that the output is the same. The reason the same efficiency program as Grande et al. cannot be used is that this program is not available as of now. Therefore, XRotor will be verified by ensuring that the results obtained with a different solver for the same problem are within acceptable margins of error.

Table 10.6: The relative difference between the results of the paper by Grande et al. and the results given by XRotor.

Parameter	NACA4412 in Grande et al.	NACA4412 in XRotor	Percentage difference
Maximum Pitch Angle [deg]	43.6	42.57	2.36 [%]
Maximum chord [cm]	3.4	3.6	5.88 [%]
Efficiency at J = 0.6	0.78	0.795	1.92 [%]

As can be seen in Table 10.6, the differences between the two methods are rather small: this gives great confidence in the program XRotor, which was thus a suitable means for analysis.

10.2.7. Validation
The validation of XRotor may only be done through experimental data. This can consist of two things: a wind tunnel experiment, as well as a CFD experiment. Due to time constraints, no validation was possible using a wind tunnel nor a computational fluid dynamics simulation. However, it is recommended that post DSE, this computation is carried on. Alternative ways to validate the results from XRotor is to perform experiments that test the real-life effect of the solutions tested in XRotor. This can only be done in a limited way, thereby it was not adopted in this case. Throughout the design, an effort was made to seek papers that would confirm the validity of the findings: for example, the thrust improvement with a duct, or the fact that having a longer propeller for the lower set is beneficial in the

co-rotating case.

10.3. Power system design

The propeller sizing gives rotational speed and power requirements for the sizing of the motors, which is explained in Section 10.3.1 and 10.3.2. Subsequently, an Electric Speed Controller (ESC) can be sized which is done in Section 10.3.3. Lastly, based on the power requirements, the batteries are sized in Section 10.3.4.

10.3.1. Relation between propeller and motor sizing

The general process as described in [13] is a method of sizing the power and propulsion system of a multi-copter. Starting with the calculations on the required thrust to weight ratios for the mission segments, the aerodynamics department can provide the power required and RPM for the propellers for each mission phase. From there it is possible to size the motors and then the Electric Speed Controllers (ESCs).

10.3.2. Motor sizing

For a given required RPM and tip radius, a motor can be selected. Generally, having large tip radii for the blades requires lower RPM for the motor as there is more lift. However, if there is a large tip radius, the torque required to spin the blades becomes larger. It is therefore desired to have a low motor zero-load-speed (K_V) for large propeller blades since that translates into higher torque generated. This does increase the voltage required to reach a certain RPM. The converse is also true. With 39 [kg] MTOW, the motor will be selected with a high torque/low K_V in mind. This is to provide sufficient torque for the larger blades. Having a low K_V also means that the current drawn will be lower compared to a higher K_V, which will help against heat generation by the system.

Furthermore, the motor should be selected based on the required power for the thrust, while satisfying the condition presented in Equation 10.10. This has to do with the fact that operating a motor at full throttle is not efficient, and can reduce the longevity of the motor itself. Therefore, for a given P_{req}^m, the operating efficiency typically lies between 40% and 70% of the throttle[28]. The overview of the motor setup used in this analysis is presented in Figure 10.10.

$$0.4P_{max}^m \leq P_{req}^m \leq 0.7P_{max}^m \tag{10.10}$$
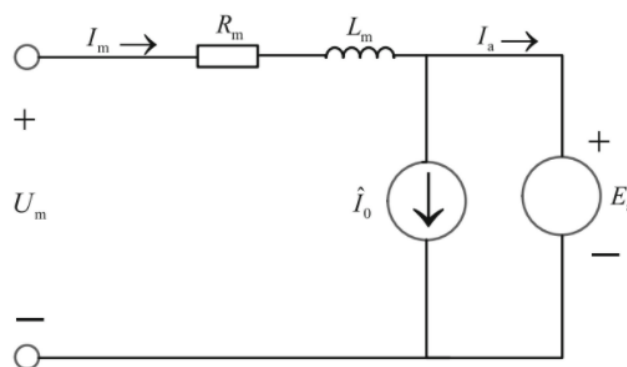
Figure 10.10: Equivalent motor setup[13]

The motor sizing start with inputs from the Aerodynamics departments. These are namely the RPM and the power required. From this the torque can be calculated using Equation 10.11.

$$T = \frac{P_{req}}{RPM \cdot 2 \cdot \pi / 60} \tag{10.11}$$

Where the zero-load current and voltage are I_{m0} and U_{m0} respectively, K_{V0} is the no-load motor

speed, and R_m is the internal resistance of the motor. From here, the force and torque constants can be calculated using Equations 10.12 and 10.13.

$$K_E = \frac{U_{m0} - I_{m0} \cdot R_m}{K_{V0} \cdot U_{m0}} \tag{10.12}$$

$$K_T = 9.955 \cdot K_E \tag{10.13}$$

Finally, the equivalent current and voltage can be calculated. These can then be used to size the ESC, as the sizing is done from the propeller working towards the batteries. Once these are known, a motor must be chosen that can take the needed current and can provide the required thrust. The results of this sizing will be discussed in Section 10.3.5.

$$I_m = \frac{T}{K_T} + \hat{I}_0 \tag{10.14}$$

$$U_m = K_E \cdot N + R_m \cdot I_m \tag{10.15}$$

For a selected motor, the required input voltage U_m and current I_m are then used to size the ESC.

10.3.3. Electric Speed Controller Sizing

Once it is known what voltage and current the motor draws, the ESC can be sized for. This is done by calculating the circuit principle using Equation 10.16, where U_{eu} is the voltage required by the ESC. Subsequently, the input throttle σ is defined as a function of the battery voltage U_b and the equivalent voltage U_{eu}, as can be seen in Equation 10.17. The setup for this analysis can be seen in Figure 10.11.
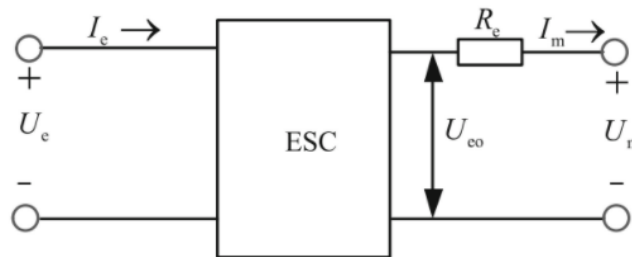
Figure 10.11: ESC setup[13].

$$U_m = U_{eu} - I_m \cdot R_m \tag{10.16}$$

$$\sigma = \frac{U_{eu}}{U_e} \approx \frac{U_{eu}}{U_b} \tag{10.17}$$

The last step in the ESC sizing is to determine the current and voltage needed by the component. This is calculated by using the input throttle σ, the number of propellers n_r, the ESC input current I_e and the internal resistance of the battery R_b, as can be seen in Equation 10.18 and Equation 10.19.

$$I_e = \sigma \cdot I_m \tag{10.18}$$

$$U_e = U_b - (n_r \cdot I_e + I_{other}) \cdot R_b \tag{10.19}$$

Table 10.7: Specifications for the selected motor.

Parameter	Value	Unit
Motor	Antigravity 8012	[-]
Maximum Service Temp.	180	[°C]
K_V	100	[RPM/V]
I_{max}	40	[A]
Internal Resistance	125	[mΩ]
Weight	351	[g]

Table 10.8: Electric Speed Controller specifications.

Parameter	Value	Unit
ESC	Flame 60A 12S	[-]
I_{max}	80	[A]
I_{cont}	60	[A]
Weight	73.5	[g]
Control frequency	600	[Hz]

Heat generation

As the first iteration for this design stage, the heat generation of the battery and electrical system has been looked at as a function of efficiency. This means that the energy lost in the system is assumed to have been transferred to heat. Due to the high efficiency of the system, it can be concluded that the performance change due to an increase in temperature, due to the operating conditions, and internal heat generation, is minimal. This aspect can be compensated for by using a safety factor in the sizing. The main effect of temperature is that the battery life, and thus performance over time, decreases. When looking at the instantaneous performance, increasing temperatures are more beneficial for the batteries. It can also be seen that the expected temperature ranges will only reduce the efficiency of the electrical system by 2-3%. The expected range for the electrical systems is 80 [°C]. This takes into account the allowable 50 [°C] from the fire conditions, also taking into account a temperature increase of 10 [°C] from the heat generated by the system itself[29].

10.3.4. Battery Sizing

Now that power requirements, and hence the current and voltage required by the system itself, are known, the batteries can be sized. This is based on two requirements. The first being whether the battery setup can give the required voltage of the system. The second is that there needs to be enough capacity in the battery setup to allow for the required mission time and rigors of the mission. The latter can be checked in Equation 10.20. The former can simply be calculated by looking at the total voltage supplied by the battery setup and checking whether this is higher than the voltage requirements.

$$Q_b = \frac{I_e \cdot M \cdot t_{phase}}{\eta_B \cdot DoD} \tag{10.20}$$

Where the battery efficiency is denoted as η_B, the Depth of Discharge as DoD, t_{phase} the time of a mission phase, I_e the current supplied by the battery, and M being the number of motors. Heat generation will be taken into account in the form of a safety factor on the battery capacity, as degradation will happen more prevalently, and the C-rating will be checked in a pass or fail capacity, to ensure that it is sufficient.

10.3.5. Propulsion component choice

Using the aforementioned method, it was possible to select the motor and the ESC.[7] The results of the sizing can be found in Table 10.7 and 10.8.

These components were chosen based on their ability to provide the required torque and RPM requirements while ensuring the current does not exceed the maximum allowable current. At this stage, off-the-shelf components were used. An extensive search for the different options was completed

---

[7]https://www.robotshop.com/nl/en/t-motor-60a-6-12s-flame-pro-brushless-motor-esc.html, Retrieved on 29/06/2021.

and these were the final components chosen. This was done due to the high complexity of the components themselves and ease of manufacturing. This will help maintain performance throughout the mission as heat generation will be kept to a minimum.

10.3.6. Final sizing power

Additional requirements for the power system originate from the communications and operations subsystems. The communications system requires power to transmit signals to allow the external operator to be able to control it, as well as ensuring the navigation systems work well. Furthermore, the control systems onboard, namely the flight computer also needs power. On the operations side of the mission, the glass cutting mechanism will also require power to operate. For this aspect, a standard motor was chosen for the glass cutting mechanism. An overview of the power required can be found in Table 10.9.

Table 10.9: Overview of the power requirements of all of the subsystems.

Sub-system	Power [W]	Voltage [V]	Current [I]	Q_b [mAh]
Take - off	7660	45.6	167.983	1686.324
Cruise	5848	45.6	128.246	21682.813
Mission	5236	45.6	114.825	35602.420
Peak power	10212	45.6	223.948	-
Glass cutting	20	12	1.667	3.206
Communications	20	5	4	288.550
Sensors	0.7337	5.5	0.1334	10.585
Total				**59273.899**
Batteries required (parallel)				3

Table 10.10, along with the voltage and current requirements for the motors and ESCs, provides a basis for the battery selection. For this, the Tattu 23000mAh LiPo[8] battery pack was deemed to be the best option. The overview of the battery specifications is given in Table 10.10.

Table 10.10: Specifications of the chosen battery.

Parameter	Value	Unit
Capacity	23000	[mAh]
Voltage	22.8	[V]
Setup	6S	[-]
Discharge rate	25	[C]
Length	207	[mm]
Width	91	[mm]
Height	62	[mm]
Guaranteed lifecycles	150	[-]
Assumed Depth of Discharge	0.8	[-]
Assumed efficiency	0.95	[-]
Charging time	60	[min]

10.3.7. Final propulsion system design

The final electrical setup can be found below in Figure 10.12. This provides an overview in the form of an electric block diagram of the composition of the system.

The total number of batteries in parallel for the capacity is 3. These batteries will be reusable to ensure sustainability and ease of use. To meet the voltage requirements, there must also be 2 bat-

---

[8]`https://www.gensace.de/tattu-23000mah-22-8v-25c-6s1p-lipo-battery-pack.html`, Retrieved on 06/05/2021

teries in series. This gives a final setup of 2 in series and 3 parallel as will be displayed in the next section.
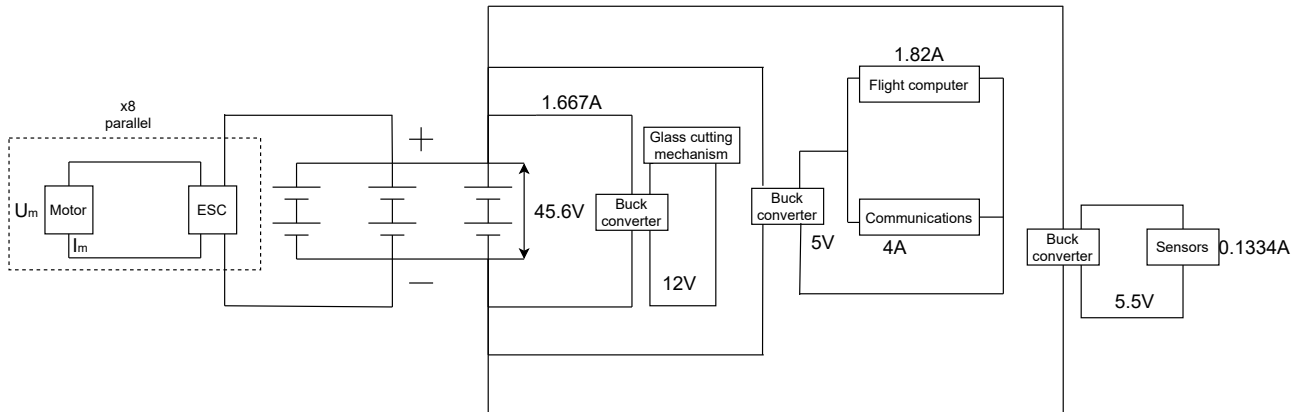
Electrical Block Diagram

Figure 10.12: Electric Block Diagram

As can be seen in Figure 10.12, there are 8 parallel circuits for each of the motors. The power draw for the motors and ESCs varies depending on the mission phase. Then there is a branch with the communications system and flight computer, using a buck converter to step down the voltage from the battery. A similar setup is used to provide the requirements for the glass cutting mechanism and the sensors.

10.4. Performance

With the propulsion system sized, the performance of the system can be determined. Relevant parameters for performance are discussed in the following sections: endurance (Section 10.4.1), range (Section 10.4.2) and maximum velocity (Section 10.4.3).

10.4.1. Endurance

The formula for endurance is given in Equation 10.21. It is the total energy in the battery (E_{bat}) divided by the power output of the battery (P_{bat}). This means that the power output must be minimized. For hovering, this is when the thrust required is lowest and the incoming velocity is stationary. The latter is beneficial because kinetic energy is related to the velocity squared. The energy required for an increase in airspeed from v_1 to v_2 is thus related to $(v_2^2 - v_1^2)$. This increase has a linear relationship with the thrust.

$$t = \frac{E_{bat}}{P_{bat}}$$ (10.21)

With the current battery setup, the energy available is $69Ah \cdot 45.6V \cdot \eta_B \cdot DoD = 8.6MJ$ and the power required for hover is calculated through the battery current required I_b, which is calculated from the procedure described in Section 10.3.2. The endurance then is found to be 1609 [s].

10.4.2. Range

The range can be found by integrating the velocity over time. Furthermore, the substitution of $dt = -dE/P$ is used to find that, to optimize for range, V/P must be maximized.

$$R = \int_{t_1}^{t_2} V dt = -\int_{E_1}^{E_2} \frac{V}{P} dE$$ (10.22)

To analyze at what velocity V/P is maximal, first a relationship between the power and velocity is sought. This is done by finding several discrete points for the power at different cruise velocities. From this, a continuous function is attained through regression. The result is displayed in Figure 10.13a.

From this function, V/P versus velocity can be plotted and a maximum can be found as is shown in Figure 10.13b. Finally, the integral can be solved using $V/P = 0.0032$ at a velocity of 23.94 [m/s]. The maximum range is then found to be 27.9 [km].
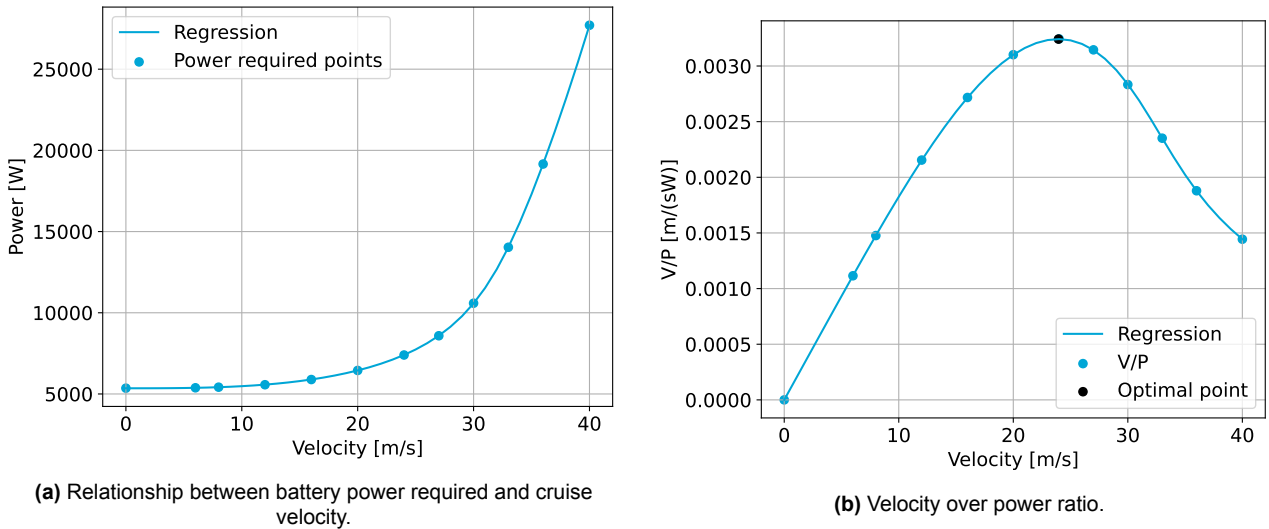

(a) Relationship between battery power required and cruise velocity.

(b) Velocity over power ratio.

Figure 10.13: Method to find the optimum cruise velocity for range.

10.4.3. Maximum speed

From experimentation with the currents in the system, it was found that the maximum speed is limited by the maximum current of the motors, which is rated at 40 [A]. The current versus the velocity can be plotted, as is presented in Figure 10.14. The maximum speed found at the intersection point is 31.95 [m/s].
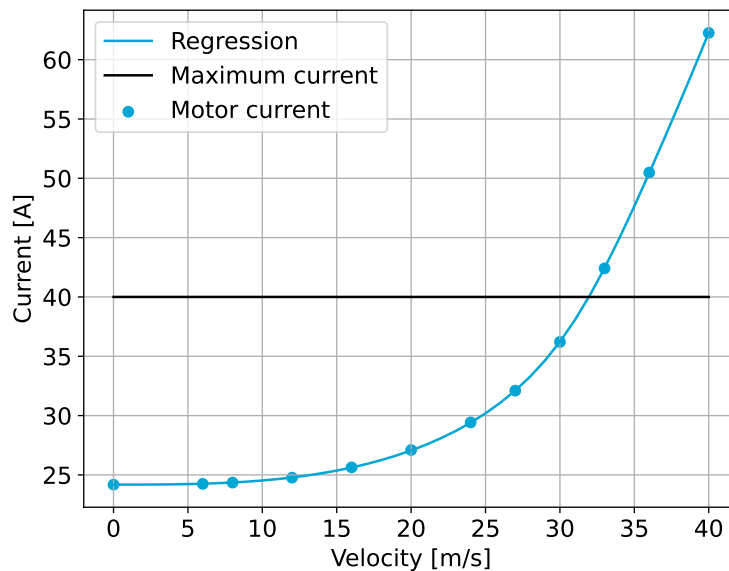
Figure 10.14: Relation between motor current and velocity.

10.4.4. Extra range or hover endurance in mission

Although the previous performance parameters were interesting, they do not prove that the UAV can perform its mission successfully. By taking a linear combination of the formulas used for endurance and range, Equation 10.23 can be found. This formula describes the total energy required. By fixing the total energy available and either the range or the endurance in hover, the remaining variable can be solved to find the available range or endurance considering the mission requirement. The result is a mission range of 15.4 [km] or 1205 [s] of mission-specific hover. The former allows for a longer

operational range than the 7 [km] designed for. The latter might allow for restocking and a second flight on site. The system will have to check its battery status if it is possible to do this. Alternatively, it can be chosen to only execute one mission with a smaller depth of discharge, which would improve battery life.

$$E = P_{hover}t + \left(\frac{P}{V}\right)_{cruise} R \tag{10.23}$$

10.4.5. Redundancy

Redundancy is an important requirement to have to maintain the ability to perform missions for 10 years. One vital requirement in regards to redundancy is the ability to make an emergency landing, should 50% of the propulsion system fail. This 50% is specifically for the case when one of the two motors on each arm would become inoperative, or when a complete set of motors would fail along a diagonal of the UAV. (For more information on this, see Section 13.4. The main criteria to check for this condition is if the motors and ESCs can handle the current and voltage required to drive the propellers at a fast enough RPM. The performance requirement for landing safely was defined at a thrust-to-weight ratio of 1.1, to take into account deceleration just before landing and for controllability considerations.

Using Xrotor, and considering both the failure of the top and bottom rotor, it was established that if the top rotors fail for all of the arms, it would still be possible to make a safe landing. The total power output would then fully be put onto the top rotors. This would demand a required RPM of 3258 and a power per motor of 1250 [W]. Found using the equivalent voltage and current sizing methods in Section 10.3.2 and 10.3.3.

This analysis concludes that voltage and current requirements for these performance characteristics are within the operational ranges of the batteries, electric speed controllers, and motors. The motor input and ESC input current were calculated at 39.5 [A] and 32.4 [A] respectively. Therefore, it is possible for the drone to safely land if 50% of the propulsion system fails, hence the requirement is met.

10.5. Sub-system Compliance Matrix Propulsion

Upon completion of the design, it is important to check whether the design matches the requirements generated at the start of the design process. These will be evaluated in a compliance matrix. Table 10.11 shows the compliance matrix of the requirements related to propulsion.

Table 10.11: Compliance matrix propulsion and power requirements.

Requirement	Verification method	Compliance
TECH-PROP-01	This thrust corresponds to the instantaneous requirement for controllability.	Yes
TECH-PROP-03	As explained in Section 10.4.2 the propulsion system meets this requirements.	Yes
TECH-PROP-04	This has been designed for in the peak power case in Section 10.3.7.	Yes
TECH-PROP-05	This has been designed for in the peak power case in Section 10.3.7.	Yes
TECH-PROP-06	Based on the power system selected in Section 10.3.7 this requirement is met.	Yes
TECH-PROP-07	This was a design requirement that contributed to the selection of batteries in the Figure 7.1. Additionally the electricity for charging will renewable as depicted in Section 3.2	Yes
	Continued on next page	

Requirement	Verification method	Compliance
TECH-PROP-08	The Section 11.3 section presents how this requirement was positively achieved.	Yes
TECH-PROP-09	This was a design requirement that contributed to the selection of batteries in the Figure 7.1.	Yes
TECH-GEN-05:	The UAV has been designed for an altitude of 90m, therefore this requirement is met.	Yes

11 Detailed Design: Material selection

During its mission, the UAV will be exposed to high temperatures, as it is close to the fire. This introduces extra limits on material choices. Section 11.1 will evaluate which temperature the materials should withstand, whereafter Section 11.2 will discuss the structural materials and Section 11.3 will elaborate upon insulation. Finally, verification & validation and requirement compliance will be done in Section 11.4 and 11.5 respectively.

11.1. Temperature Determination

To be able to estimate the temperatures the UAV will be exposed to, first, the flame height needs to be determined, as the UAV will mainly be exposed to high temperatures while it adheres to a building. The determination of the height of the flames can be done using the following relationship for rectangular wall fires[30]:

$$H_f = 0.050 Q_w^{2/3} \tag{11.1}$$

Where Q_w represents the rate of heat release per unit wall width. This number can be estimated by looking at, for example, a burning height of 1.2 [m] (4 [ft]), where the largest, and thus most limiting, value for Q_w is found to be 158 [kW/m][30]. This results in a fire height of 1.5 [m]. Subsequently, the temperature at a distance from the fire can be determined using the following equation:

$$T = aQ = 60 \left(1 - e^{-\frac{L^2}{D}} \right) \tag{11.2}$$

Where T refers to the temperature and a is a constant to relate the temperature to the heat flux. This relationship is estimated to be linear (a is often equal to 10). L indicates the flame length, which is equal to the flame height determined with Equation 11.1, as in this case vertical fires are discussed. Finally, D indicates the distance from the fire. As the UAV will not open windows close to the fire, a distance of 4 [m] is used to estimate the temperature the UAV will experience. Using Equation 11.2 a temperature of 258 [°C][31]. However, as the UAV will be located above the fire where the temperature will be higher than it is to the side of it, the temperature used in determining suitable materials will be 300 [°C] to account for the extra heat. This limit is set on the materials in the case the fire rapidly expands or a flash fire occurs and part of the UAV is exposed to it. It is not necessarily designed for continuous exposure as a human would then not be able to put his/her hand out of the window to get to the payload.

11.2. Structural material selection

For the structural material, a material with a high strength-to-weight ratio is preferred, as this will result in a lighter UAV, which in turn results in a smaller UAV. Compared to metals, composite materials show a good strength-to-weight ratio and also have a high specific modulus. Therefore, research was conducted into the different fibers and resins that can be used. The main two types of fibers are carbon fiber or fiberglass. There are other types of fibers, but those run into difficulties with processing

or have limited use cases[1]. To compare carbon fiber and fiberglass, both materials were compared on Young's modulus versus density graph. To minimize the weight of a beam, the index $\frac{E^{1/3}}{\rho}$ should be maximized. Therefore the diagonal line in Figure 11.1 represents a line on which materials perform similarly.
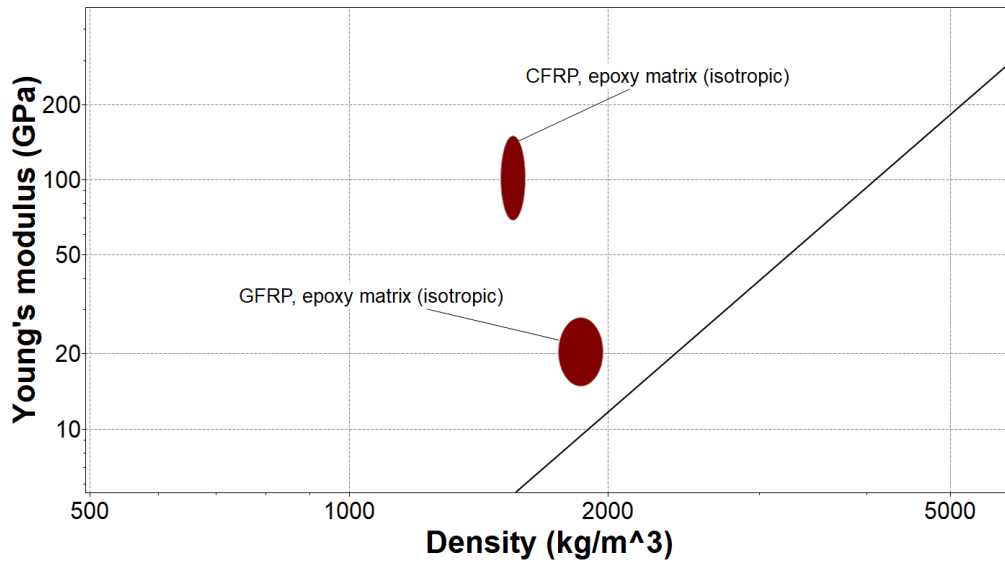
Figure 11.1: Young's modulus versus density graph showing the performance of carbon fiber and glass fiber composites[11].
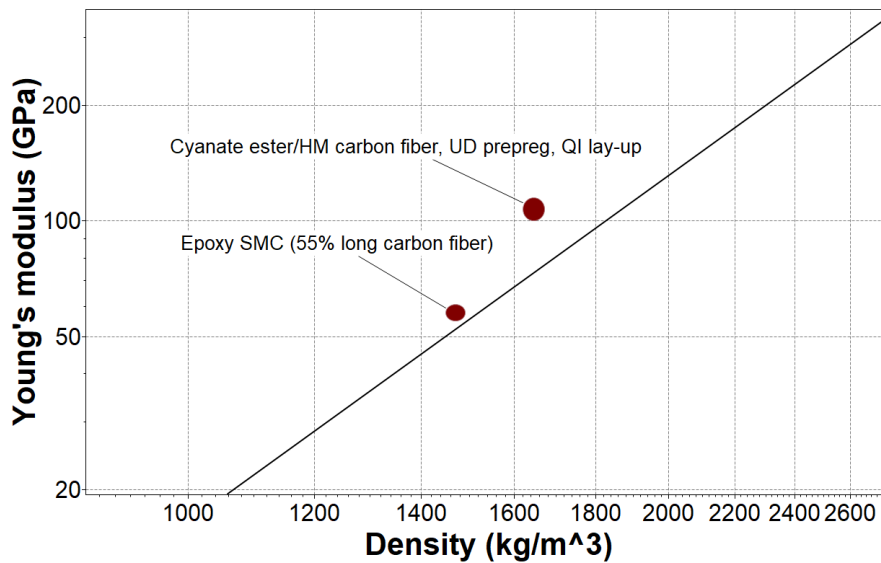
Figure 11.2: Young's modulus versus density graph showing the performance of epoxies and cyanate esters[11].

From this, it can be concluded that carbon fibers are preferred over fiberglass. Additionally, it is proven that carbon fibers perform better in tensile and flexural stresses[32].

Next comes the choice of resin. As resin will be the limiting factor in the maximum service temperature, it is important to choose it such that the maximum service temperature will be sufficient, i.e. 300 [°C]. However, it is found that essentially no resin will be able to withstand the heat on its own, so therefore additional insulation will be added to protect the resin from the heat. As research suggests that it is

---

[1] http://www.automateddynamics.com/article/thermoplastic-composite-basics/types-of-fiber-reinforcement, Retrieved on 03/06/2021

possible to shield carbon fiber reinforced polymers (CFRPs) with service temperatures of around 170 [°C] and higher against outside heats[33, 34]. The following types of resin were found:

- **Bismaleimides (BMI)** is not chosen as this resin material results in a brittle composite, which is not desired for the UAV[35].
- **Polyimide** is not chosen because the manufacturing process is difficult, as during the curing process volatiles of water and solvent arise[35].
- **Cyanate ester** is not chosen because of the high costs (164-183 [GBP/kg]) compared to for example epoxies (55-61 [GBP/kg])[11]. This high cost could be justified if the cyanate esters perform significantly better than epoxies. However, in maximizing the $\frac{E^{1/3}}{\rho}$ index cyanate performs only slightly better (see Figure 11.2) and the two resins have similar maximum service temperatures. Therefore, cyanate esters were not deemed worth their cost for this application.
- **Epoxies** are chosen for their relatively low thermal conductivity and their lower density than cyanate esters. Additionally, it has a maximum service temperature of 180 [°C]. Different manufacturing methods for carbon fiber-epoxy combinations result in different material characteristics. Woven prepreg (quasi-isotropic lay-up) was chosen for its relatively high service temperature and variety of processes to manufacture parts out of it.

Relevant material properties of the CFRP can be found in Table 11.1.

However, not all components can be made out of CFRP for example rotating parts are better made out of metal. For the choice of material, it is not only important that it has a service temperature of at least 300 [°C], but also the coefficient of thermal expansion (CTE) is of importance. If two different materials are joined with different CTEs a mismatch will occur at higher temperatures. The material choice fell upon aluminum 8019 for its relatively low density and similar CTE as the carbon fiber with epoxy[11]. The properties of this material at room temperature can also be found in Table 11.1.

Table 11.1: Material properties of carbon fiber with epoxy (woven prepreg, quasi-isotropic lay-up) and aluminum (8019, rapid solidification)[11].

Material property	Carbon fiber with epoxy	Aluminum	Unit
Percentage carbon fiber	63	-	[%]
Price	43.6	8.19	[GBP/kg]
Density	1575	2930	[kg/m^3]
Young's modulus	46.2	90	[GPa]
Yield strength	549.5	400	[MPa]
Shear modulus	17.3	34	[GPa]
Glass temperature	180	-	[°C]
Maximum service temperature	180	300	[°C]
Thermal conductivity	1.64	117.5	[W/(m°C)]
Coefficient of thermal expansion	29	24.1	[μstrain/°C]
Specific heat	1019.5	935	[J/(kg°C)]
Flammability	slow-burning	non-flammable	[-]
CO_2 footprint, primary production	45	12.8	[kg CO_2/kg CFRP]
Water usage	1315	1065	[l water/kg CFRP]

11.3. Insulation Material Selection

To protect the CFRP against the heat from the fire, a thermal barrier coating (TBC) is used. The selected TBC is an alumina-ceramic mat, hardened by Vitcas rigidizer, based on water glass. This hardening increases the mass but is necessary. Without it, the TBC would be vulnerable to erosion, mechanical damage and it would have a low strength (0.2-0.3 [MPa])[34]. A possible moment for adhering the TBC to the CFRP would be during the curing, as this is a promising technique that results in good bonding between the two materials.[36] Additional experiments need to be performed

to quantify the bonding strength. The material properties of the TBC can be found in Table 11.2.

Table 11.2: Material properties of the thermal barrier coating[34].

Material property	Value	Unit
Thermal conductivity	0.08 at 200 [°C], 0.22 at 800 [°C]	[W/(m·K)]
Density	170	[kg/m^3]
Young's modulus	5.2	[GPa]
Specific heat	1050	[J/(kg·K)]
Coefficient of thermal expansion	30	[μstrain/°C]

Not only the CFRP needs to be protected by the heat, but also the components inside the UAV. Inside the UAV, a maximum temperature of 50 [°C] is allowed. To guarantee this, a layer of foam will be added to the inside of the structure. This method adds less weight than adding more TBC to the exterior of the drone. The foam was chosen because it generally has a low thermal diffusivity, which means that it will take longer for a temperature change to reach the other side of the foam[37]. Taking into account that the CFRP will conduct a large amount of heat, the service temperature of the material should be at least 160 [°C] and it should have low thermal conductivity. Therefore, glass mineral wool was chosen. Another beneficial characteristic of glass mineral wool is the fact that it is classified as a non-combustible material[38]. This is required, as the wool will be in contact with batteries and wires. Finally, in general, glass mineral wool is usually made with recycled industrial or consumer waste with percentages up to 30 [%][2]. This is beneficial from a sustainability perspective. The material properties of glass mineral wool can be found in Table 11.3.

Table 11.3: Material properties of mineral wool[3][39].

Material property	Value	Unit
Maximum service temperature	649	[°C]
Thermal conductivity	0.035	[W/(m·K)]
Density	20	[kg/m^3]
Specific heat	1030	[J/(kg·K)]

The required thicknesses of the two insulation layers (TBC and mineral wool) can be determined using Fourier's law. Under steady state conditions, the heat flux is constant throughout the skin of the UAV. Therefore, for a unit area of wall, the following holds[40]:

$$\frac{T_1 - T_2}{L_{TBC}/k_{TBC}} = \frac{T_2 - T_3}{L_{CFRP}/k_{CFRP}} = \frac{T_3 - T_4}{L_{Foam}/k_{Foam}} \tag{11.3}$$

Where the different k's refer to the thermal conductivity of the materials. The definition of the lengths and temperatures can be found in Figure 11.3.

---

[2]https://www.greenspec.co.uk/building-design/insulation-materials-thermal-properties/, Retrieved on 03/06/2021

[3]https://www.greenspec.co.uk/building-design/insulation-materials-thermal-properties/, Retrieved on 27/05/2021
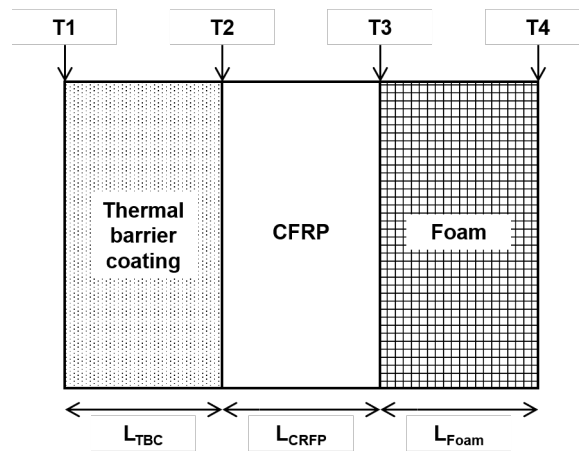
Figure 11.3: Graphical representation of the three material layers used in the UAV: A thermal barrier coating, carbon fiber reinforced polymer and an insulation layer of foam.

The temperature outside the UAV, T_1, is equal to 300 [°C] as determined in Section 11.1. T_2 is set equal to 160 [°C], which is equal to around 90 [%] of the maximum service temperature of the CFRP, to include some safety margin. It is, however, important to note that increasing the temperature results in a degradation of the mechanical properties of CFRP. The yield strength of CFRP at around 160 [°C] is found to decrease with about 30 [%] compared with the strength at room temperature, from simulation and experiments[41, p.10]. Therefore, during the structural sizing, a lower yield strength will be considered. For T_3, there is no desired value, as the foam will easily be able to withstand the temperature T_2. Finally, T_4 is set to be equal to the maximum temperature the interior can withstand, which is in this case 50 [°C]. Now, Equation 11.3 can be used to determine the thickness of the TBC and the foam, if it is assumed that T_3 will be 3 [°C] lower than T_2 to represent a case with a large amount of heat flow. This results in the thicknesses that can be found in Table 11.4.

Table 11.4: Insulation layer thicknesses for CFRP and Kovar.

Material	Thickness	Unit
Thermal barrier coating (for 1 [mm] of CFRP)	11.8	[mm]
Glass mineral wool (for 1 [mm] of CFRP)	2.23	[mm]
Glass mineral wool (for 1 [mm] of Kovar)	5.38	[mm]

To verify these calculations the software Energy2D was used[42]. The thicknesses shown in Table 11.4 are used as inputted and their effect on temperature is simulated. This results in Figure 11.4. As can be seen the total temperature difference from outside (300 [°C]) to inside the UAV (50 [°C]) is guaranteed using the insulation layers. However, the temperature at the CFRP surface is only 63 [°C], whereas it can withstand temperatures up to 180 [°C]. This means that the TBC layer thickness can be decreased and, as a result of that, the mineral wool layer should be increased. This is beneficial because the overall thickness is smaller and the mineral wool is lighter, hence resulting in a lighter overall structure. The new configuration can be found in Figure 11.5.
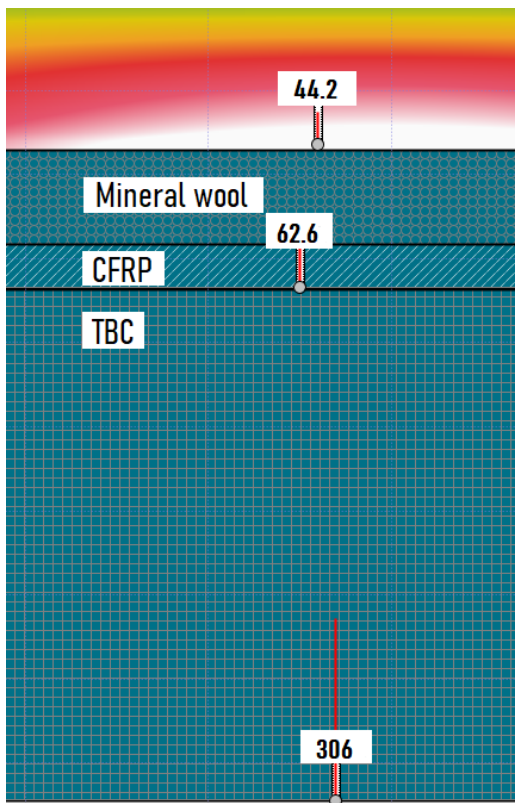
Figure 11.4: One dimensional thermal simulation according to calculations with Fourier's law, temperatures are indicated in degrees Celsius.
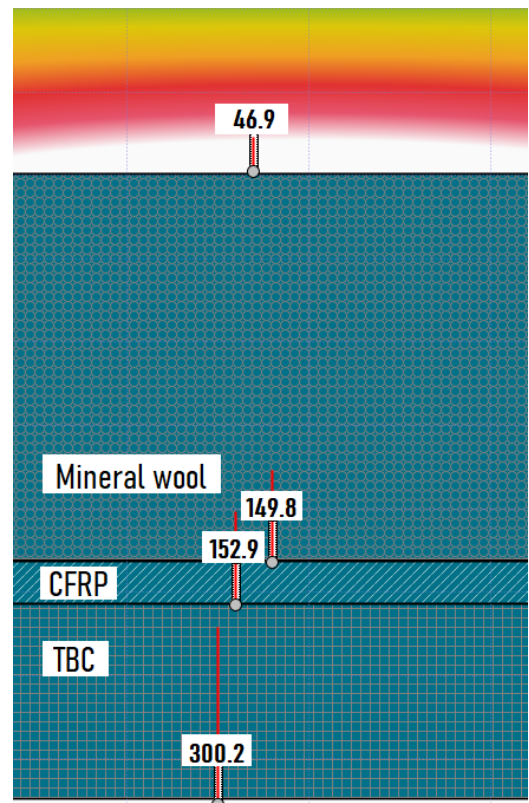
Figure 11.5: Optimization of insulation thicknesses using one dimensional thermal insulation, temperatures are indicated in degrees Celsius.

This optimization difference between calculations and software is due to the fact that Energy2D also takes into account the specific heat (c) of a material, as the program solves the following formula for conduction in a heterogeneous media[4]:

$$\rho c \left(\frac{\delta T}{\delta t} + \nabla(vT) \right) = \nabla\left(k\nabla T\right) + q \tag{11.4}$$

This results in a thinner TBC layer. The same program was used to determine the glass mineral wool needed if 1 [mm] of Kovar is used. The new thermal insulation thicknesses can be found in Table 11.5.

Table 11.5: Iterated thicknesses of insulation materials.

Material	Thickness	Unit
Thermal barrier coating (for 1 [mm] CFRP)	4.5	[mm]
Glass mineral wool (for 1 [mm] of CFRP)	9	[mm]
Glass mineral wool (for 1 [mm] of Kovar)	11.3	[mm]

The last material that is used is Kevlar. This material is chosen to make the protection ring around the glass cutting mechanism and a woven form will be used to make protection bags for the walkie-talkies (which will be further explained in Section 12.2.5). Kevlar is chosen as it is cutting-resistant and heat-resistant. Relevant material properties are given in Table 11.6.

---

[4]https://energy.concord.org/energy2d/papers/heat_solver.pdf, Retrieved on 26/05/2021

Table 11.6: Material properties of Kevlar[11]

Parameter	Value	Unit
Maximum service temperature[5]	425	[°C]
Thermal conductivity[6]	0.04	[W/(m·K)]
Density	1400	[kg/m^3]
Price[7]	54.59	[m^2]

11.4. Verification and Validation

Verification of the insulation layers is done and explained in Section 11.3 using the Energy2D software[42]. It was included in there as it resulted in a design iteration. A brief description of the software and its validity will be given. The software was developed to help students quickly get a grasp of the thermal properties of a designed system. The program can maintain the total thermal energy at a certain level accurately (99.9 [%]), when time steps smaller than 0.01 [s] are used[8] (which is done in the simulations used in this research). It should be noted that the program is particularly accurate for conduction rather than convection and radiation. However, for this research, conduction was the primary mode of heat transportation. Therefore, this limitation will not influence the accuracy significantly. For this reason, this software is used by over 40 scientific papers and recommended by two books[9].

Additionally, to determine potential hot spots or places where the thermal stresses increase dramatically, it is recommended to perform a global thermal analysis of scenarios where the fire is different in size and location with respect to the UAV.

Finally, as noted in Section 11.3 the bonding between the TBC and the CFRP needs to be quantified. This can be done in an experiment where the bonding is tested at room temperature, at 300 [°C], and when it has cooled down. Tests should be performed for both tension and bending. This should be done to validate the effectiveness of the bond for this application.

11.5. Sub-system Compliance Matrix

Table 11.7 gives the compliance matrix of the requirements related to the material selection.

Table 11.7: Compliance matrix material requirements

Requirement	Verification method	Compliance
TECH-TEMP-01	The materials that can be in contact with fire are aluminum (non-flammable) and the TBC (also designed to withstand fire), see Section 11.2 and 11.3.	Yes
TECH-OC-03	The TBC is hardened with rigidizer to prevent corrosion, as explained in Section 11.3.	Yes
TECH-OC-04	Even if the TBC will let through water, the CFRP will prevent the water from getting inside the UAV.	Yes

12 Detailed Design: Structures

The UAV structure is divided into six main parts: The main body (Section 12.2), the propeller (Section 12.3), the ducts (Section 12.4), the propeller arms (Section 12.5) and the landing gear (Sec-

---

[7]https://www.fibreglast.com/product/Kevlar_Plain_Weave_Fabric_2469/Kevlar, Retrieved on 20/05/2021
[7]http://www.matweb.com/search/datasheet_print.aspx?matguid=706f16a3a8be468284571dd36bbdea35
[7]https://www.sciencedirect.com/science/article/pii/S0011227509001271
[8]https://energy.concord.org/energy2d/conservation-of-energy.html, Retrieved on 20/05/2021
[9]https://energy.concord.org/energy2d/, Retrieved on 18/05/2021

tion 12.6). This will be followed by a design overview (Section 12.7). Verification & validation and requirement compliance will be performed in Section 12.8 and 12.9. However, first some general structural design considerations will be elaborated upon in Section 12.1.

12.1. General Structural Design Considerations

This section will elaborate on certain aspects of the structural design that will be applied for all parts and will therefore be discussed here.

Firstly, a safety factor of 1.5 is used on all loads applied to the structure. Therefore the determination of the structural geometry is done using the ultimate loads[1]. An overview of the ultimate forces induced by the propellers can be found in Table 12.1.

Table 12.1: Overview of ultimate loads (therefore including the 1.5 safety factor) induced by the propellers.

Ultimate load	Value	Unit
Thrust generated by one rotor	123.9	[N]
Torque generated by one rotor	5.47	[Nm]

Secondly, as there are multiple solutions to design for the given loads, every design will optimize for weight. This is done because lighter components will eventually result in a smaller UAV as smaller propellers, motors, and batteries are required.

Thirdly, as explained in Section 11.3 the material properties of CFRP (=Carbon Fiber Reinforced Polymer) degrade with temperature. Therefore for calculations, 70 [%] of the original value is used for structural material properties, e.g. Young's modulus and yield strength. The original values are named in Table 11.1, 11.2 and 11.3.

Fourth, as the requirement stated by TL-USER-21-01, the structure should be used for up to 20 years. Therefore, it is important to consider fatigue. However, woven carbon fiber has a fatigue limit of around ten thousand cycles in off-axis testing[43] and the UAV will not reach that range of cycles during its lifetime as is explained in Section 4.2.

Finally, the minimum thickness for the CFRP is set to 1 [mm], based on the minimum thickness required for manufacturing using an autoclave[11]. The reason for using this manufacturing process will be explained in Chapter 18.
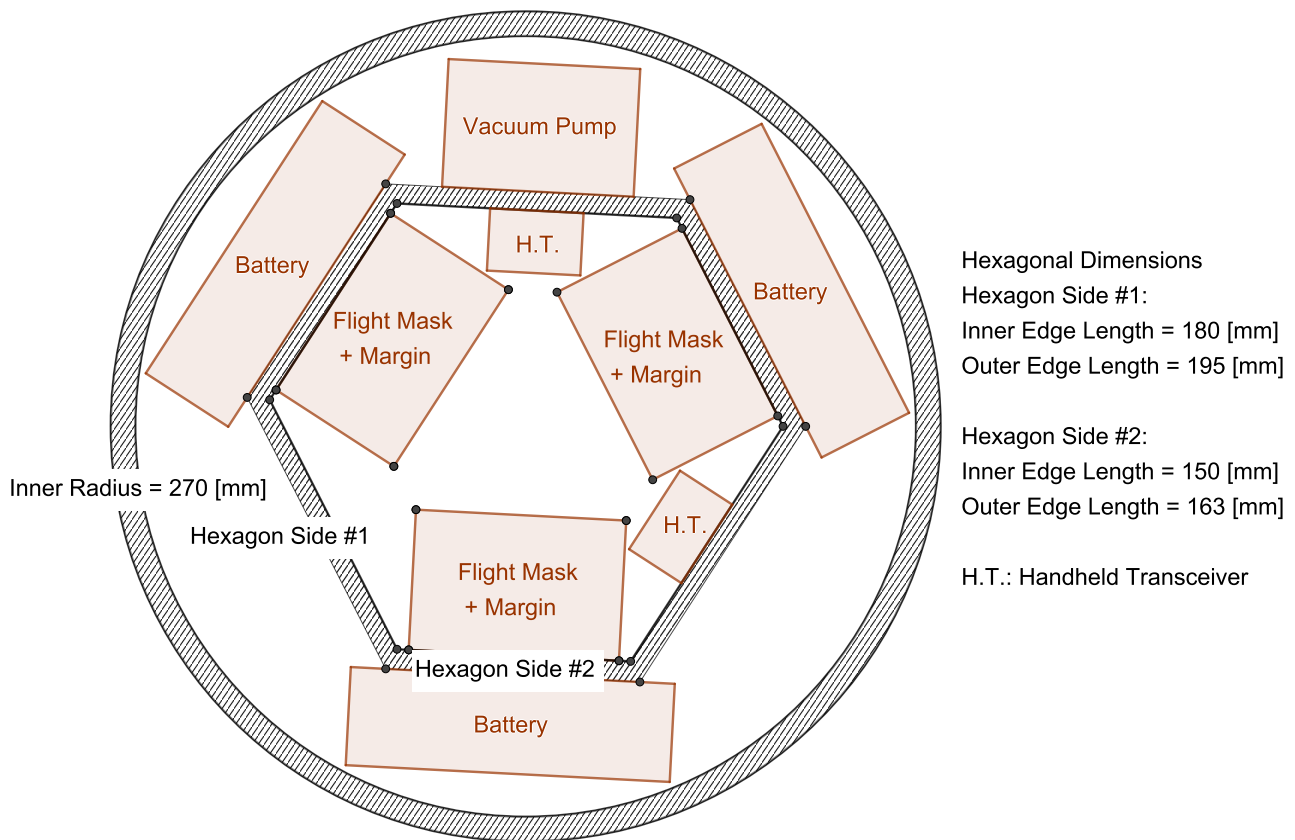
12.2. Main Body

The main body is defined to be the volume in the middle of the UAV, where components like the battery and vacuum pump are stored and where the flight masks will be located. First, the main body shape will be elaborated upon and its size will be given. After that, the access to the payload will be discussed. Then the access to internal components and the fastening of those components will be given. Finally, the thickness of the CFRP in the main body will be determined.

12.2.1. Main Body Shape

The shape of the main body is dictated mainly by the functional requirements composed by the delivery of the payload. The payload must be in reach from behind the window. For this reason, the decision was made to place the payload as centralized as possible. This was done by placing the flight masks in a circular manner around the middle axis, as can be seen in Figure 12.1. The placement allows for access to the payload with a minimal cut-out radius at the window. Then, from the combination of the dimensions of the payload and the space necessary for the glass-cutting mechanism that occupies the empty triangle in Figure 12.1, the radius of the circle going through the outer points of the payload was found to be 165 [mm]. As placing rectangular shapes in a circle is wasting space, the unnecessary space was removed reducing the circular shape to a somewhat hexagonal shape.

---

[1]https://www.skybrary.aero/index.php/Ultimate_Load, Retrieved on 07/05/2021

Hexagonal Dimensions
Hexagon Side #1:
Inner Edge Length = 180 [mm]
Outer Edge Length = 195 [mm]

Hexagon Side #2:
Inner Edge Length = 150 [mm]
Outer Edge Length = 163 [mm]

H.T.: Handheld Transceiver

Figure 12.1: Example of a cross section of the main body.

Now that area containing the payload is fixed in shape, the shape of the main body can be determined. Optimizing the outer body shape for minimized wasted space and minimized drag resulted in a cylindrical outer shell.[44]

12.2.2. Main Body Size

With the shape determined, the sizes of the main body can be inferred from the components that are actually in the body. As an example, using geometric constraints, configuring the flight masks in the configuration as shown in the middle of Figure 12.1 and setting their width and height to be 160 [mm] and 140 [mm] respectively one can determine that the radius of the circle surrounding the boxes is approximately 165 [mm]. Here the height and width of one payload were taken from Table 4.1, then adding a margin of 10 [mm] on three sides to allow for structure securing the payload to the drone and for a hand grabbing the payload.

A similar process can be done with the rest of the main body. The payload restricts the height of CFRP of the main body to be at least 385 [mm], twice the height of the payload, 150 [mm] each, plus 85 [mm] of buffer for insulation. As can be seen in Figure 12.1 the largest component (the vacuum pump) determines the minimum size of the inner diameter of the CFRP of the outer shell to be 540 [mm]. These results are also tabulated in Table 12.4. The internal placement can also be seen in 3D orientation in Figure 12.2. Which verifies that the internal orientation of the components in the main body fits.

(a) Door in a closed position.   **(b)** Door in an open position.
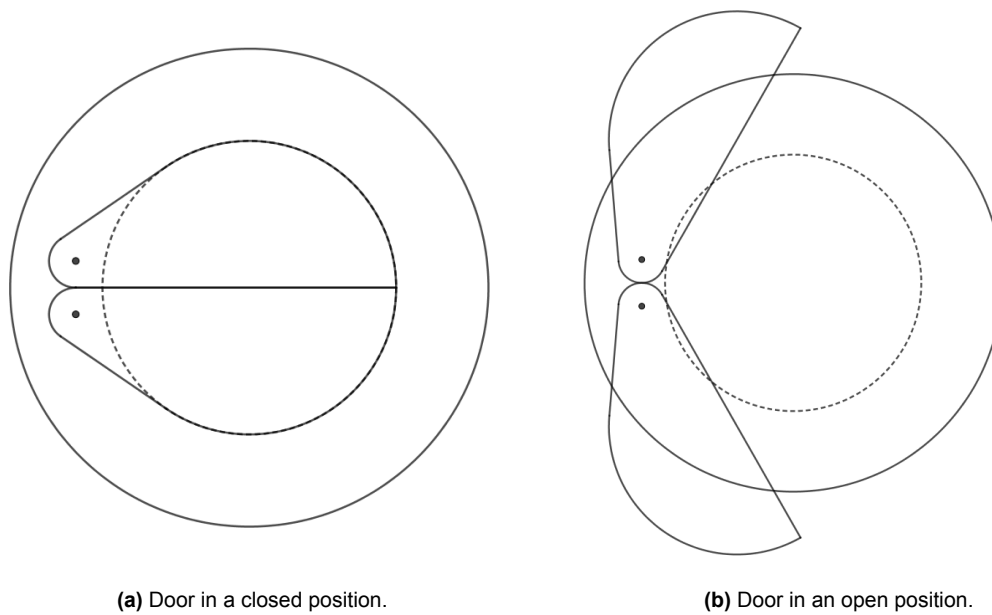
Figure 12.3: A sketch of the door mechanism.
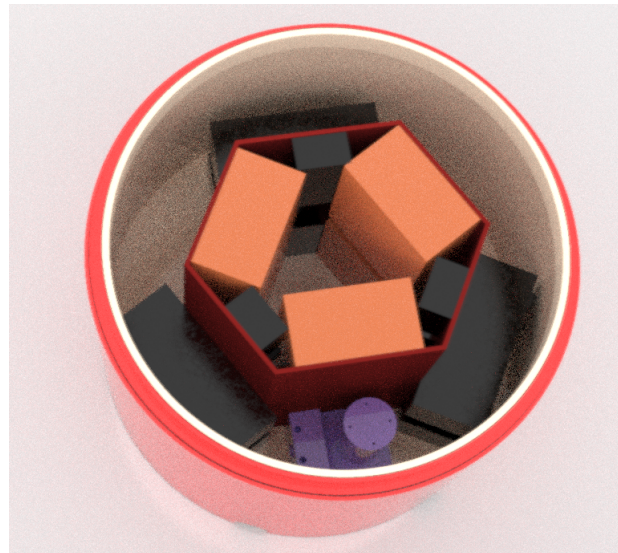
Figure 12.2: CATIA render of the placement of the components inside the main body.

12.2.3. Access to Payload

To prevent loss of payload during flight, and protect the payload before the unloading phase, a door-mechanism was designed. This door mechanism will be made of 1 [mm] aluminum. The door opens sideways to allow the UAV to be within a close distance to the window to be cut while the door is opened. Drawings of the door-mechanisms can be found in Figure 12.3.

The mechanism will be opened by a small electric motor, for which the data can be found in Table 12.2.

Table 12.2: Parameters of motor for rotation of mechanism [2].

Parameter	Final value	Unit
Efficiency	0.64	[-]
Mass motor	≈ 230	[g]
P_{out}	4.5	[W]
P_{in}	7	[W]
Torque	7.2	[Nm]
Voltage	12	[V]
ω	0.63	[rad/s]

12.2.4. Access to Internal Components

As explained in Chapter 4, it is necessary to be able to quickly change the batteries and add new flight masks when another round of flight mask delivery is needed. Therefore the main body should be designed such that it can quickly be opened, without it causing to let heat in. To be able to do this the design as seen in Figure 12.4 has been implemented. The design is comparable to a jar with a rotating lid. First, the pin has to be rotated, whereafter the clip can be opened. This clip has been added to prevent the top from coming loose due to vibrations in flight. Then the top of the main cylinder can be rotated to get it off the rest of the main body. To put the top back on is the same process but in reverse. This is a convenient design because it enables the TBC (=Thermal Barrier Coating) to still cover the entire outside of the main body and therefore protecting the CFRP and keeping the heat away from the inside.
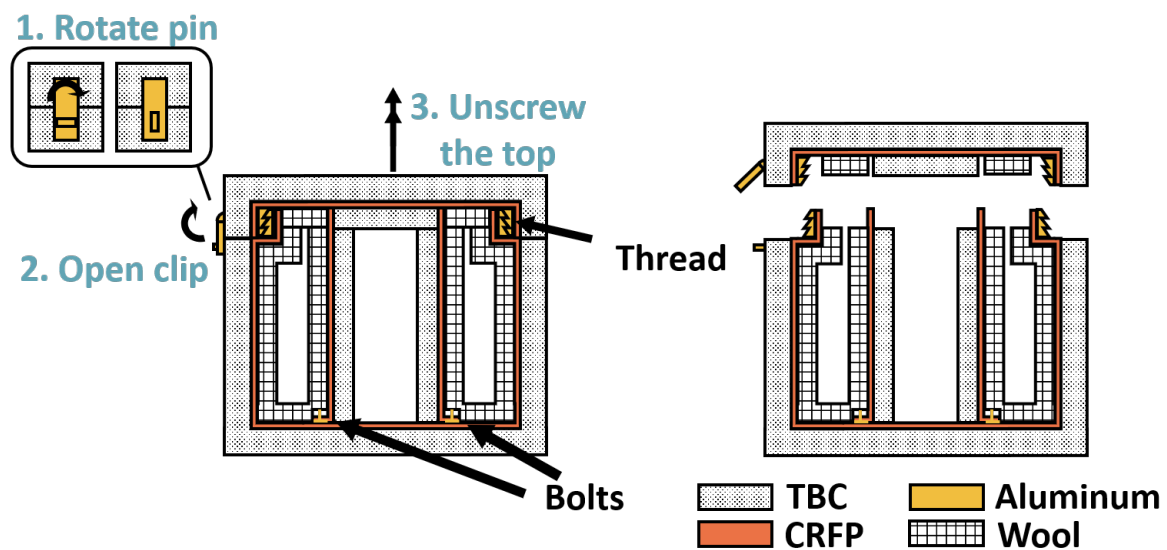
Figure 12.4: Cross sectional side view of the main body without internal components, not to scale. The process showed is for opening the main body. Closing it is the same process, but in reverse.

As the top plate will be able to turn to open the main body and it has TBC 'inside' the internal shell, it is important that the top of the internal shell is round and not a hexagon. In this way, a better-insulated UAV can be guaranteed.

The thread will be made out of aluminum, even as the clip on the outside. It is therefore important to note that when the clip is touched that the person is wearing gloves as not to burn his/her hands, as the aluminum will get hot.

---

[2] https://nl.rs-online.com/web/p/dc-motors/8347631/, Retrieved on 10/06/2021

12.2.5. Adhesion of Internal Components to the Main Body

For stability, it is required that the components inside the main body are properly secured. The adhesion of parts that do not have to be taken out during the mission, i.e. vacuum pump, vacuum distributor, vacuum switches, flight computer, and the 4G receiver, will be adhered to the outer or inner shell using bolts.

For the adhesion of the batteries, the batteries must adhere tightly so they do not get loose during flight, but also that they can be exchanged easily. Therefore the mechanism as shown in Figure 12.5 has been chosen.
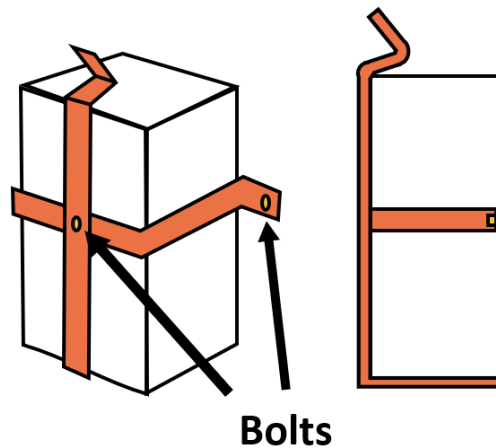
Bolts

Figure 12.5: Graphical representation of fixation of the battery in the main body, not to scale.

This mechanism is adhered to the outer shell using bolts. As can be seen in Figure 12.5, the top is left open with an end with a kink in it. To get the battery out only the end has to be pushed away slightly by hand. To put it back in some force can be applied to push it back in or the end can be pushed away a bit by hand. This will be made out of carbon fiber.

The flight masks and the handheld transceivers will be adhered using hook and loop fasteners. This method is chosen as it requires no knowledge for the persons inside the building to get them out of the main body since it is simply a matter of pulling it off. The specific fastener used is Fire Retardant High-Temperature Thermoplastic Hook & Loop Tape of Textile Technologies. This tape can withstand continuous temperatures of 218 [°C] and temperatures up to 260 [°C] for short periods of time and costs 8.66 [EUR] per meter[3]. As the flight masks and walkie-talkies will be in the inner shell in the main body they are largely shielded from the heat, therefore this temperature performance is deemed sufficient. To extra protect the walkie-talkies against the heat they will be put in a bag made out of Kevlar. This material is also used for the protection ring design and as explained in Section 9.4.7 this material is heat resistant and will therefore protect the walkie-talkie for a short amount of time it is exposed to heat. The flight masks will adhere with two 8 [cm] strips of hook and loop tape and walkie talkies will be fastened with one strip of 8 [cm], both to the inner shell. Therefore, in total 1.12 [m] is required, resulting in a price of 9.70 [EUR]. It is important to note that this is a recurring cost, as every flight mask and walkie-talkie bag has to have a hook and loop tape on it.

The glass cutting mechanism will be adhered to the main body by attaching the nut through which the shaft will rotate to the inner shell. This will be done with three small beams, as the placement of the flight masks is done in such a way that the three beams with the cutting blades on them do not interfere. Therefore, the placement of the new three beams will not cause problems. Only the walkie-talkies are then behind the beam, but when a flight mask is taken out of the main body, also the walkie-talkies should be easy to reach.

---

[3]http://www.textiletechnologies.co.uk/fire-retardant-high-temperature-thermoplastic-hook-loop-tape.html, Retrieved on 03/06/2021

12.2.6. Integration with Sensors and Lights

The sensors selected in Chapter 13 are not by themselves heat resistant. They must thus be insulated in some manner. Ideally, they are placed inside the body, as this is already very well insulated. However, the sensors must also be able to sense the environment outside the main body. For this, some form of glass is necessary. Borosilicate glass can typically resist temperatures of up to 500 [°C] and has a low thermal conductivity of 1.2 [W/mK][4]. Parts of the main body wall can thus be replaced with glass to see through.

Three cameras will be used on the drone. One faces forwards, to obtain vision in the flight direction. The second faces downwards to be able to visually inspect the glass cutting mechanism. The third one is positioned in the aft of the drone, observing the negative flight direction. The cameras facing the same direction as a LiDAR sensor, are put together in a box with the sensor. These directions are illustrated in Figure 13.8. The box has dimensions of 80x78x50 [mm], taking into account a thermal barrier coating of 4.5 [mm] and 7 [mm] mineral wool to insulate the sensors.

A similar approach can be taken to integrate the lights into the main body. Lights are required by law if one wishes to operate an aircraft at night. A challenge with the design here is again the temperature limit of LEDs. Regular LEDs often have operating limits of 60-80 [°C] ambient temperature, which causes issues for the design in question. The limit is caused by the semiconductor in an LED, which often only allows temperatures below 100 [°C]. The limit of the ambient temperature is then caused by the thermal conductivity of parts of the LED design.
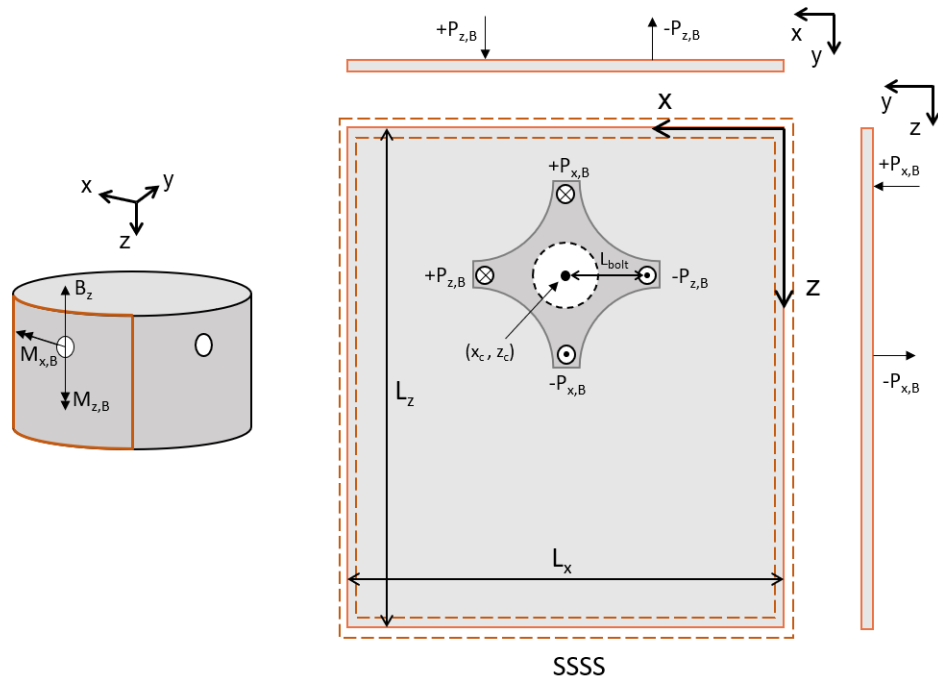
A good option for these scenarios is using a ceramic-base LED.[5] In this design, the heatsink (which is a standard component of LEDs) is combined with the base of the semiconductor. This increases efficiency and thus decreases the semiconductor temperature. Ambient temperatures up to 90-110 [°C] are possible. This is still clearly insufficient, however. The lights must thus also be placed behind a small layer of borosilicate glass.

12.2.7. Main Body Plate Thickness

In this section, the thickness of the main body shell is discussed. The main body is simplified as a cylinder with four propeller arms equally distributed around the outer surface, as displayed on the left of Figure 12.6. The shell of the body can be separated into three parts, including a curved rectangular side plate, a circular top plate, and a circular bottom plate. For simplicity, the top plate is assumed to have the minimum allowable thickness of 1 [mm] since it does not carry loading at any flight condition. On the other hand, the bottom plate is assumed to have the same thickness as the side plate since it supports the internal structure and needs to withstand inertial forces. The most critical loading on the shell is found when propellers are working and shown in Figure 12.11, which drives the sizing of the side and bottom plate. The side plate is first separated into four plates where the propeller arms are located at the middle axis. Furthermore, these plates are simplified as thin flat plates with all edges simply-supported, due to their large radius of curvature. The thickness of such an ideal plate then depends on the required strength, which is constrained by the forces and moments B_z, $M_{x,B}$ and $M_{z,B}$ generated by the rotors. The determination of these forces and moments will be discussed in the next section. The last assumption is that the moments $M_{x,B}$ and $M_{z,B}$ are manipulated as two pairs of couple forces $+P_{x,B}$, $-P_{x,B}$, $+P_{z,B}$, and $-P_{z,B}$, perpendicular to the plate and located at the bolts which connect the propeller arm and the main body. A three-view demonstration of such an assumption can be seen on the right of Figure 12.6.

---

[4] https://www.schott.com/en-gb/products/borofloat/technical-details Retrieved on 23-06-2021

[5] https://www.electronicdesign.com/markets/energy/article/21758498/cool-ceramics-help-simplify-led-heat-dissipation, Retrieved on 22/06/2021

Figure 12.6: A simplified plate model of the main body side shell, which is assumed and separated as four thin rectangular plates with all edges simply-supported (SSSS). Each of the Moments generated by the rotor is decomposed into a pair of couple forces P's perpendicular to the plate, by $M_{x,B} = 2L_{bolt} \cdot P_{x,B}$ and so for $M_{z,B}$. The effect of the shear force B_z is not shown on the right diagram.

L_{bolt} is chosen to be twice the arm diameter so that the cross-shaped washer has a proper radius of curvature at its rounded edges. To avoid tear-out of the top bolt with respect to the top edge, a distance equal to the arm diameter is reserved as well. Thus, The z-coordinate of the propeller arm center z_c is three times the arm diameter in total.

The stresses in x- and z-direction experienced by the plate at an arbitrary point (x, y, z) can be solved by applying the plate theory[45] expressed by Equation 12.1.

$$
\begin{aligned}
\sigma_{xx} &= -\frac{Ey}{1-\nu^2} \cdot \left(\frac{\partial^2 w}{\partial x^2} + \nu \frac{\partial^2 w}{\partial z^2} \right) \\
\sigma_{zz} &= -\frac{Ey}{1-\nu^2} \cdot \left(\nu \frac{\partial^2 w}{\partial x^2} + \frac{\partial^2 w}{\partial z^2} \right)
\end{aligned}
\tag{12.1}
$$

where E and ν represent the Young's modulus and Poisson's ratio respectively, and $w = w(x, z)$ is the elevation of the plate mid-surface above the x-z plane. This evaluation depends on how the loading is distributed on the plate, but normally does not have an exact analytical solution. A typical method to solve the problem is the Navier's solution by expanding it with Fourier series in Equation 12.2,

$$
w(x, z) = \sum_{m=1}^{\infty} \sum_{n=1}^{\infty} A_{mn} \cdot sin\frac{m\pi x}{L_x} sin\frac{n\pi z}{L_z}
\tag{12.2}
$$

which already satisfy the boundary conditions at the edges shown below,

$$
\frac{\partial^2 w}{\partial x^2}(x, 0) = \frac{\partial^2 w}{\partial x^2}(x, L_z) = \frac{\partial^2 w}{\partial z^2}(0, z) = \frac{\partial^2 w}{\partial z^2}(L_x, z) = 0
\tag{12.3}
$$

The Fourier coefficients A_{mn} can be then solved by[45],

$$
A_{mn} = \frac{1}{\pi^4 D} \frac{4}{L_x L_z} \left(\frac{m^2}{L_x^2} + \frac{n^2}{L_z^2} \right)^{-2} \int_0^{L_x} \int_0^{L_z} q(x, z) sin\frac{m\pi x}{L_x} sin\frac{n\pi z}{L_z} dzdx
\tag{12.4}
$$

where $q(x, z)$ is the distributed load per unit area over the plate. For a given pin load P at (x_p, z_p),

$$q(x, z)dzdx = \begin{cases} P & (x, z) = (x_p, z_p) \\ 0 & else \end{cases} \tag{12.5}$$

Thus, its corresponding Fourier coefficients are,

$$A_{mn} = \frac{P}{\pi^4 D} \frac{4}{L_x L_z} \left(\frac{m^2}{L_x^2} + \frac{n^2}{L_z^2} \right)^{-2} sin\frac{m\pi x_p}{L_x} sin\frac{n\pi z_p}{L_z} \tag{12.6}$$

with the plate stiffness D defined as,

$$D = \frac{Et^3}{12(1 - \nu^2)} \tag{12.7}$$

and a complete form of w is,

$$w(x, z) = \frac{4P}{\pi^4 D L_x L_z} \sum_{m=1}^{\infty} \sum_{n=1}^{\infty} \left(\frac{m^2}{L_x^2} + \frac{n^2}{L_z^2} \right)^{-2} sin\frac{m\pi x_p}{L_x} sin\frac{n\pi z_p}{L_z} sin\frac{m\pi x}{L_x} sin\frac{n\pi z}{L_z} \tag{12.8}$$

However, since thickness is the parameter to be determined, it is preferred to express the thickness explicitly as a function with respect to other variables, i.e. $t = t(\sigma_y, L_x, L_z, ...)$. To do so, the the plate theory derives two special terms named moments per unit length M_x and M_z, which are,

$$\begin{aligned}
M_x &= D \left(\frac{\partial^2 w}{\partial x^2} + \nu \frac{\partial^2 w}{\partial z^2} \right) \\
&= \frac{4P}{\pi^2 L_x L_z} \sum_{m=1}^{\infty} \sum_{n=1}^{\infty} \left(\frac{m^2}{L_x^2} + \nu \frac{n^2}{L_z^2} \right)^2 \left(\frac{m^2}{L_x^2} + \frac{n^2}{L_z^2} \right)^{-2} sin\frac{m\pi x_p}{L_x} sin\frac{n\pi z_p}{L_z} sin\frac{m\pi x}{L_x} sin\frac{n\pi z}{L_z} \\
M_z &= D \left(\nu \frac{\partial^2 w}{\partial x^2} + \frac{\partial^2 w}{\partial z^2} \right) \\
&= \frac{4P}{\pi^2 L_x L_z} \sum_{m=1}^{\infty} \sum_{n=1}^{\infty} \left(\nu \frac{m^2}{L_x^2} + \frac{n^2}{L_z^2} \right)^2 \left(\frac{m^2}{L_x^2} + \frac{n^2}{L_z^2} \right)^{-2} sin\frac{m\pi x_p}{L_x} sin\frac{n\pi z_p}{L_z} sin\frac{m\pi x}{L_x} sin\frac{n\pi z}{L_z}
\end{aligned} \tag{12.9}$$

Thus, M_x and M_z are expressed in a form independent of the thickness, and Equation 12.1 can be then rearranged into,

$$\begin{aligned}
\sigma_{xx}(x, z) &= -\frac{6M_x(x, z)}{t^2} = -\frac{6}{t^2} \sum M_{x,i}(x, z) \\
\sigma_{zz}(x, z) &= -\frac{6M_z(x, z)}{t^2} = -\frac{6}{t^2} \sum M_{z,i}(x, z)
\end{aligned} \tag{12.10}$$

Figure 12.6 indicates that there are four pin forces, resulting in four pairs of $M_{x,i}$ and $M_{z,i}$. After analysis of the stresses due to moments $M_{x,B}$ and $M_{z,B}$, the next step is to take the shear force B_z into account. The nominal tensile stress σ_{ts} in z-direction due to B_z is,

$$\sigma_{ts} = \frac{B_z}{A} = \frac{B_z}{L_x \cdot t} \tag{12.11}$$

which contributes to σ_{zz} as well. The thickness with the safety factor considered is then constrained using von Mises yield criterion[46],

$$\sigma_v = \sqrt{\sigma_{xx}^2 + \sigma_{zz}^2 + \frac{1}{2}(\sigma_{xx} - \sigma_{zz})^2} \leqslant \sigma_y \tag{12.12}$$

Now it is able to calculate the unit moments M_x, M_z based on the plate theory as well as the required thickness. All necessary parameters for calculation are summarized in Table 12.3.

Table 12.3: Parameters for plate stress analysis. The yield strength used for sizing is chosen at $160°C$, which is 70 [%] of the original value equal to 549.5 [MPa] at room temperature.

Plate properties	L_x [mm]	L_z [mm]	σ_y [MPa]
	424	394	384.65
Hole parameters	x_c [mm]	z_c [mm]	Diameter [mm]
	212	88	22
Pin forces parameters	x_p [mm]	z_p [mm]	Magnitude [N]
$+P_{x,B}$	212	22	591.2
$-P_{x,B}$	212	154	591.2
$+P_{z,B}$	278	88	105.7
$-P_{z,B}$	146	88	105.7

Calculation shows that the maximum stress always occurs near the bolts where the pin forces are exerted. Among the four bolts, the bolt at the bottom, on which $-P_{x,B}$ is located, is found to have the largest magnitudes of unit moments, with M_x = -243 [Nm/m] and M_z = -256 [Nm/m]. An example diagram showing how the solution varies with the series number m and n is displayed in Figure 12.7. The x in the diagram represents the x-location and coincides with the x-axis in Figure 12.6. It can be seen that as m and n increase, the diagram gradually converges to a Y-shaped curve which has a singular point in the middle. However, since the bolt has a non-zero diameter, the singular point in the middle will never be reached in practice. Thus, a distance of 2 [mm] away from the middle is chosen as the maximum stress point. As can be seen in Figure 12.7, the stress at that point converges to a singular value with increasing m and n.
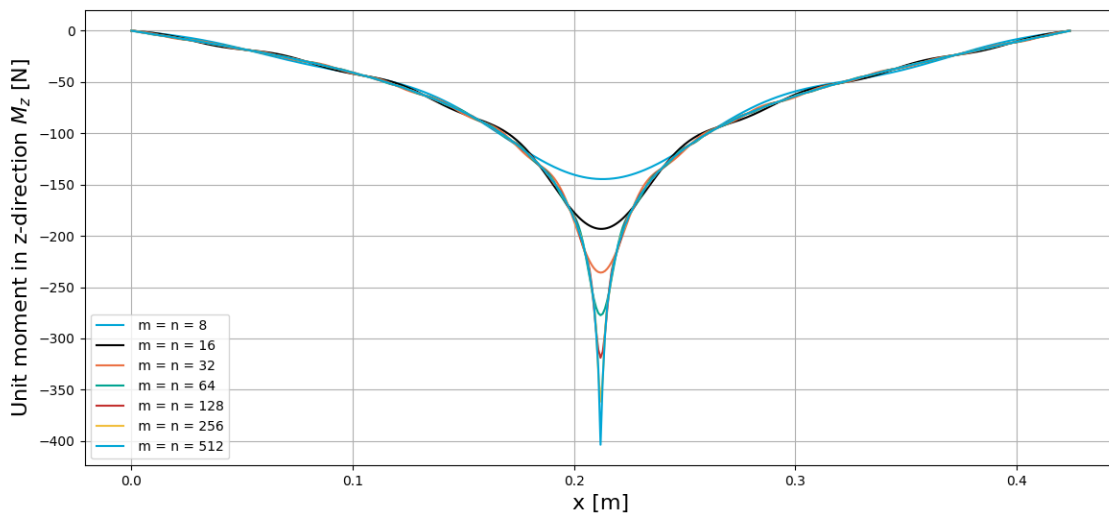
Figure 12.7: This diagram shows the unit moment M_z along the horizontal line where the bottom bolt $-P_{x,B}$ is located. A singularity emerges in the middle where the peak of unit moment continuously increases, while the convergent region also increases in the wake of the refinement.

Thus, by substituting all known parameters into Equation 12.10, Equation 12.11 and Equation 12.12, the required thickness of the side plate is found to be 2.35 [mm], thus eventually a value of 2.4 [mm] is chosen due to production constraint. This leads to a calculated maximum stress of 369 [MPa] in the plate. As mentioned at the beginning of this section, the bottom plate has the same thickness of 2.4 [mm], while the top plate only requires a thickness of 1 [mm].

An overview of the main body sizing is then given in Table 12.4.

Table 12.4: Overview of parameters of the main body.

Parameter	Value	Unit
CFRP inner diameter	540	[mm]
Height CFRP	394	[mm]
Side plate CFRP thickness	2.4	[mm]
Side plate mass incl. TBC and wool	3.025	[kg]
Bottom plate CFRP thickness	2.4	[mm]
Bottom plate mass incl. TBC and wool	1.05	[kg]
Top plate CFRP thickness	1	[mm]
Top plate mass incl. TBC and wool	589	[g]
Total mass incl. TBC and wool	5.38	[kg]
Total CFRP cost	175.68	[GBP]

12.3. Propeller Design

The propeller blade consists of a tapered wing with multiple airfoils along its section. For the structure of the propeller, the material chosen is aluminum. However, a propeller blade completely manufactured out of aluminum would be inefficient and unnecessarily heavy, therefore the choice was made to have an aluminum shell of a certain thickness reinforced by ribs at selected points. For this, the necessary thickness must be calculated: knowing the magnitude and position of the maximum moment that the propeller blade experiences, it is possible to do so using the bending equation, in Equation 12.13:

$$\sigma_z = \frac{(M_x I_{yy} - M_y I_{xy})\, y + (M_y I_{xx} - M_x I_{xy})\, x}{I_{xx} I_{yy} - I_{xy}^2}$$

(12.13)

which can be applied at an arbitrary cross-section of the blade if the x- and y-coordinates are known. Furthermore, Equation 12.13 can be simplified as follows: first, the propeller is assumed symmetric about its horizontal axis. This is possible because, albeit the blade is mounted at a pitch angle, the reference system can be aligned with the X-axis coincident with the airfoil's horizontal axis, and the forces can then be decomposed along this new coordinate system. This simplification also reduces the product moment of inertia, I_{xy}, to 0. Next, as the airfoils used along the blade have a complex shape, for easier computation of the moments of inertia their cross-section is simplified as two slanted bars of thickness t and a semicircle, also of thickness t. The thickness is assumed uniform along the cross-section, for ease of producibility. Along the blade, the cross-sections are not equal, and this will be accounted for. In Figure 12.8 the new coordinate system and the simplified airfoil geometry can be seen.
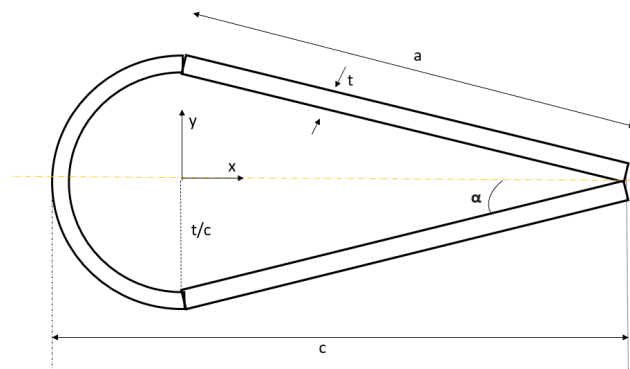

Figure 12.8: Side view of a sample cross section of the airfoil taken for structural analysis.

The thickness is what needs to be determined, in order for it to withstand the prescribed loads. With the simplified cross section in Figure 12.8, as well as the fact that the forces acting along the airfoil's

cross section are the lift and drag at each section of the blade, Equation 12.13 reduces to:

$$\sigma_z = \frac{M_x I_{yy} \cdot y + M_y I_{xx} \cdot x}{I_{xx} I_{yy}}$$ (12.14)

For which the moments of inertia and the moments acting on the structure have to be determined. The propeller blade is clamped at the hub, and moments depend on the magnitude of the lift and the drag forces, which have been calculated in Chapter 10. From these values, the moment and shear diagrams for the structure can be found and analyzed. This allows for the determination of the most critical point, which is a combination of where the highest moment happens and the structure is the smallest (smallest moment of inertia means less bending resistance). The point where this occurs has been determined by comparing the maximum stress as a function of the maximum z,y, and x distances as well as the moment of inertia in Python. Because the design should easily withstand the forces applied, a safety factor of 1.5 has been applied to the moment values. Accounting for all forces, Figure 12.9
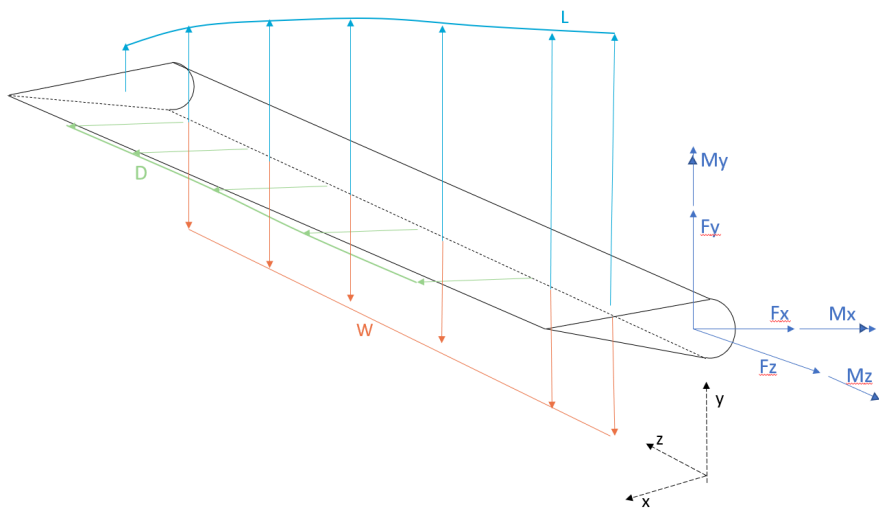
Figure 12.9: The Free Body Diagram of the propeller blade, clamped at the hub radius.

The total moment of inertia, for the circular cross-section and the two slanted bars, can be calculated as:

$$\begin{aligned} I_{circular} &= t \int_0^\pi r cos\theta r d\theta \\ I_{slantedbar} &= \frac{ta^3 sin(\alpha)^2}{12} \end{aligned}$$ (12.15)

To which the Steiner terms need to be summed. After all of the quantities have been calculated, the required thickness is determined to be 1 mm. However, this is not enough on its own for the structure to be inherently stiff, since the deflection at the blade tip is found too large (more than 10[%] of the blade length). To prevent this, reinforcements in the form of ribs have been added. As the structure has been discretized during the application of blade element theory, it has been chosen to have the ribs positions at the following cross-sections: $0.25r_{tip}$, $0.5r_{tip}$, $0.75r_{tip}$ so that the deflection is decreased to be less than 5[%] of the blade length as calculated by the element theory.

With the determination of the ribs position, the total weight of the blade, and then of the complete propeller system can be determined. The use of such low thickness and optimization of ribs position means the weight of the propellers is only 1.8 [kg]. This does not include the weight of the duct. An overview of the weight and cost can be found in Table 12.5.

There is a possibility to further optimize the geometry, which may be insightful for post DSE analysis: this is the use of topology optimization, which allows reducing the weight of the structure based on the applied loads, such that there is no part of the structure that is not carrying a useful load. This can be done through the use of specific programs.

Table 12.5: Propeller weight and cost of all propellers together.

| Parameter	Value	Unit
Weight	1.8	[kg]
Cost aluminum	14.7	[GBP]

12.4. Duct Design

To increase the efficiency of the propellers, as explained in Section 10.2.5, a duct is added around the propellers. The height of the duct is set to half the radius of the largest propeller, to limit the interference of the two propellers. The inner diameter is slightly larger than the largest propeller radius, to allow for some margin. It will be made out of CFRP with a TBC. The duct parameters can be found in Table 12.6.

Table 12.6: Parameters of the duct.

Parameter	Value	Unit
Inner diameter	0.39	[m]
Outer diameter	0.4	[m]
Height	0.17	[m]
Weight	0.4	[kg]
Cost CFRP	17.44	[GBP]

The duct will be attached to the propeller arm as shown in Figure 12.10.
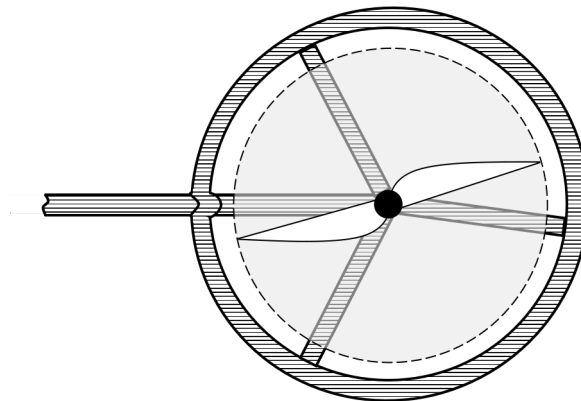
Figure 12.10: Duct design and attachment method to the propeller arm.

12.5. Propeller Arm Design

The propeller arm consists out of two main parts, a horizontal part, and a vertical part as can be seen in Figure 12.11. These different parts will be designed separately, as different loads are applied to them. Additionally, the propeller arm will be analyzed in different load cases: when the UAV is in flight, on the building, or standing on the ground.
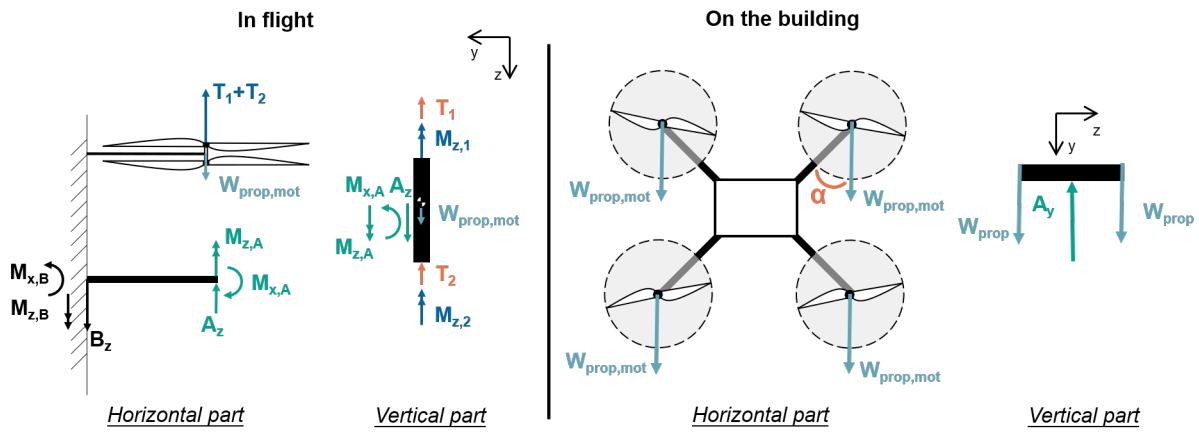
Figure 12.11: Free body diagram of the propeller arm in flight and when the UAV is adhered to the building.

12.5.1. Vertical part of the propeller arm

The length of the vertical part is determined by the propellers, as the lengths should be large enough to prevent excessive interference of the airflow of two propellers. It is set to 0.17 [m], which is half the length of the radius of the largest propeller. The cross-section, on the other hand, is mainly dictated by the size of the motor that needs to fit inside. This motor has a diameter of 87.8 [mm], therefore this (plus the thickness of the insulating wool) will also be the minimum size of the inner diameter of the shaft. The height of the motor is equal to 29 [mm]. As can be seen in Figure 12.11, the forces acting on the vertical part during flight largely cancel out as the thrust and force of both propellers are directed in the same direction. There is however slight compression and tension because of the weight of the components and the fact that the propeller thrust is not the same, however, this is of negligible small magnitude. Additionally, when the UAV has adhered to the building, the vertical part will experience bending stress[10]:

$$\sigma = \frac{(d_{out}/2)A_y L}{4I} \tag{12.16}$$

The stresses due to this should remain lower than the yield stress to prevent permanent deformation. This results in the parameters as shown in Table 12.7 for the vertical part. These parameters result in bending stress of 0.014 [MPa], which is negligibly small.

12.5.2. Horizontal part of the propeller arm

The sizing of the horizontal part in flight is based on bending around the x- and z-axis due to the thrust and torque generated by the propellers. For both the following equation will be used[10]:

$$\sigma_{bending} = \frac{M(d_{out}/2)}{I} \tag{12.17}$$

Where the stresses due to $M_{x,B}$ and $M_{z,B}$ are equal to 277 and 33.0 [MPa] respectively. As it is found that these bending stresses are the highest stresses experienced by the horizontal part they are included in Table 12.7. The stresses due to the bending have to remain lower than the yield stress. In the next load case, When the UAV has adhered to the building, the horizontal part experiences bending, compression and tension due to the weight of the propellers and the motor. For bending Equation 12.17 can be used again, with $W_{prop,mot}cos(\alpha)L$ for the moment. For the compression that the top two arms experience the following equation can be used[10]:

$$P_{crit} = \frac{\pi^2 EI}{(KL)^2} \tag{12.18}$$

Where the applied buckling load ($= W_{prop,mot}cos(\alpha)$) should be lower than the P_{crit} calculated in

Equation 12.24. Finally, the bottom two arms will be in tension, which creates stresses determined by[10]:

$$\sigma_{tension} = \frac{W_{prop,mot}cos(\alpha)}{A} \tag{12.19}$$

It should be noted that the bottom two arms are both in tension (0.16 [MPa]) and bending (15.14 [MPa]), therefore those two stresses should be added together so that the total maximum stress remains lower than the yield stress. In the final load case, when the UAV is standing on the ground, only the weight of the propellers and motors exert a bending force on the horizontal part of the propeller arm. Therefore Equation 12.17 can be used again, where the moment is set equal to $W_{prop,mot}L = 7.1$ [Nm].

12.5.3. Propeller arm parameters
Table 12.7 gives an overview of all propeller arm parameters.

Table 12.7: Overview of parameters of the propeller arm.

|	Parameter	Value	Unit
Vertical part	Length	0.1	[m]
	d_{out} CFRP	144	[mm]
	d_{in} CFRP	142	[mm]
	Stress due to bending at the building	13761	[Pa]
Horizontal part	Length	0.45	[m]
	d_{out} CFRP	22	[mm]
	d_{in} CFRP	20	[mm]
	Stress due to bending around x-axis [MPa]	277	[MPa]
	Stress due to bending around z-axis [MPa]	33.0	[MPa]
Total propeller arm	Mass four propeller arms incl. TBC and mineral wool	769	[g]
	Mass four propeller arms incl. ducts, TBC and mineral wool	2.36	[kg]
	Material cost CFRP (four arms)	20.49	[GBP]

12.6. Landing Gear
The landing gear system has a pair of configurations symmetrically equipped at the left and right sides of the drone. Each side of the landing gear consists of several components, including two main struts and one landing skid to support the drone on the ground, and a gearbox at the root for the rotation mechanism.

In this section, a detailed design will be discussed and provide the sizing of the length and thickness of struts and skids. The philosophy of sizing landing gear is to consider the ultimate stresses at extreme cases, which means that a safety factor of 1.5 will be multiplied with the forces or moments, while a stress concentration factor K_t = 3[10] is considered as well since holes are needed for the assembly of the landing gear.

12.6.1. Length of the strut
As mentioned previously, to ensure the functionality of the adhesion system, the landing gear is required to have a sufficient length so that it can touch the building without damaging the propellers. A demonstration is given in Figure 12.12.
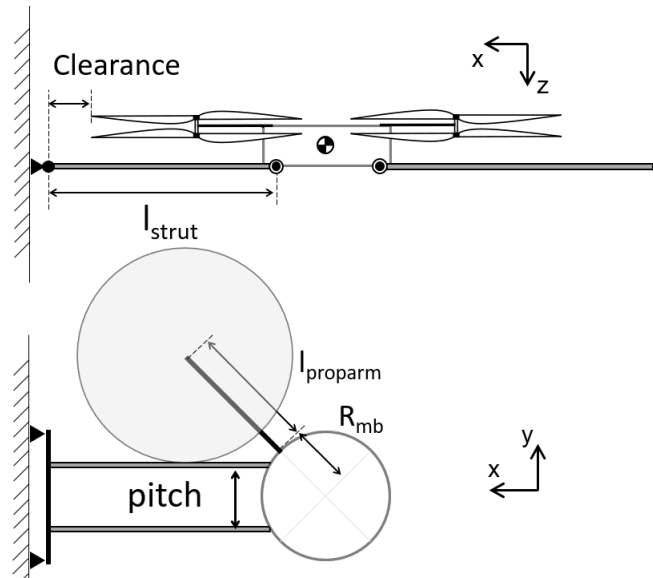
Figure 12.12: A diagram showing the drone approaching and starting to adhere to the building. A clearance is required to protect propellers, and used for landing gear sizing.

Since the suction cups are flexible and may shrink during the mission, the influence of their height on the strut sizing is neglected. Thus, the length of the strut l_{full} is given by,

$$l_{strut} = \frac{\sqrt{2}}{2} \cdot l_{proparm} + r_{prop} + clearance \tag{12.20}$$

With known values of propeller arm length $l_{proparm}$, propeller radius $l_{proparm}$, and a reserved clearance equal to half the propeller radius, the value of l_{full} is found to be 762 [mm].

12.6.2. Strut pitch

Each side of the landing gear is designed to have two struts for fail-safe consideration. The strut pitch, or the distance between two struts on the same side of the landing gear, is determined by considering the position of the propellers, as shown in Figure 12.12 as well. The strut is chosen to be located right under the edge of the propellers. Because of induced drag by the wake of the rotor, it is chosen to design the landing gear such that they are not in the wake. Therefore, the strut pitch is simply given by,

$$(l_{proparm} + R_{mb}) \cdot \sqrt{2} - r_{prop} \tag{12.21}$$

which gives a value of 231 [mm].

12.6.3. Landing configuration

The landing gear is designed to be rotatable so that it can rotate to an angle to allow for sufficient clearance between the main body and the ground at landing conditions, which can be seen in Figure 12.13.
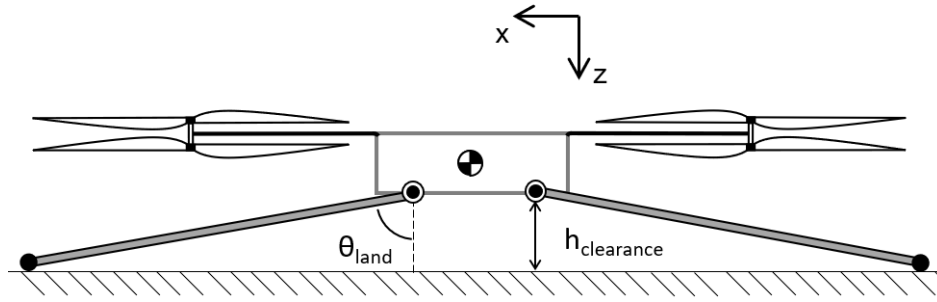
Figure 12.13: The landing gear of the drone rotates to a specific angle so that the bottom of the main body is sufficiently away from the ground.

The clearance $h_{clearance}$ is chosen to be half of the main body height, thus the standby angle θ_{land} between the landing gear and the vertical direction at landing is,

$$\theta_{land} = cos^{-1}\left(\frac{h_{clearance}}{l_{strut}}\right) \tag{12.22}$$

which leads to a value of θ_{land} equal to 72.7 [deg].

12.6.4. Cross section of the strut

After the strut length is determined, it is possible to design for the cross-section based on stress analysis. It is decided to use a hollow tube for the cross-section, with its outer diameter d_{strut} and thickness t_{strut} chosen as variables for calculation. Thus, the inner diameter simply equals d_{strut} - $2 \cdot t_{strut}$. Constraints are then given in the following list and mathematically translated into several equations with respect to these two variables.

- **Constraint 1: The strut shall be fail-safe for column buckling.** The critical case is standing on the ground. The ultimate compression is assumed equally shared by both sides of the landing gear given by,

$$P_{ult} = \frac{MTOW}{2} \cdot cos(\theta_{land}) \cdot SF \tag{12.23}$$

where the safety factor SF is selected as 1.5. Since it is a fail-safe design, the loading is assumed to be completely carried by one of the two main struts at each side of the landing gear. The critical buckling load[10] is calculated by,

$$P_{crit} = \frac{\pi^2 EI}{nL^2} \tag{12.24}$$

where EI represents the bending stiffness, n equals 2 due to the configuration of one fixed end and one free end, and L is the beam length which equals l_{main} in this case. To make sure the ultimate load is less than the critical load, Equation 12.23 and Equation 12.24 can be related as,

$$\frac{MTOW}{2} \cdot cos(\theta_{land}) \cdot SF \leqslant \frac{\pi^2 EI}{4l_{main}^2} \tag{12.25}$$

and further rewritten as,

$$I = \frac{\pi}{64}[d_{strut}^4 - (d_{strut} - 2t_{strut})^4] \geqslant \frac{MTOW \cdot SF \cdot cos(\theta_{land}) \cdot 4l_{main}^2}{2E} \tag{12.26}$$

by moving the two variables towards the opposite side of the constants. It is then able to plot the equation and the corresponding region on the optimisation map.

- **Constraint 2: The strut shall be fail-safe for bending.** Bending stress is found to be maximum when the drone is supported at two ends of the landing gear which is fully extended, as shown in Figure 12.14.
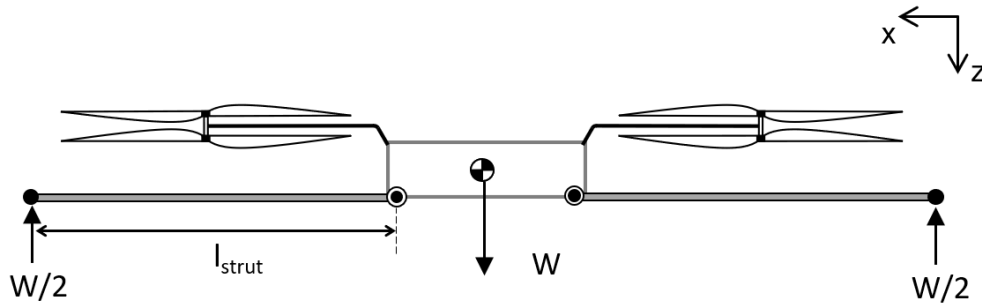
Figure 12.14: Free body diagram when the drone is supported at the ends of the landing gear.

The main body is assumed to be a rigid body, and the maximum bending stress occurs at the joint connecting the main strut and the main body. The bending moment at this point, considering fail-safe design and safety factor, is given by:

$$M_{bend} = SF \cdot \frac{MTOW}{2} \cdot l_{strut} \qquad (12.27)$$

while the maximum tensile stress due to bending[10] is given by,

$$\sigma_{bend} = \frac{My}{I} = SF \cdot M_{bend} \cdot \frac{d_{strut}}{2 \cdot [d_{strut}^4 - (d_{strut} - 2t_{strut})^4]} \qquad (12.28)$$

Considering that the bending stress σ_{bend} should not exceed the yielding stress σ_y, Equation 12.28 can be rewritten into,

$$\frac{d_{strut}}{d_{strut}^4 - (d_{strut} - 2t_{strut})^4} \leqslant \frac{12 \cdot \sigma_y}{SF \cdot MTOW \cdot l_{strut}} \qquad (12.29)$$

which is an inequality equation with respect to the diameter and the thickness as well.

- **Constraint 3: The strut shall be fail-safe for tension.** The maximum tensile stress happens when the drone is hanging on the building using one side of the suction cups. The relation is simply,

$$\frac{MTOW \cdot SF}{A_{strut}} \leqslant \sigma_y \qquad (12.30)$$

where the cross section area A_{strut} can be manipulated as,

$$A_{strut} = \frac{\pi}{4} \cdot [d_{strut}^2 - (d_{strut} - 2t_{strut})^2] \geqslant \frac{SF \cdot MTOW}{\sigma_y} \qquad (12.31)$$

which helps generate a parabola on the map.

- **Constraint 4: The strut shall provide sufficient internal space for the vacuum tube.** The vacuum tube has a diameter d_{vt} equal to 6.4 [mm]. To allow for space to contain to fix the tube, the inner diameter should be at least twice the tube diameter. Thus,

$$d_{strut} - 2t_{strut} \geqslant 2 \cdot d_{vt} \qquad (12.32)$$

which gives a straight line.

- **Constraint 5: The thickness of the strut shall be at least 1 [mm].** This is a production constraint that depends on manufacturing technologies.
- **Constraint 6: The diameter shall be a multiple of 1 [mm], and the thickness shall be a multiple of 0.1 [mm].** This is also a production constraint. These values are found on a

---

[5]https://nl.rs-online.com/web/p/process-tubing/6678457/?cm_mmc=NL-PLA-DS3A-_-google-_-CSS_NL_NL_
Plumbing_%26_Pipeline_Whoop-_-(NL:Whoop!)+Process+Tubing-_-6678457&matchtype=&pla-475725713453&gclid=
CjOKCQjwlMaGBhD3ARIsAPvWd6iMnjAWK_Eygc1pGPl1LoryFs9cApBSSOOwR_Of6M8bVJgOGwr1t7gaAu2OEALw_wcB&gclsrc=aw.
ds, Retrieved on 22/06/2021

manufacturer website[6].

The optimization map containing all the constraint inequality equations is displayed on Figure 12.15, with material properties obtained from Table 11.1. Eventually, an outer diameter of 24 [mm] and a thickness of 1.3 [mm] are chosen for the strut cross-section, according to Constraint 6. The ultimate stress under a safety factor of 1.5 and the fail-safe condition is then calculated to be 375 [MPa].
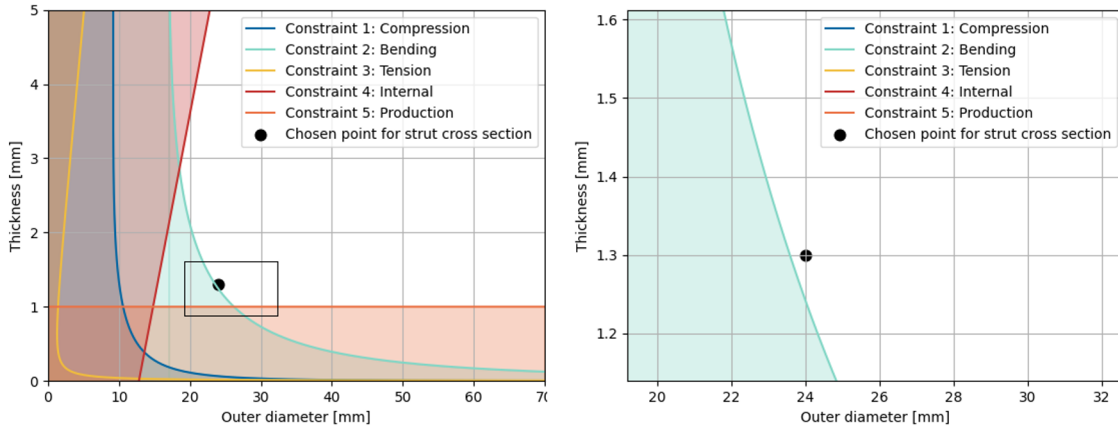
Figure 12.15: Optimisation map of strut cross section design. The diagram on the right is a zoom-in view of the neighborhood of the chosen point, which is marked by the black frame on the left diagram.

12.6.5. Skid length

The length of the skid is found by applying the overturn rule again. As shown in Figure 12.16, the upper limit of the angle β is 55 degrees[47], which is also the optimal value to minimize the length of the skid l_{skid}. With clearance height obtained previously and a known main body height h_{mb}, l_{skid} is simply given by Equation 12.33.
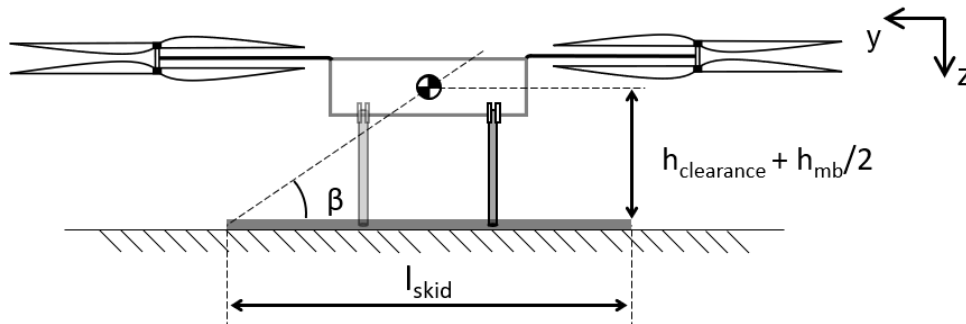
Figure 12.16: A demonstration of the drone configuration from the left. The length of the skid is determined by the angle β and the height of the c.g of the drone.

$$tan^{-1}\left(\frac{h_{clearance} + h_{mb}/2}{l_{skid}/2}\right) = 55 \quad [deg] \tag{12.33}$$

This gives a skid length equal to 602 [mm].

12.6.6. Skid cross section

The cross-sectional property of the skid is determined by bending stress and yield stress. The critical case is found one side of the landing gear adheres to the building the ground, thus the weight of the drone is completely carried by this side of the landing gear. In addition, the skid is assumed to be

---

[6] http://www.carbontubes.eu/, Retrieved on 09/06/2021

clamped at its two ends where suction cups are equipped since the suctions cups are designed not to rotate in the x-direction. A free-body diagram is shown in Figure 12.17.
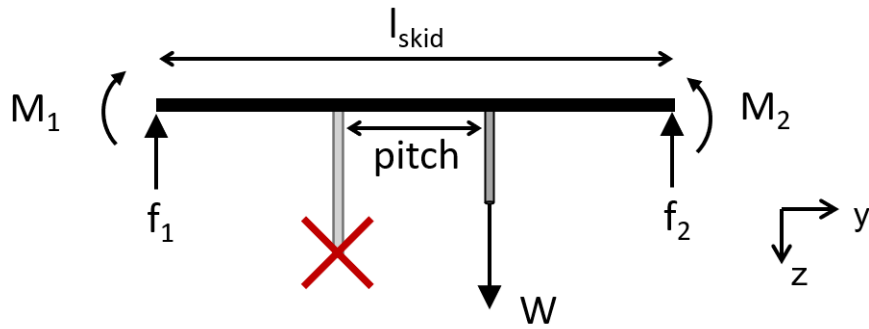
Figure 12.17: The skid can be simplified as a beam clamped at two ends where two reaction forces f_1 and f_2 are located. One of the struts is assumed absent when designing the required strength of the skid, due to the consideration of fail-safe.

The diagrams of internal shear and moment, as well as the equations of the moments[10], are displayed in Figure 12.18.

$$M_1 = -Wa\frac{b^2}{L^2}$$

$$M_2 = -Wb\frac{a^2}{L^2}$$

$$M_W = 2W\frac{a^2b^2}{L^3}$$
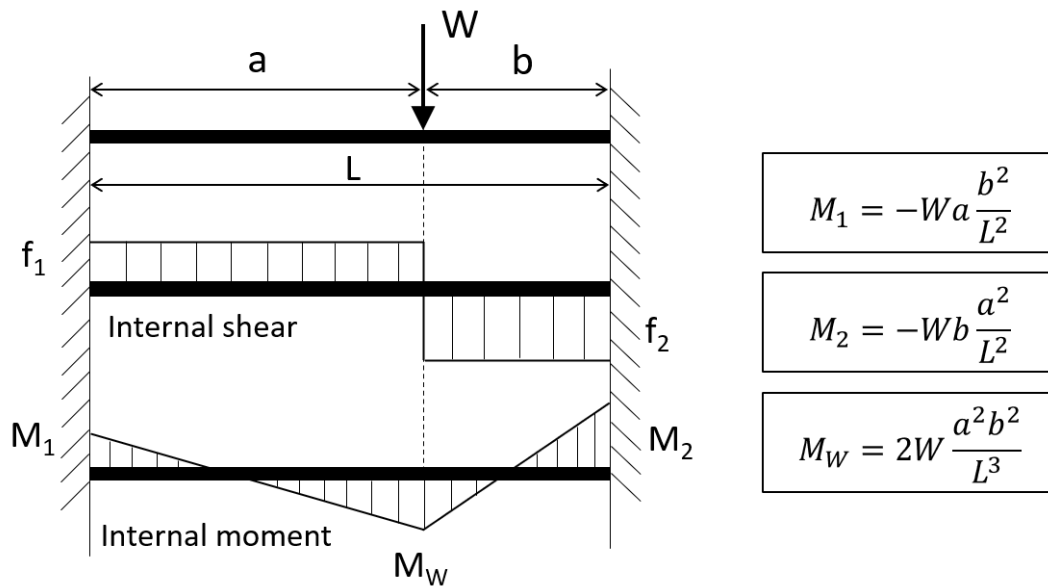
Figure 12.18: The simplified internal loading demonstration of the bottom skid when the weight is applied at an arbitrary point along the beam. Both the ends experience reaction moments since they are clamped. Here a and b are distances of W to the ends. Mathematically, M_2 has the largest magnitude with $b < L/2$.

Thus, according to Figure 12.18, the maximum moment in the beam is found at the right end where f_2 is exerted on and equal to,

$$M_{bend} = W \cdot \frac{l_{skid}^2 - pitch^2}{l_{skid}^2} \cdot \frac{l_{skid} + pitch}{l_{skid}} \tag{12.34}$$

Thus, by inputting MTOW as the weight, the maximum bending moment in this case is,

$$M_{bend} = MTOW \cdot SF \cdot \frac{l_{skid}^2 - pitch^2}{l_{skid}^2} \cdot \frac{l_{skid} + pitch}{l_{skid}} \tag{12.35}$$

while the ultimate bending stress constrained by,

$$\sigma_{bend} = \frac{M_{bend} \cdot y}{I} \leqslant \sigma_y \tag{12.36}$$

which can be rearranged into the following inequality equation with respect to the skid outer diameter d_{skid} and thickness t_{skid}.

$$\frac{d_{skid}}{d_{skid}^4 - (d_{skid} - 2t_{skid})^4} \leqslant \frac{\pi \sigma_y}{32 M_{bend}} \qquad (12.37)$$

Similar to Figure 12.15, an optimization map of skid cross section design can be generated as shown in Figure 12.19, with the internal and production requirements considered again. It can be seen that in this case stress is no longer the driven constraint. Thus eventually, an outer diameter of 16 [mm] and thickness of 1 [mm] are chosen for the skid. The ultimate stress in this case is then 259 [MPa].
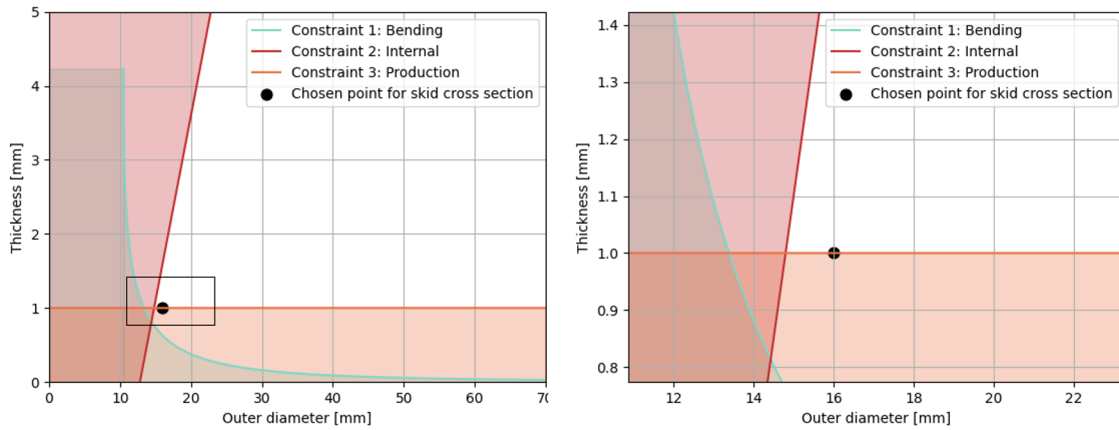
Figure 12.19: Optimization map of skid cross section design. The diagram on the right is a zoom-in view of the neighborhood of the chosen point, which is marked by the black frame on the left diagram.

A summary of the landing gear sizing is then given in Table 12.8.

Table 12.8: Overview of landing gear parameters, excluding the integration part with the adhesion system or main body.

Side strut		
Parameter	**Value**	**Unit**
Length	762	[mm]
Pitch	231	[mm]
Standby angle	72.7	[deg]
Outer diameter	24	[mm]
Thickness	1.3	[mm]
Unit mass	57.1	[g]
Number	4	[-]

Bottom skid		
Parameter	**Value**	**Unit**
Length	602	[mm]
Outer diameter	16	[mm]
Thickness	1	[mm]
Unit mass	23.1	[g]
Number	2	[-]

General		
Total mass	274.9	[g]
Total cost	11.98	[GBP]

12.7. Structural design overview

Table 12.9 gives an overview of the structural design of the UAV.

Table 12.9: Overview of chosen materials for the structural components, their weights, whether they need power and how much the part is going to cost.

Component	Material	Weight [kg]	Required power [W]	Cost CFRP [GBP]
Main body	CFRP and TBC	5.38	-	175.68
Propellers	Aluminum	1.8	-	14.7
Propeller arms and ducts	CFRP and TBC	2.36	-	111.13
Feet	CFRP and TBC	0.275	-	11.98
Feet rotation mechanism	Aluminum	0.63	20	80

12.8. Verification and Validation

The verification of the structural design is performed by applying von Mises stress analysis in CATIA. The main body plate, propeller arm, and landing gear will be analyzed respectively based on their simplified models which have been used for sizing.

12.8.1. Main body plate

According to Table 12.3, a simply supported plate with dimensions of $424 \times 394 \times 2.4 \ [mm^3]$ and a yield strength of 384.65 [MPa] is generated in CATIA. Four pin forces as ultimate loads are then applied to their corresponding locations, and the result of von Mises stress analysis is shown in Figure 12.20.
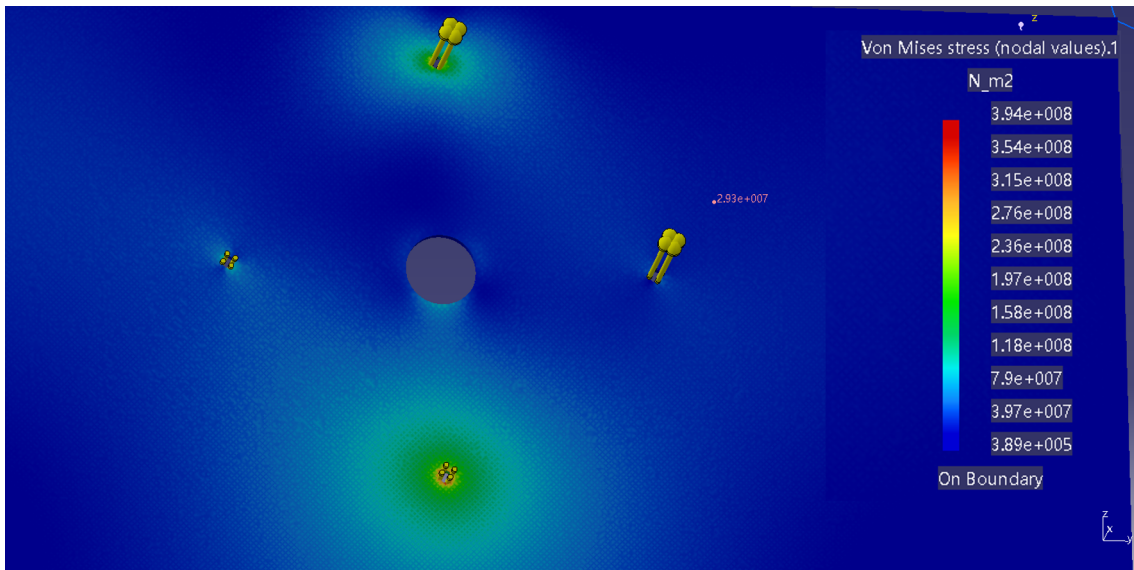
Figure 12.20: The von Mises stress analysis of the main body plate. Around the propeller arm hole in the middle, four holes for bolts are equally spaced and carry the pin forces. Analysis shows that the neighbor of the hole at the bottom experiences the highest von Mises stress, which is consistent with the results of Navier's solution.

As can be seen from the analysis, the stress distribution shows four local extrema occur at the exerting points of pin forces. Thus, the results by Navier's analytical solution and by von Mises computational simulation at these four points are compared and given in Table 12.10.

Table 12.10: A comparison between the plate stress solved by Navier's solution and von Mises simulation in CATIA.

	Force [N]	Navier's solution [MPa]	Von Mises simulation [MPa]	Error
$-P_{x,B}$	591.2	369	394	6.80 [%]
$+P_{x,B}$	-591.2	228	262	15.1 [%]
$+P_{z,B}$	105.7	99.4	127	27.5 [%]
$-P_{z,B}$	-105.7	17.4	72.1	314 [%]

It can be seen that the von Mises simulation gives a similar result of maximum stress to Navier's solution, with an error of 6.80 [%]. Besides, among the four forces, both the solution and the simulation show the same descending order in terms of the stress magnitude, i.e. $-P_{x,B}$ > $+P_{x,B}$ > $+P_{z,B}$ > $-P_{z,B}$. However, the error increases as well, especially for $-P_{z,B}$. The reason for such a large error is that in Navier's solution, the mutual impact of the pin force on its neighbor region is more significant than the CATIA simulation, which can be seen in Figure 12.7. Since the magnitude of $+P_{z,B}$ and $-P_{z,B}$ is much lower than the other two forces, the calculation of their local stresses becomes less accurate. Apart from this, it is still acceptable to conclude that Navier's solution can be used to calculate the maximum stress in the plate.

12.8.2. Propeller arm

The propeller arm was separated into a vertical part and a horizontal part when designing their cross-sectional properties. As explained previously, the cross-section of the vertical part, which carries the propeller, is mainly constrained by the required space for the rotor, thus over-designed from the structural point of view. On the contrary, the design of the horizontal part depends on strength requirement since it transfers the thrust force to the main body, thus it is more of interest in the structural analysis. To perform the stress simulation, a model of one of the propeller arms with integrated vertical and horizontal parts is generated in CATIA, treated as a cantilevered beam. Forces and moments are applied as well based on Figure 12.11. A demonstration of the simulation is displayed in Figure 12.21.
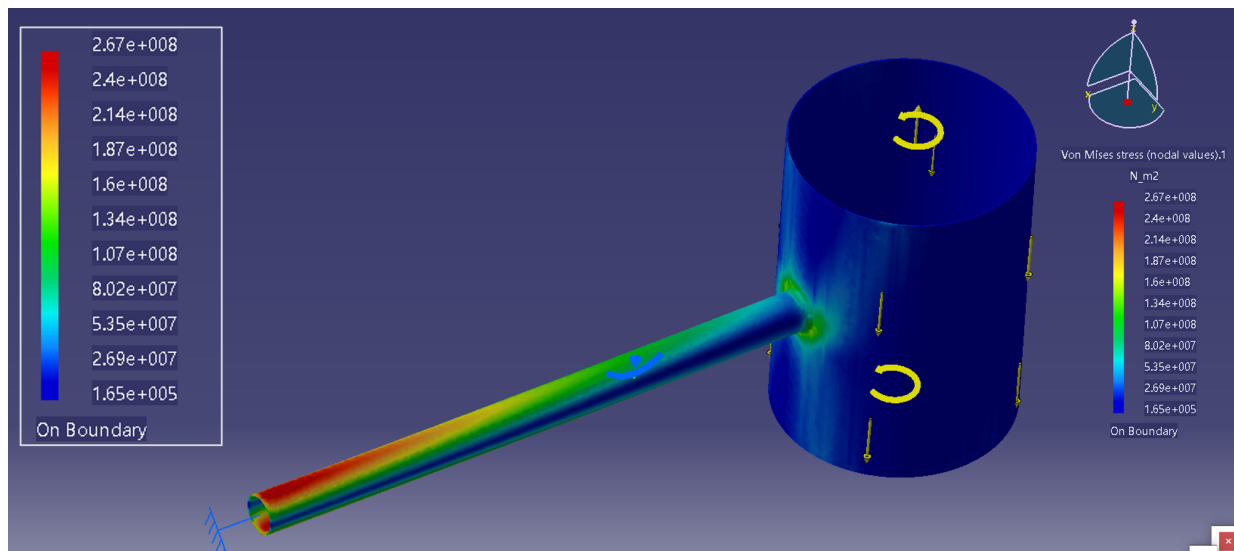

Figure 12.21: The von Mises stress analysis of the propeller arm, including both the vertical and horizontal parts. The maximum bending stress is found at the left side of the horizontal part. Due to a large difference between the diameters of these two parts, a significant stress concentration emerges at the joint.

This diagram indicates that the maximum stress, which is equal to 267 [MPa], occurs at the left end as expected, and the stress decreases along the propeller arm. As given in Table 12.7, the stresses in x- and z-directions are calculated to be -224.8 [MPa] and 28.07 [MPa]. By substituting these two values into Equation 12.12, the analytical von Mises stress at this point is 288.6 [MPa], which gives an error of 7.48 [%] compared with the analytical value. Although a stress concentration emerges at the integrated position, its value does not exceed the yield strength. Thus, it is safe to conclude that the structural strength of the propeller arm is verified.

12.8.3. Landing gear

The stress analysis of the landing gear is performed for the side strut and the bottom skid separately. The strut is simplified as a beam with a clamped end and a free end. The ultimate load, which equals half the drone weight times the safety factor, is perpendicularly applied to the free end. The simulation shows a result in Figure 12.22.
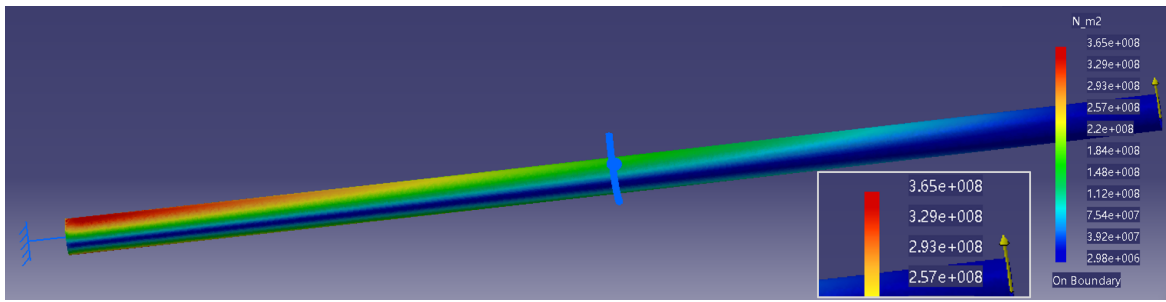
Figure 12.22: The strut is simplified as a beam clamped at one end (close to the main body) and exerted on by a force at the other free end (integrated with the suction cup). Due to the fail safe design, only one of the two struts carries the load.

The bottom skid has a relatively more complicated structure. As displayed in Figure 12.23, the skid is assumed as a beam clamped at both ends. There are two extrusions near its middle, which are used as the integration with, and transfer the loading from the side strut.
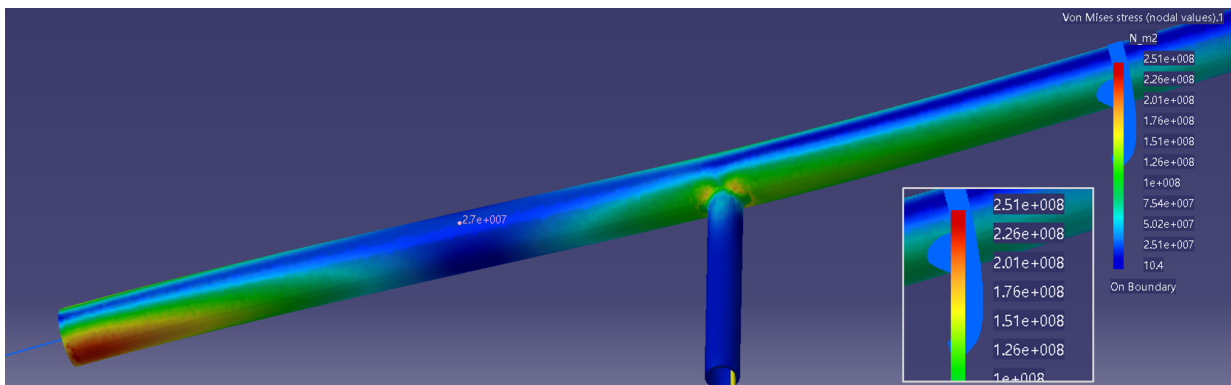
Figure 12.23: The skid is simplified as a beam with both ends clamped. Due to the fail-safe design, the stress in the skid is simulated assumed one of the side struts fails, thus only one of the extrusions carries the load. A stress concentration can be seen at the extrusion, but it is lower than the maximum stress at its left end.

The comparison between the calculated stresses and simulated stresses is then summarized in Table 12.11. The calculated results are already discussed previously in the section of landing gear sizing, and simulated results are directly obtained from the figures above. It can be observed that both the relative errors of the strut and the skid are small enough to verify the sizing.

Table 12.11: Comparison between calculation and simulation of maximum stresses occurring in the landing gear.

	Calculated stress [MPa]	Simulated stress [MPa]	Relative error
Side strut	375	365	2.67 [%]
Bottom skid	259	251	3.09 [%]

Up to now, the structural design of the main body, propeller arm, and landing gear are all verified. It is suggested to validate the design by testing or simulating the drone as an entirety in a later stage.

12.9. Sub-system Compliance Matrix
Table 12.12 will give the compliance matrix for the structural design of the UAV.

Table 12.12: Compliance matrix structural requirements

Requirement	Verification method	Compliance
TECH-PAY-02	The flight masks are designed to withstand 300 [°C], therefore they do not need extra heat protection. Additionally, the walkie-talkies are protected for a short period against the heat through a Kevlar bag around them as explained in Section 12.2.5.	Yes
TECH-STRUC-01	The main structural component, CFRP, virtually has no degradation over its normal life time[7]. However, the heat exposure to heat might degrade the CFRP, therefore post-DSE complex thermal structural simulations have to be performed to predict the behavior of the CFRP over time.	TBD
TECH-STRUC-02	The structural design is designed to be modular hence making it easier to inspect the principal structural elements. The influence and inspecting of the TBC are yet unknown as it is applied using a relatively new method and more research has to be done into this post-DSE.	TBD
TECH-AR-01	The bolts an glues used to assemble the UAV are chosen to withstand 300 [°C] as will be further explained in Section 18.3	Yes
TECH-AR-02	As explained in Section 12.1 a safety factor of 1.5 is used on the forces and moments applied to the structure. Additionally, Section 12.8 verifies the determination of structural parameters.	Yes
TECH-SPAIR-01	As explained in Chapter 4, six flight masks and two hand-held receivers will be taken on board which will be adequate for the mission. Their total weight is about 3.2 [kg] (see Table 4.1). In discussion with the client this requirement has been dropped.	Dropped
TECH-SPAIR-02/TECH-PAY-04	The flight masks and walkie-talkies are attached using a hook and loop fastener, therefore no loss of functionality of the UAV is guaranteed as it does not interfere with the structural integrity (Section 12.2.5).	Yes
TECH-SPAIR-03	Section 12.2.2 shows that the main body is sized to fit the six flight masks.	Yes
TECH-SPAIR-04	As explained in Section 12.2.3 the botttom of the main body will have a door that can automatically open so that the payload can be reached.	Yes
TECH-SPRIR-01	As explained in Section 12.2.4 the top of the main body can be screwed off, so that internal component as the power source can be reached.	Yes
TECH-SPRIR-02	As explained in Section 12.2.4 the top of the main body can be screwed off, so that internal component as the power source can be reached.	Yes
TECH-SCIR-01	As explained in Section 12.2.4 the top of the main body can be screwed off, so that internal component as the onboard computer can be reached.	Yes

---

[7]https://www.technewsworld.com/story/76172.html, Retrieved on 11/06/2021

13 Analysis Stability & Control

One of the major challenges of drone design is the stability and control of the drone. Only with recent developments in electric motors have multicopter designs even become feasible, and drone stability is still a topic of extensive research.

Nonetheless, this chapter aims to give a short introduction to drone stability and control. Two different analysis methods will be presented, in Section 13.2 and Section 13.3. Afterward, a short overview of the collision avoidance system selected for this drone will be given in Section 13.5. The inputs obtained from this discussion will then be used in the final section, which will discuss the actual control of the aircraft in Section 13.4.

13.1. Center of Gravity and Moment of Inertia

To properly analyze the stability of a multicopter, the center of gravity ranges and the moment of inertia around these centers of gravity must be determined. The calculations to obtain these parameters require a defined reference frame. This reference frame is shown in Figure 13.1. The origin of the XY-plane is chosen at the geometric center of the UAV. For the inertial calculations, it is assumed that the center of gravity lies on the z-axis at the geometric center.
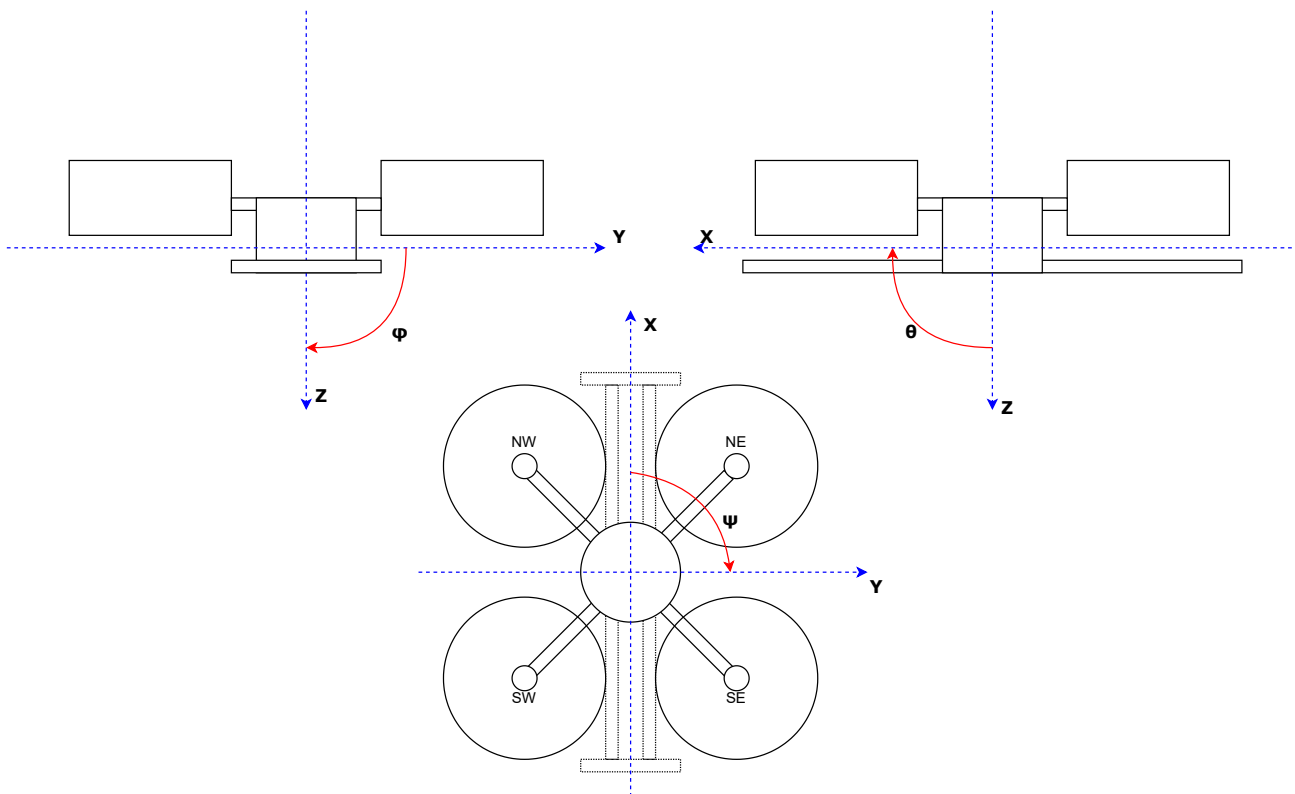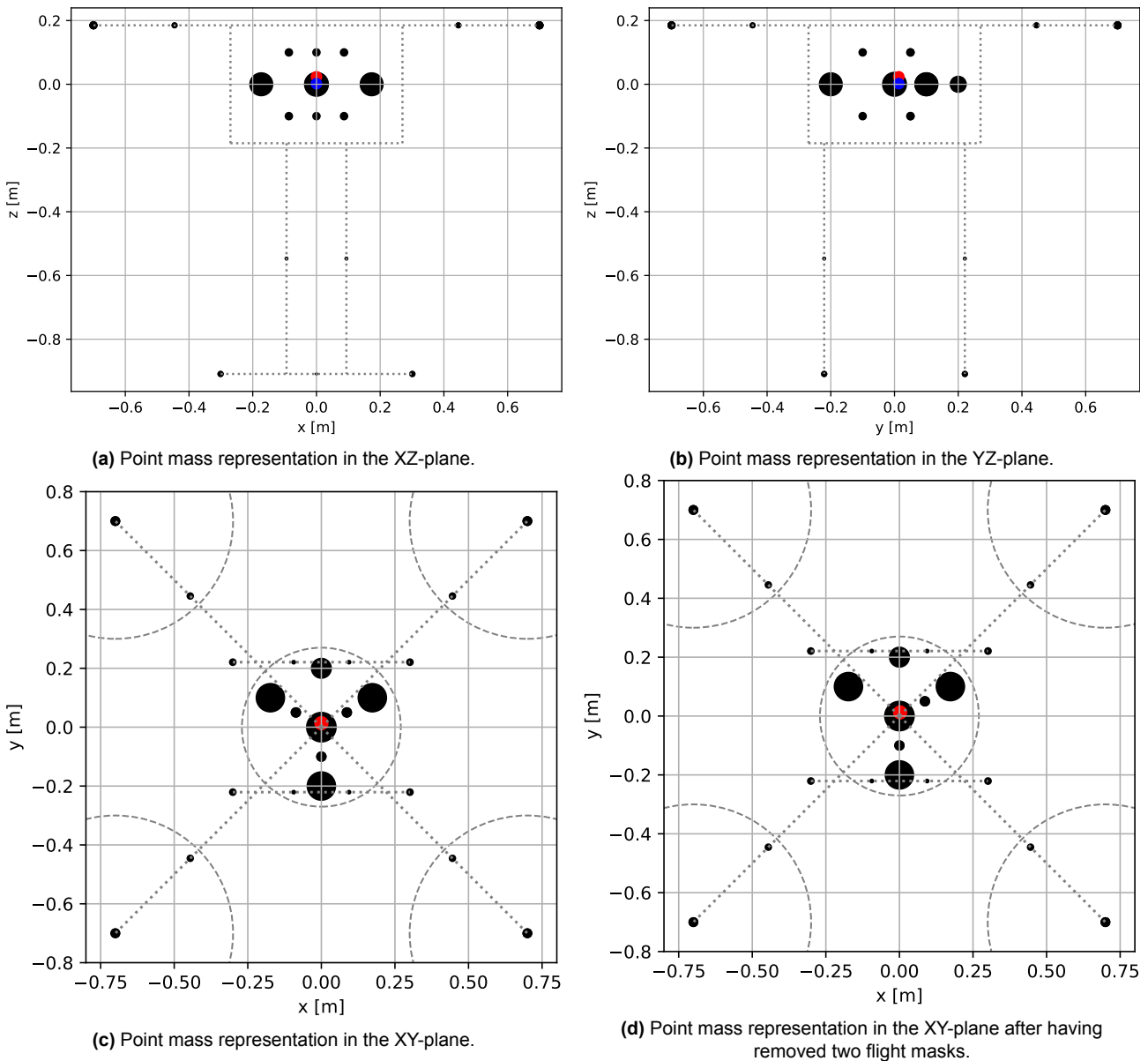

Figure 13.1: The defined UAV body reference frame, with the positive directions and rotations indicated.

13.1.1. Center of Gravity

The center of gravity is significant for the stability analysis. A center of gravity that is far off-center from the geometric centroid of the quadcopter causes significant inefficiencies: A moment is generated on the body, which must be compensated for by adjusting the RPM of various propellers. This is less efficient and thus undesirable.

To find the location of the center of gravity, the UAV is decomposed in point masses, placed at the geometric centers of each component. The distribution of the point masses in each plane, as well as the center of gravity, is shown in Figure 13.2. This clearly shows that the center of gravity is nearly in

the geometric center of the drone. The c.g. is only deflected by 1.3 [cm] in the y-direction and only by 2.3 [cm] in the z-direction. Even in the extreme situation of removing two flight masks, the center of gravity only moves by 2.5 [cm]. The influence of these minor differences is deemed negligible and is thus not taken into account in the following calculations.

(a) Point mass representation in the XZ-plane.

(b) Point mass representation in the YZ-plane.

(c) Point mass representation in the XY-plane.

(d) Point mass representation in the XY-plane after having removed two flight masks.

Figure 13.2: Point mass representation of the drone. A larger point indicates a larger mass concentration at that location. Note that the red dot indicates the center of gravity with the landing gears retracted, and the blue dot the center of gravity with the landing gears extended.

13.1.2. Mass Moment of Inertia

To assess the dynamic stability of the UAV, the mass moment of inertia (MMoI) needs to be calculated. For this purpose, the UAV body is assumed to consist of a set of hollow cylinders. The center of gravity of each component is assumed to be coincident with its geometric center. The MMoIs are then calculated about the main body axes of the UAV, as indicated in Figure 13.1. The calculated MMoIs are then used to set up an inertia tensor for the component, as seen in Equation 13.1.[48]. Once the inertia tensor of each component is calculated, the tensors will be superimposed to find the total mass moment of inertia of the UAV. Note that the result is expected to reflect a symmetric body, hence the tensor should only have non-zero values in its main diagonal. This serves as a code verification check. This approach is presented in Equation 13.2.

$$I = \begin{bmatrix} I_{xx} & -I_{xy} & -I_{xz} \\ -I_{yx} & I_{yy} & -I_{yz} \\ -I_{zx} & -I_{zy} & I_{zz} \end{bmatrix} \quad (13.1) \qquad \sum I = \begin{bmatrix} I_{xx} & 0 & 0 \\ 0 & I_{yy} & 0 \\ 0 & 0 & I_{zz} \end{bmatrix} \quad (13.2)$$

Using this approach, the values for the mass moments of inertia as given in Table 13.1 are found.

Table 13.1: The mass moments of inertia of the UAV assembly.
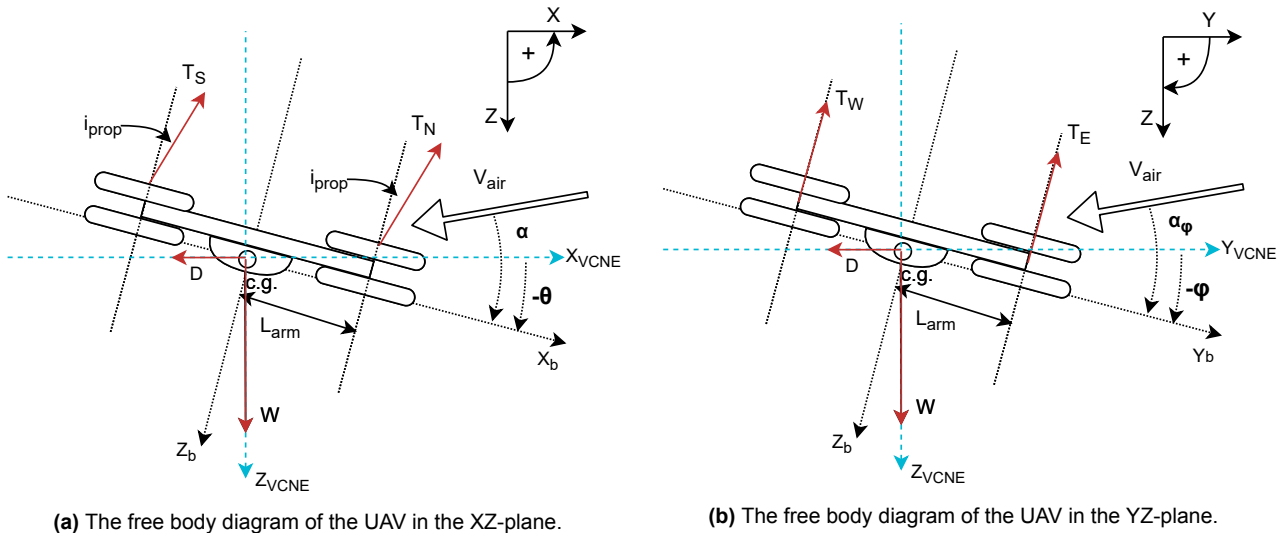
Parameter	Value	Unit
I_{xx}	0.354	[kg · m ^{2}]
I_{yy}	0.396	[kg · m ^{2}]
I_{zz}	0.161	[kg · m ^{2}]

13.2. Stability: Traditional Approach

The first approach that will be used to analyze the latent stability of the drone is the approach also used for conventional aircraft, as specified by J.A. Mulder et al.[49].   In this method, the first step is to determine the equations of motion (EoM) of the UAV. Using the reference frames defined in Figure 13.1, free body diagrams (FBD) are created for each plane. The thrust components are inserted per co-axial assembly since the moments they induce are different for each set of rotors. They are labeled according to the compass directions, as shown in Figure 13.1. Lastly, it is assumed that the UAV body is non-lifting, and therefore does not produce any lift. Aerodynamic forces are assumed to act at the center of gravity.

After the equations of motion are established, they can be linearized and non-dimensionalized to facilitate analysis of the aircraft motion, using established linear techniques like the state-space system approach. For the non-dimensionalization, it is assumed that the chord length and the wingspan are equal to the distance between the center hub of the propeller: $\bar{c} = b = l_{arm}$.

Equations of Motion in XZ-Plane (Pitch)

(a) The free body diagram of the UAV in the XZ-plane.

(b) The free body diagram of the UAV in the YZ-plane.

Figure 13.3: The free body diagrams of the UAV in roll (YZ) and pitch (XZ).

Derived from Figure 13.3, the equations of motion in the XZ-plane can be described by equations 13.3a, 13.3b and 13.3c. In the corresponding FBD of Figure 13.3a, the northern thrusters are grouped as $T_N = T_{NE} + T_{NW}$, while the southern thrusters are grouped as $T_S = T_{SE} + T_{SW}$. Note that a small

angle was assumed for i_{prop}, which gives $\cos(i_{prop}) \approx 1$ and $\sin(i_{prop}) \approx i_{prop}$.

$$\xleftarrow{+} \sum F_x = m \cdot a_x; \quad W \cdot \sin(\theta) - D \cdot \cos(\alpha) + (T_{NE} + T_{NW} + T_{SE} + T_{SW})i_{prop} = m \cdot \dot{u} \tag{13.3a}$$

$$\xdownarrow{+} \sum F_z = m \cdot a_z; \quad W \cdot \cos(\theta) + D \cdot \sin(\alpha) - (T_{NE} + T_{NW} + T_{SE} + T_{SW}) = m(\dot{w} - qV) \tag{13.3b}$$

$$\circlearrowleft+ \sum M_y = I_{yy} \cdot \dot{q}; \quad (T_{NW} + T_{NE}) \cdot l_{arm} \cdot (1 - i_{prop}) - (T_{SE} + T_{SW}) \cdot l_{arm} \cdot (1 + i_{prop}) = I_{yy} \cdot \dot{q} \tag{13.3c}$$

Linearizing the equations of motion given in Equation 13.3 gives the equations of Equation 13.4. Note that $X_0 = W \sin(\theta_0)$ and $Z_0 = W \cos(\theta_0)$.

$$\xleftarrow{+} \sum F_x \approx W \cos(\theta_0)\theta + X_u u + X_w w + X_q q + X_{T_N} T_N + X_{T_S} T_S = m \cdot \dot{u} \tag{13.4a}$$

$$\xdownarrow{+} \sum F_z \approx W \sin(\theta_0)\theta + Z_u u + Z_w w + Z_{\dot{w}} \dot{w} + Z_q q + Z_{T_N} T_N + Z_{T_S} T_S = m(\dot{w} - q \cdot V) \tag{13.4b}$$

$$\circlearrowleft+ \sum M_y \approx M_0 + M_u u + M_w w + M_{\dot{w}} \dot{w} + M_q q + M_{T_N} T_N + M_{T_S} T_S = I_{yy}\dot{q} \tag{13.4c}$$

Using the linearized EoM, the equation can be non-dimensionalized by dividing by $0.5\rho V^2 S\bar{c}$. The results of these equations are given in Equation 13.5, or, in matrix form, in Equation 13.6. Note the shift from w to α ($w/V = \alpha$) and the application of $D_c = \frac{\bar{c}}{V}\frac{d}{dt}$. Additionally, $\hat{u} = u/V$ and $\mu_c = \frac{m}{\rho S\bar{c}}$. A more extensive derivation can be found in [49].

$$\xleftarrow{+} \sum F_x; \quad C_{Z_0}\theta + C_{X_u}\hat{u} + C_{X_\alpha}\alpha + C_{X_q}D_c\theta + C_{X_{T_N}}T_N + C_{X_{T_S}}T_S = 2\mu_c D_c \hat{u} \tag{13.5a}$$

$$\xdownarrow{+} \sum F_z; \quad C_{X_0}\theta + C_{Z_u}\hat{u} + C_{Z_\alpha}\alpha + C_{Z_{\dot{\alpha}}}D_c\alpha + C_{Z_q}D_c\theta + C_{Z_{T_N}}T_N + C_{Z_{T_S}}T_S = \mu_c(D_c\alpha - D_c q) \tag{13.5b}$$

$$\circlearrowleft+ \sum M_y; \quad C_{m_0} + C_{m_u}\hat{u} + C_{m_\alpha}\alpha + C_{m_{\dot{\alpha}}}D_c\alpha + C_{m_q}D_c\theta + C_{m_{T_N}}T_N + C_{m_{T_S}}T_S = 2\mu_c K_Y^2 D_c\frac{q\bar{c}}{V} \tag{13.5c}$$

$$\begin{bmatrix} C_{X_u} - 2\mu_c D_c & C_{X_\alpha} & C_{Z_0} & C_{X_q} \\ C_{Z_u} & C_{Z_\alpha} + (C_{Z_{\dot{\alpha}}} - 2\mu_c)D_c & C_{X_0} & C_{Z_q} + 2\mu_c \\ 0 & 0 & -D_c & 1 \\ C_{m_u} & C_{m_\alpha} + C_{m_{\dot{\alpha}}}D_c & 0 & C_{m_q} - 2\mu_c K_Y^2 D_c \end{bmatrix} \begin{bmatrix} \hat{u} \\ \alpha \\ \theta \\ \frac{q\bar{c}}{V} \end{bmatrix} = \begin{bmatrix} -C_{X_{T_N}} & -C_{X_{T_S}} \\ -C_{Z_{T_N}} & -C_{Z_{T_S}} \\ 0 & 0 \\ -C_{m_{T_N}} & -C_{m_{T_S}} \end{bmatrix} \begin{bmatrix} T_N \\ T_S \end{bmatrix} \tag{13.6}$$

Note the addition of a fourth equation in the matrix equation of Equation 13.6. This equation is given in Equation 13.7 and represents the change in pitch.

$$\frac{\dot{\theta}\bar{c}}{V} = \frac{q\bar{c}}{V} (= D_c\theta) \tag{13.7}$$

Using the matrix in Equation 13.6, the equations of motion can be put into state-space form, the general form of which is given in Equation 13.8. For sake of space, the full state-space derivation is not given here but can be extracted easily from[49].
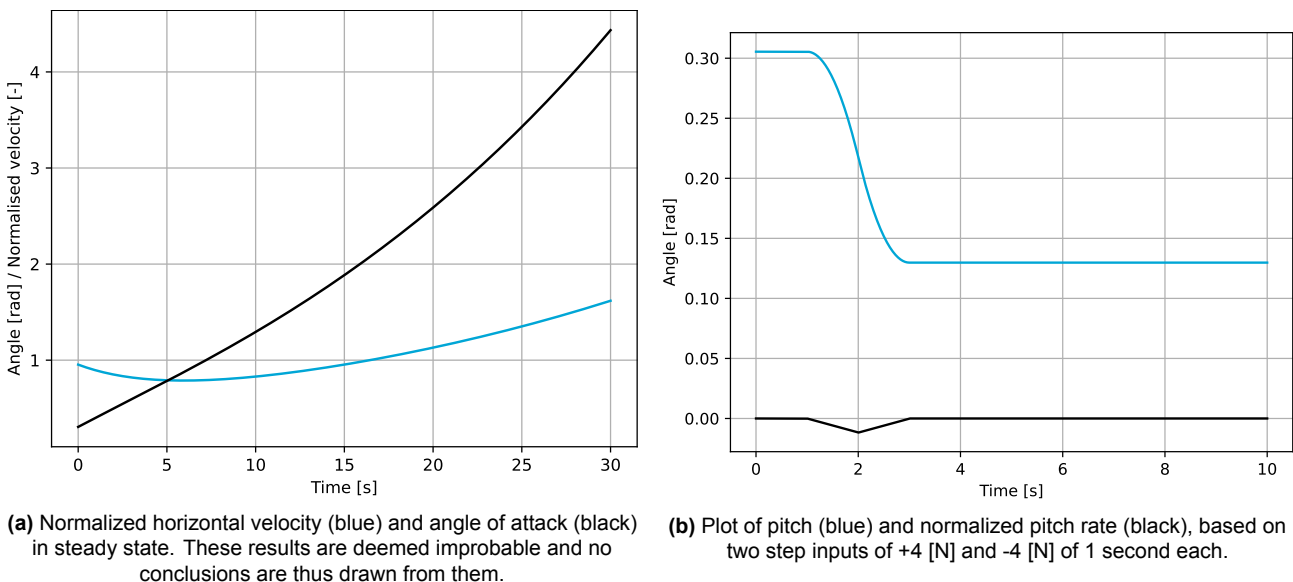
$$\dot{\mathbf{x}} = A\mathbf{x} + B\mathbf{y} \tag{13.8}$$

Once the state-space system is set up and the stability derivatives are calculated, the system's re-

sponse to a control input can be calculated. It should be noted that the model is not fully verified, and thus it is likely it may still contain errors. Specifically, the results for normalized horizontal velocity and angle of attack, as shown in Figure 13.4a, seem improbable. It is unlikely that the angle of attack increases as much as shown, while the pitch stays completely steady without any input. (see Figure 13.4b as well). At the time of writing, no cause has been found for this error, and it is one of the first steps in future work.

However, some conclusions about the system as a whole can be drawn. Determining the eigenvalues of matrix A of the state-space system, it can be shown that these are equal to -0.22, 0.036, 0, and 0. As they are all real numbers, no oscillations are expected, which correlates with the team's expectations and the knowledge of rotorcraft stability expert Dr. Ir. M. Pavel. The second eigenvalue of the system relates to the state variable α, which is shown to tend to infinity. This is hypothesized to be caused by the absence of counteracting aerodynamic moments, as the UAV is modeled as a non-lifting body. Therefore, a disturbance needs to be actively controlled by the 4 possible control inputs (namely, the varying thrust output of a rotor), something which this analysis does not incorporate. Therefore, it can be concluded that the UAV is inherently unstable without a controller in place.

One can also look at Figure 13.4b, which shows the response of the pitch and the normalized pitch rate to a step input. It is evident that without any input, the pitch rate and pitch are constant. Note that this is assuming zero propeller inclination, which is what has been designed at this stage. It is also interesting to see that for a relatively small input (4 [N]), a significant change in pitch can be seen. The drone is thus very agile.

(a) Normalized horizontal velocity (blue) and angle of attack (black) in steady state. These results are deemed improbable and no conclusions are thus drawn from them.

(b) Plot of pitch (blue) and normalized pitch rate (black), based on two step inputs of +4 [N] and -4 [N] of 1 second each.

Figure 13.4: Results from the traditional stability analysis.

In the future, this method must be further verified to confirm the suspicions regarding Figure 13.4a. The error must then be found and corrected, after which a controller can be designed. The controller will be discussed in Section 13.4, however.

Equations of Motion in YZ-Plane (Roll)
For the YZ-plane, one should note the similarities between Figure 13.3a and Figure 13.3b. They are nearly identical, with only certain variables bearing different names. A large part of the analysis is thus the same, and will not be elaborated on here. For completeness, the equations of motion are given in Equation 13.9a, 13.9b and 13.9c. Note that in the FBD, the western thrusters are grouped

as $T_W = T_{NW} + T_{SW}$, while the eastern thrusters are grouped as $T_E = T_{NE} + T_{SE}$.

$$\xrightarrow{+} \sum F_y = m \cdot a_y; \quad W \cdot \sin(\phi) - D \cdot \cos(\alpha) = m \cdot (\dot{v} + r \cdot V) \tag{13.9a}$$

$$+\downarrow \sum F_z = m \cdot a_z; \quad W \cdot \cos(\phi) + D \cdot \sin(\alpha) - (T_{NE} + T_{NW} + T_{SE} + T_{SW}) = m(\dot{w} - r \cdot V) \tag{13.9b}$$

$$\circlearrowleft + \sum M_x = I_{xx} \cdot \dot{p}; \quad (T_{NW} + T_{SW}) \cdot l_{arm} - (T_{NE} + T_{SE}) \cdot l_{arm} = I_{xx} \cdot \dot{p} \tag{13.9c}$$
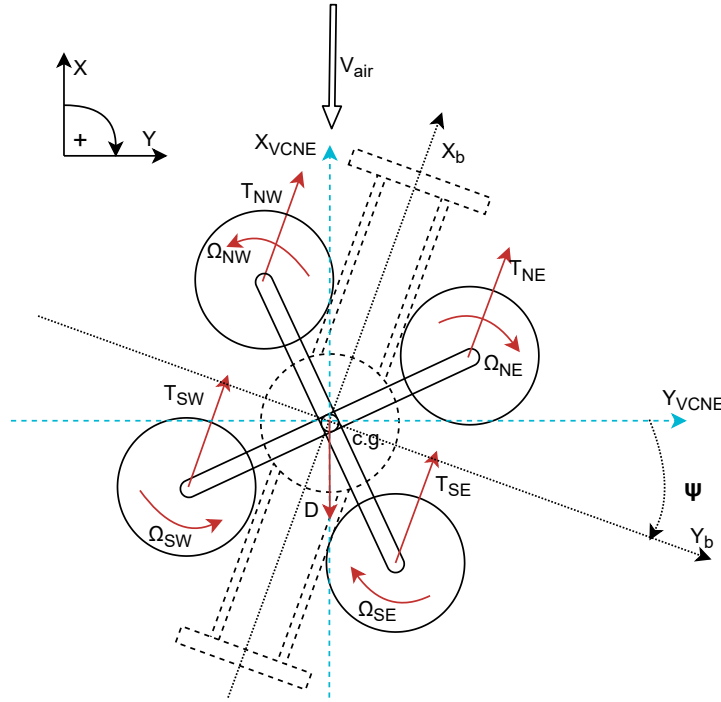
Equations of motion in XY-plane (Yaw):

Figure 13.5: The free body diagram of the UAV in the XY-plane.

The equations of motion in the XZ-plane can be described by equations 13.10a, 13.10b and 13.10c, which are based on Figure 13.5. Note that the torque and thrust created by each pair of co-rotating propellers are labeled with the compass directions, and the torque is denoted by Ω. The thrusts only contribute to the moment if a non-zero propeller inclination is chosen, which is not the case. For sake of time, no full analysis of the stability in the XY-plane was performed. This is thus a topic for further research. However, it is evident from the free body diagram and the equations of motion that for equal propeller torques (and thus RPM), there will be no yaw moment.

$$+\uparrow \sum F_x = m \cdot a_x; \quad (T_{NE} + T_{NW} + T_{SE} + T_{SW}) \cdot \sin(-\iota_{prop}) - D \cdot \cos(\phi) = m \cdot \dot{u} \tag{13.10a}$$

$$\xrightarrow{+} \sum F_y = m \cdot a_y; \quad D \cdot \sin(\phi) = m \cdot \dot{v} \tag{13.10b}$$

$$\circlearrowleft + \sum M_z = I_{zz} \cdot \dot{r}; \quad \begin{aligned} (T_{SW} + T_{NW}) \cdot \sin(-\iota_{prop}) \cdot l_{arm} - (T_{NE} + T_{SE}) \cdot \sin(-\iota_{prop}) \cdot l_{arm} \\ + (\Omega_{NW} + \Omega_{SW} - \Omega_{SE} - \Omega_{NE}) = I_{zz} \cdot \dot{r} \end{aligned} \tag{13.10c}$$

13.3. Stability: Drone-oriented Approach

A second method for stability analysis is outlined in [50]. This paper presents two equivalent models that can be used in the study of the UAV dynamics, namely the Newton-Euler method and the Lagrange-Euler method. The Newton-Euler method is chosen since it is a more intuitive approach to the dynamic system. This method, however, does not depend on the non-dimensionalization of the forces, but it uses a direct approach with the use of a state-space system with the forces and

moments present.

The coordinate system of the method is adapted to match the positive angles and directions, as specified in Figure 13.1. The rotation matrix to express the inertial frame in the body frame, R_{IB}, is then defined with the following rotation order: $\phi \to \theta \to \psi$. The rotation matrix is shown in Equation 13.11. Since the matrix is orthogonal, the transpose of the matrix can be used to express the body frame in the inertial frame of reference, $R_{IB}^T = R_{BI}$.

$$
R_{IB} = \begin{bmatrix} 1 & 0 & 0 \\ 0 & cos(\phi) & sin(\phi) \\ 0 & -sin(\phi) & cos(\phi) \end{bmatrix} \begin{bmatrix} cos(\theta) & 0 & -sin(\theta) \\ 0 & 1 & 0 \\ sin(\theta) & 0 & cos(\theta) \end{bmatrix} \begin{bmatrix} cos(\psi) & sin(\psi) & 0 \\ -sin(\psi) & cos(\psi) & 0 \\ 0 & 0 & 1 \end{bmatrix}
$$
$$
= \begin{bmatrix} cos(\theta)cos(\psi) & cos(\theta)sin(\psi) & -sin(\theta) \\ sin(\phi)sin(\theta)cos(\psi) - cos(\phi)sin(\psi) & sin(\phi)sin(\theta)sin(\psi) + cos(\phi)cos(\psi) & sin(\phi)cos(\theta) \\ cos(\phi)sin(\theta)cos(\psi) + sin(\phi)sin(\psi) & cos(\phi)sin(\theta)sin(\psi) - sin(\phi)cos(\psi) & cos(\phi)cos(\theta) \end{bmatrix}
$$
$$(13.11)$$

The transformation matrix for angular velocities from the inertial frame to the body frame is defined by Equation 13.12. The inverse of this transformation matrix can be used to relate the body frame angular accelerations to the inertial frame.

$$
\nu = \begin{vmatrix} x & R_x y & R_x R_y y \end{vmatrix} \begin{pmatrix} \dot{\phi} \\ \dot{\theta} \\ \dot{\psi} \end{pmatrix} \Rightarrow \begin{bmatrix} p \\ q \\ r \end{bmatrix} = \begin{bmatrix} 1 & 0 & -sin(\theta) \\ 0 & cos(\phi) & sin(\phi)cos(\theta) \\ 0 & -sin(\phi) & cos(\phi)cos(\theta) \end{bmatrix} \begin{bmatrix} \dot{\phi} \\ \dot{\theta} \\ \dot{\psi} \end{bmatrix} \qquad (13.12)
$$

Equation 13.11 and 13.12 can then be utilized to express the linear and angular velocities in both reference frames respectively.

Using the free body-diagrams as presented in Figure 13.3a, the equations of motion as given in Equation 13.13, expressed in the body frame of the UAV, have been derived. It is assumed that the propeller inclination is equal to zero.

$$
\xleftarrow{+} \sum F_x = m \cdot a_{x_b}; \quad W \cdot \sin(\theta) - D \cdot \cos(\alpha) = m \cdot (\dot{u} + qw - rv) \qquad (13.13a)
$$

$$
+\downarrow \sum F_z = m \cdot a_{z_b}; \quad W \cdot \cos(\theta) + D \cdot \sin(\alpha) - (T_{NE} + T_{NW} + T_{SE} + T_{SW}) = m(\dot{w} - qV) \qquad (13.13b)
$$

$$
\circlearrowright + \sum M_y = J \cdot \dot{\omega}; \quad (T_{NW} + T_{NE}) \cdot l_{arm} - (T_{SE} + T_{SW}) \cdot l_{arm} = I_{yy} \cdot \dot{q} + (I_{xx} - I_{zz})rp \qquad (13.13c)
$$

Linearizing the non-linear terms in the equation, the equations can then be adapted for the state-space method. The assumptions of the initial conditions are based on a steady, straight, symmetric flight condition.

$$
\xleftarrow{+} \sum F_x \approx W \cos(\theta_0)\theta + D \sin(\alpha_0)\alpha = m \cdot \dot{u} \qquad (13.14a)
$$

$$
+\downarrow \sum F_z \approx W \sin(\theta_0)\theta - D \cos(\alpha_0)\alpha - (T_{NE} + T_{NW} + T_{SE} + T_{SW}) = m(-qu_0) \qquad (13.14b)
$$

$$
\circlearrowright + \sum M_y \approx (T_{NW} + T_{NE}) \cdot l_{arm} - (T_{SE} + T_{SW}) \cdot l_{arm} = I_{yy}\dot{q} \qquad (13.14c)
$$

The drag is a function of the angle θ, as is discussed in Chapter 10. This estimation is also used for the stability analysis here. The linearization of the drag function leads to two terms, which are a function of the states u and θ. The state-space matrix for symmetric motion can then be defined as presented in Equation 13.15. Note that the drag at the point of analysis is defined as $D_0 = C_D(\theta_0)\frac{1}{2}\rho u_0^2 S$.

Furthermore, the control inputs are simulated as a change in thrust inputs from the initial state. In reality, the change in RPM of the rotor changes the thrust output, but this step is skipped in this

analysis.

$$
\begin{bmatrix} \dot{u} \\ \dot{\theta} \\ \dot{\alpha} \\ \dot{q} \end{bmatrix} = \begin{bmatrix} C_D(\theta_0)\rho u_0 S & \frac{W cos(\theta_0)}{m} + C_{D\theta}\rho u_0{}^2 S & \frac{D_0 sin(\alpha_0)}{m} & 0 \\ 0 & -\frac{W sin(\theta_0)}{m \cdot u_0} & -\frac{D_0 cos(\alpha_0)}{m \cdot u_0} & 0 \\ 0 & 0 & 0 & 0 \\ 0 & 0 & 0 & 0 \end{bmatrix} \begin{bmatrix} u \\ \theta \\ \alpha \\ q \end{bmatrix} + \begin{bmatrix} 0 & 0 & 0 & 0 \\ 0 & 0 & 0 & 0 \\ 0 & 0 & 0 & 0 \\ \frac{l_{arm}}{I_{yy}} & \frac{l_{arm}}{I_{yy}} & -\frac{l_{arm}}{I_{yy}} & -\frac{l_{arm}}{I_{yy}} \end{bmatrix} \begin{bmatrix} T_{NE} \\ T_{NW} \\ T_{SE} \\ T_{SW} \end{bmatrix}
$$

$$(13.15)$$

The moment arms of the thrust to the axis of rotation is defined as $l_{arm} = \sqrt{\frac{l_{proparm}^2}{2}}$. The relevant parameters used for the simulation are presented in Table 13.2.

Table 13.2: Parameter values for the Newton-Euler simulation

Parameter	Value	Unit		Parameter	Value	Unit
g	9.81	$[m/s]^2$		I_{xx}	0.354	$[kg\ m^2]$
m	31	$[kg]$		I_{yy}	0.396	$[kg\ m^2]$
S	1	$[m^2]$		I_{zz}	0.161	$[kg\ m^2]$
l_{arm}	0.3535	$[m]$		u_0	7.2	$[km/h]$
$C_D(\theta_0)$	0.1778	$[-]$		ρ	1.225	$[kg/m^3]$
$C_{D\theta}$	0.003132	$[-]$				

The linear horizontal speed was taken to be the induced velocity at hover, as described in Section 10.1 with Equation 10.6. For the symmetric flight condition, an analysis of the positions of the poles and zeroes was performed, using the eigenvalues of the A matrix of the State-Space. These values are 0.44, -1.02, 0.0 and 0.0. The values are plotted in a pole-zero map, as presented in Figure 13.6.
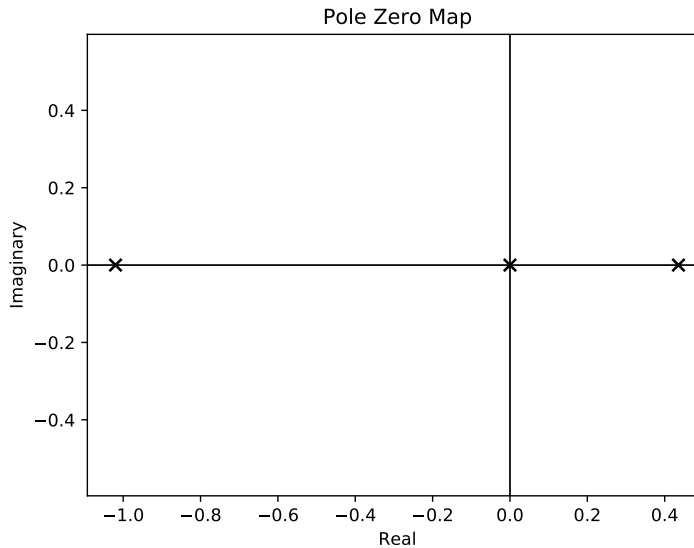
Figure 13.6: The locations of the poles and zeroes of the verification model. As can be observed from the plot, the system is unstable due to a positive valued pole, which is related to the horizontal speed state variable.

The system does not have oscillatory movements due to the lack of poles, but it is unstable due to a zero positioned on the positive real axis of the complex plane. This instability is associated with the phugoid flight mode and is inherent to rotorcraft aerial vehicles.[1] Furthermore, due to symmetry, the asymmetrical flight condition faces similar instabilities, as also evident from Figure 13.3a and

---

[1]As discussed with Dr. Ir. M. Pavel, an expert on rotorcraft control and stability at the TU Delft, Faculty of Aerospace Engineering.

Figure 13.3b. The aforementioned instabilities are generally corrected by a flight controller. A choice for a cascade PID-controller for further development is elaborated on in the next section.

13.4. Control of a Multicopter Aircraft

As explained in Section 13.2 and Section 13.3, a drone is initially unstable without a proper controller. The tuning of such a system is complicated, however, as it concerns a Multiple-Input-Multiple-Output system, which requires more advanced methods to design for. Such measures are beyond the resources of the current project. The coupling of moments about the three different axis increases the complexity of the analysis, as a thrust input will produce a change in torque in the XY-plane, and generate moments about the X and Y-axis. This problem is also encountered in [50], where the author states that a proper controller to stabilize accelerations in all three axes is subject to further research.

However, most flight computer boards, like the PX4 VOXL Flight board[2], come with a flight control package to allow for a stable flight of the UAV. For the current prototype, the manufacturer standard flight controller, ModalAI VOXL Flight[3], will be used for stabilization. Other methods of PID-control, such as a cascade PID-control, can be investigated for application on this UAV since they can handle large disturbance inputs, which may occur in the volatile environment close to a burning building.[51] For the prototype, the ModalAI VOXL Flight board is selected. However, a flight controller optimized specifically for this UAV will be a subject for further research.

An interesting note can still be made regarding control in case of propeller failure. In case one or two (opposite) propellers fail, the UAV is still able to maintain altitude and maintain relative control over the pitch and roll axes. Yaw control however is lost in such a scenario, meaning that the drone would spin with a constant yaw velocity $\dot{\psi}$. This problem is studied more in-depth in [52] and [53], where the authors simulate a 1- or 2-propeller inoperative scenario. In case of constant spin in yaw, the mission itself will have to be aborted, since the payload deployment requires stable yaw control. However, a safe emergency landing can still be performed in these conditions, making recovery of the entire UAV possible without damages due to a crash. A similar emergency landing can be performed in the case of lengthy signal loss.

13.5. Collision Avoidance System

To be able to fly autonomously from the fire station to the emergency site, the UAV should be equipped with a Collision Avoidance System (CAS). Given that the cruise speed will be 100 [km/h], and the fact that the deployment includes urban environments, the need for timely detection of obstacles arises. First, the minimum detection radius due to the Field of View (FOV) will be calculated, then the minimum detection radius due to the maximum flight speed needs to be determined. The UAV geometry and the field of view are depicted in Figure 13.7.

---

[2]`https://docs.px4.io/master/en/getting_started/flight_controller_selection.html`, Retrieved on 20/06/2021

[3]`https://docs.px4.io/master/en/flight_controller/modalai_voxl_flight.html#modalai-voxl-flight`, Retrieved on 20/06/2021
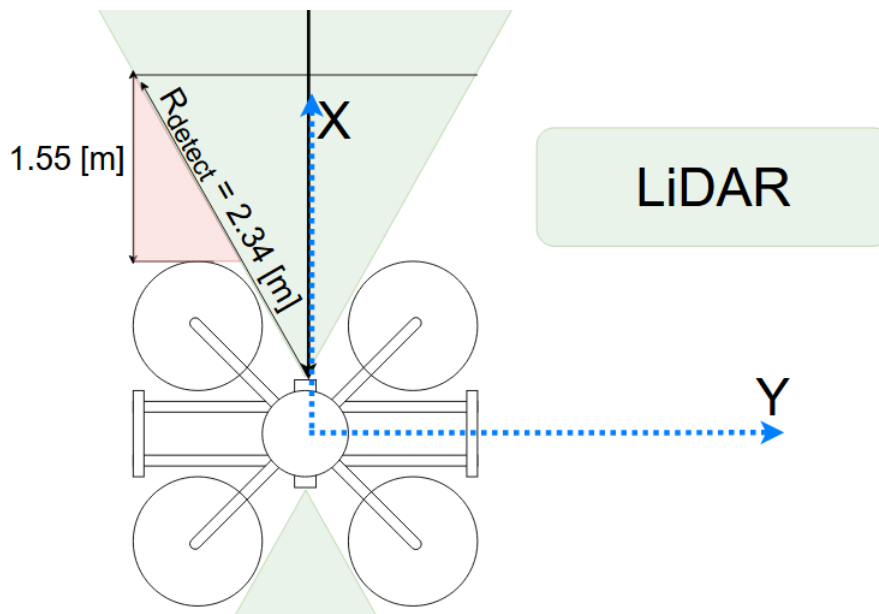
Figure 13.7: The horizontal field of view of the sensor in flight direction. The sensor blindspot with its dimensions are shown on the left red triangle.

From the geometry, the Field of View (FOV) in the XY plane is determined to be 45 [deg]. The sensor blind spot in the flight direction due to the ducts is a 1.55 [m] by 0.59 [m] triangle, which brings the need for a minimum detection range of 1.59 [m], extending from the front of the UAV body to the flight direction. The minimum detection radius to avoid a collision, R_{detect}, measured from the front of the LiDAR lens then becomes 2.34 [m].

From the cruise velocity of 100 [km/h] = 27.78 [m/s], the average reaction time of a CAS needs to be determined, which depends on the type of sensors and the algorithm. The author of [54] suggests an algorithm that is capable of detecting an obstacle, and successfully finding an obstacle-free path, in 100 [ms]. Taking into account processing time and an added layer of safety, a reaction time of 1 [s] will be used for the sizing of the CAS. The minimum detection range for cruise conditions is then determined to be 27.78 [m]. This will be the driving number for the selection of the sensors.

Sensor Selection

For the Collision Avoidance System, different types of sensors exist, and they can be divided into two categories: passive sensors, like visual light and Thermal or IR cameras. And active sensors, with LiDAR, SONAR, and RADAR as examples. A summary of the strengths and weaknesses of each type of sensor is presented in Table 13.3.[55] Following from Table 13.3, LiDAR and SONAR were

Table 13.3: Table showing the strengths and weaknesses of different sensors.

Sensor	Mode	Accuracy	Weather Condition	Light Sensitivity	Range	Sensor Size	Processing Requirement	Power Required
LiDAR	Active	High	Low Dependency	No	Medium	Small	Low	Medium
Radar μ-wave	Active	High	Not dependant	No	Long	Large	Low	High
MMW	Active	High	Dependant	No	Long	Small	Low	Medium
Ultrasonic	Active	Medium	Partial Dependency	No	Short	Small	Low	Medium
Thermal or IR	Passive	Medium	High Dependency	No	Medium	Small	High	Low
Camera	Passive	Medium	High dependency	Yes	Short	Small	High	Low

selected to be used in the CAS. RADAR, while having high accuracy and no weather dependence, is deemed too heavy and bulky for the UAV. MMW has the drawback of being weather dependent, which leaves LiDAR and Ultrasonic sensors as a viable option. For the forward flight direction, LiDAR is selected for its long range detection capabilities, while the short ranged Ultrasound/SONAR will be

used when the UAV is close to the building for payload deployment. The quantities and specifications of the sensor setup are summarized in Table 13.4. The LiDAR sensor is obtained from[4] and the SONAR sensors is selected from[5]. Although not part of the CAS, 3 visual light cameras are included in the sensor setup, to provide situational awareness and sight to the drone operator.[6]

Table 13.4: Specifications of the sensors used in the CAS, as well as the camera used for remote observation.

Parameter	LiDAR	SONAR	Camera	Unit
Quantity	2	12	3	[-]
Model	LW20-C	MB1260 XL-MaxSonar-EZ/AEL0	1/2.7" Omnivision OV1270	[-]
Update rate	48	10	30	[Hz]
Range of detection	0.2 - 100	0 - 5.8 (Beam pattern B)		[m]
Unit Weight	30	5.9	200	[g]
Unit Dimensions (HxWxD)	19.5x30.2x43.0	22.1x19.9x25.11	38x38x27	[mm]
Unit Power required	0.715	0.016	0.038	[W]
Unit Voltage required	4.5-5.5	3.3-5.5	5	[V]
Unit Current draw	130	3.4	190	[mA]
Connection type	I2C, Serial	Analog (Vcc/1024/2cm), RS232 Serial	USB	[-]
Unit cost	250	50 - 60	75	[EUR]

CAS Sensor Lay-Out

In order to have effective coverage over all sectors of the UAV, the setup presented in Figure 13.8 is proposed.
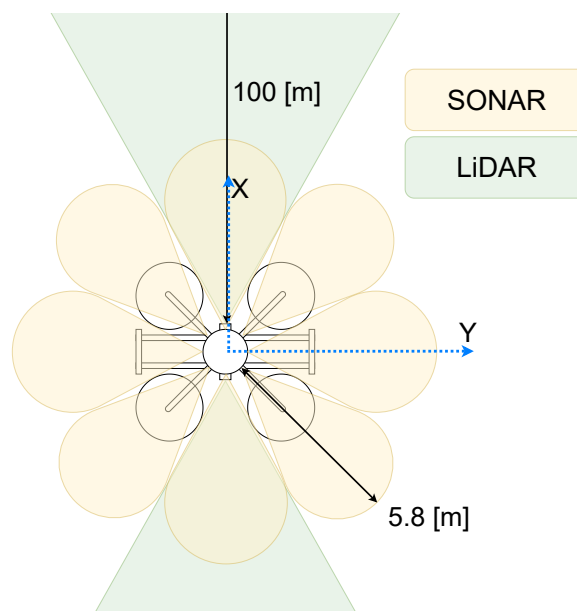
Figure 13.8: The sensor layout of the CAS in the XY-plane. The ranges extending beyond the borders of the plot are indicated.

---

[4]https://www.lidarsensor.nl/product/lw20-c-lidar-afstandsmeter/, Retrieved on 14/06/2021.

[5]https://www.maxbotix.com/ultrasonic_sensors/mb1240.htm, Retrieved on 14/06/2021.

[6]https://nl.grandado.com/products/fabriek-levering-beste-camera-2mp-ov2710-full-hd-1080p-6-mm-lens-usb-2-0-hoge-snelheid-web-camera-voor-pc?gclid=Cj0KCQjw5uWGBhCTARIsAL70sLK5Z5LbTpAJRMXJt817qFQSv33ypLEQHwVIA7DWN7BwcB&variant=UHJvZHVjdFZhcmlhbnQ6ODc2OTc4MA, Retrieved on 25/06/2021.

In the forward flight direction, a LiDAR sensor will be placed with a detection range of 100 [m]. With a field of view of 45 [deg], the LiDAR sensor can capture obstacles that may obstruct the flight path. For redundancy purposes, a second one will be placed in the opposite direction, such that in case of failure the drone might continue its mission by only rotating around its axis. The measurement rate ranges from 48 to 388 [Hz]. Higher rates are used for scanning environments and collecting data. The lower measurement rates are sufficient for obstacles detection, as it does not need to make a detailed scan of the environment to accomplish collision avoidance. Therefore, the 48 [Hz] rate is deemed sufficient.[7]

The SONAR sensors will be placed at all 6 sides of the drone. This includes the sides with LiDAR already installed since SONAR is more accurate in short-range obstacle detection than LiDAR. Furthermore, 4 units will be placed at a 45 [deg] angle with respect to the XY-axis, to prevent blind spots in the corners of the UAV. The SONAR product in Table 13.4 is selected due to its ability to detect people within a 5.8 [m] range, using a beam pattern that is wide enough to prevent blindspots from occurring. The interference of the propeller assembly to the ultrasound sensor signal can be estimated. Noting that the ultrasound sensor uses a 42 [kHz] signal, the blade pass frequency (BPF) of the propeller can be calculated, using Equation 13.16 [56], to assess possible frequency interference between the two systems.

$$BPF = \frac{RPM}{60} \cdot (number \quad of \quad blades) \tag{13.16}$$

From Equation 13.16, it is concluded that the BPF is not in the same range as the SONAR, which in theory should not hamper the ultrasound signal from detecting an obstacle. This claim however needs validation with a test setup of the prototype. Lastly, the sensor in the positive z-direction will be used to range the UAV to the ground during landing operations, as well as to detect and range the surface during payload deployment.

Flight Path Planning
During flight, a CAS strategy of sense & avoid and optimization is chosen. For the optimization strategy, the UAV will be provided with the latest geographical information on standby. This information includes the dimensions and positions of all possible static obstacles within the operational range of 10 [km]. Based on this data, the UAV will be able to compute an optimal flight path to the emergency site. During flight, a sense & avoid strategy will be implemented to change course. The LiDAR sensor will be able to detect objects up to 100 [m] away, which gives the system 4 seconds to react at cruising speed. An evasive maneuver can be calculated for the UAV, after which the drone will try to get back to the original flight path at the closest following waypoint.[54, 55]

The translation of the UAV will be monitored using 4G, Inertial Measurement Unit data, and GNSS where possible, as to avoid Loss of Signal in signal obscured zones, which is a known problem in urban environments.[57]

13.6. Sub-system Compliance Matrix
Table 13.5 shows the compliance matrix of the requirements related to control and stability.

Table 13.5: Compliance matrix control and stability requirements

Requirement	Verification method	Compliance
TECH-CS-04	As summarized in Table 15.1, the C&S system uses 20.7 [W] in total.	Yes
TECH-CS-05	The update rates of the sensors, as shown in Table 13.4, meet the requirement.	Yes
		Continued on next page

---

[7]https://www.lidarsensor.nl/wp-content/uploads/2018/10/LiDAR-Sensor-datasheet-LW20-ENG.pdf Retrieved on 14/06/2021.

Requirement	Verification method	Compliance
TECH-CS-06	The UAV will be equipped with a PID-controller, which will be capable of controlling the UAV to perform an emergency landing, as discussed in Section 13.4.	Yes
TECH-ATT-01	This is achieved by the IMU on the PX4 VOXL flightboard.	Yes
TECH-GEN-01	The current sensor setup is sensitive enough to accomplish landing in urban areas	Yes
TECH-GEN-03	This is accomplished by an off-the-shelf flight control system, such as the PX4 VOXL board has, or an implementation of existing algorithms such as described in [51]	Yes
TECH-GEN-04	This is accomplished by an off-the-shelf flight control system, such as the PX4 VOXL board has, or an implementation of existing algorithms such as described in [51]	Yes
TECH-OC-02	The suggested cascade PID-controller is capable of handling large disturbance inputs, as described in [51].	Yes

14 Detailed Design: Data Handling and Communications

The communications system is a vital subsystem of the UAV. The drone is planned to be semi-autonomous, which requires communication with a remote pilot and ground stations to fulfill its mission. The current location and attitude of the drone, as well as information about the emergency site, can then be relayed to the operator and emergency services on site. This chapter will discuss how the communication system is set up.

First, a general introduction to drone communication systems, together with their advantages and disadvantages, will be given in Section 14.1. Afterwards, Section 14.2 will discuss the design for the UAV's communication system.

14.1. Introduction to Drone Communication Frequencies

In general, radio wave communication is used for nearly all drone applications. Other communication technologies, such as infrared, require either a direct line of sight or work on a too limited range. This research will therefore focus exclusively on radio wave communication.

Radio waves can be broadcast at several frequencies, each having specific properties in regards to data capacity and ranges. In general, lower frequencies have a higher range and penetration, at the cost of a lower data capacity. Vice versa, higher frequencies give higher data capacities at a lower range and penetration. Examples of frequencies currently used are presented in Table 14.1, together with their their main capabilities and limitations[1,2,3,4,5].

It is important to clearly define the term *data capacity*, as it does not directly indicate data rate. A higher signal speed is possible if the data capacity is high, but a lower capacity frequency could be faster if the said frequency is less crowded. The 2.4 [GHz] band, for instance, is widely used, and thus very crowded. Consequently, it rarely reaches its maximum theoretical speed. However, it is difficult

---

[1] http://www.emfexplained.info/?ID=25916, Retrieved on 18/06/2021

[2] https://www.thedronegirl.com/2017/07/26/longest-fpv-range-drone/, Retrieved on 18/06/2021

[3] https://diydrones.com/profiles/blogs/what-can-t-be-missing-for-a-long-distance-900-mhz-drone, Retrieved on 18/06/2021

[4] https://antennekaart.nl/page/frequencies, Retrieved on 18/06/2021

[5] https://www.techradar.com/news/phone-and-communications/mobile-phones/4g-and-lte-everything-you-need-to-know-926835, Retrieved on 18/06/2021

Table 14.1: Examples of frequencies which can be used for drone communication.

Frequency [GHz]	Max. range [km]	Data capacity	Applications
0.900	7.0 - 10.0	Low	Direct, 3G, 4G
2.4	1.0 - 4.0	Decent	WiFi, Bluetooth, appliances
5.8	0.5 - 1.0	High	Direct, WiFi
20+ (mmWave)	0.010 - 0.100	Extremely high	5G

to precisely quantify the data capacity, as it is also dependent on the technology used, the bandwidth chosen, and the error rate that is deemed acceptable.

There are also some notes to be placed regarding the maximum range. The maximum ranges as specified in Table 14.1 are valid for low noise circumstances and a direct line of sight (no obstructions between transmitter and receiver). This range will decrease in more complex situations. Especially in urban areas, where the UAV is expected to operate, it is unlikely any of these frequencies will be able to reach their maximum range as advertised here. After all, cities generally have high electromagnetic noise levels, are crowded, and present many obstructions.

Finally, it is relevant to mention the impact of fire on radio signals. Based on research performed by the University of Adelaide[58], fire has a serious impact on the propagation of radio signals. In some cases, firefighters were able to see each other but unable to communicate by radio. This impact of fire, even on line of sight communications, must be taken into account when designing the communication system of the drone.

14.2. Proposed Design for Drone Communication System

The frequencies presented in the previous section form the basis of any communication that will be performed with the drone. The required communications between agents are presented in Figure 14.1. In the figure, three phases are identified, each adding different requirements to the communication system. Note that many systems regarding emergency service communication are already in place: C2000 is used in the Netherlands[6]. Additionally, air traffic control communication is dominated by very high frequency (VHF) communications at short range[7]. This is also established technology and will not be discussed here. This section will thus focus on the design of just two communication lines: the communication between the operator, the fire brigade, and the drone as well as the communication between the victim and the fire brigade.

First, the design of the communication system between the operator, the fire brigade, and the drone will be presented. As previously discussed, the range of a direct radio link between the drone and the operator will be limited. Assuming high noise levels in urban areas, these ranges can even drop below the required range of 7 [km]. A direct radio connection is thus not possible.
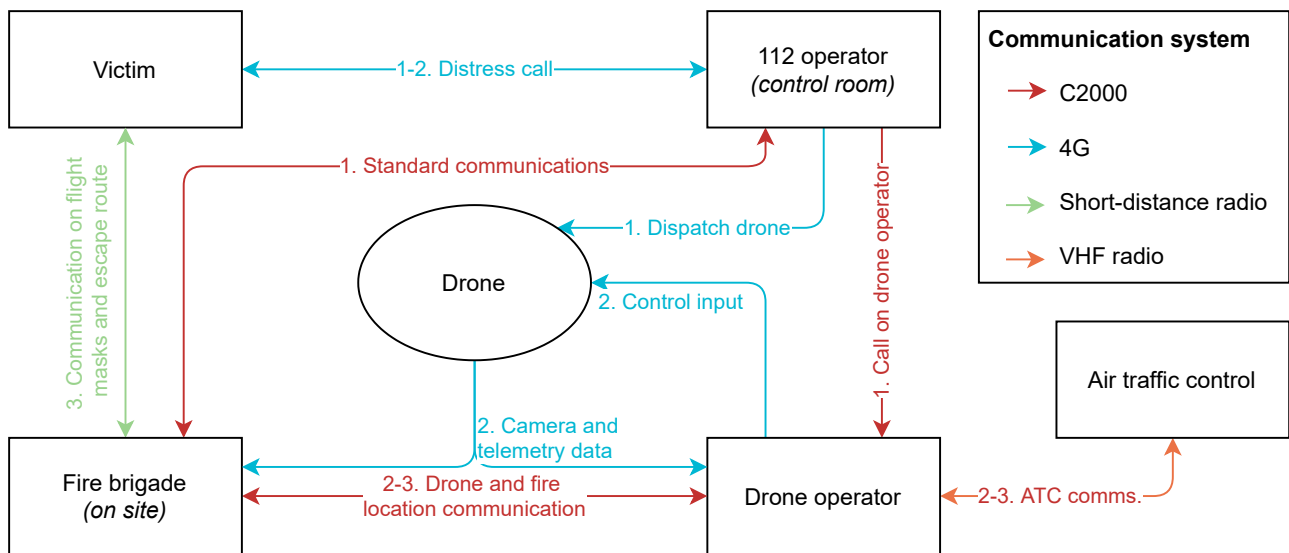
On the other hand, cellular networks have significantly expanded over recent years and now provide generally widespread and reliable coverage, especially in urban areas. A multi-point system then becomes possible. Such a system has multiple advantages: Allowing for multiple points of access for the UAV expands its operational range, as the cellular network is accessible in a vast number of locations. Furthermore, it increases reliability, as multiple access points enable the drone to fall back to a different antenna when a signal faces interference by, for example, fire. Finally, cellular networking is a proven technology and many components are available off the shelf.

It is interesting to compare the various technologies currently used for cellular multi-point systems: 3G, 4G, and 5G. Note that each cellular networking technology generation has multiple variants, not all of which will be discussed here. The capabilities of each of the mentioned technologies are presented in Table 14.2[8].

---

[6]https://www.rijksoverheid.nl/onderwerpen/communicatie-hulpdiensten-c2000/c2000, Retrieved on 29/06/2021.

[7]https://thepointsguy.com/guide/how-pilots-communicate-with-atc-in-air/, Retrieved on 29/06/2021.

[8]https://kenstechtips.com/index.php/download-speeds-2g-3g-and-4g-actual-meaning, Retrieved on

Figure 14.1: Communication flow diagram for the drone. Three phases are identified, each requiring a different form of communication. These are labeled 1, 2 and 3. Note that the directions of arrows indicate whether a person is a transmitter, a receiver, or both.

Table 14.2: Networking technologies currently in use and their respective capabilities.

Technology	Data rate [Mbit/s]	Latency [ms]
3G	1-8	100
4G	15-90	30-50
5G	150-200	1

For stable HD video downlink, at least 3-4 [Mbit/s] is required. In the ideal case, 3G could supply these speeds. However, such speeds are never realistically reached due to noise and busy networks. On the other hand, 4G and 5G's data rates are usable. Additionally, studies performed by Qualcomm show that using 4G to control drones is feasible[59]. The latency of 4G is thus deemed sufficient for the control required in this design, especially as no 5G receivers for drones are available off-the-shelf. On the other hand, for better performance, 5G receivers should be investigated in the future.

Based on their research, Qualcomm developed a flight computer platform for drone applications, dubbed the Snapdragon Flight Pro[9]. A flight computer and controller combination based on this platform were selected for this UAV: The ModalAI VOXL Flight[10]. This system was chosen as it provides out-of-the-box support for easy connections with a 4G receiver, electric speed controllers, cameras, and GPS. It also comes installed with a fully programmed collision avoidance system (excluding cameras), inertial measurement units, and a WiFi receiver for debugging purposes. The subsystems that are still missing (G/LTE receiver, antennas, and a GPS) can also be purchased directly from ModalAI, easing development and ensuring compatibility. After all, this team does not possess extensive knowledge of chip design and electrical engineering. Therefore, ModalAI's suggestions for purchasing the subsystems mentioned before will be followed.
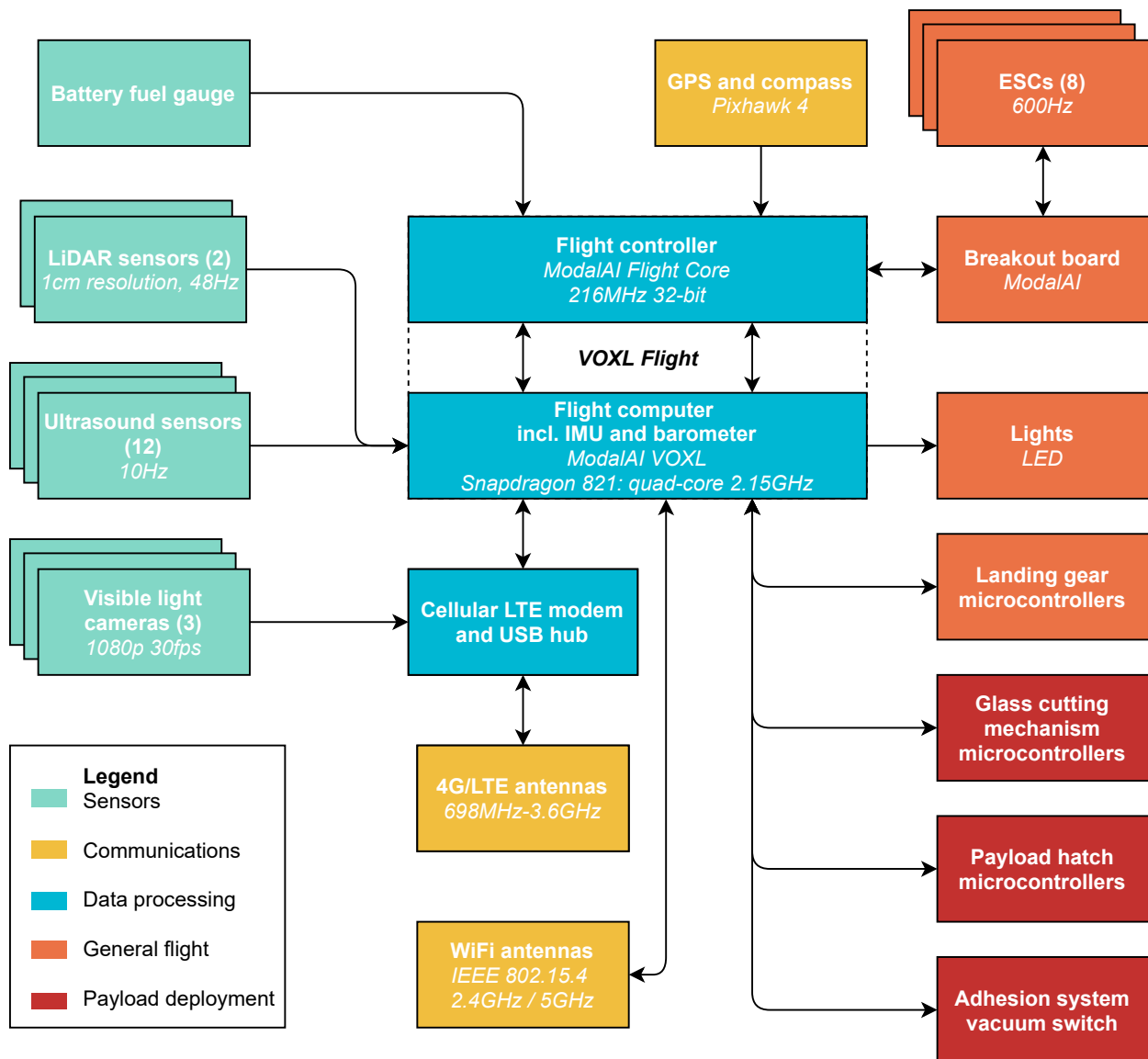
For the 4G/LTE receiver, frequencies of 698 [MHz] to 3.6 [GHz] can be received. This provides support for a wide number of frequency bands used in various countries. The WiFi antennas are based on the IEEE 802.15.4 protocol and can operate at either 2.4 [GHz] or 5 [GHz]. WiFi is installed for easy debugging and maintenance of the drone.

The integration of these components, as well as those selected in Chapter 10 and Chapter 13, is schematically represented in Figure 14.2.

18/06/2021

[9]https://developer.qualcomm.com/hardware/qualcomm-flight-pro, Retrieved on 18/06/2021

[10]https://www.modalai.com/products/voxl-flight?variant=31636287094835, Retrieved on 18/06/2021

Figure 14.2: Data handling block diagram for the proposed mission. Some specifications and comments are placed below each component in italics. Note that some specifications are drawn from Section 13.5 and Section 10.3.3

Some final notes can be placed regarding the communication between the victim and the fire brigade. The victim will often have contacted the emergency services themselves through the use of the (inter)national emergency hotline (112 in many parts of Europe). Direct communication between the victim and the fire brigade can be valuable, especially once the flight masks have been delivered and instructions can be directly relayed to the victims. The fire brigade will have a better awareness of the situation at the emergency site and can provide information on safe to use evacuation routes and instruct the victims on the proper use of the flight masks.

Although an integrated communication system was initially considered, the fact that the system should be portable, led to the choice for a handheld transceiver. The fire brigade, as well as many individuals, have experience using these systems. Additionally, they are inexpensive and intuitive to use. A major drawback is the sensitivity of the radio signal to fire, especially once the victim starts to move inside the building. However, as established previously, this is a challenge with any radio communication system and would not change the choice of system.

14.3. Sub-system Compliance Matrix

A complete list of data handling and communication requirement compliance can be found in Table 14.3.

Table 14.3: Compliance matrix data handling and communication requirements

Requirement	Verification method	Compliance
TECH-OR-01	The drone can be controlled via 4G, as explained in Section 14.2.	Yes
TECH-OR-02	The drone can be controlled via 4G, as explained in Section 14.2.	Yes
TECH-OR-03:	The drone can be controlled via 4G, which has a latency of 30-50 [ms], as explained in Section 14.2.	Yes

15 Detailed Design: Overview

In this section, the final design, budgets, and technical resources will be summarized and presented. Initially, the detailed design of all subsystems will be presented then an integrated system will be displayed.

The final configuration designed for was an X8-copter, using this as a basis, all of the subsystems were sized to provide the final design.

As a result of the design of the data and communication system, it was concluded that a flight computer will be used with GPS, there will be a two-way communications system to communicate with the victims, and finally that the drone can be controlled via 4G.

The next aspect designed for was the adhesion system. This allows the drone to be able to deliver the payload to the victims. A method of suctions cups will be used. First and foremost, the drone has been designed to initially take the option of landing on a roof or balcony, where the payload will be deployed very easily. If this cannot be done, the drone will adhere to the building using suction cups and rotate. The necessary components are suction cups, a vacuum pump, vacuum switches, three-way valves, and a vacuum distributor. The total power needed by the system will be between 50-60 [W]. The integration of the system can be found later in this chapter.

Once the system has adhered to the building, in the case that the window cannot be opened, a glass cutting mechanism must be deployed. This is done with a combination of a scoring tool and a blow torch to help propagate the crack.

Moving onto the aerodynamic performance of the UAV the airfoils were sized using XRotor and CRotor, these were then used as inputs for the power and propulsion sizing.

The power and propulsion system was designed from the propellers towards the motors, electric speed controllers, and finally the batteries. This resulted in a sizing that has X in series and Y parallel branches. The breakdown of different subsystems and the associated electrical parameters can be found in Table 15.1.

The materials and structure have been created to provide enough thermal insulation from the extreme environment while providing rigidity and structural performance. An overview of the mass of all of the components can be found in Table 15.2

Lastly, the analysis of controllability and stability was done. Here, the equations of motions were derived, where it was found to be inherently unstable. This is compensated by the control system employing a cascade PID controller. A ModalAI VOXL flight computer was chosen which is capable of collision avoidance. In addition to this, sensors were also chosen, namely SONAR and LiDAR.

The integration of all the subsystems leads to the overall configuration which can be seen in the technical drawings (Figure 15.2 and 15.3).

Power budget

An overview of the power budget can be found in Table 15.1 below. This summarizes the most significant power contributions to the UAV.

Table 15.1: Summary of all of the power requirements of the UAV

Sub-system	Power requirement [W]	Voltage [V]	Current [A]
Propulsion	10,000	45.6	167.983
Adhesion mechanism	50-60	24	2
Communications	20	12	4
Glass cutting	20	12	1.667
Other operations	0.7337	5.5	0.1334

Mass budget

An overview of the mass budget can be found in Table 15.2. This provides a breakdown of the contribution of each subsystem to the total mass.

Table 15.2: Summary of the mass breakdown of the UAV

Sub-system	Mass [kg]	Sub-system	Mass [kg]
Payload	2.892	Adhesion system	4.132
Glass cutting	1.033	Propellers	1.790
Batteries	14.850	Ducts	1.600
Motors	2.808	Propeller arms	0.790
ESC	0.588	Landing gear	0.877
Collision avoidance system	0.750	Main body	5.384
Communication systems	0.050	Contingency	1.277
Walkie-talkies	0.200	**Total**	39.000

A top and side view can be found in the technical drawings in Figure 15.2 and Figure 15.3. Furthermore, a full render is provided in Figure 15.1.
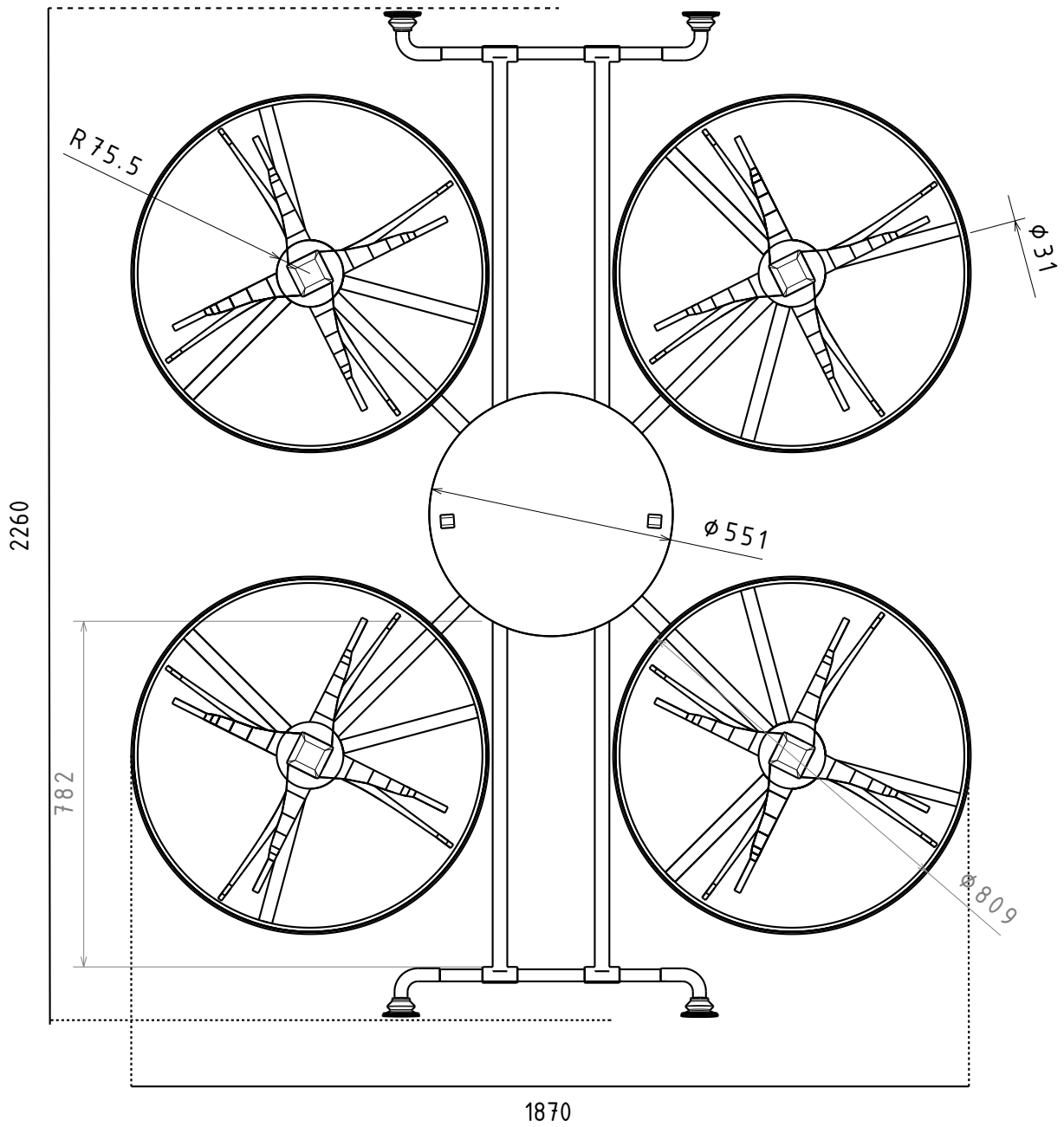

Figure 15.1: Render of the UAV design.

R 75.5

φ 31

2260

782

ø 551

ø 809
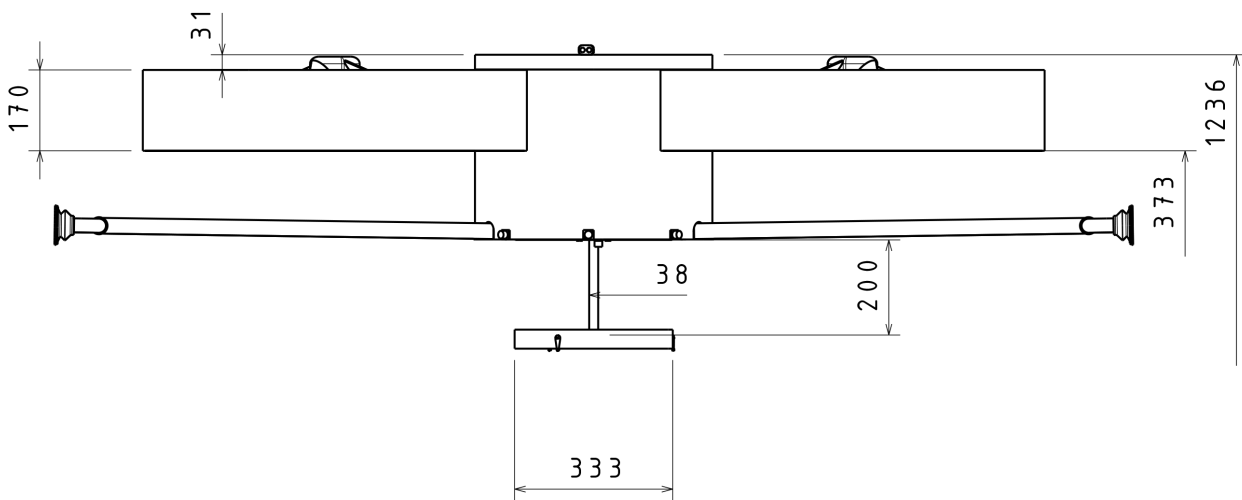
1870

Figure 15.2: Technical drawing top view.

Figure 15.3: Technical drawing side view.

16 Requirement Compliance and System Sensitivity

This chapter serves for both verification and validation of the system. After designing the system it is important to look back and see whether it can do what is expected of it and in later stages of the project if the mission can be accomplished. Section 16.1 and 16.2 discusses the verification of the requirements defined in Chapter 6. Secondly, Section 16.3 discusses the effect of uncertainty in important parameters on the feasibility of the design. Lastly, Section 16.4 looks ahead at required validation procedures for the system.

16.1. Compliance Matrix User Requirements

Having designed the system, it is time to take a look at the requirements defined by the user, to confirm that the system does what is expected from it. For this reason, the user requirements compliance matrix is set up. Table 16.1 presents the requirement through its code, the method of verification, and if the requirement is met.

Table 16.1: Compliance matrix user requirements

Requirement	Verification method	Compliance
TL-USER-01	As explained in Chapter 4, six flight masks and two hand-held transceivers will be taken on board which will be adequate for the mission. Their total weight is about 3.2 [kg] (see Table 4.1). In discussion with the client this requirement has been dropped.	Dropped
TL-USER-02	The six flight masks have dimensions 8x16x14 [cm] (see Table 4.1). Furthermore the two handheld transceivers have 11x6x4 [cm] as dimensions. This results in a total volume of about 0.01 [m^3].	Yes
TL-USER-03	The UAV has a maximum cruise speed of 115 [km/h], as explained in Section 10.4.3.	Yes
		Continued on next page

106

Table 16.1: continued from previous page

Requirement	Verification method	Compliance
TL-USER-04	As explained in Chapter 3, the night noise regulations require the vehicle to fly above 90 [m] altitude, as explained in Section 3.2. This has been implemented in a typical flight plan. It must be noted that at take-off and landing the noise might be higher but due to the function as an emergency vehicle this is deemed acceptable	Yes
TL-USER-06	The UAV has a maximum range of 15.4 [km] while executing a mission. This is derived in Section 10.4.4.	Yes
TL-USER-07	As explained in Section 4.2, annually it is expected the UAV will take flight eight times. The most critical elements are the batteries, with a guaranteed number of life cycles 150. This therefore confirms that the vehicle shall have a lifetime of more than 10 years.	Yes
TL-USER-08	The CFRP is protected by a TBC, which is verified in Chapter 11. The aluminum can withstand the high temperatures.	Yes
TL-USER-09	The internal components are protected with insulation. It is verified with a thermal simulation in Chapter 11.	Yes
TL-USER-10	This was dropped to semi-autonomous in discussion with the client.	Dropped
TL-USER-11	A GPS antenna and receiver are installed. See also Chapter 14.	Yes
TL-USER-12-01	This requirement was dropped for weight reasons, as the drone makes sufficient noise by itself.	Dropped
TL-USER-12-02	The drone has lights which indicate its location at night, as is explained in Section 12.2.6.	Yes
TL-USER-13	The UAV is equipped with SONAR to facilitate proximity detection, as explained in Section 13.5.	Yes
TL-USER-14-01	GPS/4G is used for the navigation, in combination with the pre-flight planning and CAS to facilitate navigation in urban areas (Section 13.5).	Yes
TL-USER-14-02	The SONAR model MB1260, as explained in Section 13.5 can detect people up to 5.4 [m].	Yes
TL-USER-14-03	The SONAR is able to detect object within 5.4 [m] from all sides.	Yes
TL-USER-15:	The vehicle respects the maximum noise of 85 [dB], as proven by XRotor analysis (Section 3.2).	Yes
TL-USER-16	As explained in Section 2.2 regulations are not in place yet. However, to improve visibility lights are installed on the UAV, as is explained in Section 12.2.6.	TBD
TL-USER-17	This must be accomplished by a flight controller which is optimized for the UAV, something which is beyond the scope of the project due to complex analysis of MIMO-systems.	TBD
TL-USER-18	The TBC is corrosion resistant, as explained in Section 11.3. Moreover, all electrical components are located within the UAV and will therefore not be exposed to water. Hence, the UAV can fly in both dry and wet weather conditions	Yes
TL-USER-19	The UAV will be able to make a safe landing if 50% of the motors fall out, in this case, the bottom rotors or the ones located on a diagonal. It will also be controllable and will not cause any long-term damage. This explained Section 13.4.	Yes

Table 16.1: continued from previous page

Requirement	Verification method	Compliance
TL-USER-20	Cost analysis in Table 19.1 shows that the material cost is 7,446 [EUR], well below the maximum budget. It must be noted that the production cost will elevate this number, but together with the client, it was determined that the 10,000 [EUR] should refer to material cost only.	Yes
TL-USER-21-01	As explained in Section 12.1 fatigue will not be a problem in the UAV life under normal conditions.	Yes
TL-USER-21-02	The UAV consists of seven main parts to facilitate modularity: propeller arm, main body, landing gear, landing gear mechanism, main body outer shell, main body inner shell, and main body doors. Those will be attached with bolts to enable them to be taken apart as explained in Section 18.3.	Yes
TL-USER-22	The battery shall be reusable for at least 150 cycles as specified by the manufacturer. All battery info is described in Table 10.10	Yes
TL-USER-23	Follows from the choice for a X-8 configuration.	Yes
TL-USER-24	As described in Section 12.2.5, the payload is adhered to the body through hook and loop fasteners. These can simply be pulled loose and thus doesn't require any additional knowledge to operate.	Yes
TL-USER-25	The drone carries a handheld transceivers as payload, as is explained in Section 4.1.	Yes
TL-USER-26	The UAV will be equipped with a 4G transceiver (Section 14.2) to enable control by a certified pilot.	Yes

16.2. Compliance Matrix Safety Requirements

A proper design also takes its safety into account. Therefore Table 16.2 gives an overview of the safety requirements and how they are met.

Table 16.2: Compliance matrix safety requirements.

Requirement	Verification method	Compliance
TECH-SSR-01-01	The UAV has LED lights installed on it, as explained in Section 12.2.6, which allows it to be visible during the night. However, post-DSE experimental research has to be done into the exact distance from which the lights can be seen.	TBD
TECH-SSR-03	The only sharp edges on the UAV are the propellers, however, the ducts around the propellers (Section 10.2.5) prevent anyone from accidentally coming close to it. Also, the sharp edges of the glass after a hole has been made are shielded from the user with a Kevlar protection ring (Section 9.4.7)	Yes
TECH-SSR-04	As explained in Section 2.2 there are no new certification regulations in place yet. Therefore this should be assessed with EASA on a case-to-case basis post-DSE.	TBD
TECH-SSR-05	The UAV produces a maximum noise of 50 [dB], as is explained in Section 3.2.	Yes
TECH-SSR-06	The UAV produces a maximum noise of 50 [dB]. However if the UAV flies at an altitude of 90 [m] a noise level of 40 [dB] can be measured, which is required.	Yes

Table 16.2: continued from previous page

Requirement	Verification method	Compliance
TECH-SSR-08	The flight computer is programmed such that an landing is initiated after a LOS of 3 [sec] as is explained in Section 13.4.	Yes
TECH-SSR-09	The usage of 4G for communication ensures a high reliability as is further detailed in Section 14.2.	Yes
TECH-SSR-10	If one physical control system (one rotor) fails the UAV will be able to come back to its original orientation as is explained in Section 13.4.	Yes

16.3. Sensitivity analysis

The sensitivity analysis investigates the sensitivity of a design for a change in major system parameters. This analysis is used to test the robustness of the design. This section will focus on the effect on the range, endurance, and top speed, for a change of two major system parameters: a change in weight and a change in drag.

System sensitivity to weight is relevant since the weight can still change during production (items can turn out to be heavier than anticipated). Additionally, this parameter is relevant if there is a different amount of payload needed than initially designed for (for example fewer flight masks).

Sensitivity for drag is important, since the drag calculation induces some uncertainty, as there has not been a prototype test in a wind tunnel yet. Additionally, it is a relevant dimensional parameter, since an increase in size will translate to an increase in the drag coefficient.

16.3.1. Sensitivity to weight

As mentioned earlier, this section describes what will happen to the top speed, the range, and the endurance for a weight change. It was decided to test the three different outputs for an input of three different weights: 80%, 100% and 120% of the calculated weight from Chapter 15 of 39 [kg] (see Chapter 15).

It is expected that all three outputs will decrease in performance for an increase in weight because a heavier UAV requires more power for hover and flight. The results can be found in Figure 16.1. It can be seen that the range and endurance are inversely correlated with the weight, and the maximum speed approximately remains constant. This is a logical result, as only the acceleration towards the maximum speed changes, while the force equilibrium remains unchanged.

16.3.2. Sensitivity to drag

Similar to the previous subsection, this section describes what will happen to the top speed, the range, and the endurance, for a change in the drag coefficient. Once more, it was decided to test the three different outputs for the input of three different values of the drag coefficient: 80%, 100%, and 120% of the calculated drag coefficient of Figure 10.2.

It is expected that the top speed and the range will decrease in performance for an increasing drag coefficient because higher drag requires more power to fly. However, the endurance is expected to remain unchanged, since the endurance is calculated for the hover phase (for which there is no drag). The results can be found in Figure 16.1. The expectations here are met.
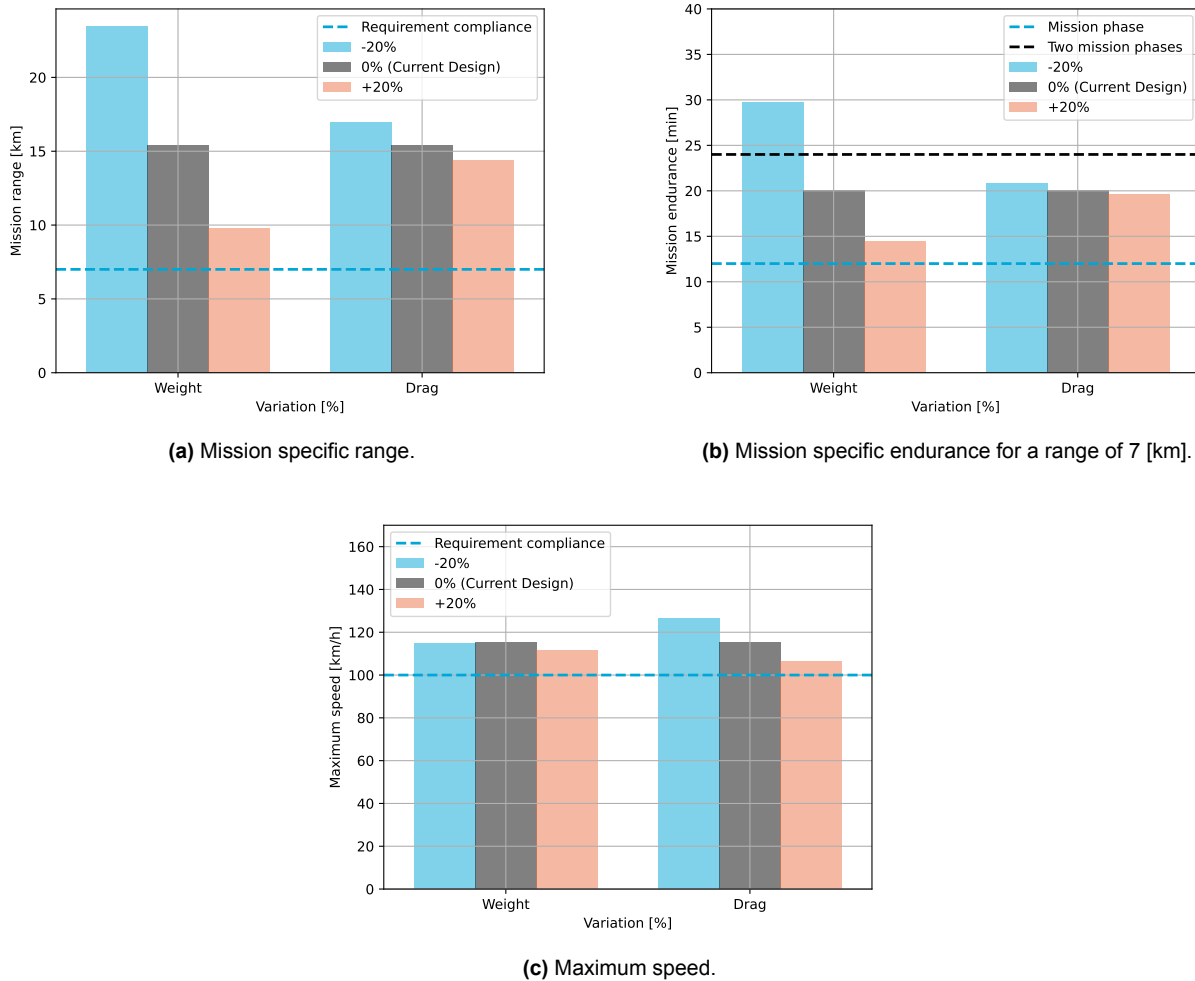
(a) Mission specific range.

(b) Mission specific endurance for a range of 7 [km].

(c) Maximum speed.

Figure 16.1: Performance parameters varied for sensitivity analysis.

To conclude this section, the performance is affected by weight and drag. However, a change in these parameters will not lead to an unfeasible design, within the limits examined here. The possibility to add a second mission phase, where the UAV is resupplied with masks, can be investigated in later stages of the design. If the weight turns out favorable there is enough endurance for two mission phases as can be seen in Figure 16.1b.

16.4. Validation Procedures

In future design phases, it will be important to validate the methods used in the design process, as well as the design itself. This section aims to give an overview of what tests need to be done to fully validate the system.

- **Structural tests**: These tests can take multiple shapes. Firstly, simple structures can be tested to get data, that can subsequently be used to validate the code that was used to analyze the structure. Secondly, manufactured parts can undergo acceptance testing to confirm the analysis.
- **Thermal tests**: As the mission being designed for requires the UAV to withstand high temperatures, it is important to validate the resistance against heat. This can be done both on sub-assemblies and the UAV as a whole.
- **Electrical tests**: By breadboarding the system first, it can be checked if the determined power consumption is correct. Furthermore, these tests should be used to check for faulty wiring.
- **CFD analysis**: Although a preliminary analysis has been performed for the drag it is important to validate these results with a CFD analysis of the whole system.

- **Wind tunnel tests**: In addition to the previous point, wind tunnel tests will tell a great deal about the system. The drag and CFD analysis can be validated. Furthermore, noise quantification can be done more accurately. Lastly, it can serve to validate the results gained from XRotor.
- **Mission tests**: These tests include the opening of the payload bay, glass cutting, and release of the payload.
- **Flight tests**: Taking flight will help validate the performance characteristics calculated. It can also test the collision avoidance and navigation systems.

17 Risk Analysis

The development and operation of a product are always accompanied by risks, among which the technical risks are the most worthy of attention. They refer to potential failures of performance that could happen in any systems or components of the product and may result in catastrophic consequences without paid attention to. Therefore, it is of necessity to apply risk management, which aims to determine, assess, and further mitigate potential risks in advance to minimize their negative impact on the product. This is done by performing the RAMS analysis to provide a general overview of all possible failure modes which may influence or generate new requirements for the design. Some of these failure modes can be generally prevented by applying redundant design or regular maintenance. Meanwhile, there exist some failures more difficult to predict and deal with. They are defined as technical risks in system levels and need to be mitigated.

Therefore, this chapter is divided into two parts, respectively discussing the RAMS analysis in Section 17.1 and technical risk analysis in Section 17.2. Five aspects of the RAMS analysis are given from Section 17.1.1 to Section 17.1.5, after which a list of technical risks are identified and evaluated in Section 17.2.1, before mitigated in Section 17.2.2.

17.1. RAMS Analysis
The RAMS analysis refers to a combination of the Reliability, Availability, Maintainability, and Safety characteristics, which investigate with what philosophies the drone is designed. The process of RAMS analysis includes five aspects, which are safety-critical functions (SCF) as a starting point, the redundancy philosophy and the maintenance plan as measures to deal with SCF, and finally the expected reliability and availability as a result of these two applied measures. They will be discussed step by step in the following sections.

17.1.1. Safety critical functions
As a start of the RAMS analysis, the safety-critical functions are defined, which may result in injury or death of humans, damage of the drone or the environmental damage, or increased severity of the fire case. After considering all possibilities that the drone can fail due to internal or external reasons, the safety-critical functions are identified as follows:

- SCF-01: Start-up systems
- SCF-02: Power supply and batteries
- SCF-03: Propulsion system
- SCF-04: Control and communication
- SCF-05: Sensors and electronics
- SCF-06: Visual and audible warning system
- SCF-07: Payload and cutting mechanism
- SCF-08: Landing gear and adhesion
- SCF-09: Load carrying structures
- SCF-10: Thermal control

These defined safety-critical functions above are important aspects to be paid attention to during the design. To investigate the effect of a critical failure happening, a failure tree has been made in an operational order based on the functional flow diagram displayed in Section 5.1. This can be seen in Figure 17.1. It allowed identifying the safety-critical functions, to prevent the drone from causing damage to buildings and people, and to perform its mission safely. The redundancy philosophy and maintenance plan are then discussed in the next two sections.
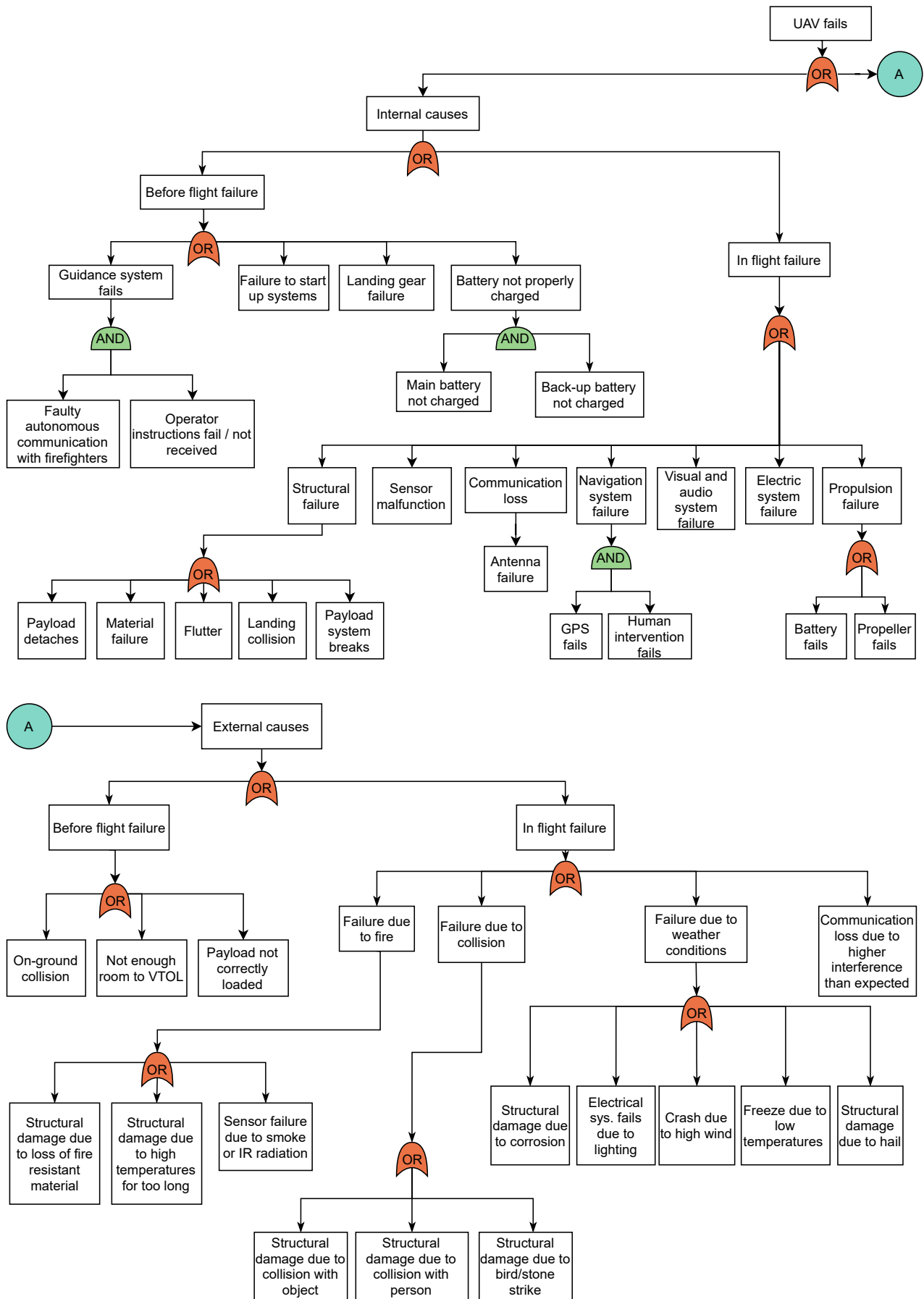
Figure 17.1: The failure tree that allows to identify the safety critical functions.

17.1.2. Redundancy philosophy

Redundancy in designing is of great importance, especially if the product has to operate in harsh environments and is of life-saving importance, as is the case for this drone. It is required that the failure of one component does not necessarily lead to the failure of the entire mission. The application of the redundant strength, for example, is a typical method for structural design. In addition, there exist two more redundancy philosophies, which are hardware redundancy and information redundancy[60]. More details of these redundancy philosophies are given below.

- **Strength redundancy**
  The strength redundancy is commonly applied in structural design. To be more specific, a safety factor of 1.5 is multiplied by all the physical loads when designing the structural strength of every load-carrying component, including the landing gear, the cutting mechanism, and the suction cups, as mentioned in Section 12.1. Thus, the structure of the drone is intentionally built much stronger than required, offering it a capability against emergencies, unexpected loads and shocks, or degradation over its lifetime.

- **Hardware redundancy**
  It refers to the application of extra hardware to make sure that the effects of a failed component are limited[60]. For subsystems that allow for multiple components, hardware redundancy is applicable, such as sensors, LEDs, and batteries. Additionally, the number of rotors also adds to the hardware redundancy, since if one propeller arm breaks or propeller stops functioning, the drone can still have a possibility of being controlled or performing an emergency landing.

- **Information redundancy**
  This refers to the repetition of measurement or data transmission multiple times so that different data points can be compared[61], which is important for control and communication of the drone as well as distance detection by sensors. When designing the drone, the information redundancy is incorporated by relaying information multiple times with a relatively high frequency, to provide higher accuracy of information transmission.

Table 17.1 then provides a match of these redundancy philosophies with their corresponding safety-critical functions defined in Section 17.1.1. One safety-critical function can be applied to multiple redundancy philosophies.

Table 17.1: A match between redundancy philosophies and safety critical functions

Redundancy philosophy	Related safety critical functions
Strength redundancy	SCF-07, SCF-08, SCF-09, SCF-10
Hardware redundancy	SCF-02, SCF-03, SCF-05, SCF-06, SCF-07
Information redundancy	SCF-01, SCF-04, SCF-05

17.1.3. Maintenance plan

After the drone is put into operation, it is important to properly maintain it to ensure each component can work as expected so that the required lifetime of the whole drone can be met, especially for such a life-saving drone that works in harsh environments. Due to limited sources for drone manufacturing and maintenance, the maintenance plan in this project is based on those used by airliners but adapted to the actual situation of a drone. For scheduled maintenance, there are five typical checks with different intervals and focuses, which are line maintenance, A-, B-, C- and D-check[62]. C-check is discarded since line maintenance, A- and B-check already cover all necessary checks of the drone, while D-check is needed at the drone's end of life. The remaining four types of maintenance are demonstrated below.

Maintenance name	Line maintenance (LM)
Interval	After every flight
Expected duration	1 man hour
Executed by	Firefighter with minimal training
Description	• Visual check of structure, e.g. cracks, plastic deformations. • Visual check of the propellers, e.g. cracks, rotational speed. • Visual check and test of payload deployment and cutting mechanism, e.g. deformations, clamp tightness, gas leakage. • Clean and dry the drone from any dust, rain, soot, dirt etc. • Reload drone with new payload or check whether the payload that has not been used yet can be used again.

Maintenance name	A-check
Interval	Every month
Expected duration	8 man hours
Executed by	Firefighter with short training
Description	• Check battery status, power level, energy storage and recharging. • Check landing gear deployment and status of the rotation mechanism. • Check adhesion mechanism, including the suction cups, vacuum tubes and vacuum pump. • Check cutting mechanism, including force direction, force magnitude, gas transport and leakage. • Check visual and audio warning systems by manually turning them on. • Add lubrication to rotating/moving elements.

Maintenance name	B-check
Interval	Every year
Expected duration	24 man hours
Executed by	Employee of UAV company can execute maintenance at the fire brigade
Description	• Check power supply systems, e.g. check voltage, current and power distribution. • Check propulsion system, e.g. their thrust capacity and direction. • Perform non-destructive testing to verify the material integrity, e.g. Liquid penetrant Testing, acoustic emission testing, infrared testing etc[1]. Focus of the non-destructive testing is primarily aimed at load-carrying critical components.

Maintenance name	D-check
Interval	After ten years (end of life of the UAV)
Expected duration	100 man hours
Executed by	Employee of UAV company at the company
Description	As the structure needs to be reused in another drone at the end of life of the UAV, it needs to be thoroughly tested. For this non-destructive testing will be used, similarly to the methods described in the B-check. However this check will be performed more thoroughly and on all structural elements, even if they are not critical ones.

Apart from scheduled maintenance, arrangement of unscheduled maintenance is important as well, as damage may accidentally occur during the mission. The severity of the damage can be roughly

---

[1]https://www.twi-global.com/technical-knowledge/faqs/what-is-non-destructive-testing#MethodsofNonDestructiveTesting, Retrieved on 18/06/2021

divided into three types, which are minor damage, moderate damage, and serious damage. Minor damage is defined such that the maintenance can be finished quickly with portable tools and spare parts, such as a screwdriver. In this case, the drone can return to operation after the maintenance. If the unexpected damage is found that the disassembly is necessary, or the spare part is non-portable, it is then regarded as moderate damage and applies to type-II maintenance. The last type refers to special damage, which is not necessarily more severe than moderate damage but requires external assistance for maintenance. For instance, if the main body is seriously deformed or destroyed, the fire brigade then needs to ask for reproduction from the manufacturer. More details about these three types of maintenance are then given below.

Maintenance type	Type-I
Damage severity	Minor: portable and quick maintenance
Executed by	Accompanying maintenance personnel during the mission
Responsible for	• Replacement of propellers, suction cups, flight masks.
	• Dealing with lubricant, loose screws and adhesives.

Maintenance type	Type-II
Damage severity	Moderate: disassembly-needed or non-portable maintenance
Executed by	Fire brigade maintenance center
Responsible for	• Power and propulsion: batteries, motors
	• Electronics: ESC, sensors, camera, speaker
	• Simple structures: landing gear struts, propeller arms

Maintenance type	Type-III
Damage severity	Special: external assistance required
Executed by	Manufacturer or supplier
Responsible for	• Adhesion system: vacuum pump and tubes
	• Cutting mechanism: actuator, gas tank, cutting tools
	• Complicated structures: main body, integration parts

17.1.4. Expected reliability

Reliability refers to the amount of time the product can perform its functions as expected. Such a property has multiple methods for interpretation, among which there are two metrics used frequently. The first one is expressed in terms of the failure probability or failure rate. For instance, current research has verified that the failure rate for typical drones is 10^{-3} per flight hour[63]. The other commonly used metric is the Mean Time Between Failures (MTBF), which provides an expectation of the effective operation time of the product.

According to the maintenance plan in Section 17.1.3, the overall reliability of the drone is expected to be at least one month. However, in reality, it is strongly dependent on the reliability of the single components used. For example, one individual component that contributes greatly to the reliability of the overall drone is the battery. It is found that the chosen batteries have a guaranteed life of 150 charging cycles[2], which indicates the MTBF is at least 150 flight hours, but possibly insufficient for a one-month operation. Besides, the drone designed in this project is equipped with several special systems, i.e. cutting mechanism and adhesion system, the actual reliability is difficult to accurately quantify. Due to the installation of these systems, as well as the requirements of a relatively large payload and thermal control, the structure of the drone is more complicated than a conventional drone and even increases the difficulty to estimate the reliability. Therefore, tests are suggested to be conducted to determine the reliability of these systems and the drone structure.

---

[2]`https://www.genstattu.com/ta25c230006s1phvas150.html/`, Retrieved on 16/06/2021

17.1.5. Expected availability

A clear understanding of the availability of the drone is of importance since it is designed to deal with emergencies that can occur at any time. A higher availability, or to be more specific, the less time and effort required to put it into use, is more desired. A typical formula for calculating the availability of a system is given by[3],

$$A = \frac{Uptime}{Uptime + Downtime} \tag{17.1}$$

which describes the ratio of the effective time to a complete operational cycle of the system. In this project, the availability of a drone is mainly analyzed based on the following three aspects: availability on the market, availability during one mission, and availability of consecutive missions. Thus, the three aspects of the availability of the drone will be evaluated by this equation as follows.

Availability on the market

The availability of the drone on the market relates to the required time interval which the product takes to be on sale. Therefore, the downtime, in this case, is the summation of manufacturing time, transportation time, and some buffer time reserved for others such as certification. The manufacturing time including parts production and assembly is roughly estimated as 6 months. The transportation time from the workshop to the market can vary significantly, depending on the location and the vehicle types, thus a rough estimation is given considering the shipping time from the U.S. to the Netherlands is 8 days[4]. With a buffer time of 1 month, a total downtime of 7.5 months is given, while the uptime is the expected lifetime, i.e. 10 years. Thus, the availability on the market is,

$$A_1 = \frac{10 \cdot 12}{10 \cdot 12 + 7.5} = 94.1\% \tag{17.2}$$

Availability in one mission

As explained in the functional analysis in Chapter 5, each mission can be simply divided into four phases, which are cruising from the station emergency site, performing first delivery, reloading the drone with replaced batteries and payload, and performing second delivery if necessary. Their required time length are summarised in Table 17.2.

Table 17.2: Required time length of each activity involved in one mission.

Activity	Cruise	First delivery	Reloading	Second delivery
Required time [s]	300	480	180	960

The downtime in this case is the summation of cruise time and reloading time. Thus the availability is,

$$A_2 = \frac{480 + 960}{300 + 480 + 180 + 960} = 75\% \tag{17.3}$$

Availability for consecutive missions

Finally, how quickly the drone can be put into the next mission is of interest as well. This is dominantly dependent on the line maintenance time explained in Section 17.1.3, which specifies 1-hour maintenance after every flight. Even though the batteries require an hour to fully recharge, since the batteries are removable, recharging can be done simultaneously during the line maintenance, which results in a necessary downtime between two consecutive missions equal to 1 hour. Thus, considering the mission time in Table 17.2, the availability for consecutive missions is,

$$A_3 = \frac{300 + 480 + 180 + 960}{300 + 480 + 180 + 960 + 1 \cdot 3600} = 34.8\% \tag{17.4}$$

---

[3]https://www.fiixsoftware.com/how-do-maintainability-and-reliability-affect-availability/, Retrieved on 16 June 2021

[4]https://www.icontainers.com/us/2017/04/25/us-to-netherlands-shipping-times/, Retrieved on 16 June 2021

which is significantly lower than the values obtained previously, due to a relatively long time of line maintenance. However, it is understandable since an emergency drone deserves more effort on maintenance to ensure its reliability. In addition, the drone is expected to deal with emergencies rather than commercial usage, which means the drone is not designed for continuous and extensive operations. Therefore, the availability for consecutive missions only provides a theoretical fraction of the effective operation time and is less significant compared with the previous ones.

17.2. Technical Risk Management

The technical risks management is then performed by considering the technical risks inspired by the RAMS analysis. It includes the identification of risks based on the safety-critical functions in Section 17.1.1 and the corresponding evaluation in terms of likelihood of occurrence as well as the seriousness of consequence. As two significant factors, both likelihood and consequence will be respectively classified into five levels as interpreted in Table 17.3 and Table 17.4.

Table 17.3: The scoring of likelihood

Score	Likelihood	Customized detail
1	Improbable	Almost inconceivable to occur
2	Remote	Unlikely to occur or may occur after a large number of operations
3	Occasional	Likely to occur sometimes
4	Probable	Likely to occur in most missions
5	Frequent	Can occur one or multiple times at every flight

Table 17.4: The scoring of consequence

Score	Consequence	Customised detail
1	Negligible	Almost no effect on the product performance
2	Minor	Slightly influenced but still able to complete the mission
3	Moderate	A significant delay in time or rise in cost required
4	Critical	Unable to complete the mission
5	Catastrophic	Counterproductive to the mission or causing injuries

Please note that the likelihood, however, is desired to be quantitatively evaluated concerning the MTBF or failure probability of each involved subsystem. Since the entire system consists of several unconventional subsystems, the drone is much more complicated than a normal one. Thus, the likelihoods of these risks are qualitatively assessed by estimation.

Based on these tables, risks are divided into three levels concerning both the likelihood and consequence, as shown in Figure 17.2. Risks in the red region are considered unacceptable risks which have a significantly negative impact on the mission, thus necessary to be researched and mitigated. The orange region refers to undesirable risks that can have a moderate effect on the mission and require mitigation as well. The difference between them is that unacceptable risks need multiple mitigation measures to decrease to the acceptable level, while the mitigation for undesirable risks is relatively simpler. Lastly, the acceptable risks are those in the green region having negligible or acceptable influences on the mission from a statistical perspective and are decided to be observed during the operation. Especially, for acceptable risks labeled with an asterisk (G^*), they are defined as emergencies, while those labeled with a number sign ($G^{\#}$) are defined as an additional cost, and several measures will be applied to them as well. More details will be discussed in Section 17.2.2.

Figure 17.2: The ranking of technical risks are determined by dividing them into three main levels. Some of the green risks (G^*, $G^\#$) are treated differently.

17.2.1. Risk Identification and Evaluation

Table 17.5 provides a summary of the technical risks that may happen to the product in its future operation. All risks are given two scores for their likelihood and consequence respectively.

Table 17.5: Technical risks identification and evaluation.

Risk-ID	Risk Identification and Evaluation (with scores in brackets)
RSK-01	**The remaining energy storage is found to be insufficient to finish the mission.**
	Likelihood: (2) This could happen if the actual mission time exceeds the planned time.
	Consequence: (3) The mission has to pause until the drone is recharged.
RSK-02	**One of the rotors or propellers fails and loses its thrust during flight.**
	Likelihood: (3) Propulsion units may fail by disturbance from glass slags, small debris or other external objects, due to the complexity of the fire case.
	Consequence: (3) The failure of rotors can cause moderate effect since it takes time to react to such an emergency, and the pilot needs to analyse if this drone can still continue the mission.
RSK-03	**Short circuiting occurs among electronics.**
	Likelihood: (2) This may happen since the power supply of the drone is completely based on electricity.
	Consequence: (4) The consequence varies from losing the functionality of only a sub-system, to the whole system losing power and dropping. In general, a consequence of 4 is determined.
RSK-04	**The signal received or transmitted by the drone is interfered by external sources.**
	Likelihood: (3) Application of radio waves or electromagnetic waves by other devices is common in real life.
	Consequence: (3) The exchange of information between the drone and control center will be delayed or needs to be repeated multiple times.
RSK-05	**Altitude or horizontal distance detection fails.**
	Likelihood: (2) Even though a large number of sensors will be used, the probability of a system failure is not 1 as the fire might complicate the measuring.
	Consequence: (5) An autonomous drone losing its detection on objects or people is extremely dangerous to the public.
RSK-06	**Visual warning system fails.**
	Likelihood: (3) Small components such as LEDs may fail in an extreme environment like a fire case.
	Consequence: (2) The drone may need to slow down so that people nearby can notice the drone more easily.
RSK-07	**The recipient does not know how to use the payload.**
	Likelihood: (3) This may happen since most people are not familiar with flight masks.
	Consequence: (4) The recipient cannot be saved.
RSK-08	**The payload gets released during flight by accident.**

Table 17.5 – continued from previous page

Risk-ID	Risk Identification and Evaluation (with scores in brackets)
	Likelihood: (1) This might happen if the drone experiences serious external impact, or both the door and hook and loop fastener.
	Consequence: (5) The free-falling payload may hurt people on the ground.
RSK-09	**The suction system fails to adhere to the building.**
	Likelihood: (3) This can happen when the building wall is made of rough materials such as bricks.
	Consequence: (4) The payload cannot be reached by the recipient as planned.
RSK-10	**The suction system suddenly loses grip.**
	Likelihood: (2) This could happen if the vacuum pump fails or three of the suction cups lose functionality.
	Consequence: (5) The drone starts dropping and may hurt people on the ground.
RSK-11	**The temperature experienced by the drone or any systems of the drone exceeds the design limit.**
	Likelihood: (2) This may happen due to prolonged exposure to high temperatures or a local failure on the thermal coating. However, the drone normally operates outside the building where the temperature is much lower than inside, thus this risk will seldom happen.
	Consequence: (5) The drone may lose some of its functionality or even fall apart during the mission.
RSK-12	**The glass shard after cutting falls from the window and drops outside the building.**
	Likelihood: (2) Normally the glass shard will fall into the building due to the pushing force of the cutting mechanism. However, this could happen if the glass shard breaks into several pieces.
	Consequence: (5) The glass shard may hurt people on the ground.
RSK-13	**The drone experiences strong air turbulence.**
	Likelihood: (4) The Netherlands is a coastal country where sea wind usually occur.
	Consequence: (3) The drone requires extra time or extra power to remain on the flight path.
RSK-14	**Noise generated during operation exceeds the maximum level in the requirements.**
	Likelihood: (2) The noise generated by the drone (50 [dB]) is higher than the night limit but lower than the day limit. Since high-rise buildings usually open in the daytime, the number of night missions is significantly lower.
	Consequence: (3) The noise is still lower than the dangerous level. It may annoy people nearby, but does no harm.
RSK-15	**The drone gets impacted or attacked by birds.**
	Likelihood: (1) Normally birds will fly away when the UAV approaches, while aggressive birds such as seagulls or eagles might attack the drone.
	Consequence: (5) Bird impact may destroy the structure or propulsion of the drone especially when the drone flies at high speed, resulting in the dropping of the drone.

17.2.2. Risk Mitigation and Additional Measures

As mentioned previously, the effect of unacceptable and undesirable risks on the mission will be reduced to an acceptable extent, by applying mitigation measures. For unacceptable risks, the mitigation is found to reduce both the likelihood and the consequence, thus multiple measures can be applied. For undesirable risks, considering that mitigation also increases the cost of the mission, the measure can be reducing either the likelihood or the consequence, depending on the feasibility and price.

For a risk defined as emergencies in the region G, an emergency plan will be given if such a risk occurs. The difference between a mitigation measure and an emergency plan is that the former is

usually done in advance to decrease the likelihood or consequence of the risk, while the latter works as a remedy to deal with the situation after the emergency happens. As for risk in the region $G^{\#}$, it is regarded as an additional cost, and no specific measures will be applied. These measures are listed below.

- **RSK-01: The remaining energy storage is found not enough to perform the rest tasks.**
  Emergency plan: Always reserve sufficient energy so that the drone can automatically return if it happens at cruise. Besides, firefighters can bring portable recharging devices or extra replacement batteries to the scene in case that this risk happens when delivering the payload.
- **RSK-02: One of the rotors or propellers fails and loses its thrust during flight.**
  Mitigation: The likelihood can be decreased from 3 to 2 by performing regular NDT for engines, propellers, shafts, and power transmission. It can be further reduced by developing and updating the system for small disturbance detection and avoidance if the technology is available. Setting up a quick response command for the drone can decrease the consequence from 3 to 2, such as emergency landing or moving c.g. to a location where the drone can easily stay stable with the remaining rotors.
- **RSK-03: Short-circuiting occurs among electronics.**
  Mitigation: As part of the maintenance, regular checks for insulation are necessary. The consequence may be reduced by applying a backup energy supply for important systems. Reduction in likelihood is not discussed since it requires further research on technologies regarding electrical engineering.
- **RSK-04: The signal received or transmitted by the drone is interfered with by external sources.**
  Mitigation: Applying uncommon signals, such as a different frequency region, can decrease the likelihood from 3 to 2 since it becomes more difficult to interfere. To reduce the consequence from 3 to 2, multiple communication measures can be applied in parallel so that the system can switch the communication measures when one of them gets interfered with.
- **RSK-05: Altitude or horizontal distance detection fails.**
  Mitigation: The likelihood of entire system failure can be reduced significantly by applying multiple sensors, leading to a score of 1 after mitigation. The consequence also goes from 5 to 4 by setting up a response command such that the drone will perform an emergency landing at a low descending rate, to prevent the drone from rampaging and hurting people.
- **RSK-06: Audible or visual warning systems fail.**
  Additional cost: The speaker and LEDs will be equipped in a way such that they are easy to be repaired or replaced. Always prepare sufficient spare parts.
- **RSK-07: The recipient does not know how to use the payload.**
  Mitigation: To reduce the likelihood, the drone will prepare a manual in multiple languages and deliver it together with the payload. The control center can also use the transceiver to contact the recipient and provide more instructions. However, there is no way to decrease the consequence.
- **RSK-08: The payload gets released during flight by accident.**
  Mitigation: The maintenance plan will include regular checks for the release door and payload clamp. The consequence can be reduced from 5 to 4 by applying a backup method to prevent sudden dropping, such as a chain tied on the payload.
- **RSK-09: The suction system fails to adhere to the building.**
  Mitigation: Collect the information of those potential target buildings in advance, and identify which part of the building allows the drone to adhere. The likelihood is then reduced from 3 to 2. However, the consequence remains the same since when it happens, the drone has to release the payload somewhere outside the building and wait for the fire brigade.
- **RSK-10: The suction system suddenly loses grip.**
  Mitigation: To reduce the likelihood from 3 to 2, the drone is expected to be equipped with a grip test mechanism, so that when one side of the suction cups adheres to the building, the drone can test the suction functionality, before it starts to decrease the lift and rotate downwards. The consequence is reduced by setting up an emergency response command such that the drone can quickly retrieve propulsion to avoid free falling. Since in this case, the drone is unable to

continue on the mission, a score of 4 has to be reserved.

- **RSK-11: The temperature experienced by the drone or any system exceeds the limit.**
Mitigation: The likelihood decreases 2 to 1 by applying conservative design and setting up a design temperature limit that has an acceptable margin against the ultimate limit of the material. The likelihood can be further decreased by investigating and applying new materials with low thermal conductivity and strong thermal shock resistance. To decrease the consequence from 5 to 4, the drone will continuously detect the internal temperature of each component of the drone. If the design limit is reached, the drone should suspend the mission and perform an emergency landing.
- **RSK-12: The glass shard falls from the window and drops outside the building.**
Mitigation: This risk is unpredictable and difficult to mitigate at this stage, thus further research is required to deal with such a risk. It is also recommended to perform tests to see if one can prevent the glass from breaking during cutting, such as adjusting the cutting force magnitude or direction.
- **RSK-13: The drone experiences strong air turbulence.**
Mitigation: Increase the gust resistance level if the drone is designed to be used in coastal countries, thus the likelihood can be reduced by one level, thus from 4 to 3. Besides, the design reserves additional power and thrust-to-weight ratio for gust resistance, which decreases the consequence from 3 to 2.
- **RSK-14: Noise generated exceeds the maximum level in the requirements.**
Emergency plan: The drone can slow down to keep the noise within the limit, or choose a path away from residential areas in case of a night mission.
- **RSK-15: The drone gets impacted or attacked by birds.**
Mitigation: The flight path can be chosen to be away from those areas where flocks of birds gather. Furthermore, the consequence can be decreased from 5 to 3 by letting the drone quickly descend or leave the area when birds are detected in proximity. The drone can still perform the mission, though the change in the flight path may result in a delay.

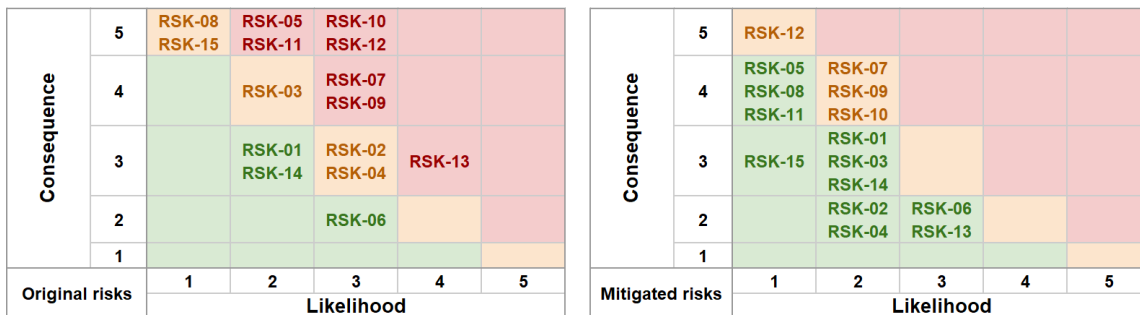The risk maps before and after mitigation are shown in Figure 17.3.

Figure 17.3: Risk maps before and after mitigation.

It can be seen that most risks are now located in the acceptable region, except for RSK-07, RSK-09, RSK-10, and RSK-12 which have limited available mitigation measures. The reasons are previously discussed together with their mitigation measures. It is suggested to keep observing and applying other technologies to decrease these three risks in future development.

18 Production Plan

After the design has been finalized, a practical product can be made. To do this, a plan needs to be made to manufacture the UAV, which illustrates the methods involved for part manufacturing and assembly and will be discussed in this chapter. First, a general production flow chart will be given in Section 18.1. Secondly, the manufacturing (Section 18.2) and assembly methods (Section 18.3) will be discussed. Finally, the integration of the separate parts will be shown in Section 18.4.

18.1. General Production Plan

The UAV consists of a great number of components and parts. To indicate the manufacturing and assembly process, a flowchart has been made starting from the end design phase and can be found in Figure 18.1.
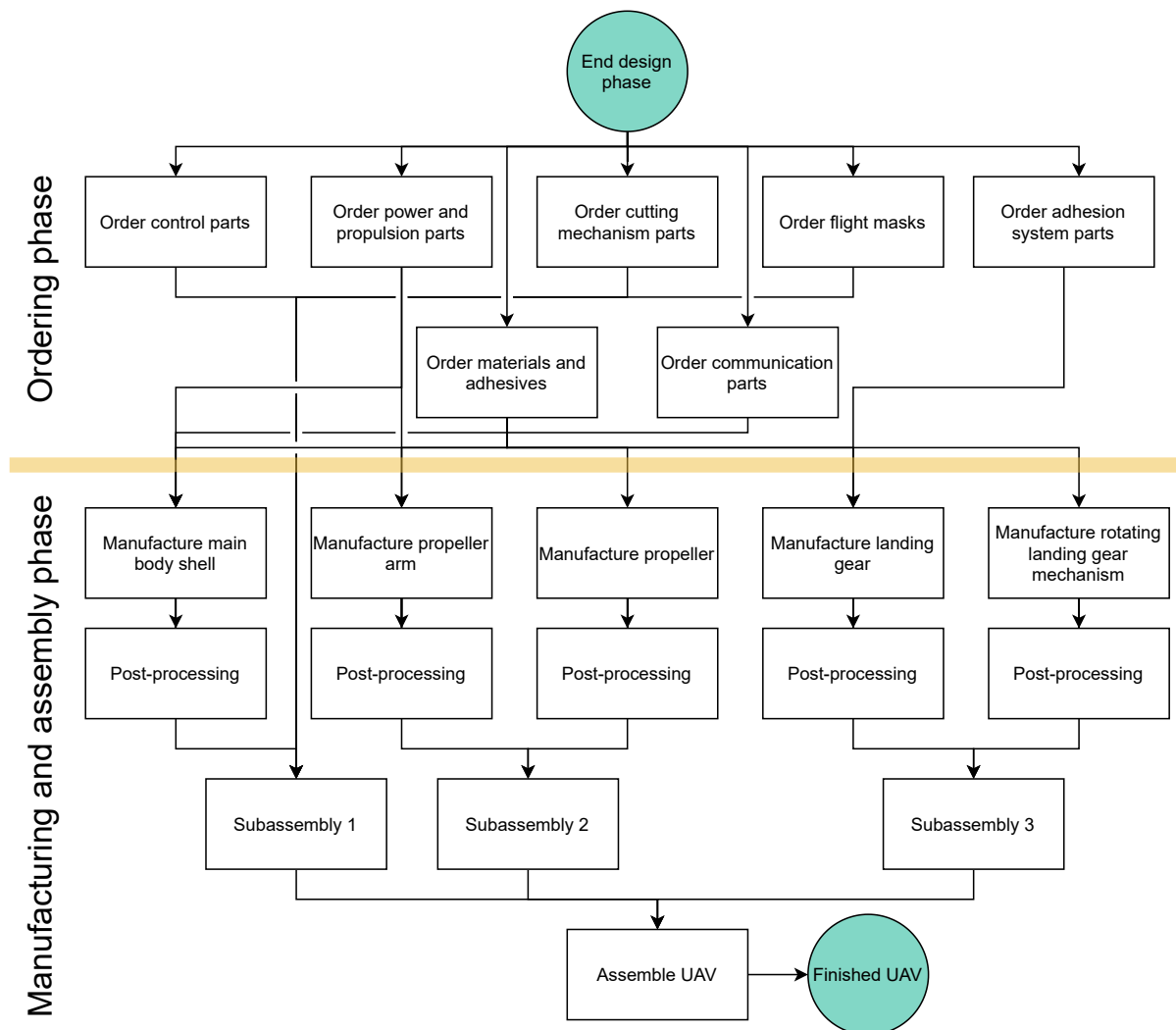

Figure 18.1: Flowchart describing the manufacturing and assembly order.

The creation of the UAV consists of two phases: the ordering phase and the manufacturing & assembly phase. In the former, the parts and materials will be ordered from suppliers. It is important to account for the difference in delivery times of the components. The second phase consists of manufacturing as well as post-processing of the individual parts. Thereafter sub-assemblies can be made for systems or subsystems, which in turn can be finally assembled to create a complete UAV.

18.2. Manufacturing Methods

This section will elaborate upon the methods used for manufacturing the parts. It is divided into several categories for different materials: Thermal barrier coating, carbon fiber with epoxy, and aluminum.

18.2.1. Thermal Barrier Coating

A ceramic mat will be used as TBC and will be purchased[34]. As a further process, the ceramic mat will be hardened by adding rigidiser and rolling it into the mat using a paint roller. This is a necessary process for the application of the TBC, as a non-hardened ceramic mat is very susceptible to erosion

and mechanical damage[34].

Thereafter, the TBC needs to be bonded to the CFRP. To do this the epoxy of the CFRP will be used to bond the two materials together. This will be done in an autoclave so that the bonding happens under pressure, which causes strong bonds without voids as can be seen in Figure 18.2[34].
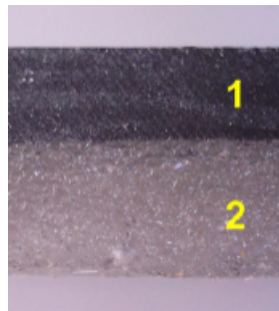
Figure 18.2: Adhesion between the CFRP (1) and the TBC (2)[34].

18.2.2. Carbon fiber With Epoxy

As explained in Table 11.1, the CFRP will be used in a woven prepreg form. The shapes can be made by hand lay-up, whereafter they will be cured together with the TBC in an autoclave. A flexible bag is put on top of the part so that the bag is drawn to the laminate under an applied pressure of around 0.55 [MPa]. This results in enhanced densification.

When using this method the economic batch size (units) is between 1 and 500, which is a suitable range for the application of this UAV. Additionally, this method of manufacturing has a high labor intensity, which means less labor cost. Even though the relative cost index per unit is largely dependent on the complexity of the mold, as the majority of the shapes are simple geometric shapes, the total cost can stay relatively low.

From a sustainability perspective, it is beneficial that the curing process takes place within the autoclave which is closed off from the environment. The vacuum enables the extraction of solvents in an efficient manner. Additionally, the material utilization fraction of this method is relatively high: between 0.8 and 0.95[11].

18.2.3. Aluminum

The aluminum parts are made by additive manufacturing (AM). This manufacturing method is chosen because:

- Custom products can be made.
- As complex products can be made, the number of assembly points can be greatly reduced[1], which can also decrease cost[2].
- The speed, adaptability, and versatility of AM enables the manufacturer to reduce the response time[64].

It is worth noting that AM also has its limitations. For example, the maximum printing size is limited by the printer, complex printers can become expensive[3], and only a limited number of metals can be applied to this method[4]. Nevertheless, the advantages are deemed overwhelming. To solve the problem, the limiting size can be taken into account while deciding the assembly points. Besides,

---

[1]`https://www.horizontechnology.biz/blog/advantages-and-disadvantages-of-additive-manufacturing-process-vs-powder-metallurgy`, Retrieved on 11/06/2021

[2]`https://beamler.com/what-are-the-advantages-of-metal-3d-printing/`, Retrieved on 11/06/2021

[3]`https://www.horizontechnology.biz/blog/advantages-and-disadvantages-of-additive-manufacturing-process-vs-powder-metallurgy`, Retrieved on 11/06/2021

[4]`https://www.3deo.co/metal-3d-printing/pros-cons-3d-printing-metal-components/`, Retrieved on 11/06/2021

AM is found to be applicable for aluminum[11]. Therefore, this method is valid and will be used for manufacturing parts made of aluminum.

The chosen type of aluminum can be used in either of the following AM processes: laminated object manufacture, ultrasonic consolidation, and selective laser melting. The latter of the three is chosen, as it requires less complex machine parts and it is not required to make supports for the printed product[11]. The printer to be used is the SLM 800 printer of SLM solutions, which has a building volume of 500x280x850 [mm][5].

As the product is built up layer by layer, surface finishing is needed to smooth out the surfaces to improve the durability of the part. First, the surface will be cleaned, as proper cleaning will increase the quality of the surface finish by 50 [%][6]. This will be done by sanding. However, some places are hard to reach, for these areas bead blasting will be used. This method is less time-consuming than sanding, but it should be executed with care. As the method relies on shooting small thermoplastic beats onto the surface, the pressure should be increased gradually not to blast away the product[7].

Concerning sustainability additive manufacturing is a good option, as there is less material waste in additive manufacturing relative to other manufacturing methods which results in a smaller CO_2-footprint[8]. This also results in less required energy, as less material is used and some production process steps are eliminated with respect to other manufacturing methods[9].

18.3. Assembly Methods

To join the parts together, assembly methods have to be investigated. Two methods will be used for adhesion: Adhesive bonding and bolts. Adhesive bonding is beneficial as it seals the joint, works well with thin structures, has relatively lightweight and there are no holes necessary that weaken the adherents. However, one of the main disadvantages of adhesive bonding is the fact that the process is irreversible (or it results in damage to the adherents)[65]. This contradicts the requirement which states that the UAV is modular. Therefore, the connection of the propeller arms and landing gear to the main body will be done using bolts, so that if one part breaks it can be substituted by another one, hence increasing modularity.

Adhesive bonding

The adhesive will be used to glue CFRP parts to each other or a CFRP part to an aluminum part. Therefore, it is important that the glue can withstand high temperatures, as aluminum has a relatively high thermal conductivity compared with CFRP. However, it is not required to go up to 300 [°C] as it will still be partially shielded by the TBC. Thus, a glue-based on bismaleimide (BMI) will be used, which has to be toughened as only BMI will result in a brittle adhesion[66]. Therefore, Hex-Bond HP655 is used, which is an adhesive film based on a hardened BMI that can withstand temperatures up to 240 [°C] for prolonged periods of time[10]. Before the adhesive film can be applied, the surfaces of the adherents need to be prepared. Therefore the CFRP should be degreased and mildly abraded. A frequently used method for preparing aluminum parts is first degreasing the material and then acid etching. This is often done using chromic/sulphuric acid[65]. The parts should be added to a bath of water, sulphuric acid, and chromium trioxide (or sodium dichromate) with a temperature between 60-65 [°C], for 30 minutes. The final part of the preparation for bonding is rinsing the part and drying it. Within 8 hours after the pretreatment, the bonding should take place[11].

---

[5] https://www.slm-solutions.com/products-and-solutions/machines/slm-800/, Retrieved on 10/06/2021

[6] https://www.additivemanufacturing.media/articles/3d-printing-with-postprocessing-in-mind, Retrieved on 10/06/2021

[7] https://www.sharrettsplating.com/blog/guide-surface-finishing-3d-printed-parts/, Retrieved on 10/06/2021

[8] https://www.dimanex.com/2019/06/03/3d-printing-and-sustainability-less-waste-and-carbon-emissions-from-miles-travelled/, Retrieved on 03/06/2021

[9] https://www.cmtc.com/blog/benefits-of-additive-manufacturing, Retrieved on 03/06/2021

[10] https://www.hexcel.com/user_area/content_media/raw/HexBond_HP655_DataSheet_eu.pdf, Retrieved on 03/06/2021

[11] https://www.hexcel.com/user_area/content_media/raw/Adhesive_Bonding_Technology.pdf, Retrieved on 03/06/2021

Bolts

Bolts will be used to adhere the propeller arms and the landing gear to the main body to increase modularity. A disadvantage of bolts is, however, that it weakens the material as holes need to be made in them, causing stress concentrations[65]. Additionally, it is not desired to make holes through the TBC, as this might damage the ceramic mat and will create a thermal gateway as the bolt will transport the heat inside. To partially solve this Big-Head bolts from Big-Head Bonding Fasteners Ltd. will be used[12]. These bolts can be glued to one of the two parts and therefore only in one of the two parts a hole needs to be made. Additionally, as the fastener will be glued to a part, it is invisible from the outside and hence it will not create a thermal gateway[13]. A graphical representation of how the bolt can be installed is illustrated in Figure 18.3. Additionally, an insert is needed to ensure better load transfer to prevent delamination.
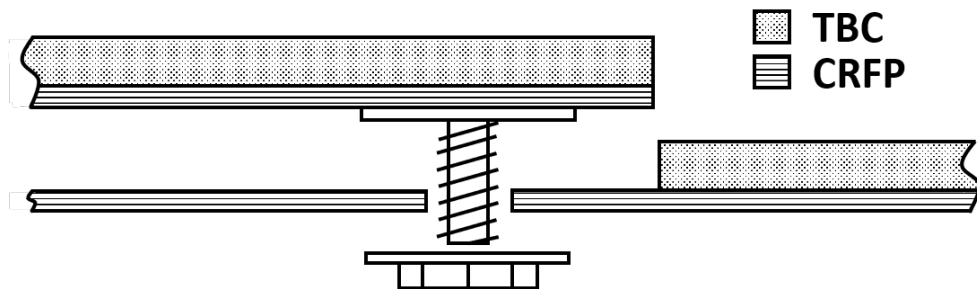
Figure 18.3: Graphical representation of the use of Big-Head bolts

18.4. Integration

The integration is divided up into two parts: Part integration and subsystem integration. Where the former refers to how different structural parts adhere together and the latter to how subsystems (e.g. the motors) are integrated into the body.
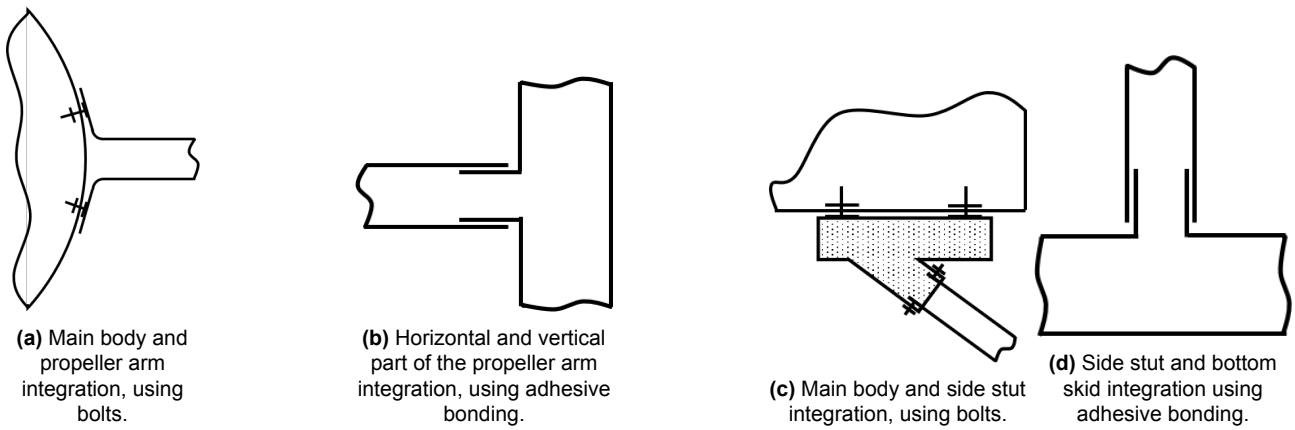
18.4.1. Part Integration

The following parts of the UAV are identified:

- Main body (1x) - CFRP
- Horizontal part of the propeller arm (4x) - CFRP
- Vertical part of the propeller arm (4x) - CFRP
- Side stut (4x) - CFRP
- Bottom skid (2x) - CFRP
- Rotation mechanism suction cups (4x) - Aluminum
- Rotating mechanism landing gear (4x) - Aluminum

To attach the propeller arm to the main body, bolts will be used as shown in Figure 18.4a. This allows for detachable propeller arms. The vertical part of the propeller arm is connected to the horizontal part by adhesive bonding as illustrated in Figure 18.4b. Both the attachment of the side strut to the rotating mechanism and from the rotating mechanism to the main body is done using bolts, as can be seen in Figure 18.4c. This ensures that if the rotating mechanism needs to be replaced it can be easily removed. Finally, Figure 18.4d shows how the side struts and bottom skids are assembled. To do this adhesive bonding is used.

---

[12]`https://www.bighead.co.uk/`, Retrieved on 09/06/2021

[13]`https://www.fastfixtechnology.com/automotive/fastener-solutions-for-composites/`, Retrieved on 09/06/2021

(a) Main body and propeller arm integration, using bolts.

(b) Horizontal and vertical part of the propeller arm integration, using adhesive bonding.

(c) Main body and side stut integration, using bolts.

(d) Side stut and bottom skid integration using adhesive bonding.

Figure 18.4: Graphical representation of the part integration

18.4.2. Subsystem Integration

The integration of the subsystems is already discussed in Section 12.2 and will therefore not be further elaborated upon. The integration of the motor and the electric speed controller can be found in Figure 18.5, which is a graphical representation and not to scale.
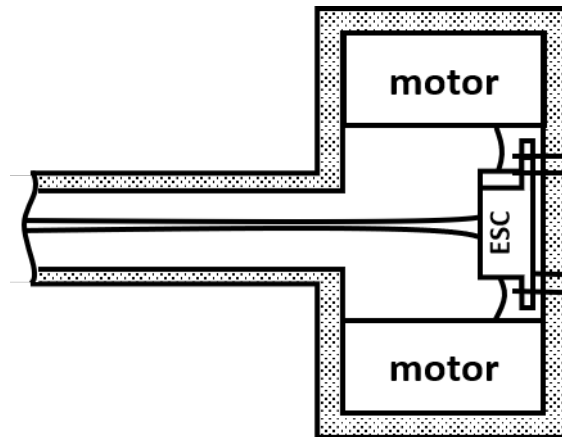
Figure 18.5: Integration of the motor and electronic speed controllers (ESC) in the propeller arm (not to scale). The second ESC is located behind the one drawn.

The integration of the vacuum system with the landing gear is shown in Figure 18.6.
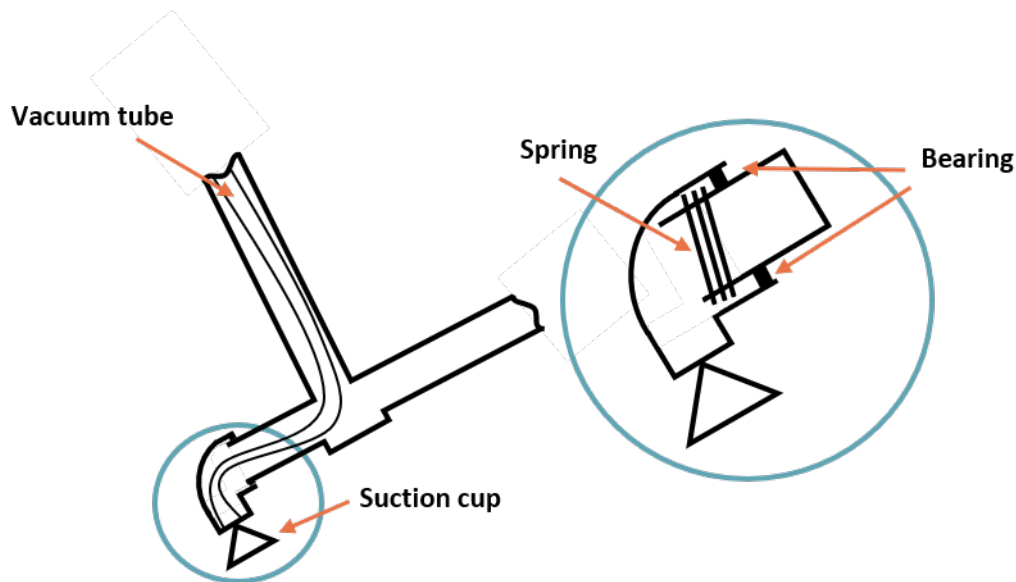
Figure 18.6: Landing gear and vacuum system integration.

To keep the suction cups perpendicular to the building when the UAV is approaching, a spiral spring is used as this will not require a motor. The spring will still allow the suction cups to rotate with respect to the bottom skid when attached to the building. Bearings are added as well to allow for a smooth rotation.

19 Future Development and Cost Analysis

This chapter aims to provide an overview of what the total cost of the UAV is, as well as financial analysis and an overview of the future developments.

19.1. Cost Analysis

In this section, the cost for all of the components will be estimated. The way the costs have been broken down can be seen in Figure 19.1. There are three main costs: overhead, which refers to the legal teams and publicity, the development, which includes the engineers and manufacturers, and finally the production costs that include the outsourced components as well as the required facilities for production. It is important to note that the costs of the sub-departments do not include the man-hours needed for production, which will be considered in an additional chapter, under labor costs (personnel in Figure 19.1. The cost mentioned in Figure 19.1 can be estimated per sub-department. This estimation is not final, as the design is still at a preliminary stage, therefore margins have been included. For the cost estimation, it is important to recognize which of the required parts need to be made, and which can be bought or outsourced. This can be done via a make-or-buy decision.
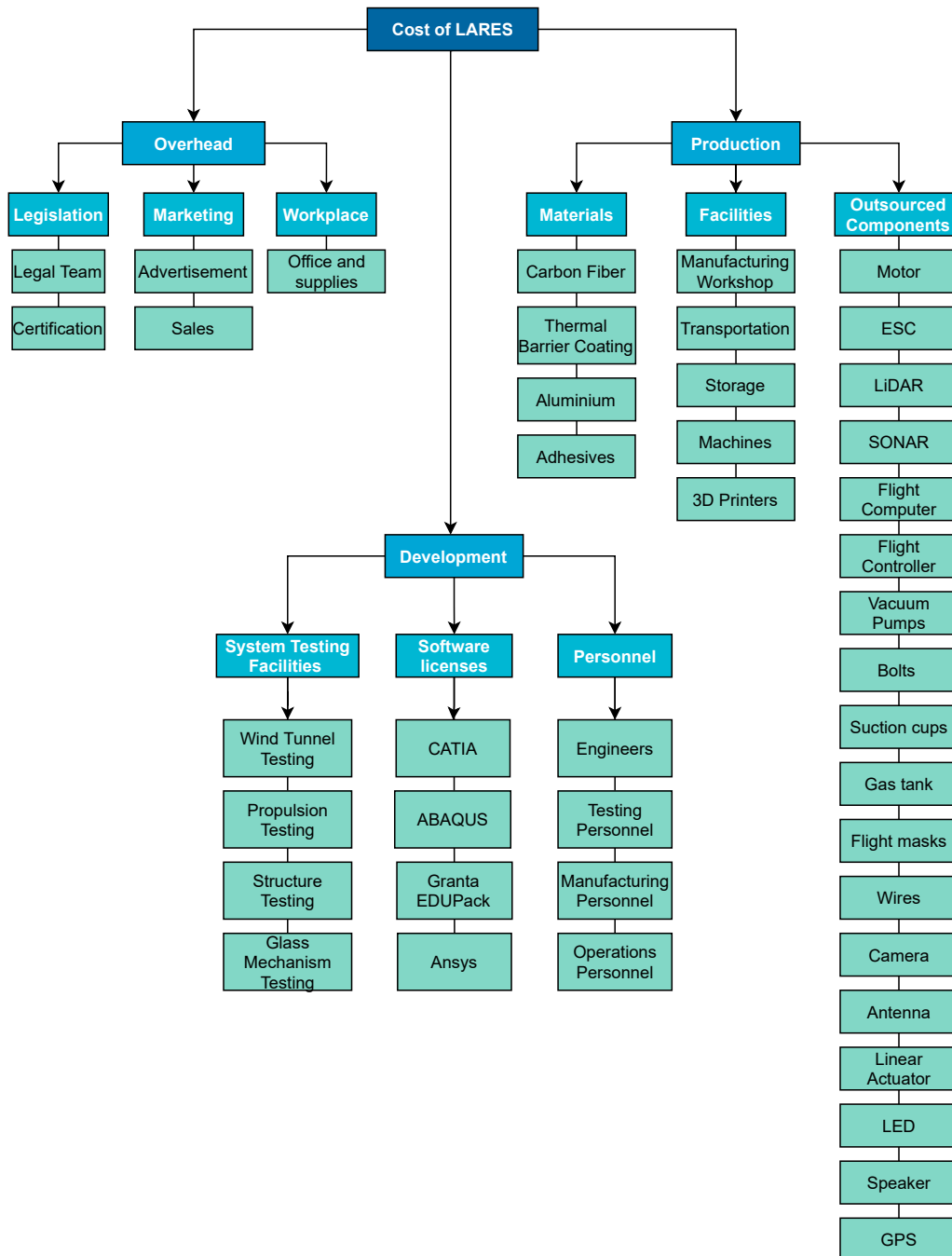
Figure 19.1: The cost breakdown structure for the UAV.

19.1.1. Make or Buy decisions

It is not always possible to self-produce the parts. It is sometimes necessary to outsource the parts, which can be done by trusted companies. This saves time, as well as resources. It does not always end up being more costly, and if the company is trusted, it can also be a warranty of a high-quality product. To decide whether a product is to be made or bought, the diagram in Figure 19.2 can be used.
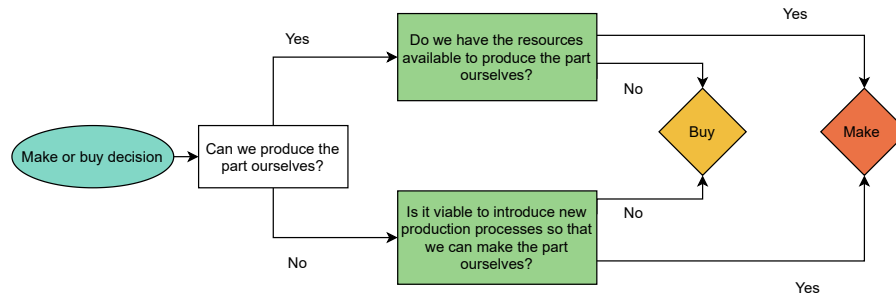
Figure 19.2: The schematics of the make or buy decisions.

19.1.2. Prototype costs

The requirement TL-USER-20 sets a maximum budget for the cost of one prototype. To verify whether this requirement has been met, the cost of the prototype only (which includes the materials, the components, the payload, and the fireproof structure) has been calculated. This can be done using the total price of the materials and the components that have been used.

Structures & Materials

The four materials used throughout the project are carbon fiber, aluminum, a ceramic mat for thermal barrier coating, and mineral wool. With regards to carbon fiber, the price varies depending on the quality and thickness of the fiber. On average, a carbon fiber roll of fibers oriented in the ± 45 [°] direction will cost between 45 and 80 [EUR/m^2][1]. With regards to aluminum, selective laser melting requires expensive tooling as well as knowledge, therefore it will be outsourced at a chosen company. Mineral wool has a price of 0.23 [EUR/m^2], which is quite inexpensive[2]. Finally, the thermal barrier coating has a stock price of approximately 11 [EUR/m^2][3]. With the total amount of carbon fiber needed of 50 [m^2], and accounting for the difficulty of producing some parts with adequate precision (which leads to parts being scrapped at times), the total price of the carbon will be between 3,000 - 4,500 [EUR], and with the same quantities for thermal coating and mineral wool plus an extra safety margin, the prices are between 600-700 [EUR] and 15-20 [EUR] respectively. For the aluminum, given also the manufacturing process, the total cost will be taken with a margin, so it is estimated to be between 2,000-3,000 [EUR] for the processed aluminum.

For production, the required tooling will either need to be bought or rent at another company, as well as machines such as a mill or a late, and a 3D printer for the manufacturing of some parts. Sanding paper is also needed for the finishing of some parts. Its price is 25 [EUR/roll][4], with one roll being 25x38 [mm^2], more than will be needed to make a prototype. With regards to carbon fiber production, which will be done by a manual layup, the cost has been included in the labor costs. Aluminum will be outsourced, thereby, once a suitable company is found post-DSE, the cost can be updated. Finally, the remaining materials will also be manually integrated into the structure.

Communications and Collision Avoidance

For electrics and embedded, most of the components will be bought, as they are already present on the market. There will be in total 2 LiDAR units, with a price of 250-270 [EUR][5], 12 SONAR with a price of 50 [EUR] per component[6] and one flight computer with a price of 600 [EUR][7]. The 4G/5G receiver was estimated at 50 [EUR] per component. Because the costs can be found from shipping websites, the values are taken as rather precise. The shipping has been included. The uncertainty in the price for this subsystem stems from the fact that the prices are not including the electrical cables, whose design will be tackled in the final detailed design.

---

[1] https://shop1.r-g.de/en/list/Fibre-reinforcements/Carbon-fibre, Retrieved on 17/06/2021

[2] https://www.alibaba.com/showroom/price-mineral-wool.html, Retrieved on 17/06/2021

[3] https://www.alibaba.com/showroom/ceramic-fiber-mat.html, Retrieved on 17/06/2021

[4] https://nl.rs-online.com/web/c/?searchTerm=sanding+paper, Retrieved on 18/06/2021

[5] https://www.lidarsensor.nl/product/lw20-c-lidar-afstandsmeter/. Retrieved on 29/06/2021

[6] https://www.maxbotix.com/ultrasonic_sensors/mb1260.htm, Retrieved on 29/06/2021

[7] https://www.modalai.com/products/voxl-flight?variant=31636287094835. Retrieved on 29/06/2021

Propulsion system
Then, for propulsion, the prices of the motor, the batteries, and the electric speed controllers can be found. The batteries[8] cost between 1,190-2,100 [EUR], the ESCs[9] are estimated at 1,000-1,500 [EUR], and the motors[10] are 2,100-2,200 [EUR]. The cost for the manufacturing of the duct and the propellers have been included in the total material costs.

Adhesion to building and glass cutting mechanism For the adhesion to buildings, the cost of the complete adhesion system is set to be 787 [EUR]. This comes from the costs of the vacuum cups[11] which were investigated with the company, as well as the vacuum pump[12], the valve system[13] and the switch[14]. it is a rather precise value since components can be bought from a company. For the glass cutting mechanism, the purchased components have the following costs: the gas tank has a cost of 5.95 [EUR][15], while the to motors have a cost of approximately 50 [EUR][16] and 30 [EUR][17]. Because the production costs are unknown for now, the total cost is then estimated to be between 200-300 [EUR], accounting for the expenses of the glass.

Finally, the total cost, as well as the relevant margins and the percentage that each subsystem contributes to the total cost can be found as the sum of the components in Table 19.1

Table 19.1: Total costs of the prototype development, including the contribution of each subsystem to the total costs.

Part or assembly	Cost [EUR]	Margin [%]	System cost percentage [%]
Payload	270	20	*Payload*
Velcro for payload	10	5	
Walkie Talkies	50	5	4.1
Glass Cutting Mechanism	250	30	2.8
Collision Avoidance Systems	1,490	30	17
Propellers	20	10	*Aerodynamics*
Ducts	80	10	1.1
Motors	2,100	10	*Propulsion*
ESC	1,250	15	
Batteries	2,000	10	62
Propeller Arm	40	20	*Structures*
Adhesion Systems	787	20	
Landing Gear	100	20	
Main Body	200	20	13
Total	**8647**	20	100

The total cost is almost 9000 [EUR], with a margin of 20 % due to the large uncertainties. The total margin has been found as a weighted average of the other margins. It can be seen that there is a

---

[8]https://www.genstattu.com/ta-25c-23000-6s1p-hv-as150.html, Retrieved on 29/06/2021.

[9]https://store.tmotor.com/goods.php?id=370, Retrieved on 29/06/2021.

[10]https://store.tmotor.com/goods.php?id=1130, Retrieved on 29/06/2021.

[11]https://www.schmalz.com/nl-nl/vacuuemtechniek-voor-de-automatisering/vacuuem-componenten/vacuuemzuignappen/zuignappen-voor-de-behandeling-van-glas/bellows-suction-cups-sab-ht1-1-5-folds-305668/10.01.06.03632, Retrieved on 28/06/2021.

[12]https://www.schmalz.com/nl-nl/vacuuemtechniek-voor-de-automatisering/vacuuem-componenten/vacuuemgenerator/vacuuempompen/dry-running-vacuum-pumps-eve-tr-308333/10.03.01.00192, Retrieved on 28/06/2021.

[13]https://www.schmalz.com/nl-nl/vacuuemtechniek-voor-de-automatisering/vacuuem-componenten/filters-en-aansluitingen/vacuuemverdeler/vacuum-compressed-air-distributors-vtr-309029/10.09.03.00058, Retrieved on 28/06/2021.

[14]https://www.schmalz.com/nl-nl/vacuuemtechniek-voor-de-automatisering/vacuuem-componenten/schakelaars-en-systeembewaking/mechanische-vacuuemschakelaars/vacuum-switches-vs-v-pm-em-st-308806/10.06.02.00456, Retrieved on 28/06/2021.

[15]https://www.allprepare.com/jetboil-jetpower-gastank-100-gram, Retrieved on 28/06/2021.

[16]https://nl.rs-online.com/web/p/dc-motors/4540883, Retrieved on 28/06/2021.

[17]https://nl.rs-online.com/web/p/dc-motors/8347631/. Retrieved on 28/06/2021.

margin of more than 1000 [EUR] on the maximum permitted budget. This margin is useful to account for possible delays and production mistakes.

19.1.3. Additional company costs
If the drone had to be made by a company, the costs would inevitably increase due to the

Labor costs
The labor costs will be estimated based on the average salary in the Netherlands. The average hourly salary for an engineer in the Netherlands is 24 [EUR] per hour[18]. For a working week of 40 hours, and with a team of 9 design engineers, the total cost of labor would be 8,640 [EUR] per week, which is a yearly expense of 449,280 [EUR] on salaries only, assuming that 52 weeks have to be paid. To this, the cost of the manufacturing crew, which is also responsible for maintenance, needs to be summed. Assuming that the manufacturing crew is made of 10 employees, which are each paid 18 [EUR] per hour, the total yearly cost is 374,400 [EUR]. The total labor costs then become 823,680 [EUR].

License costs
A CATIA license has a price of 9,238 [EUR] for a one-time purchase, to which 1,650 [EUR] of yearly maintenance shall be added[19]. This includes the right to use ABAQUS for FEM. The price of a full ANSYS license is not disclosed[20], but estimated to be around 50,000 [EUR]. GRANTA Edupack is often included in the Ansys license, and the price is known only by contacting the company. With these prices, the total license costs amount to 62,538 [EUR].

Delivery
The UAV will need to reach its final destination within the Netherlands. The average shipping cost for an item of 2 m^3 with TNT Express is 1,012 [EUR][21]. As initially only a prototype will be made, the cost is for now only estimated for one delivery. This is then accounted to be between 1,000 and 2,000 euros, depending on the distance.

With all of the considerations made above, the total cost of the project, for a year, if the design was executed as a company is almost 900,000 [EUR], with a margin of 10 % based on the above considerations.

19.2. Financial Analysis
This section will give an analysis of the financial part of the project. It will first explain the philosophy behind the market price, where after the market price will be set, the net income will be determined and finally, the return on investment will be given.

19.2.1. Market Price Philosophy
To determine the market price of the product it first has to be determined what the financial aim of the company is. As the UAV is designed with the incentive to save lives and increase public safety, it was decided that it is desired to have as many UAVs in practice as possible. Therefore, the company will be a nonprofit organization. This entails that the company will not make a profit for personal benefit or the stakeholder's wealth, but that any profit made will flow back into the company[22]. E.g. the profit is used to improve marketing or to perform research into new materials.

For a nonprofit organization, there is a possibility for an exemption on taxes. However, as the product will be sold on a market where eventually other competitors will sell their products with an aim at making a profit, this exemption is unlikely to be gained. However, the government can look on a one-to-one basis to a company to provide such an exemption or reduction[23]. Therefore it is recommended

---

[18]http://www.salaryexplorer.com/salary-survey.php?loc=152&loctype=1&job=22&jobtype=1, Retrieved on 18/06/2021.

[19]https://3dsman.com/catia-pricing/, Retrieved on 18/06/2021.

[20]https://www.howmuchisit.org/how-much-does-ansys-cost/, Retrieved on 18/06/2021.

[21]https://www.tnt.com/express/en_nl/site/how-to/calculate-size-and-weight.html, Retrieved on 18/06/2021.

[22]https://www.upcounsel.com/what-is-profit-called-in-a-non-profit-organization, Retrieved on 18/06/2021

[23]https://www.belastingdienst.nl/wps/wcm/connect/bldcontentnl/belastingdienst/zakelijk/winst/

that post-DSE a request will be made at the Dutch tax authorities.

19.2.2. Market Price Determination

The market price is dependent on the competitors, the cost of producing the UAV, and the profit margin.

Cost Relative to Competitors

An explanation of possible competitors on the market and the prices of similar products are discussed in Chapter 2. However, the competitors have different applications of their UAVs, so a direct comparison is not entirely sensible. For a normal UAV around 10,000 [EUR] would make sense for the price, but because of the specific application and additional functions this UAV can fulfill (e.g. adhesion to a building, glass cutting, high-temperature resistance), the price can be higher without losing potential clients.

The market share of this company will initially be 100 [EUR] as no direct competitors are on the market yet. It is expected to decline over time, as after a proof of concept new competitors will join the market. This will take time as the UAV is a complex product, hence the development time of competitors will be long. Therefore it is expected that 20 UAVs will be sold within The Netherlands as explained in Section 2.3. As this number is quite small it is not profitable to heavily invest in machinery, e.g. to buy an autoclave, therefore the production will be outsourced to manufacturing companies.

Production Cost

The production of the UAV consists of two parts: the off-the-shelf costs (components like batteries and material cost) and the manufacturing cost. The former was estimated in Section 19.1.2 to be 7,436 [EUR]. The latter is harder to estimate. All structural components have to be custom-made as the thermal barrier coating has to be cured together with the CFRP. How expensive the cost will be to manufacture is dependent on the complexity of the part. It is found that for producing CFRP with an autoclave the manufacturing cost ranges from 210 [EUR] to 3,240 [EUR] per part[11]. For the CFRP in total 20 parts are needed (e.g. main body inner and outer shell, duct, propeller arm vertical and horizontal part), which differ in complexity. However, the majority of them are relatively easy tubes (e.g. the side struts of the landing gear) or cylinders (e.g. the ducts), therefore the price is estimated to be at the lower side of this range, so a total CFRP manufacture cost of 4,500 [EUR] is set.

For manufacturing parts with aluminum with selective laser melting the cost ranges between 108 [EUR] and 3,980 [EUR] per part. Eight rotors are needed to be made out of aluminum, even as the glass cutting mechanism and the rotating parts of the main body and the landing gear. These parts are slightly more complex than the CFRP parts, however, fewer of them are needed. Therefore the cost of manufacturing aluminum parts lays around 4,000 [EUR]. An overview of the production costs is given in Table 19.2.

Table 19.2: Overview of the production cost per UAV.

Cost build up	Cost	Currency
Off-the-shelf cost per UAV	7,913	[EUR]
Manufacture cost per UAV	8,500	[EUR]
Total production cost per UAV	16,413	[EUR]

Profit Margin

The profit margin should be such that the company has enough money to endure a financial setback, e.g. testing shows that another design iteration is necessary, or unforeseen costs have to be made for instance for administration purposes. A net profit margin around 10 percent is considered average[24][25].

---

vennootschapsbelasting/belastingplicht_en_aangifte/wanneer_moet_een_stichting_vereniging_of_
vergelijkbare_organisatie_aangifte_doen/, Retrieved on 18/06/2021

[24]https://corporatefinanceinstitute.com/resources/knowledge/accounting/profit-margin/, Retrieved on 18/06/2021

[25]brex.com/blog/what-is-a-good-profit-margin/, Retrieved on 18/06/2021

The profit margin can be determined using[26]:

$$\text{net profit margin} = 10\% = \frac{\text{net income}}{\text{revenue}}100\% \tag{19.1}$$

Where the revenue and net income are determined assuming that 20 UAVs are sold. An explanation of how the net income is found can be found in the next subsection.

19.2.3. Determine Net Income

To determine the net income, fist the gross income has to be determined. The gross income is equal to[27]:

$$\text{gross income} = \text{number of products sold}\cdot\text{price per product}-\text{number of products sold}\cdot\text{cost per product} \tag{19.2}$$

From the gross income, the operating income can be determined. This refers to the gross income minus the operating expenses, e.g. marketing[28]. A comparison with another UAV company, Parrot, has been made to estimate the costs for marketing and administration & overhead costs. For the year 2020, it was 16.3 [%] and 13.6 [%] of the revenue respectively. It is, however, important to note that Parrot aims to sell UAVs to the general public, whereas this UAV aims to sell to the fire brigade. Therefore less money needs to be spent on broad advertisement, so half of the percentage for marketing has been used. Therefore:

$$\text{operating income} = \text{gross income} - 0.0815\text{revenue} - 0.136\text{revenue} \tag{19.3}$$

From the operating income the net income can be determined with the following formula[29]:

$$\text{net income} = \text{operating income} - \text{taxes} \tag{19.4}$$

As the UAV will in essence reduce the number of people that need serious help from the medical emergency services, the UAV can be categorized as a medical help. This entails that only 9[%] tax has to be paid over the operating income[30]. After the determination of the net income, the market price can be set based on the profit margin. An overview of the different incomes and market prices can be found in Table 19.3.

Table 19.3: Income overview for the company developing the UAV.

Income	Amount	Currency
Gross income	177,840	[EUR]
Operating income	55,616	[EUR]
Net income	50,611	[EUR]
Market price	25,305	[EUR]

---

[26]https://www.nav.com/blog/profit-margin-formula-what-is-it-how-to-calculate-it-how-to-improve-profit-margin-432870/, Retrieved on 18/06/2021

[27]https://corporatefinanceinstitute.com/resources/knowledge/accounting/gross-income/, Retrieved on 18/06/2021

[28]https://money.howstuffworks.com/operating-vs-gross-income.htm, Retrieved on 18/06/2021

[29]wallstreetmojo.com/operating-income-vs-net-income/, Retrieved on 18/06/2021

[30]https://www.belastingdienst.nl/wps/wcm/connect/bldcontentnl/belastingdienst/zakelijk/btw/tarieven_en_vrijstellingen/goederen_9_btw/goederen_met_9_btw, Retrieved on 18/06/2021

19.2.4. Return on Investment

To evaluate the the efficiency of different efficiencies a return on investment can be determined. This refers to the ratio between the investment and the cost of the investment, or written as an equation[31]:

$$\text{return on investment} = \text{net income}/\text{investment} \tag{19.5}$$

Where the investment is equal to 318,720 [EUR], which is the cost to produce one UAV times the amount of UAVs produced. This results in a return on investment of 0.15 for this UAV. This is just above the average of 0.1 over different industries[32]. This entails that investing in this UAV results in relatively more payback than investing in an average other company. This is beneficial in the search for investors, as a higher return on investment means that the investors can expect to be paid back for their investments including interest.

19.3. Project Design and Development Logic

The project design and development logic is meant to show the sequence of activities that must be carried out post DSE. This can be seen in Figure 19.3.

Finalize design

The proposed design has been engineered in only ten weeks. Therefore, it is expected that more detail will be needed before the engineering design can be considered complete. The estimated time for this phase is of **six months**. Delays add between 1 and 2 months, depending on the severity.

Acquire financial resources

Acquiring adequate resources is not a single step in time. This will be done continuously throughout the design and production, however, it is fundamental to have enough resources to begin the production of the prototype. These resources are not only financial but consists also of the necessary machines, expertise, and locations for manufacturing to begin. This phase is done continuously throughout the design, as it is fundamental to always have enough liquidity throughout the design.

Build prototype

Next, a prototype is built and tested: this is the most efficient and complete way to validate the design. Here, risk management is taken into account by performing continuous quality control checks of every part, before and after it is assembled. This will help to prevent that parts have to be discarded due to poor production. Every time that the outcome of the test is negative, the process goes back to the previous phase and re-assesses the mistakes. The construction of the prototype is expected to take a minimum of **8 months**, including a margin that for every discarded part, up to a month delay is possible. Each assembly will also provide a month's delay at most.

Validate prototype

Validation has been designed to be as complete as possible; this means testing every system separately, and then in combination with each other. Possible tests include wind tunnel tests, intending to test the aerodynamic properties, as well as noise measurements in a low-speed wind-tunnel test lab, such as the one at TUDelft. Psychological tests will also be performed: here the escape from a building facilitated by the use of LARES UAV will be simulated to quantify its ease of use in a stressful situation. As the drone will have to perform in a harsh environment, it is fundamental that its environmental resistance is also tested. This will be done by operating the drone in a test room with a temperature of 300 [°C] for a time of 5 minutes. Each test may have a positive or negative outcome: whenever the outcome is negative, the design must be re-evaluated and, if necessary, revised. The testing phase is also expected to take **between 6 and 8 months**, including the design of new tests,

---

[31]`https://www.investopedia.com/terms/r/returnoninvestment.asp`, Retrieved on 18/06/2021
[32]`https://www.investopedia.com/terms/r/returnoninvestment.asp`, Retrieved on 18/06/2021

with a safety margin to account for the possible re-designs and failures. Naturally, this time margin is just an indication: in the case that multiple components fail at the same time, the time will lengthen significantly, depending on the failure type.

Certify drone
After successful validation of the prototype, the drone can be certified in its respective category at EASA. It is of course possible that certification is not awarded: in that case, the design will need to be revised, depending on the reason behind the missed certification. The missed certification adds up to 6 months of delay. To prevent this from taking too much additional time, a risk management sheet will be made where all possible reasons for missed certification will be documented; a mitigation measure for each reason will be listed, to have a clear plan of what to do in the case that it happens. The certification process is **expected to take 4 months**, including the time required to get into contact with EASA.

Sell Product and Start Production
Finally, with certification achieved, the product is presented to the firefighters. Once this is By the end, the drone will have effectively entered service to help the firefighters safely perform their missions, so that more lives can be saved. The selling process and the organization of production shall take **3 months**, as before these phases most of the contact with firefighters and sponsors will be done thanks to the operations and finance team.

End of Life
Finally, the end of life phase refers to those activities that will be carried after the drone has finished its mission. The design is intended to be modular, as requirement TL-USER-21-02 specifies. This means that some components can be re-purposed, as the sustainability analysis has shown. The following components will be re-purposed:

- Lithium-Ion batteries preserve quite some charge after intensive use: although they cannot be re-used in other drones, the remaining charge is enough to power less energy-intensive uses, such as phone batteries[67].
- The carbon fiber that is extensively used in the drone can be re-purposed as different panels; this is done by chopping the carbon fiber, subjecting it to high heat, and mixing it with fresh resin to produce a new panel[33]. This is sustainable as carbon fiber produces great amounts of CO_2, as discussed in Chapter 3.
- The aluminum that forms the propellers can also be recycled: this process simply involves re-melting the metal, and only requires 5 % of the energy required to make a new bauxite ore, as well as does not require additional excavations for the bauxite ore[34].

Those components that cannot be recycled will need to be brought to a facility that sustainably disposes of them.

As a time frame has been given to each activity, as well as some margins in the case of a bad outcome, a Gantt chart was made showing the activities that must be performed post DSE. According to the estimations made, the product will be ready by the beginning of 2024. It is important to note that these estimations were made if for no delays, thereby the time might increase. The end of life is not included as the drone has been built to last for 10 years, and a plan for the end of life was introduced earlier.

---

[33]`https://www.rockwestcomposites.com/blog/3-reasons-we-love-repurposed-carbon-fiber/`, Retrieved on 29/06/2021.

[34]`https://www.economist.com/leaders/2007/06/07/the-price-of-virtue`, Retrieved on 29/06/2021.
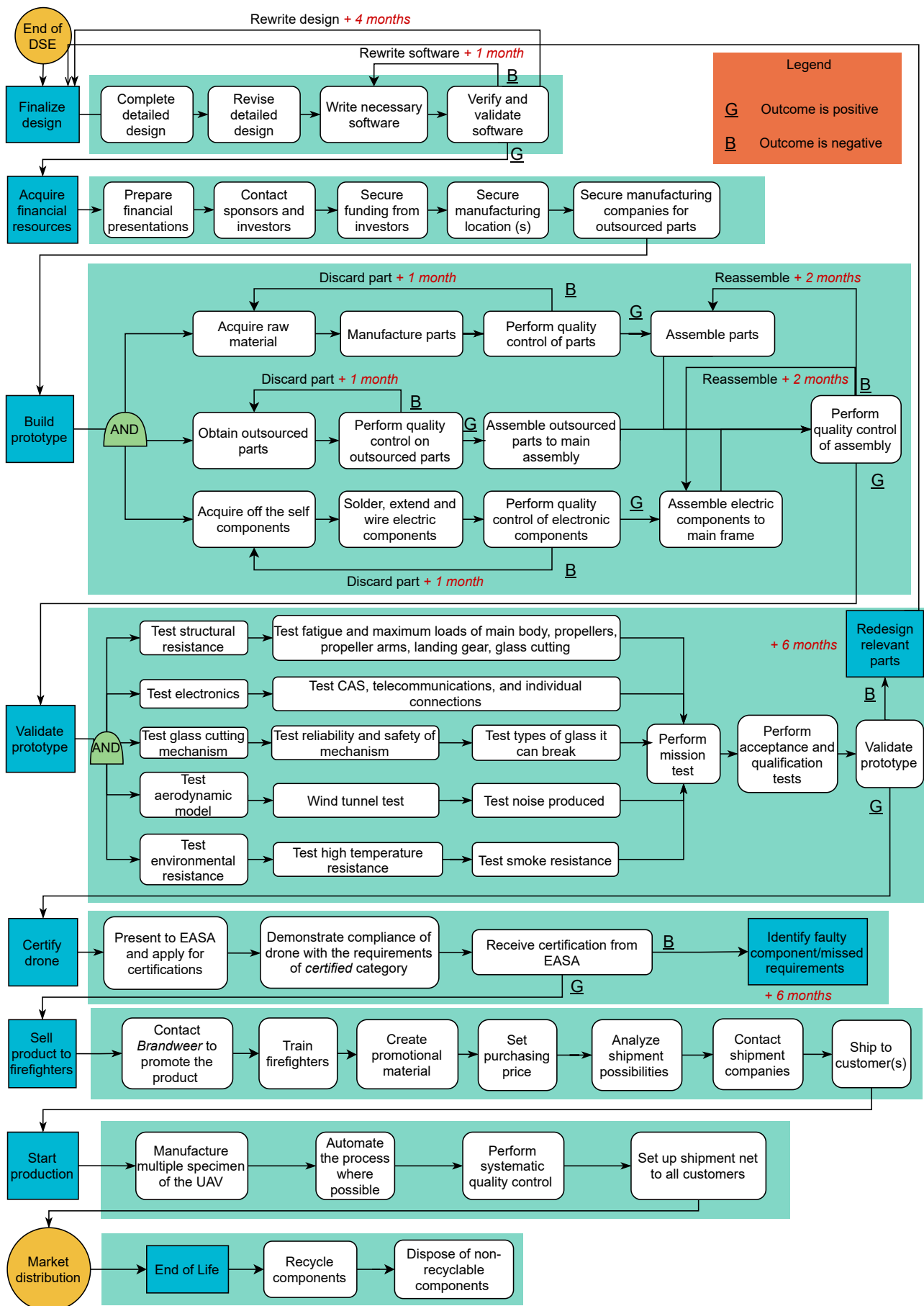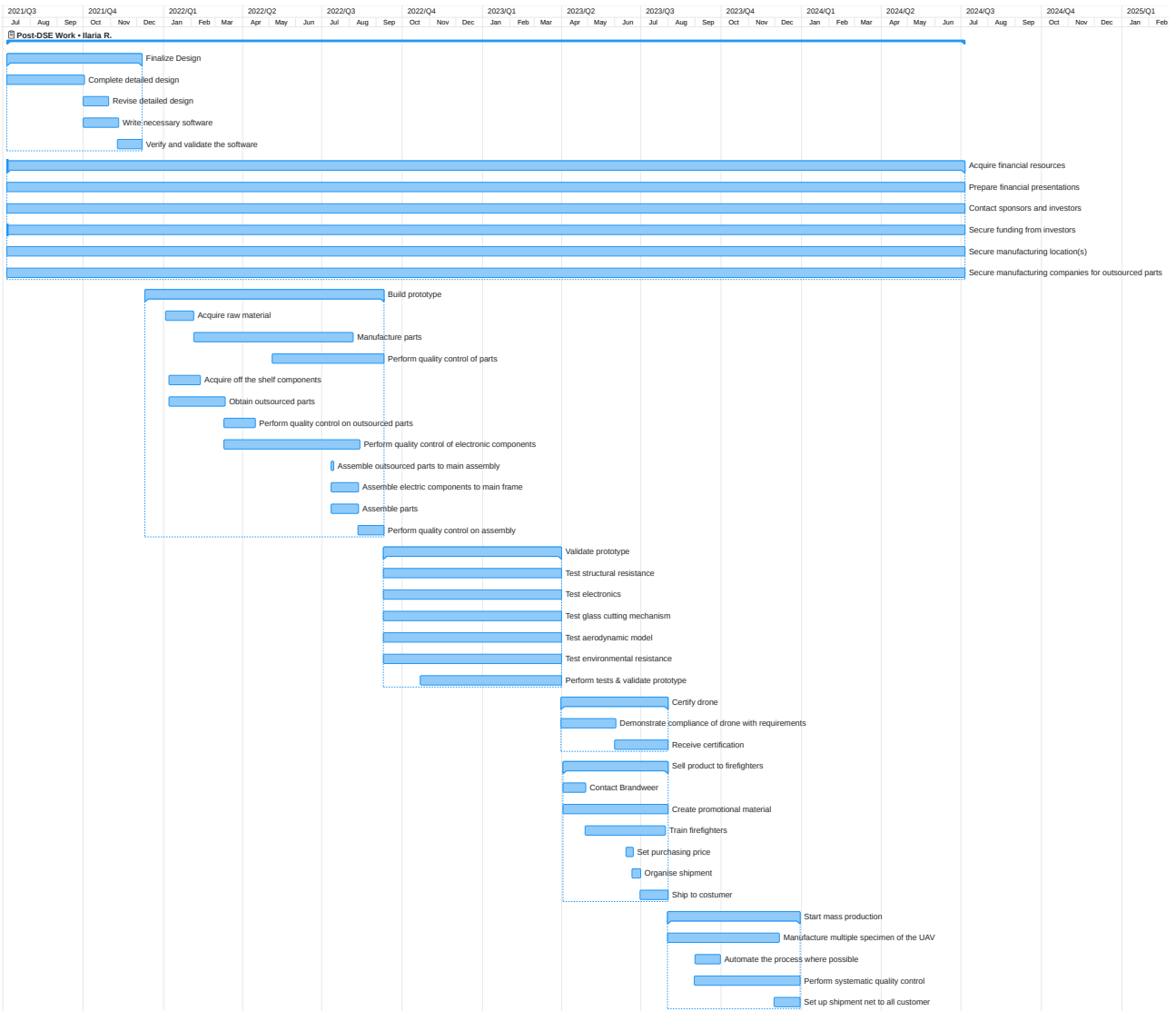
Figure 19.3: The workflow of post DSE activities.

Figure 19.4: Gantt chart showing the flow of post DSE activities

References

[1] M. Ahrens and B. Evarts. "Fire Loss in the United States During 2019". In: *National Fire Protection Association (NFPA)* (2020).

[2] M. Kobes and K. Groenewegen. "Consumer fire safety: European statistics and potential fire safety measures". In: *Netherlands Institute for Safety, Nibra* (Jan. 2009). Versie: 431N8032/3.0.

[3] A. Momont. "Drones for good". In: *Master's thesis TU Delft* (2015).

[4] Stichting Hoogbouw. "Hoogbouw in Nederland 2020". In: (2020). Accessible through: `https://issuu.com/hoogbouw/docs/hoogbouw_in_nederland_2020`.

[5] C.W. Babbitt. "Sustainability perspectives on lithium-ion batteries". In: *Clean Techn Environ Policy* 22 (2020), pp. 1213–1214. DOI: `https://doi-org.tudelft.idm.oclc.org/10.1007/s10098-020-01890-3`.

[6] C. E. Tinney and J. Valdez. "Thrust and Acoustic Performance of Small-Scale, Coaxial, Corotating Rotors in Hover". In: *AIAA Journal* 58.4 (2020). DOI: `doi.org/10.2514/1.J058489`.

[7] C. van Duin, S. te Riele, and L. Stoeldraijer. *Huishoudensprognose 2018-2060: opmars eenpersoonshuishoudens zet door.* Dec. 2018.

[8] A.L. de Ruijter et al. *Short Range Emergency UAV: Providing timely delivery of adequate payload to patients in emergency situations*. Delft, 2021.

[9] A.L. de Ruijter et al. *UAV to Facilitate Fire Escape: Providing timely delivery of fire emergency masks to facilitate a successful fire escape*. Unpublished Work. Delft, 2021.

[10] R.C. Hibbeler. *Mechanics of Materials*. 10th ed. Harlow, UK: Pearson, 2018.

[11] Granta Design Ltd. *GRANTA EduPack 2020*. Version 20.1.1. Cambridge, UK, 2020. Software Available through TU Student IT Desk.

[12] M.V. Swain, J.C. Metras, and C.G. Guillemet. "A deformation and fracture mechanics approach to the scoring and breaking of glass". In: *Journal of Non-Crystalline Solids* 38-39 (1980). XIIth International Congress on Glass, pp. 445–450. ISSN: 0022-3093. DOI: `https://doi.org/10.1016/0022-3093(80)90459-7`. URL: `https://www.sciencedirect.com/science/article/pii/0022309380904597`.

[13] Q. Quan. *Introduction to Multicopter Design and Control*. Springer Singapore, 2018.

[14] F.M. White. *Fluid Mechanics*. McGraw-Hill series in mechanical engineering. McGraw Hill, 2011. ISBN: 9780073529349. URL: `https://books.google.nl/books?id=egk8SQAACAAJ`.

[15] T. Sinnige. *Propeller aerodynamics AE4135 - Rotor/Wake Aerodynamics*. Lecture. Delft.

[16] J. Gordon Leishman. *Principles of Helicopter Aerodynamics*. 2nd ed. Maryland: Cambridge University Press, 2006. ISBN 978-0-521-85860-1.

[17] E. Bernini. "Significance of blade element theory in performance prediction of marine propellers". In: *Elsevier* 31 (2003), pp. 957–974. doi:10.106/j.oceaneng.2003.12.001.

[18] N. van Arnhem. "Design and Analysis of an Installed Pusher Propeller with Boundary Layer Inflow". In: *MA thesis, Delft University of Technology* (2015).

[19] J. Dorfling and K. Rokhsaz. "Constrained and Unconstrained Propeller Blade Optimization". In: *Journal of aircraft* 52.4 (June 2015). DOI: `DOI:10.2514/1.C032859`.

[20] U. Reuben, K. Hiraki, and M. Shohei. "Airfoil considerations in the design of high performance, low reynolds number propellers". In: *International Journal of Research Granthaalayah* 6.9 (Sept. 2018). DOI: `DOI:10.29121/granthaalayah.v6.i9.2018.1250`.

[21] M.D. Hamada. "High-performance airfoil with low reynolds-number dependence on aerodynamic characteristics". In: *Fluid Mechanics Research International Journal* 3.2 (2019), pp. 76–80. DOI: `2019;3(2):76 80.`.

[22] H.B. Freeman. "Comparison of full-scale propellers having R.A.F 6 and Clark Y airfoil sections". In: *Langley memorial Aeronautical Laboratory* 378 (2019).

[23] J. Chung, J. Hough, and R. Nagel. "Interaction Between Rotors of a Counter Rotating Propeller". In: *AIAA 13th Aeroacoustics Conference* (1990). DOI: 10.2514/6.1990-3976.

[24] B. Theys et al. "Influence of propeller configuration on propulsion system efficiency of multi-rotor Unmanned Aerial Vehicles". In: *2016 International Conference on Unmanned Aircraft Systems (ICUAS)* (2016), pp. 195–201. DOI: `10.1109/ICUAS.2016.7502520`.

[25] C. M. Simões. "Optimizing a Coaxial Propulsion System to a Quadcopter". In: *Dept. Engenharia Mecânica, Instituto Superior Técnico* (2019).

[26] Y. Jiang, H. Li, and H Jia. "Aerodynamics Optimization of a Ducted Coaxial Rotor in Forward Flight Using Orthogonal Test Design". In: *Shock and Vibration* Vol. 2018.2670439 (2018). https://doi.org/10.1

[27] E. Grande et al. "Aeroacoustic Investigation of a Propeller Operating at Low-Reynolds numbers". In: *AIAA* (2020).

[28] D. Cheng et al. "Morphing Concept for Multirotor UAVs Enabling Stability Augmentation and Multiple-Parcel Delivery". In: AIAA SciTech Forum. San Diego, CA, USA: AIAA, Jan. 2019. DOI: `10.2514/6.2019-1063`.

[29] S. Ma et al. "Temperature effect and thermal impact in lithium-ion batteries: A review". In: *Progress in Natural Science: Materials International* (2018), pp. 1–14.

[30] R. Zalosh. *Appendix A: Flame Radiation Review*. John Wiley & Sons, Ltd, 2003, pp. 337–346.

[31] E.S. Manolakos, D.V. Manatakis, and G. Xanthopoulos. "Temperature field modeling and simulation of wireless sensor network behavior during a spreading wildfire". In: 2008 16th European Signal Processing Conference. 2008, pp. 1–5.

[32] C. Elanchezhian, B. Vijaya Ramnath, and J. Hemalatha. "Mechanical behaviour of glass and carbon fibre reinforced composites at varying strain rates and temperatures". In: *Proceda Materials Science* 6 (2014), pp. 1405–1418.

[33] C. Elanchezhian, B. Vijaya Ramnath, and J. Hemalatha. "Mechanical Behaviour of Glass and Carbon Fibre Reinforced Composites at Varying Strain Rates and Temperatures". In: *Procedia Materials Science* 6 (2014), pp. 1405–1418.

[34] P. Golewski and T. Sadowski. "Description of thermal protection against heat transfer of carbon fiber reinforced plastics (CFRP) coated by stiffened ceramic mat (TBC)". In: *Composite Structures* 229 (2019).

[35] P. Mangalgiri. "Polymer-matrix Composites for High-temperature Applications". In: *Defence Science Journal* 55.2 (2005).

[36] P. Golewski and T. Sadowski. "A novel application of alumina fiber mats as TBC protection for CFRP/epoxy laminates - Laboratory tests and numerical modeling". In: *Journal of the European Ceramic Society* 38.8 (2018), pp. 2920–2927.

[37] M. Ashby, H. Shercliff, and D. Cebon. *Materials: Engineering, Science, Processing and Design*. 1st ed. Oxford, UK: Elsevier Ltd., 2007.

[38] P. Leppänen and M. Malaska. "Experimental Study on the Smouldering Combustion of Mineral Wool Insulation in Chimney Penetrations". In: *Fire Technology* 55 (2019), pp. 2171–2194.

[39] M. Stewart. *Surface Production Operations Volume 3: Facility Piping and Pipeline System*. Gulf Professional Publishing, 2016, pp. 159–192.

[40] R.K. Rajput. *Engineering thermodynamics*. 3rd ed. Laxmi Publications (P) LTD, 2007, pp. 778–856.

[41] F.Zhou et al. "Effect of Temperature on Material Properties of Carbon Fiber Reinforced Polymer (CFRP) Tendons: Experiments and Model Assessment". In: *MDPI* (2019). DOI: `10.3390/ma12071025`.

[42] C. Xie. "Interactive Heat Transfer Simulations for Everyone". In: *The Physics Teacher* 5.4 (2012), pp. 237–240.

[43] Alam P. et al. "The fatigue of carbon fibre reinforced plastics - A review". In: *Composites Part B: Engineering* 166 (2019), pp. 555–579.

[44] W. E. Baker. *Explosion hazards and evaluation electronic resource*. Elsevier.

[45] P.Kelly. *Solid Mechanics Part II, Chapter 6: Plate Theory*. The University of Auckland, 2013.

[46] *Von Mises Criterion (Maximum Distortion Energy Criterion*. Engineer's edge. URL: `https://www.engineersedge.com/material_science/von_mises.htm`.

[47] J. Roskam. *Airplane Design Part IV: Layout Design of Landing Gear and Systems*. DARcorporation, 1985.

[48] R.C. Hibbeler. *Dynamics*. 13th ed. Jurong, Singapore: Pearson, 2012. p. 583.

[49] J.A. Mulder et al. *Flight Dynamics: Lecture Notes*. Version 20.1.1. Delft, NL, 2013.

[50] Teppo Luukkonen. "Modelling and control of quadcopter". In: *Independent research project in applied mathematics, Espoo* 22 (2011), p. 22.

[51] Wang P. et al. "Dynamics modelling and linear control of quadcopter". In: *2016 International Conference on Advanced Mechatronic Systems (ICAMechS)*. 2016, pp. 498–503. DOI: `10.1109/ICAMechS.2016.7813499`.

[52] R. Arasanipalai, A. Agrawal, and D. Ghose. "Mid-flight Propeller Failure Detection and Control of Propeller-deficient Quadcopter using Reinforcement Learning". In: *eprint arXiv:2002.11564* (2020).

[53] S. Tashreef, L. Iftekhar, and S. Azmeen-ur-Rahman. "Design of a crash-resistant PD-controlled quadcopter using coaxial propeller system". In: *2016 International Conference on Unmanned Aircraft Systems (ICUAS)*. 2016, pp. 986–992. DOI: `10.1109/ICUAS.2016.7502628`.

[54] Stefan Hrabar. "Reactive obstacle avoidance for Rotorcraft UAVs". In: *2011 IEEE/RSJ International Conference on Intelligent Robots and Systems*. 2011, pp. 4967–4974. DOI: `10.1109/IROS.2011.6094629`.

[55] J. Yasin et al. "Unmanned Aerial Vehicles (UAVs): Collision Avoidance Systems and Approaches". In: *IEEE Access* 8 (2020), pp. 105139–105155. DOI: `10.1109/ACCESS.2020.3000064`.

[56] Jian-Cheng Cai, Da-Tong Qi, and Yong-Hai Zhang. "A Numerical Study of the Blade Passing Frequency Noise of a Centrifugal Fan". In: vol. 12. Nov. 2012. DOI: `10.1115/IMECE2012-86745`.

[57] Hyojung Yoon et al. "An Online SBAS Service to Improve Drone Navigation Performance in High-Elevation Masked Areas". In: *Sensors* 20 (May 2020), p. 3047. DOI: `10.3390/s20113047`.

[58] J.A. Boan. "Radio Propagation in Fire Environments". PhD Thesis. Australia: Department of Electrical, Electronic Engineering, School of Engineering, Computer, and Mathematical Sciences, University of Adelaide, 2009.

[59] Qualcomm Technologies, Inc. *LTE Unmanned Aircraft Systems*. Qualcomm Technologies, Inc., 2017.

[60] I. Koren and C.M. Krishna. *Fault-Tolerant Systems*. 1st ed. San Fransico, CA, USA: Morgan Kaufmann Publishers Inc., 2007.

[61] E. Dubrova. "Time Redundancy". In: *Fault-Tolerant Design* (2013). DOI: `https://doi.org/10.1007/978-1-4614-2113-9_6`.

[62] H. A. Kinnison and T. Siddiqui. *Aviation Maintenance Management*. The McGraw-Hill Companies, 2013.

[63] E.Petritoli, F.Leccese, and L.Ciani. "Reliability and Maintenance Analysis of Unmanned Aerial Vehicles". In: *MDPI* (2018). DOI: `10.3390/s18093171`.

[64] W.E. Frazier. "Metal Additive Manufacturing: A Review". In: *Journal of Materials Engineering and Performance* 23 (2014), pp. 1917–1928.

[65] A. Pramanik et al. "Joining of carbon fibre reinforced polymer (CFRP) composites and aluminium alloys - A review". In: *Composites Part A: Applied Science and Manufacturing* 101 (2017), pp. 1–29.

[66] L.F.M. da Silva, R.J.C. Carbas, and M.D. Banea. "Adhesive Joints for Low - and High - Temperature Use: An Overview". In: *The Journal of Adhesion* 91.7 (2014), pp. 556–585.

[67] D. Hall and N. Lutsey. "Effects of battery manufacturing on electric vehicle life-cycle greenhouse gas emissions". In: *ICCT* (February 2018). Available at `https://theicct.org/publications/EV-battery-manufacturing-emissions`.